EXPERIMENTAL AND FIELD BASED INVESTIGATIONS INTO THE BEHAVIOR OF ZIRCON IN HYDROTHERMAL AND DEEP-TECTONIC ENVIRONMENTS DURING MOUNTAIN-BUILDING AND CRUSTAL-EVOLUTION EVENTS.

By

Timothy J. Peters

Dissertation

Submitted to the Faculty of the

Graduate School of Vanderbilt University

in partial fulfillment of the requirements

for the degree of

DOCTOR OF PHILOSOPHY

in

Environmental Engineering

Vanderbilt University

August, 2012

Nashville, Tennessee

Approved:

Dr. John Ayers Ph.D

Dr. James Clarke Ph.D

Dr. George Hornberger Ph.D

Dr. Calvin Miller Ph.D

DEDICATION

To my parents,

For a lifetime of encouragement and support.

ACKNOWLEDGEMENTS

This work was made possible by the financial support of the National Science Foundation, grants EAR-0838391 and EAR-0510092, and the MOST special funds from the State Key Laboratory of Continental Dynamics, Department of Geology, Northwest University, Xi'an, China, and the State Key Laboratory of Geological Processes Mineral Resources, China University of Geosciences, Wuhan, China, grants National Nature Science Foundation of China (40973020) and Chinese Ministry of Education (B07039).

I am particularly grateful to Professor John C. Ayers, who provided me the opportunity to move from my home country of England and live in the United States, and who guided and supported my intellectual growth through completion of my studies at Vanderbilt University.

I am also grateful to Professor Calvin Miller and Professor Shan Gao, who played important roles during my studies, providing valuable insights, knowledge, and guidance, and Professor James Clarke and Professor George Hornberger for their important roles as members of my dissertation committee.

For those who have provided help and assistance during my research, I owe a large thanks to Aaron Covey for support with collection of a number of fundamentally important images that have provided significant insights for my research, to Rossane Delap and Dr Yan Luo for guidance with collection of LA-ICP-MS data, to Dr Xiaoming Liu and his colleagues at the State Key Laboratory of Continental Dynamics, Northwest University, Xi'an, China, for use of their MC-LA-ICP-MS, to Dr YuanBao Wu for his assistance in collecting samples in China and his knowledge of sampling locations, to Professor Charles M. Lukehart and Andrew Harris in the Department of chemistry for assistance collecting XRD information, and to Professor Graham Layne And Dr Glenn Piercey at Memorial University for use of their SIMS.

Finally, I am grateful to the community of people, past and present, who have worked or studied in the Department of Earth Sciences at Vanderbilt University, and my supportive friends and who have made the experience of being a student an enjoyable and rewarding one.

TABLE OF CONTENTS

LIST OF TABLES

LIST OF FIGURES

CHAPTER II:

CHAPTER IV

CHAPTER I

INTRODUCTION

1. Overview.

The mineral zircon (nominally $ZrSiO_4$) is a particularly robust geochronometer and arguably one of the most important minerals available to study the geochemical and geodynamic evolution of the Earth (e.g. Amelin et al., 1999, 2000; Mojzsis et al., 2001; Wilde et al., 2001; Valley et al., 2005; Watson and Harrison 2005; Harrison et al., 2005; Liu et al., 2006; Zheng et al., 2007; Rubatto and Hermann 2007; Harley et al., 2007; Liu and Liou 2011). Zircon's fame is fundamentally tied to its ability to accommodate significant quantities of the radioactive elements Th and U, whilst rejecting Pb, leading to large parent/daughter isotopic ratios (i.e. $^{238}U/^{206}Pb$) and highly precise U-Pb dates (e.g. Harley and Kelly 2007). During residence in the crust, the strong chemical bonds in zircon result in extremely low rates of chemical diffusion, preventing disturbance to the U-Pb geochronological system, even during ultrahigh temperature metamorphism (T = 900–1100°C) (Harley 1998; Cherniak and Watson, 2003; Cherniak 2010).

Zircon has a robust crystalline lattice, and one that can survive extreme pressures (van Westrenen et al., 2005), temperatures (>800°C to ~1670°C: Vaczi et al., 2009), and mechanical reworking (e.g. Claouelong, et al., 1991). Further to this, the incompatibility of Zr in nearly all major rock forming minerals makes zircon a ubiquitous mineral phase in most geochemical environments, and the low solubility of zircon in crustal fluids (silicate melts and aqueous fluids) makes zircon a largely chemically inert mineral (e.g. Ayers and Watson 1991; Miller et al., 2003; Rubatto and Hermann 2007).

Zircon grains extracted from high-grade metamorphic rocks frequently display evidence of alteration, recrystallization, or new-growth associated with metamorphic overprint (e.g. Corfu et al., 2003; Rubatto and Hermann 2007). Micro-geochemical analysis (typically ~10-40 µm diameter analysis spot) of these metamorphic zircon domains yields U-Pb dates that are routinely interpreted to represent the timing of peak metamorphic conditions (e.g. Wu et al. 2006, and references therein). Despite advances in the spatial resolution and precision of zircon trace-element and isotopic micro-geochemical analysis, we are still limited in our understanding of the conditions and mechanisms responsible for zircon recrystallization and growth during metamorphism, and therefore in our ability to accurately interpret U-Pb ages of metamorphic domains. Because high pressure (HP) and ultra-high pressure (UHP) metamorphic rocks are witnesses to the most extreme tectonic and metamorphic processes associated with mountain-building events and crustal recycling, linking the trace-element and isotopic geochemistry of in-situ zircon grains to their metamorphic environment remains one of the most vital yet unresolved barriers to understanding HP/UHP metamorphic geodynamics.

Geochemical and textural evidence suggests that metamorphic domains in zircon grains from high-grade metamorphic rocks grow or recrystallize under sub-solidus conditions in the presence of hydrous metamorphic fluids, which are typically dominated by H_2O and minor amounts of CO_2 (e.g. Carson et al., 2002; Corfu et al., 2003; Breeding et al., 2004; Manning 2004; Rubatto and Hermann 2003, 2007; Geisler et al., 2007; Gerdes et al., 2009; Wu et al., 2006, 2009). Considerable uncertainty, however, limits our understanding of hydrothermal fluids in deep crustal environments (see Hack et al., 2007). Fluids produced during progressive high/ultra-high-pressure metamorphism are considered to be limited in volume relative to prior stages of prograde metamorphism (e.g. Bebout 2007; Yardley 2009), and generated by decomposition of the few remaining hydrous phases (e.g. phengite, epidote, lawsonite,

zoisite/clinozoisite: see review in Zhang et al., 2011). Compositions of primary metamorphic fluids are variable and determined by specific metamorphic conditions and whole rock compositions. Evidence of primary metamorphic fluids can be erased by fluid escape, metamorphic recrystallization, and secondary fluid production events at lower-grade conditions.

A number of experimental approaches have been used to characterize trace-element partitioning behavior between fluids and rocks or minerals at high-grade metamorphic conditions (e.g. Ayers and Watson 1991; Keppler 1996; Kessel et al., 2005; Feineman et al., 2007; Spandler et al., 2007). These experimental studies have provided a broad framework to evaluate measured trace element compositions of metamorphic mineral grains believed to have grown in the presence of metamorphic fluids. However, to date no experimental studies have been performed to identify trace element signatures in zircon that are characteristic of hydrothermal growth. Without this information, we cannot identify "hydrothermal" zircon grains or assign measured zircon U-Pb dates to hydrothermal events.

The primary objective of my research is to identify and characterize the effect of hydrothermal fluids on zircon growth and recrystallization, and explore the behavior of zircon during HP/UHP metamorphism.

Specifically, it has been my intention to:

1. Identify the influence of metamorphic fluids and host-rock geochemistry upon the mechanism of U-Pb age resetting for natural zircon grains from HP/UHP rocks.
2. Experimentally measure zircon/fluid trace element partition coefficients at HP/UHP conditions.
3. Identify chemical characteristics that can be used to distinguish zircon grains grown from hydrothermal fluids and silicate melts.

The importance of this research will be in expanding our understanding of high-grade metamorphic fluid-mineral and fluid-rock reactions and their effects on measured radiometric ages. Results can be applied to aid interpretations of the chronology of high-grade crustal metamorphic terrain formation, improve our ability to trace metamorphic fluids in deep tectonic environments, and increase our understanding of continent scale geodynamic and geochemical processes.

2. Approach:

2.1. Central China Field based study:

The field- based studies are focused upon the Hong'an-Dabie segment of China's extensive Qinling-Tongbai-Hong'an-Dabie-Sulu orogenic belt (Fig. 1). The region exceeds 10,000 km^2 and comprises a diverse suite of metamorphic lithologies that document a protracted period of continental convergence associated with the modern tectonic configuration of China. In the eastern portion of the belt, the Hong'an, Dabie, and Sulu metamorphic terrains preserve in-situ coesite and diamond, and are one of only a few places on earth that record subduction of continental material to depths $\geq$125 km (e.g. Xu et al., 1992). Due to the large surface-area of exposure and the extreme inferred depths of continental subduction, the region has been the subject of intense interest over the last ~25 years, with numerous discoveries that have advanced our understanding of mountain building and the behavior of tectonic plates.

Specifically, the region has become particularly famous owing to the presence of an unusually large number of eclogite bodies (Fig. 2), of which a large percentage contain zircon, abundant hydrous phases (talc, zoisite/epidote, phengite), coesite and diamond (Fig. 2), with some of the highest pressure- temperature equilibration conditions recorded (Liou et al., 2000).

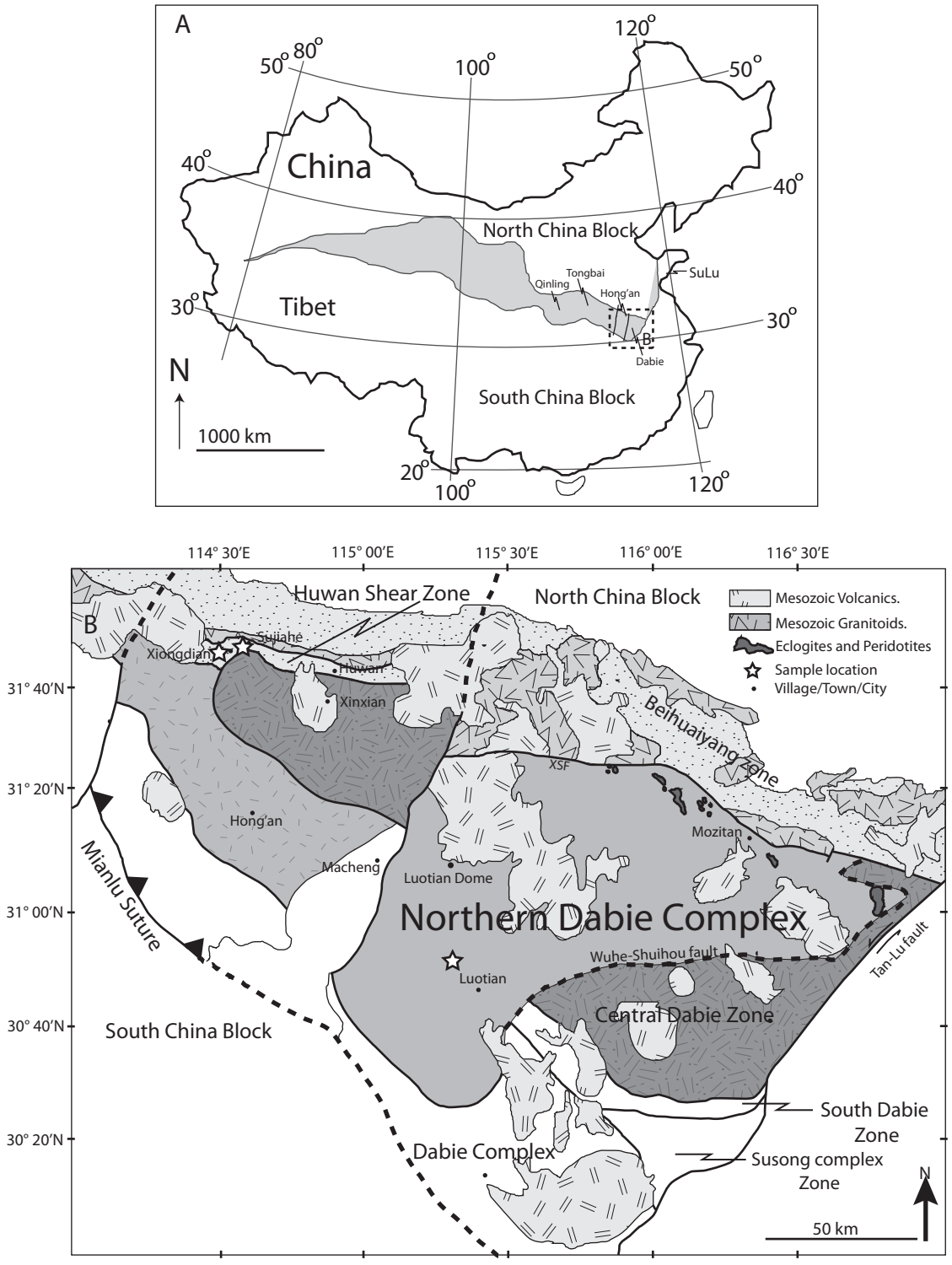

Figure.1. (A) Map of China, the grey shaded region represents the extensive Paleozoic-Mesozoic central China orogenic belt, which includes, from west to east, the Qinling, Tongbai, Hong'an, Dabie and Su-Lu orogenic blocks. (B) Schematic tectonic map of the Dabie orogen, showing the Northern Dabie Complex, Huwan Shear Zone, and the location of samples collected for this study this area. Compiled after Bryant et al (2004), Zhao et al., (2008) and Liu et al., (2011).

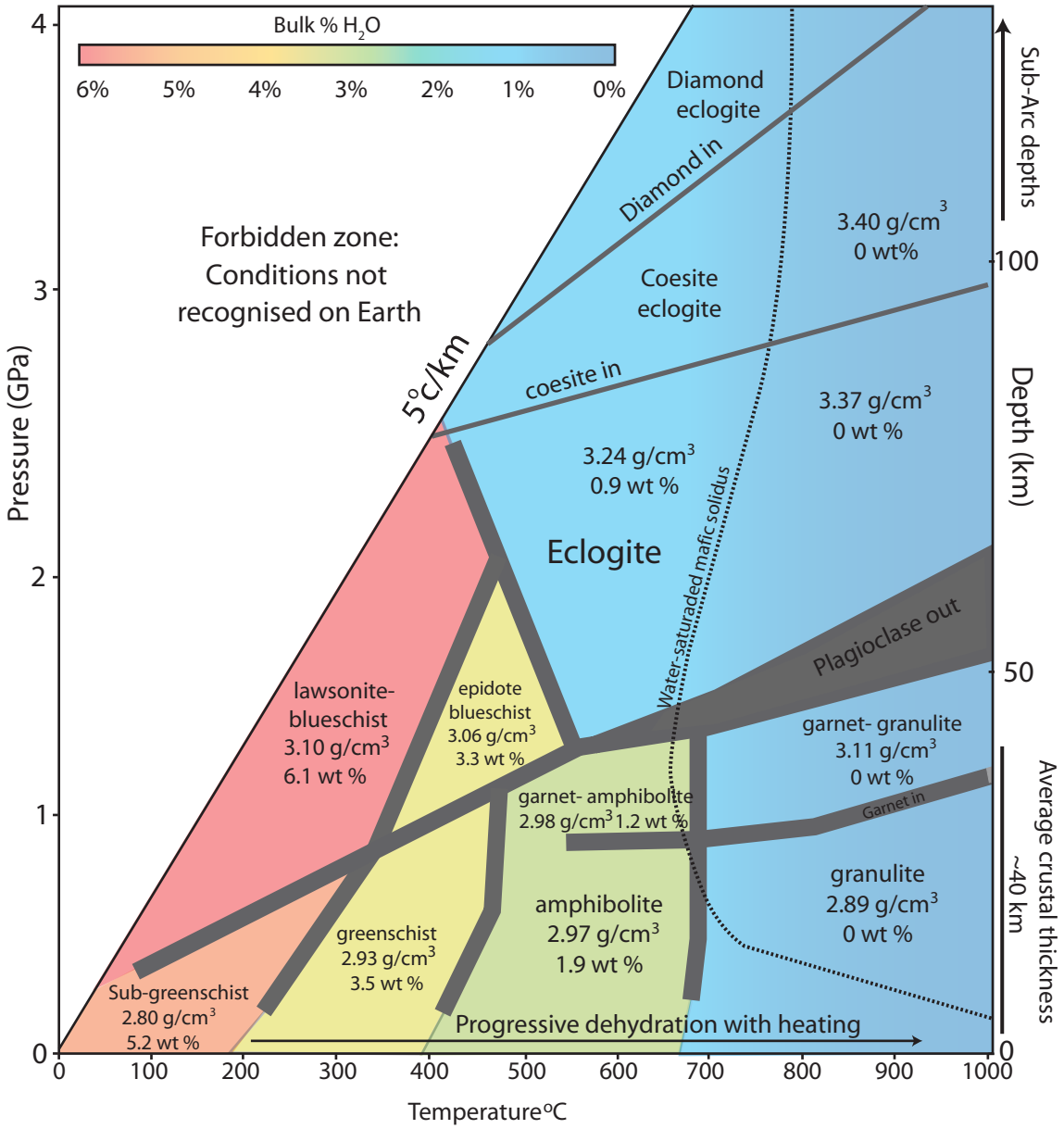

Figure. 2. Metamorphic facies during metamorphism of mafic crustal lithologies: after Hacker (2006) and references therein. The numbers beneath each facies name are their respective density (g/cm^3) and water contents (H_2O wt.%). Note that no metamorphic facies occur at pressures greater than the Eclogite facies; higher pressures only introduce higher density minerals to an eclogite assemblage (i.e. coesite and diamond).

Eclogites within the region have also become the focus of extensive investigations into the influence of fluids on the evolution of metamorphic systems at the base of the crust. This is largely due to eclogites containing a mineralogy that, relative to felsic meta-lithologies, is less susceptible to retrograde metamorphic overprint, leading to the preservation of HP/UHP phases (i.e. coesite) during exhumation and retrograde metamorphism. Many studies make use of accessory minerals that can preserve features generated during high- grade metamorphism. Zircon has proven to be ideally suited for this approach (Wu et al., 2006, 2009; Zhang et al., 2006; Zheng et al., 2003, 2007).

In chapters two and three I describe the results of work performed in collaboration with researchers in two institutions in China, the Key Laboratory of Continental Dynamics at Northwest University in Xi'an, and the Faculty of Earth Sciences at China University of Geosciences in Wuhan. Our objective was to further understanding of the behavior of zircon in eclogite during continental subduction. Our approach has been to integrate whole-rock compositional and Sr-Nd isotopic data with in-situ measurements of zircon trace-element concentrations and U-Pb and Lu-Hf isotopes for eclogite samples from the western portion of the Huwan Shear Zone (HSZ: Fig. 1 in Chapter 2) and a tonalite gneiss from the Luotian Dome (Fig. 1 in Chapter 3). For each location I evaluate geochemical and geodynamic models of the formation of eclogite protoliths and subsequent HP/UHP metamorphism using zircon geochemistry as a tool.

2.2. Zircon/fluid partitioning experiments:

A significant limitation on the interpretation of zircon U-Pb ages in metamorphic rocks is the lack of complementary experimental studies that aim to identify trace-element signatures

diagnostic of different zircon growth environments or recrystallization mechanisms, i.e., magmatic, metamorphic, or hydrothermal.

The approach of my experimental study has been to build upon prior zircon-melt and zircon-fluid experimental research projects performed at Vanderbilt University by synthesizing zircon from its oxide components (SiO_2 and ZrO_2) in the presence of a trace-element doped hydrothermal fluid (H_2O, NaOH, HCl). The focus of the study has been to develop criteria to use trace elements as diagnostic tools for identifying hydrothermal zircon grains precipitated from aqueous fluids and to reconstruct compositional features of metamorphic fluids from compositions of hydrothermal zircon grains from metamorphic rocks. I focus on HP conditions (1.5 GPa: Fig. 2) in the eclogite facies where the behavior of trace elements and fluids are not well known, and at temperatures high enough that equilibrium is likely to be maintained (800°C to 900°C). The results of this study are discussed in Chapter 4.

3. Metamorphism and fluids.

The impact of fluids and volatile components (dominantly H_2O and CO_2) upon metamorphic and crustal evolution processes is a subject of substantial importance (e.g. Watson and Harrison, 2005; Valley et al., 2005; Hawkesworth and Kemp 2006; Yardley, 2009; Jamtveit and Austrhein, 2010; Putnis and Austrheim 2010). Metamorphic fluids exert a fundamental control over geodynamic and geochemical processes by:

- Catalyzing mineral reactions, especially those required for eclogitization (e.g. Rubie 1986; Austrhein 1987; Pennacchioni 1996).
- Changing the melting temperatures of earth materials (e.g. Yoder and Tilley 1962; Kushiro 1969, 2007).

- Acting as agents for chemical and thermal transfer (e.g. Elliott et al., 1997; Spandler et al., 2003, 2006; Hermann et al., 2006).
- Altering the rheology of rocks by increasing their ductility and hence degree of deformation (e.g. Etheridge et al., 1984; Koch et al 1989; Tsang 1991; Spear 1993; Engvik et al., 2001, 2005).

3.1. Generation of fluids during HP/UHP metamorphism.

During subduction of continental crust progressive metamorphism from greenschist facies to amphibolite- or blueschist-facies (Fig. 2) leads to the high pressure and low temperature breakdown of hydrous-phases through a complex series of continuous mineral reactions that progressively dehydrate the crust and produce hydrous fluids (e.g. Peacock, 1993; Poli and Schmidt, 1997, 2002; Breeding et al., 2003). Approaching lower crustal depths (1 to 3 GPa), the transition from amphibolite and blueschist to eclogite facies (Fig. 2) in mafic lithologies causes a significant reduction in the number and modal abundance of hydrous phases. Eclogites consist primarily of garnet and clinopyroxene, often with trace amounts of one or more hydrous phases such as Paragonite, Phengite, Glaucophane, Crosstie, Zoisite, Clinozoisite, and Lawsonite (Kogiso et al., 1997; Poli and Schmidt, 1997; Bebout et al., 1999; Cartwright and Barnicoat, 1999; Becker et al., 2000; Spandler et al., 2003; Spandler and Hermann , 2006; Wu et al., 2006; Zhang et al,. 2009).

3.2. The nature and composition of metamorphic fluids:

Our constraints upon the composition of hydrothermal fluids produced during HP/UHP metamorphism is largely limited to experimental and theoretical studies. As summarized and discussed in Manning (2004), Hack et al., (2007) and Liebscher (2010), the water molecule's polar character and its ability to dissociate make it a powerful ionic solvent in geochemical

systems. For a pure H_2O system, as temperatures and pressures increase along the liquid-vapor boiling curve, the short-range ordering of H_2O molecules in liquid water begins to break down. Upon reaching the first critical point, the system transitions from a two-phase mixture to a single super-critical fluid, where the hydrogen-bond network becomes highly disordered and H_2O acts as a molecular solvent, rather than a polar solvent (e.g. Manning 2004; Hack et al., 2007). It is thought that supercritical aqueous fluids are generally dilute, but as pressure and temperature increase, solute contents increase until a second critical point is reached, above which aqueous fluids and hydrous silicate-melts are completely miscible. Thus, at conditions corresponding to the earth's lower crust and upper mantle (i.e. ~1.0 GPa and 750–1130 °C) supercritical aqueous fluids are likely to be effective metasomatic agents (Newton and Manning, 2008).

At the elevated temperatures experienced during eclogite facies metamorphism (i.e. > 600°C: Fig. 2), mineral-fluid reaction rates are high so that, at the meter scale, metamorphic systems are generally at or close to chemical equilibrium. As a result, the composition of any fluid produced in the eclogite facies during continental subduction will be controlled by the pressure, temperature, and whole rock composition. Thermodynamic models developed to predict the major element compositions of fluids at these high pressures and temperatures, however, can be quite complex, and we currently lack the thermodynamic data required for advancement of these models.

In contrast, the behavior of trace elements that obey Henry's Law is quite simple (Eq. 1). For trace element i at equilibrium, the partition coefficient ($D_i^{zircon/fluid}$) will equal the concentration recorded in the zircon (C_i^{zircon}) over that of the fluid (C_i^{fluid}):

Eq. 1. $$D_i^{zircon/fluid} = C_i^{zircon}/C_i^{fluid}.$$

For a given element, the value of the partition coefficient and the measured concentration of the element in a hydrothermal zircon domain allows estimation of the concentration in the fluid at the time of zircon growth. Thus, my objective was to measure trace element partition coefficients over a range of temperatures and fluid compositions.

4. Zircon:

4.1. Zircon and HP/UHP metamorphism:

Zircon grains extracted from rocks that have experienced continental subduction commonly display textural and geochemical evidence of growth, replacement, and recrystallization associated with HP/UHP metamorphism (Fig. 3). It is proposed and generally accepted that a mobile catalyzing hydrothermal component is required to overcome the thermodynamic barriers that would otherwise prevent zircon from recrystallizing during sub-solidus crustal metamorphism (e.g. Tole, 1984; Rubie, 1986; Shina et al., 1992; Ayers et al., 2003; Salje and Zhang 2006; Geisler et al., 2007; Carlson 2010). This is supported, in part, by the observation of resorption textures and zircon rims (Fig. 3 D-F) on pre-existing cores, which are thought to represent new growth associated with localized fluid segregation and Zr transport, and the occurrence of rare HP/UHP metamorphic mineral inclusions (i.e. garnet, omphacite, coesite, diamond), indicating co-genetic HP/UHP growth (e.g. Rubatto and Hermann, 2003; Wu et al., 2006; Rubatto and Hermann 2007; Rubatto et al., 2008; Riemann et al., 2009).

Despite extensive documentation of zircon hydrothermal growth and fluid alteration during high-grade metamorphism, it remains difficult to identify the responsible fluid generating reactions and their specific PT conditions. This severely limits our ability to link zircon U-Pb dates to specific PT conditions during continental subduction and exhumation (Zheng 2009).

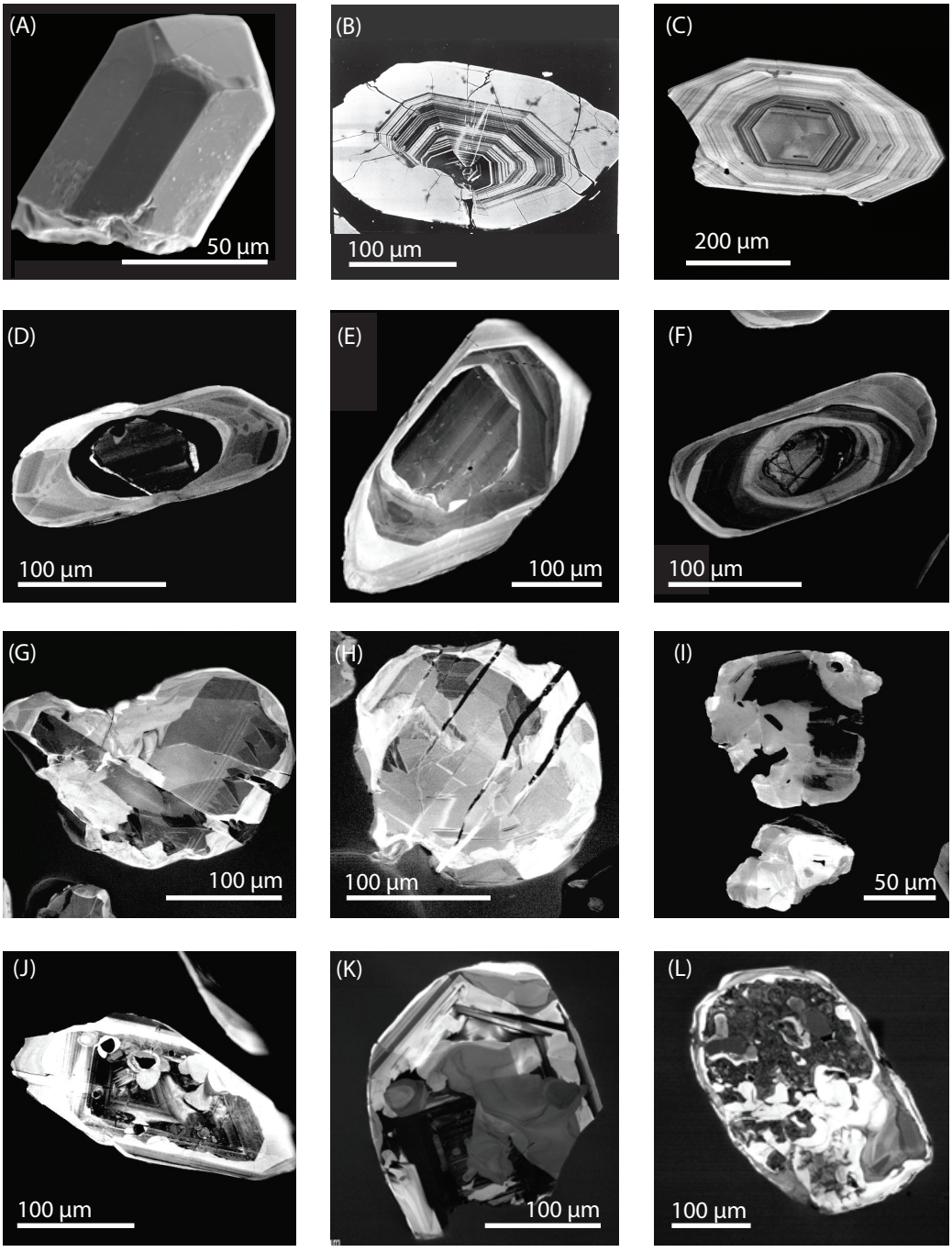

Figure. 3. (A) Secondary Electron image of a zircon grain displaying tetragonal crystal form. (B-L) Cathode Luminescence images of zircon grains from magmatic and metamorphic rocks. (B) Image from Ayers et al., (2003) and (C) from Claiborne et al., (2010). Note clear oscillatory zoning, typical of zircon crystallization from a magmatic component. All others are un-published images of zircon grains in rocks collected from the Dabie-Sulu metamorphic terrain. (D-F) Zircon grains display clear core-overgrowth components. Growth of external components is thought to have occurred during metamorphism and domains lack clear evidence of magmatic zonation. (G-H) Fractured and sheared zircon grains with complex crystal forms. (I) Zircon aggregate. (J-L) Complex internal zonation patterns and inclusions, thought to represent extensive hydrothermal alteration during metamorphism.

Wu et al. (2006) proposed that during eclogite-facies HP/UHP metamorphism of the Dabie-Sulu metamorphic terrain, new zircon growth occurred either during prograde metamorphism, in response to fluid produced at temperatures of 500–700°C by the dehydration of hydrous bearing phases such as paragonite, chlorite, biotite, serpentine, glaucophane, and amphibole, or during immediate post-peak retrograde metamorphism through decomposition of low-temperature hydrous minerals, such as lawsonite, during heating that can occur with exhumation, or through decompressive exsolution of hydroxyl from nominally anhydrous phases such as omphacite, garnet, and rutile. During retrograde stages, it is also thought that Zr and Hf for zircon growth may be released or exsolved from clinopyroxene/omphacite (Schmitz and Bowring, 2000), garnet (Fraser et al., 1997; Degeling et al., 2001), hornblende (Fraser et al., 1997), or ilmenite (Bingen et al., 2001).

Alternatively, zircon recrystallization can cause geochemical and isotopic re-equilibration of zircon via a number of important mechanisms, including interface-coupled dissolution-reprecipitation (Tomaschek et al., 2003; Geisler et al., 2007; Rubatto et al., 2008), coarsening/Ostwald ripening and defect migration (Hoskin and Black, 2000; Ayers et al., 2003), and deformation-enhanced diffusion along high diffusivity pathways (Timms et al., 2006; Reddy et al., 2006, 2009), that can occur independently or be coupled mechanisms. Nevertheless, it remains unclear how zircon trace-element and isotopic features are affected by these mechanisms, and how their resulting features may be used to constrain the presence and influence of metamorphic fluids (e.g. Wu et al., 2006).

4.2. Zircon solubility in hydrothermal fluids:

In HP/UHP terrains, the rare occurrence of ZrO_2 in fluid inclusions (e.g. Philipot and Selverstone 1991) and zircon in eclogite-facies quartz veins (e.g. Williams et al 1996), suggests

some mobility of Zr in metamorphic fluids associated with high-grade metamorphism and continental subduction. In regions containing metasomatized mafic and ultra-mafic rocks (i.e. subduction zone melanges containing serpentinite, jadeitite, albitite, and rodingite), unusually high Zr and Hf concentrations have been recorded and provide evidence of extensive hydrothermal fluid flow and Zr mobilization during HP/LT metamorphism and oceanic crust subduction (e.g. Bebout, 2007). These melanges preserve important evidence of deep tectonic fluid-rock reactions and chemical-recycling pathways involving alkaline hydrothermal fluids (Brocker and Enders, 1999, 2001; Dubinska et a., 2004; Tsujimori et al., 2005; Sorensen et al., 2010).

The hydrothermal dissolution of many metal cations typically involves formation of aqueous complexes and solvation shells containing H_2O molecules in the primary shell (i.e. inner sphere). Due to its high charge, low ionic radius (r = 0.84Å) in 8-fold coordination (Shannon, 1976), and a high ionic potential (surface charge density, z/r = 4/0.84 = 4.8), Zr^{+4} falls into the High Field Strength Element group (HFSE: including: Ti, V, Zr, Nb, Hf and Ta). The high ionic potential of Zr^{+4} results in repulsion of the H^+ on the coordinating H_2O molecules, promoting dissociation of H_2O and formation of Zr-hydroxyl complexes (Langmuir, 1997). At ambient conditions (i.e. 25°C), the neutral tetrahydroxide species ($Zr(OH)_4$) is the dominant form for dissolved Zr^{+4} over a wide range of fluid pH. Formation of neutral complexes in near-neutral pH hydrous fluids results in very low solubilities of minerals containing Zr and other HFSE.

The dissolution of zircon in H_2O is expected to occur incongruently, beginning with the formation of aqueous species of Zr and Si (Tole 1985):

Eq. 2. $$ZrSiO_{4\,(xt)} + 4H_2O = Zr(OH)_4 + H_4SiO_4$$

Eq. 3. $$Keq = a\,Zr(OH)_4 \times a\,H_4SiO_4 = 2.48x10^{-17}$$ at 25°C.

Followed by the precipitation of baddeleyite (ZrO_2) upon reaching saturation:

Eq. 4. $$Zr(OH)_4 = ZrO_{2(xt)} + 2H_2O$$

As fluid pH changes, these Zr-hydroxyl complexes display an amphoteric behavior, being able to donate or accept a hydrogen cation (i.e. proton). This feature makes the solubility of Zr-phases pH-dependent with the formation of other Zr-hydroxide complexes in the fluid: i.e. $Zr(OH)^{+3}$, $Zr(OH)_2^{+2}$, $Zr(OH)_3^{+}$, $Zr(OH)_4^{0}$, and $Zr(OH)_5^{-}$. Under low pH conditions, positively charged Zr-hydroxide complexes stabilize (e.g. Migdisov et al., 2011), while high pH conditions stabilize negatively charged Zr-hydroxide complexes yielding a U-shaped solubility curve (Fig. 4) (e.g. Ayers et al., in revision).

At higher pressures and temperatures, the dissociation of H_2O increases, raising the activities of H+ and OH^- in water. At sub-arc depths, the neutral pH of water becomes 3-4 (e.g. Manning 2004). Zircon solubility experiments at these conditions (Temperatures of 800-1200°C, and Pressures of 1.0-3.0 GPa), by Ayers and Watson (1991), noted the solubility of zircon, while still extremely low for all experiments, was considerably higher than those conducted at ambient conditions.

4.3. Zircon as a tool for reconstructing geochemical and geodynamic processes:

Zircon is an orthosilicate with isolated $[SiO4]^{4-}$ tetrahedra connected only by interstitial Zr cations to form a tetragonal crystalline lattice. Zircon's simple structure has two sites for cation substitution: Firstly, a tetragonal (Si) site, and secondly, a triangular dodecahedral (Zr) site (Speer, 1980). The most common mineral solid-solutions with the zircon structure include Hafnon (HfSiO4), Thorite, (ThSiO4), Coffinite (USiO4) and Xenotime (YPO4) (Hoskin and Schaltegger 2003; Ferriss et al., 2010).

Zircon's crystalline lattice can accommodate a diverse suite of trace-elements of interest to petrologists and geochemists, preferentially incorporating many ppm of the Rare Earth

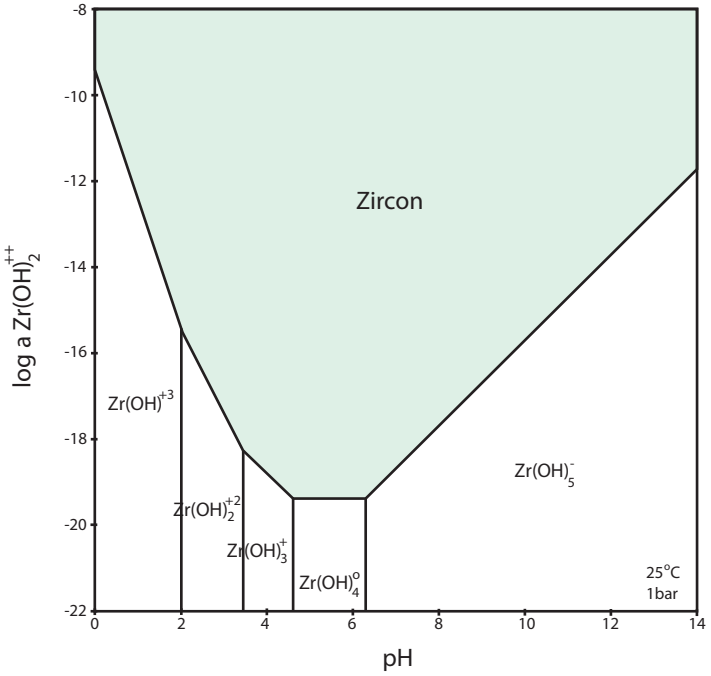

Figure. 4. The solubility of zircon in a quartz-saturated fluid at ambient conditions, reproduced from Ayers et al., (in revision).

Elements (REE: notably middle REE (MREE) and heavy REE (HREE)), Ti, Hf, Nb, Th and U, while excluding lead (Fig. 5), making it ideal for U-Pb geochronology (e.g. see below and reviews in Hoskin and Schaltegger, 2003; Finch and Hanchar, 2003; Harley and Kelly, 2007b).

Due to their isovalent +3 electronic configuration the REE (except Eu^{+2} and Ce^{+4}) typically exhibit a similar geochemical behavior and enter the same zircon structural site (Hanchar and van Westrenen 2007). Since the ionic radii of REE decrease continuously from LREE (e.g. La^{+3} 1.160 Å) to HREE (e.g. Lu^{+3} 0.977 Å) (values from Shannon, (1976) for octahedral (8-fold) coordination), known as the lanthanide contraction, REE partitioning into zircon favors the MREE and HREE, as the $HREE^{+3}$ radii approach that of Zr^{+4}: 0.84 Å; resulting in positively trending chondrite normalized zircon REE profiles (Fig. 5b) that flatten as they approach Lu (Finch et al., 2001; Hanchar et al., 2001; Hoskin and Schaltegger, 2003; Finch and Hanchar, 2003; Luo and Ayers 2009).

Zircon REE partitioning experiments by Finch et al., (2001) and Hanchar et al., (2001) highlighted the importance of P^{+5} substitution for Si^{+4}, allowing the charge-coupled substitution of M^{+3} (i.e. REE^{+3}) for Zr^{+4}. This substitution mechanism, the xenotime substitution, is particularly important for allowing REE^{+3} to partition into zircon. Although the ability of zircon to incorporate the REE^{+3} through the xenotime substitution mechanism is limited (Hanchar et al., 2001), other substitution mechanisms involving pentavalent cations V^{+5}, Nb^{+5}, and Ta^{+5} can occur (Hoskin and Schaltegger, 2003; Luo and Ayers, 2009).

Eq. 5. $$M^{+3} + N^{+5} = Zr^{+4} + Si^{+4}$$

Trivalent cations: REE, Ce (reduced), Eu, Y, Al, Cr, Sc, Mn

Tetravalent cations: Zr, Si, Hf, Ti, U, Th, Ce (oxidized)

Pentavalent Cations: P, Ta, Nb, V

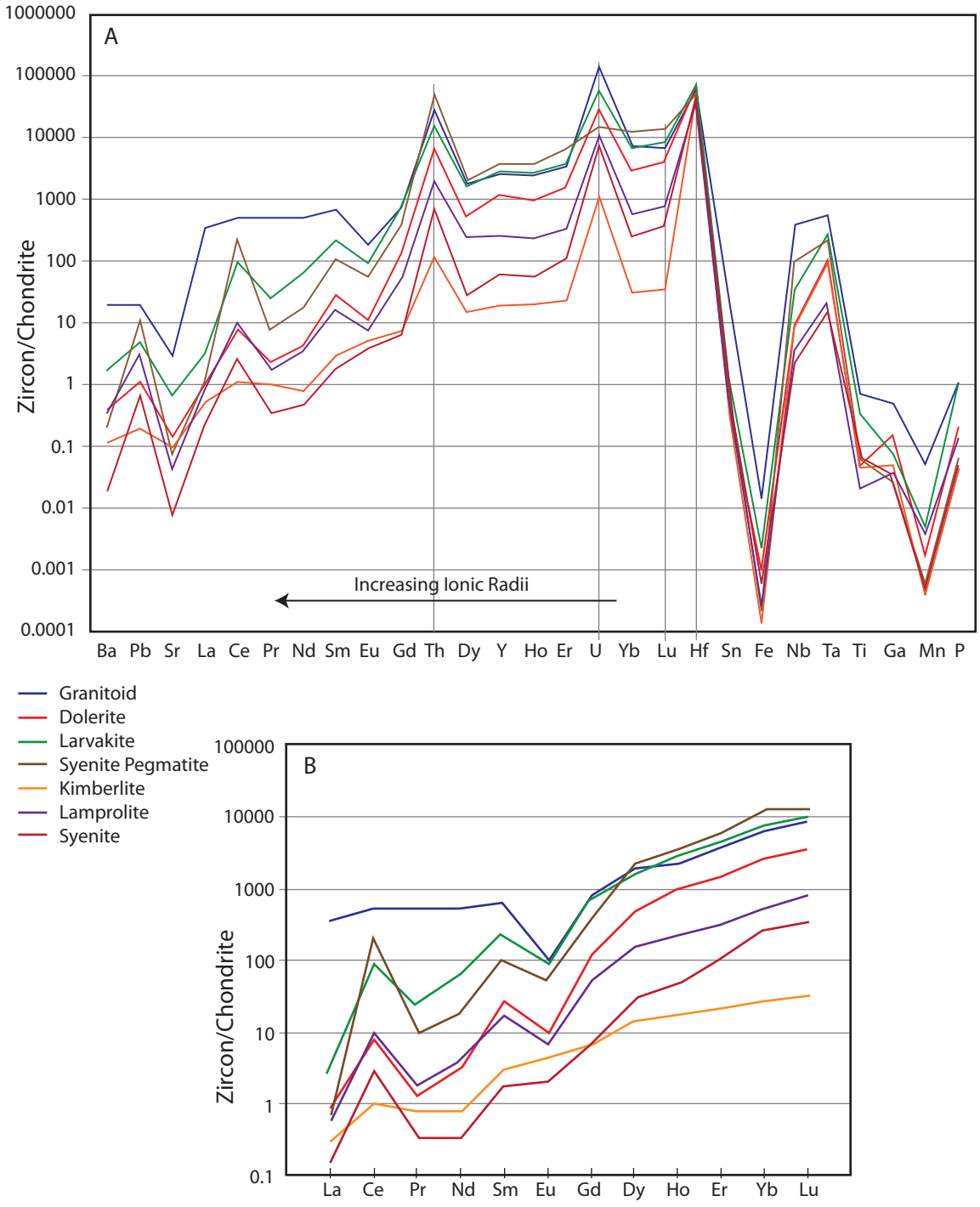

Figure. 5. (A) Fig. 1. Chondrite-normalised averaged trace element abundances of zircons from different rock types. (B) Chondrite-normalised averaged REE patterns of zircons from a range of rock types. Figures are reproduced from (Belousova et al., 2002).

4.4. Zircon Geochronology: The U-Pb isotopic system.

U-Pb dating involves the generation of isotopic ratios $^{206}Pb/^{238}U$ and $^{207}Pb/^{235}U$ measured in zircon grains to estimate the zircon crystallization age. With time, ^{238}U and ^{235}U decay to ^{206}Pb and ^{207}Pb, respectively. On a plot of $^{206}Pb/^{238}U$ vs. $^{207}Pb/^{235}U$ (Fig. 6) the set of points for which $^{206}Pb/^{238}U$ ages equal $^{207}Pb/^{235}U$ ages define the Concordia curve. Because U and Pb have large nuclei, very little fractionation of their respective isotopes occurs during natural processes. Provided no post-crystallization elemental fractionation or diffusion of either U or Pb in the zircon grain occurs, the measured $^{206}Pb/^{238}U$ and $^{207}Pb/^{235}U$ ratios will plot on, or within error of, the Concordia curve and their ages are termed concordant (Fig. 6). Analyses for which measured $^{206}Pb/^{238}U$ and $^{207}Pb/^{235}U$ ratios plot off the Concordia curve are termed discordant (Fig. 6). These grains experienced post-crystallization fractionation of Pb and U. Discordance may result from hydrothermal alteration or fluid-aided recrystallization of zircon.

4.5. Zircon Lu-Hf isotopes:

The decay of ^{176}Lu involves the emission of a beta particle and generation of a ^{176}Hf daughter atom. The half-life for this system is approximately 34.9 billion years, with a ^{176}Lu decay constant of 1.867×10^{-11} $year^{-1}$ (Soderlund et al., 2004). The Lu-Hf isotopic composition of a rock or mineral is expressed through the ratios $^{176}Lu/^{177}Hf$ and $^{176}Hf/^{177}Hf$, where ^{177}Hf has a constant natural abundance (See review in Kinny and Maas, 2003). The decay equation for this system is:

Eq. 6. $$^{176}Hf\ ^{177}Hf\ t = {}^{176}Hf\ ^{177}Hf\ o + {}^{176}Lu\ ^{177}Hf\ \ e^{-\lambda t} - 1$$

Zirconium (Zr) and hafnium (Hf) are both HFSE with identical +4 charges and near-identical radii: 0.84 and 0.83 Å (8-fold coordination), respectively (Shannon, 1976). As a result, Zr

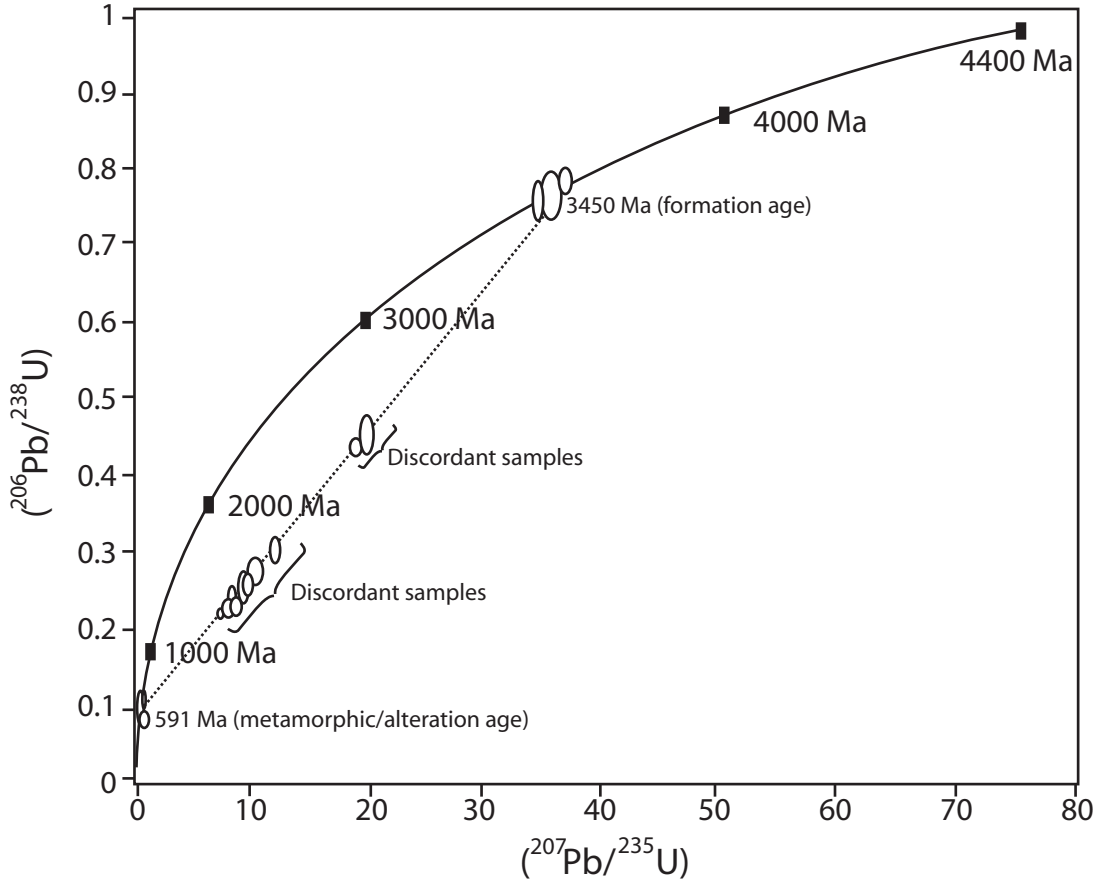

Figure. 6. Schematic U-Pb concordia diagram, after Harley and Kelly (2007).

and Hf are particularly difficult to fractionate from one another during most geochemical processes and typically display a coupled behavior (e.g. Claiborne et al., 2006).

Due to their high relative incompatibility in most major rock-forming phases, Zr and Hf are usually concentrated in zircon, which subsequently controls the behaviors of Zr and Hf in rocks and by extrapolation the crust (e.g. Kemp et al., 2007). The Hf content of zircon can be up to a few tens of wt.%, and it is proposed that zircon ($ZrSiO_4$) and its isostructural partner hafnon ($HfSiO_4$) share a complete solid-solution relationship (Ramakrishnan et al. 1969; Ferriss et al,. 2010). While, as previously discussed, Lu is a compatible element in zircon, its concentration is insignificant relative to that of Hf. This results in $^{176}Lu/^{177}Hf$ ratios that typically range from 10^{-3} to 10^{-6} and subsequently near-negligible changes to their $^{176}Hf/^{177}Hf$ ratios over time (Fig. 7a).

4.5.1. Lu-Hf isotopes and evolution of the crust-mantle system.

During mantle melting and crust generation, Hf preferentially enters the melt-phase relative to Lu. This leads to differentiation into a crustal reservoir with a low Lu/Hf ratio, and a residual (i.e. depleted) mantle with an elevated Lu/Hf ratio. The original isotopic composition of the mantle prior to differentiation is considered to be analogous to that represented by undifferentiated rocky meteorites, termed chondrites, which have been used to calculate the "Chondritic Uniform Reservoir", known commonly under the abbreviation CHUR (DePaolo and Wasserburg 1976). With time, the Hf isotopic compositions of these two regions diverge from one another (Fig. 7a), leading to $^{176}Hf/^{177}Hf$ ratios in the crust that evolve on a lower gradient to the original mantle (i.e. CHUR, Fig. 7a: i.e. Bouvier et al., 2008) whilst the depleted mantle evolves on a higher gradient to the original mantle (Fig. 7a) (e.g. Blichert-Toft and Albarède 1997; Vervoort and Blichert-Toft 1999).

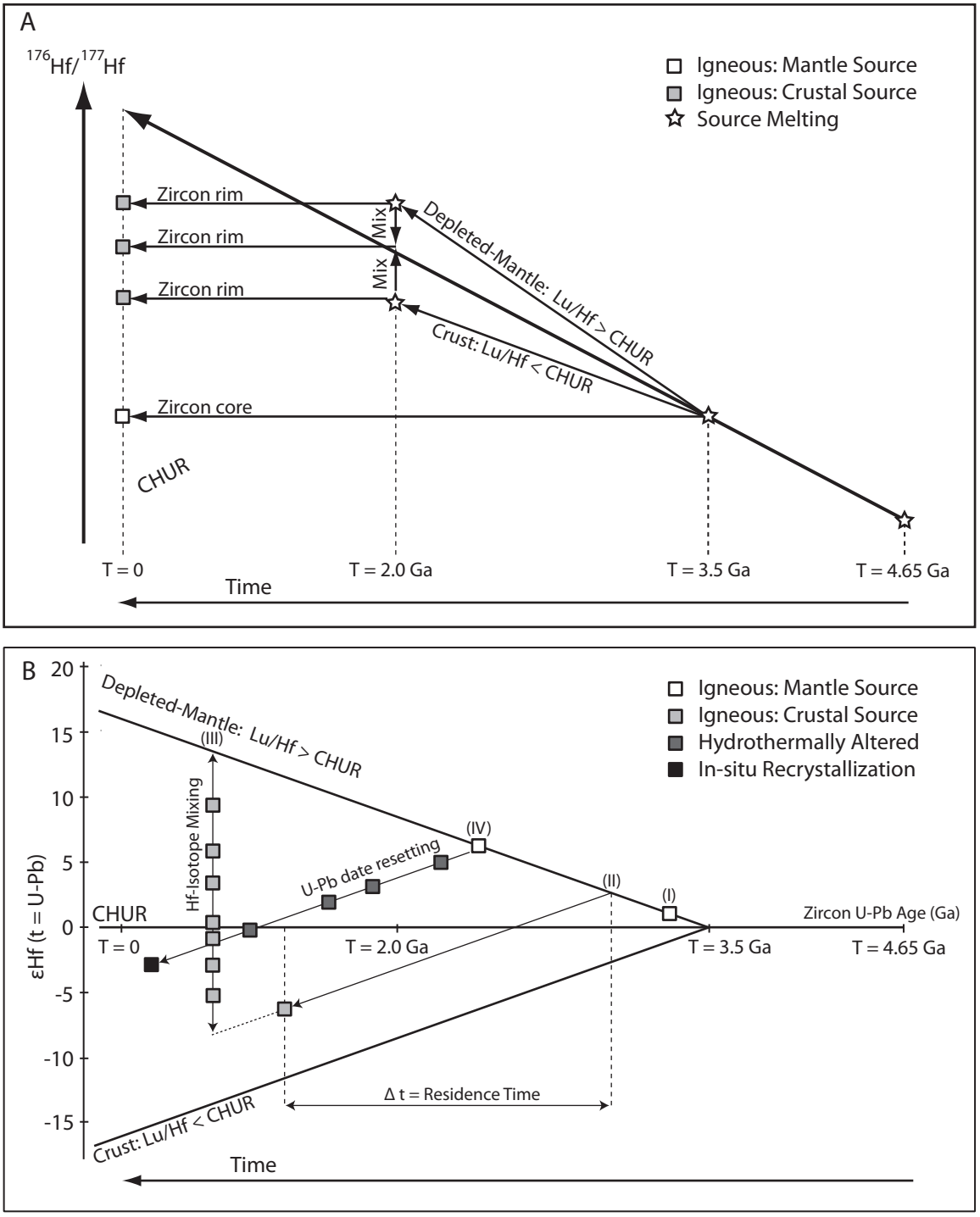

Figure. 7. (A) Schematic Hf isotope evolution diagram reproduced from Kinny and Maas (2003). (B) Schematic diagram of zircon εHf (t = U-Pb) vs. U-Pb age. See text for description.

The Lu-Hf isotopic system behaves similarly to the Sm-Nd isotopic system (i.e. ^{147}Sm decays to ^{143}Nd) during differentiation of the crust and depleted mantle, as described immediately above, although the differences in valence between Lu^{+3} and Hf^{+4} leads to significantly different geochemical behaviors relative to Sm^{+3} and Nd^{+3}. These differences include a greater sensitivity to elemental fractionation during crustal generation and evolution, and a greater resistance to mobilization, alteration, and isotopic resetting during metamorphism or surface weathering processes (e.g. Amelin et al., 1999; Harrison et al., 2005; Hawkesworth et al., 2010).

Provided no disturbance to the Lu-Hf isotopic system for a mineral, rock, or reservoir (i.e. closed system behavior), the timing of divergence or extraction from their source or the timing of closed system conditions attainment can be calculated when the Lu-Hf isotopic composition of the source is known (Eq. 7). In many cases the source is the depleted mantle and ages calculated using Eq. 7 are referred to as Depleted-Mantle (DM) melting model ages $T(Hf)_{[DM]}$)

Eq. 7.
$$T[Hf] \quad Ma = \frac{1}{\lambda} \times LN \frac{^{176}Hf\ ^{177}Hf_{Sample} - {}^{176}Hf\ ^{177}Hf_{DM}}{^{176}Lu\ ^{177}Hf_{Sample} - {}^{176}Lu\ ^{177}Hf_{DM}} + 1$$

where DM ($^{176}Hf/^{177}Hf$) = 0.28325 and ($^{176}Lu/^{177}Hf$) = 0.0384, from Vervoort and Blichert-Toft (1999).

Hafnium isotopic ratios are often expressed as εHf(t) values (Eq. 8), which normalize $^{176}Hf/^{177}Hf$ relative to CHUR at the time of crystallization, t:

Eq. 8.
$$\varepsilon Hf\ t = \frac{^{176}Hf\ ^{177}Hf_{Sample\ t}}{^{176}Hf\ ^{177}Hf_{CHUR\ t}} - 1 \times 10{,}000$$

Where CHUR $^{176}Hf/^{177}Hf$= 0.282785 and $^{176}Lu/^{177}Hf$ = 0.0336, from Bouvier et al. (2008), and t is typically its U-Pb age.

The majority of juvenile mantle melts that become new additions to the crustal reservoir originate from the depleted mantle, which formed during crust-mantle differentiation in the past (i.e. Fig. 7a). If a juvenile melt becomes saturated in zircon upon emplacement in the crust, the zircon grains will inherit the Hf-isotopic composition of the depleted mantle and display U-Pb dates that record the timing of mantle melting and crustal emplacement (Fig. 7b position I).

If zircon does not crystallize at the time of its crustal emplacement, the juvenile crustal component will migrate away from the DM evolution line and evolve on a gradient similar to that of the bulk-crust (Fig. 7b line II). In this case, the U-Pb age of zircon will record the timing of zircon crystallization in response to a crustal metamorphic or anatectic event, while the εHf(t) of zircon records the evolved whole rock Hf-isotopic composition at the time of crystallization t after emplacement in the crust, where Δt represents the residence of the crustal component between emplacement and recycling (Fig. 7b line II). This process is commonly referred to as a two-stage crustal formation or evolution model (e.g. Zheng et al., 2006).

The diffusivity of Hf in zircon is extremely low and effectively preserves its original $^{176}Hf/^{177}Hf$ ratio during residence in the crust (Cherniak 2010). Changes to the original Hf-isotopic composition of zircon can only occur if zircon recrystallizes and exchanges Hf isotopes with coexisting phases (Fig. 7b line III: i.e. crustal anatexis and high-grade metasomatism). This process can be recognized in grains that display core-overgrowth textural relationships, each with a distinct Hf-isotope composition and separated by a boundary that represents resorption prior to new growth. In many cases, however, Hf isotopes are not exchanged during zircon recrystallization, so that zones that are dissolved and reprecipitated by fluids preserve their original Hf-isotopic composition even when their U-Pb ages are entirely reset (Fig. 6) and (Fig. 7b line IV: i.e. Martin et al., 2008; Chen et al., 2010).

5. Structure of the Thesis

Here, I use complementary field and laboratory based approaches to explore the behavior of zircon during sub-solidus metamorphism. In chapters 2 and 3 I present two field based reports that integrate bulk-rock elemental and isotopic information with high-precision micron-scale in-situ U-Th-Pb and Lu-Hf isotopic and trace-element analyses of zircon, while chapter 4 comprises a laboratory based study of zircon/fluid trace element partitioning behavior.

For chapter 2, I address the behavior of zircon in eclogite using samples collected from the towns of Xiongdian and Sujiahe in the Huwan Shear Zone (HSZ), central China. The HSZ is one of a number of thin and highly deformed shear zones associated with formation of the Shangdan Suture, Hong'an-Dabie-Sulu HP/UHP metamorphic terrains, and construction of the modern Chinese continent.

Zircon grains from a sample of Sujiahe eclogites in this region display clear trace-element and isotopic evidence of dissolution-reprecipitation recrystallization during prograde in-situ hydrothermal fluid infiltration, and development of features that represent an equilibrium relationship with garnet growth and HP metamorphism. In contrast, analyses of zircon grains from our samples of the Xiongdian eclogite display a rather ambiguous response to metamorphic events. Despite this, we present evidence that outlines a history involving in-situ zircon recrystallization in response to fluid infiltration events. Focusing on the zircon Hf-isotopic composition for each sample locality, notably different $^{176}Hf/^{177}Hf$ distributions, provides additional constraints on the origin of zircon and crustal evolution processes operating prior to final HP metamorphism.

For chapter 3, I focus on further exploring the role of zircon Lu-Hf isotopes and U-Pb dates to constrain the nature of geodynamic processes and the timing of high pressure metamorphism using a tonalite sample collected from the Luotian Dome in the Northern Dabie Complex (NDC), central China. The NDC is a particularly famous metamorphic terrain and has received considerable attention through attempts to understanding metamorphic processes associated with continental subduction and crustal recycling. More recently, attempts to identify evidence of ultra-high pressure metamorphism have led some authors to reevaluate the Dabie mountain belt crustal architecture and propose alternate geodynamic models for continental subduction of the region.

Using zircon grains extracted from our sample, I discuss features that can be used constrain the origin of zircon during growth and evolution of the continental crust, and to unravel their subsequent behavior during continental subduction and metamorphism. I provide a critical evaluation on the use of zircon Lu-Hf isotopes to constrain the crustal architecture of a complex orogenic belt and highlight the limitations that may have been overlooked in recent published studies.

In chapter 4, I use an experimental approach to explore the geochemical composition of zircon grains grown in equilibrium with a high pressure hydrothermal fluid. This study represents the first ever attempt to measure zircon/hydrothermal-fluid (H_2O, NaOH, HCl) trace-element partition coefficients at high pressure metamorphic conditions. The project proved to be technically challenging and in this chapter I discuss the limitations and successes of the study along with chemical features that may be used to identify zircon grown in hydrothermal environments.

7. References:

Amelin, Y., Lee, D.C., Halliday, A.N., 2000. Early-middle Archaean crustal evolution deduced from Lu-Hf and U-Pb isotopic studies of single zircon grains. Geochimica Et Cosmochimica Acta 64, 4205-4225.

Amelin, Y., Lee, D.C., Halliday, A.N., Pidgeon, R.T., 1999. Nature of the Earth's earliest crust from hafnium isotopes in single detrital zircons. Nature 399, 252-255.

Austrheim, H., 1987. Eclogitization Of Lower Crustal Granulites By Fluid Migration Through Shear Zones. Earth and Planetary Science Letters 81, 221-232.

Ayers, J.C., De La Cruz, K., Miller, C., Switzer, O., 2003. Experimental study of zircon coarsening in quartzite +/- H2O at 1.0 GPa and 1000 degrees C, with implications for geochronological studies of high-grade metamorphism. American Mineralogist 88, 365-376.

Ayers, J.C., Watson, E.B., 1991. Solubility Of Apatite, Monazite, Zircon, And Rutile In Supercritical Aqueous Fluids With Implications For Subduction Zone Geochemistry. Philosophical Transactions Of The Royal Society Of London Series A-Mathematical Physical And Engineering Sciences 335, 365-375.

Ayers J.C., Zhang L., Luo Y., Peters T., 2012. Zircon and Baddeleyite Solubility in Alkaline Aqueous Fluids at Upper Crustal Conditions. Submitted

Bebout, G.E., 2007. Metamorphic chemical geodynamics of subduction zones. Earth And Planetary Science Letters 260, 373-393.

Bebout, G.E., Ryan, J.G., Leeman, W.P., Bebout, A.E., 1999. Fractionation of trace elements by subduction-zone metamorphism - effect of convergent-margin thermal evolution. Earth and Planetary Science Letters 171, 63-81.

Becker, H., Jochum, K.P., Carlson, R.W., 2000. Trace element fractionation during dehydration of eclogites from high-pressure terranes and the implications for element fluxes in subduction zones. Chemical Geology 163, 65.

Belousova, E.A., Griffin, W.L., O'Reilly, S.Y., Fisher, N.I., 2002. Igneous zircon: trace element composition as an indicator of source rock type. Contributions to Mineralogy And Petrology 143, 602-622.

Bingen, B., Austrheim, H.K., Whitehouse, M., 2001. Ilmenite as a Source for Zirconium during High-grade Metamorphism? Textural Evidence from the Caledonides of Western Norway and Implications for Zircon Geochronology. Journal of Petrology 42, 355-375.

Blichert-Toft, J., Albarède, F., 1997. The Lu-Hf isotope geochemistry of chondrites and the evolution of the mantle-crust system. Earth And Planetary Science Letters 148, 243-258.

Bouvier, A., Vervoort, J.D., Patchett, P.J., 2008. The Lu-Hf and Sm-Nd isotopic composition of CHUR: Constraints from unequilibrated chondrites and implications for the bulk composition of terrestrial planets. Earth and Planetary Science Letters 273, 48.

Breeding, C.M., Ague, J.J., Brocker, M., 2004. Fluid-metasedimentary rock interactions in subduction-zone melange: Implications for the chemical composition of arc magmas. Geology 32, 1041-1044.

Breeding, C.M., Ague, J.J., Brocker, M., Bolton, E.W., 2003. Blueschist preservation in a retrograded, high-pressure, low-temperature metamorphic terrane, Tinos, Greece: Implications for fluid flow paths in subduction zones. Geochemistry Geophysics Geosystems 4.

Brocker, M., Enders, M., 1999. U-Pb zircon geochronology of unusual eclogite-facies rocks from Syros and Tinos (Cyclades, Greece). Geol. Mag. 136, 111-118.

Brocker, M., Enders, M., 2001. Unusual bulk-rock compositions in eclogite-facies rocks from Syros and Tinos (Cyclades, Greece): implications for U-Pb zircon geochronology. Chemical Geology 175, 581-603.

Bryant, D.L., Ayers, J.C., Gao, S., Miller, C.F., Zhang, H., 2004. Geochemical, age, and isotopic constraints on the location of the Sinoâ€“Korean/Yangtze Suture and evolution of the Northern Dabie Complex, east central China. Geological Society of America Bulletin 116, 698-717.

Carlson, W.D., 2010. Dependence of reaction kinetics on H(2)O activity as inferred from rates of intergranular diffusion of aluminium. J. Metamorph. Geol. 28, 735-752.

Carson, C.J., Ague, J.J., Grove, M., Coath, C.D., Harrison, T.M., 2002. U-Pb isotopic behaviour of zircon during upper-amphibolite facies fluid infiltration in the Napier Complex, east Antarctica. Earth And Planetary Science Letters 199, 287-310.

Cartwright, I., Barnicoat, A.C., 1999. Stable isotope geochemistry of Alpine ophiolites: a window to ocean-floor hydrothermal alteration and constraints on fluid–rock interaction during high-pressure metamorphism. International Journal of Earth Sciences 88, 219.

Chen, R.-X., Zheng, Y.-F., Xie, L., 2010. Metamorphic growth and recrystallization of zircon: Distinction by simultaneous in-situ analyses of trace elements, U-Th-Pb and Lu-Hf isotopes in zircons from eclogite-facies rocks in the Sulu orogen. Lithos 114, 132.

Cherniak, D.J., 2010. Diffusion in Accessory Minerals Zircon, Titanite, Apatite, Monazite and Xenotime, in: Zhang, Y.X.C.D.J. (Ed.), Diffusion in Minerals and Melts, pp. 827-869.

Cherniak, D.J., Watson, E.B., 2003. Diffusion in zircon, in: Hanchar, J.M.H.P.W.O. (Ed.), Zircon, pp. 113-143.

Claiborne, L.L., Miller, C.F., Flanagan, D.M., Clynne, M.A., Wooden, J.L., 2010. Zircon reveals protracted magma storage and recycling beneath Mount St. Helens. Geology 38, 1011-1014.

Claiborne, L.L., Miller, C.F., Walker, B.A., Wooden, J.L., Mazdab, F.K., Bea, F., 2006. Tracking magmatic processes through Zr/Hf ratios in rocks and Hf and Ti zoning in zircons: An example from the Spirit Mountain batholith, Nevada. Mineral Mag 70, 517-543.

Claouelong, J.C., Sobolev, N.V., Shatsky, V.S., Sobolev, A.V., 1991. Zircon response to diamond-pressure metamorphism in the Kokchetav massif, USSR. Geology 19, 710-713.

Corfu, F., Hanchar, J.M., Hoskin, P.W.O., Kinny, P., 2003. Atlas of Zircon Textures. Reviews in Mineralogy and Geochemistry 53, 469-500.

Degeling, H., Eggins, S., Ellis, D.J., 2001. Zr budgets for metamorphic reactions, and the formation of zircon from garnet breakdown. Mineral Mag 65, 749-758.

DePaolo, D.J., Wasserburg, G.J., 1976. Nd isotopic variations and petrogenetic models. Geophys. Res. Lett. 3, 249-252.

Dubinska, E., Bylina, P., Kozlowski, A., Dorr, W., Nejbert, K., Schastok, J., Kulicki, C., 2004. U-Pb dating of serpentinization: hydrothermal zircon from a metasomatic rodingite shell (Sudetic ophiolite, SW Poland). Chemical Geology 203, 183-203.

Elliott, T., Plank, T., Zindler, A., White, W., Bourdon, B., 1997. Element transport from slab to volcanic front at the Mariana arc. J. Geophys. Res. 102, 14991.

Engvik, A.K., Austrheim, H., Erambert, M., 2001. Interaction between fluid flow, fracturing and mineral growth during eclogitization, an example from the Sunnfjord area, Western Gneiss Region, Norway. Lithos 57, 111-141.

Engvik, A.K., Bertram, A., Kalthoff, J.F., Stockhert, B., Austrheim, H., Elvevold, S., 2005. Magma-driven hydraulic fracturing and infiltration of fluids into the damaged host rock, an example from Dronning Maud Land, Antarctica. J. Struct. Geol. 27, 839-854.

Etheridge, M.A., Wall, V.J., Cox, S.F., Vernon, R.H., 1984. High fluid pressures during regional metamorphism and deformation: Implications for mass transport and deformation mechanisms. Journal of Geophysical Research 89, 4344-4358.

Feineman, M.D., Ryerson, F.J., DePaolo, D.J., Plank, T., 2007. Zoisite-aqueous fluid trace element partitioning with implications for subduction zone fluid composition. Chemical Geology 239, 250-265.

Ferriss, E.D.A., Ewing, R.C., Becker, U., 2010. Simulation of thermodynamic mixing properties of actinide-containing zircon solid solutions. American Mineralogist 95, 229-241.

Finch, R.J., Hanchar, J.M., 2003. Structure and chemistry of zircon and zircon-group minerals, in: Hanchar, J.M., Hoskin, P.W.O. (Eds.), Zircon. Mineralogical Soc America, Washington, pp. 1-25.

Finch, R.J., Hanchar, J.M., Hoskin, P.W.O., Burns, P.C., 2001. Rare-earth elements in synthetic zircon: Part 2. A single-crystal X-ray study of xenotime substitution. American Mineralogist 86, 681-689.

Fraser, G., Ellis, D., Eggins, S., 1997. Zirconium abundance in granulite-facies minerals, with implications for zircon geochronology in high-grade rocks. Geology 25, 607-610.

Geisler, T., Schaltegger, U., Tomaschek, F., 2007. Re-equilibration of zircon in aqueous fluids and melts. Elements 3, 43-50.

Gerdes, A., Zeh, A., 2009. Zircon formation versus zircon alteration -- New insights from combined U-Pb and Lu-Hf in-situ LA-ICP-MS analyses, and consequences for the interpretation of Archean zircon from the Central Zone of the Limpopo Belt. Chemical Geology 261, 230.

Hack, A.C., Thompson, A.B., Aerts, M., 2007. Phase relations involving hydrous silicate melts, aqueous fluids, and minerals, in: Liebscher, A., Heinrich, C.A. (Eds.), Fluid-Fluid Interactions. Mineralogical Soc Amer, Chantilly, pp. 129-185.

Hacker, B.R., 2006. Pressures and temperatures of ultrahigh-pressure metamorphism: Implications for UHP tectonics and H2O in subducting slabs. International Geology Review 48, 1053-1066

Hanchar, J.M., Finch, R.J., Hoskin, P.W.O., Watson, E.B., Cherniak, D.J., Mariano, A.N., 2001. Rare earth elements in synthetic zircon: Part 1. Synthesis, and rare earth element and phosphorus doping. American Mineralogist 86, 667-680.

Harley, S.L., 1998. On the occurrence and characterization of ultrahigh-temperature crustal metamorphism. Geological Society, London, Special Publications 138, 81-107.

Harley, S.L., Kelly, N.M., 2007. Zircon - Tiny but timely. Elements 3, 13-18.

Harley, S.L., Kelly, N.M., Moller, A., 2007. Zircon behaviour and the thermal histories of mountain chains. Elements 3, 25-30.

Harrison, T.M., Blichert-Toft, J., Muller, W., Albarede, F., Holden, P., Mojzsis, S.J., 2005. Heterogeneous Hadean hafnium: Evidence of continental crust at 4.4 to 4.5 Ga. Science 310, 1947-1950.

Hawkesworth, C.J., Dhuime, B., Pietranik, A.B., Cawood, P.A., Kemp, A.I.S., Storey, C.D., 2010. The generation and evolution of the continental crust. Journal of the Geological Society 167, 229-248.

Hawkesworth, C.J., Kemp, A.I.S., 2006. Evolution of the continental crust. Nature 443, 811-817.

Hermann, J., Spandler, C., Hack, A., Korsakov, A.V., 2006. Aqueous fluids and hydrous melts in high-pressure and ultra-high pressure rocks: Implications for element transfer in subduction zones. Lithos 92, 399-417.

Hoskin, P.W.O., Black, L.P., 2000. Metamorphic zircon formation by solid-state recrystallization of protolith igneous zircon. J. Metamorph. Geol. 18, 423.

Hoskin, P.W.O., Schaltegger, U., 2003. The composition of zircon and igneous and metamorphic petrogenesis, in: Hanchar, J.M.H.P.W.O. (Ed.), Zircon, pp. 27-62.

Jamtveit, B., Austrheim, H., 2010. Metamorphism: The Role of Fluids. Elements 6, 153-158.

Kemp, A.I.S., Hawkesworth, C.J., Foster, G.L., Paterson, B.A., Woodhead, J.D., Hergt, J.M., Gray, C.M., Whitehouse, M.J., 2007. Magmatic and crustal differentiation history of granitic rocks from Hf-O isotopes in zircon. Science 315, 980-983.

Keppler, H., 1996. Constraints from partitioning experiments on the composition of subduction-zone fluids. Nature 380, 237-240.

Kessel, R., Schmidt, M.W., Ulmer, P., Pettke, T., 2005. Trace element signature of subduction-zone fluids, melts and supercritical liquids at 120-180 km depth. Nature 437, 724-727.

Kinny, P.D., Maas, R., 2003. Lu–Hf and Sm–Nd isotope systems in zircon. Reviews in Mineralogy and Geochemistry 53, 327-341.

Koch, P.S., Christie, J.M., Ord, A., George, R.P., 1989. Effect of Water on the Rheology of Experimentally Deformed Quartzite. Journal of Geophysical Research-Solid Earth and Planets 94, 13975-13996.

Kogiso, T., Tatsumi, Y., Nakano, S., 1997. Trace element transport during dehydration processes in the subducted oceanic crust .1. Experiments and implications for the origin of ocean island basalts. Earth and Planetary Science Letters 148, 193-205.

Kushiro, I., 2007. Origin of magmas in subduction zones: a review of experimental studies. Proc. Jpn. Acad. Ser. B-Phys. Biol. Sci. 83, 1-15.

Langmuir, D., 1997. Aqueous Environmental Geochemistry. Prentice Hall, Upper Saddle River, NJ.

Liebscher, A., 2010. Aqueous fluids at elevated pressure and temperature. Geofluids 10, 3-19.

Liou, J.G., Zhang, R.Y., Jahn, B.M., 2000. Petrological and geochemical characteristics of ultrahigh-pressure metamorphic rocks from the Dabie-Sulu terrane, east-central China. International Geology Review 42, 328-352.

Liu, D.Y., Jian, P., Kroner, A., Xu, S.T., 2006. Dating of prograde metamorphic events deciphered from episodic zircon growth in rocks of the Dabie-Sulu UHP complex, China. Earth and Planetary Science Letters 250, 650-666.

Liu, X.C., Jahn, B.M., Hu, J., Li, S.Z., Liu, X., Song, B., 2011. Metamorphic patterns and SHRIMP zircon ages of medium-to-high grade rocks from the Tongbai orogen, central China: implications for multiple accretion/collision processes prior to terminal continental collision. J. Metamorph. Geol. 29, 979-1002.

Liu, F.L., Liou, J.G., 2011. Zircon as the best mineral for P-T-time history of UHP metamorphism: A review on mineral inclusions and U-Pb SHRIMP ages of zircons from the Dabie-Sulu UHP rocks. Journal of Asian Earth Sciences 40, 1.

Luo, Y., Ayers, J.C., 2009. Experimental measurements of zircon/melt trace-element partition coefficients. Geochimica Et Cosmochimica Acta 73, 3656-3679.

Manning, C.E., 2004. The chemistry of subduction-zone fluids. Earth And Planetary Science Letters 223, 1-16.

Martin, B., Fyfe, W.S., 1970. Some experimental and theoretical observations on the kinetics of hydration reactions with particular reference to serpentinization. Chemical Geology 6, 185-&.

Migdisov, A.A., Williams-Jones, A.E., van Hinsberg, V., Salvi, S., 2011. An experimental study of the solubility of baddeleyite (ZrO2) in fluoride-bearing solutions at elevated temperature. Geochimica Et Cosmochimica Acta 75, 7426-7434.

Miller, C.F., McDowell, S.M., Mapes, R.W., 2003. Hot and cold granites? Implications of zircon saturation temperatures and preservation of inheritance. Geology 31, 529-532.

Mojzsis, S.J., Harrison, T.M., Pidgeon, R.T., 2001. Oxygen-isotope evidence from ancient zircons for liquid water at the Earth's surface 4,300 Myr ago. Nature 409, 178-181.

Newton, R.C., Manning, C.E., 2008. Thermodynamics of SiO2-H2O fluid near the upper critical end point from quartz solubility measurements at 10 kbar. Earth And Planetary Science Letters 274, 241-249.

Peacock, S.M., 1993. The Importance Of Blueschist -] Eclogite Dehydration Reactions In Subducting Oceanic-Crust. Geological Society of America Bulletin 105, 684-694.

Pennacchioni, G., 1996. Progressive eclogitization under fluid-present conditions of pre-Alpine mafic granulites in the Austroalpine Mt Emilius Klippe (Italian Western Alps). J. Struct. Geol. 18, 549-561.

Philippot, P., Selverstone, J., 1991. Trace-element-rich brines in eclogitic veins: implications for fluid composition and transport during subduction. Contributions To Mineralogy And Petrology 106, 417-430.

Poli, S., Schmidt, M.W., 1997. The high-pressure stability of hydrous phases in orogenic belts: an experimental approach on eclogite-forming processes. Tectonophysics 273, 169-184.

Poli, S., Schmidt, M.W., 2002. Petrology of subducted slabs. Annual Review Of Earth And Planetary Sciences 30, 207-235.

Putnis, A., Austrheim, H., 2010. Fluid-induced processes: metasomatism and metamorphism. Geofluids 10, 254-269.

Ramakrishnan, S.S., Gokhale, K.V.G.K., Subbarao, E.C., 1969. Solid solubility in the system zircon - hafnon. Materials Research Bulletin 4, 323-327.

Reddy, S.M., Timms, N.E., Hamilton, P.J., Smyth, H.R., 2009. Deformation-related microstructures in magmatic zircon and implications for diffusion. Contributions to Mineralogy and Petrology 157, 231-244.

Reddy, S.M., Timms, N.E., Trimby, P., Kinny, P.D., Buchan, C., Blake, K., 2006. Crystal-plastic deformation of zircon: A defect in the assumption of chemical robustness. Geology 34, 257-260.

Riemann, A., Oberhansli, R., Moller, A., Gerdes, A., Xu, Z.G., 2009. In situ LA-SF-ICP-MS U-Pb dating of metasomatic zircon growth during retrogression of UHP eclogites, Sulu deep drilling hole, China. European Journal Of Mineralogy 21, 1251-1264.

Rubatto, D., Hermann, J., 2003. Zircon formation during fluid circulation in eclogites (Monviso, Western Alps): Implications for Zr and Hf budget in subduction zones. Geochimica Et Cosmochimica Acta 67, 2173-2187.

Rubatto, D., Hermann, J., 2007a. Zircon behaviour in deeply subducted rocks. Elements 3, 31-35.

Rubatto, D., Muntener, O., Barnhoorn, A., Gregory, C., 2008. Dissolution-reprecipitation of zircon at low-temperature, high-pressure conditions (Lanzo Massif, Italy). American Mineralogist 93, 1519-1529.

Rubie, D.C., 1986. The catalysis of mineral reactions by water and restrictions on the presence of aqueous fluid during metamorphism. Mineralogical Magazine 50, 399-415.

Salje, E.K.H., Zhang, M., 2006. Hydrous species in ceramics for the encapsulation of nuclear waste: OH in zircon. J. Phys.-Condes. Matter 18, L277-L281.

Schmitz, M.D., Bowring, S.A., 2001. The significance of U-Pb zircon dates in lower crustal xenoliths from the southwestern margin of the Kaapvaal craton, southern Africa. Chemical Geology 172, 59.

Shannon, R.D., 1976. Revised effective ionic radii and systematic studies of interatomic distances in halides and chalcogenides. Acta Crystallographica Section A 32, 751-767.

Sinha, A.K., Wayne, D.M., Hewitt, D.A., 1992. The Hydrothermal Stability Of Zircon - Preliminary Experimental And Isotopic Studies. Geochimica Et Cosmochimica Acta 56, 3551-3560.

Sorensen, S.S., Sisson, V.B., Harlow, G.E., Lallemantd, H.G.A., 2010. Element residence and transport during subduction-zone metasomatism: evidence from a jadeitite-serpentinite contact, Guatemala. International Geology Review 52, 899-940.

Söderlund, U., Patchett, P.J., Vervoort, J.D., Isachsen, C.E., 2004. The 176Lu decay constant determined by Lu-Hf and U-Pb isotope systematics of Precambrian mafic intrusions. Earth and Planetary Science Letters 219, 311.

Spandler, C., Hermann, J., 2006. High-pressure veins in eclogite from New Caledonia and their significance for fluid migration in subduction zones. Lithos 89, 135-153.

Spandler, C., Hermann, J., Arculus, R., Mavrogenes, J., 2003. Redistribution of trace elements during prograde metamorphism from lawsonite blueschist to eclogite facies; implications for deep subduction-zone processes. Contributions to Mineralogy and Petrology 146, 205-222.

Spandler, C., Mavrogenes, J., Hermann, J., 2007. Experimental constraints on element mobility from subducted sediments using high-P synthetic fluid/melt inclusions. Chemical Geology 239, 228-249.

Spear. F.S., (1993), Metamorphic Phase Equilibria and Pressure-Temperature-Time Paths, Mineral. Soc. Amer. Monograph 1.

Speer, J.A., 1980. Zircon. Reviews in Mineralogy and Geochemistry 5, 67-112.

Timms, N.E., Kinny, P.D., Reddy, S.M., 2006. Enhanced diffusion of Uranium and Thorium linked to crystal plasticity in zircon. Geochemical Transactions 7.

Tole, M.P., 1985. The Kinetics Of Dissolution Of Zircon (Zrsio4). Geochimica Et Cosmochimica Acta 49, 453-458.

Tomaschek, F., Kennedy, A.K., Villa, I.M., Lagos, M., Ballhaus, C., 2003. Zircons from Syros, Cyclades, Greece - Recrystallization and mobilization of zircon during high-pressure metamorphism. Journal of Petrology 44, 1977-2002.

Tsang, C.F., 1991. Coupled hydromechanical-thermochemical processes in rock fractures. Reviews of Geophysics 29, 537-551.

Tsujimori, T., Liou, J.G., Wooden, J., Miyamoto, T., 2005. U-pb dating of large zircons in low-temperature jadeitite from the Osayama serpentinite melange, Southwest Japan: Insights into the timing of serpentinization. International Geology Review 47, 1048-1057.

Valley, J., Lackey, J., Cavosie, A., Clechenko, C., Spicuzza, M., Basei, M., Bindeman, I., Ferreira, V., Sial, A., King, E., Peck, W., Sinha, A., Wei, C., 2005. 4.4 billion years of crustal maturation:

oxygen isotope ratios of magmatic zircon. Contributions To Mineralogy And Petrology 150, 561-580.

van Westrenen, W., Frank, M.R., Fei, Y.W., Fei, Y.W., Hanchar, J.M., Finch, R.J., Zha, C.S., 2005. Compressibility and phase transition kinetics of lanthanide-doped zircon. J. Am. Ceram. Soc. 88, 1345-1348.

Vervoort, J.D., Blichert-Toft, J., 1999. Evolution of the depleted mantle: Hf isotope evidence from juvenile rocks through time. Geochimica Et Cosmochimica Acta 63, 533.

Watson, E.B., Harrison, T.M., 2005. Zircon thermometer reveals minimum melting conditions on earliest Earth. Science 308, 841-844.

Wilde, S.A., Valley, J.W., Peck, W.H., Graham, C.M., 2001. Evidence from detrital zircons for the existence of continental crust and oceans on the Earth 4.4 Gyr ago. Nature 409, 175-178.

Williams, I.S., Buick, I.S., Cartwright, I., 1996. An extended episode of early Mesoproterozoic metamorphic fluid flow in the Reynolds Range, central Australia. J. Metamorph. Geol. 14, 29-47.

Wu, Y.-B., Zheng, Y.-F., Zhao, Z.-F., Gong, B., Liu, X., Wu, F.-Y., 2006. U-Pb, Hf and O isotope evidence for two episodes of fluid-assisted zircon growth in marble-hosted eclogites from the Dabie orogen. Geochimica Et Cosmochimica Acta 70, 3743.

Wu, Y.B., Gao, S., Zhang, H.F., Yang, S.H., Liu, X.C., Jiao, W.F., Liu, Y.S., Yuan, H.L., Gong, H.J., He, M.C., 2009. U-Pb age, trace-element, and Hf-isotope compositions of zircon in a quartz vein from eclogite in the western Dabie Mountains: Constraints on fluid flow during early exhumation of ultra high-pressure rocks. American Mineralogist 94, 303-312.

Xu, S.T., Okay, A.I., Ji, S.Y., Sengor, A.M.C., Wen, S., Liu, Y.C., Jiang, L.L., 1992. Diamond From The Dabie-Shan Metamorphic Rocks And Its Implication For Tectonic Setting. Science 256, 80-82.

Yardley, B.W.D., 2009. The role of water in the evolution of the continental crust. Journal of the Geological Society 166, 585-600.

YODER, H.S., TILLEY, C.E., 1962. Origin of Basalt Magmas: An Experimental Study of Natural and Synthetic Rock Systems. Journal Of Petrology 3, 342-532.

Zhang, R.Y., Liou, J.G., Ernst, W.G., 2009. The Dabie-Sulu continental collision zone: A comprehensive review. Gondwana Research 16, 1.

Zhang, Z.M., Shen, K., Liou, J.G., Dong, X., Wang, W., Yu, F., Liu, F., 2011. Fluid–rock interactions during UHP metamorphism: A review of the Dabie–Sulu orogen, east-central China. Journal of Asian Earth Sciences 42, 316-329.

Zhang, Z.M., Shen, K., Xiao, Y.L., Hoefs, J., Liou, J.G., 2006. Mineral and fluid inclusions in zircon of UHP metamorphic rocks from the CCSD-main drill hole: A record of metamorphism and fluid activity. Lithos 92, 378-398.

Zhao, Z.-F., Zheng, Y.-F., Wei, C.-S., Chen, F.-K., Liu, X., Wu, F.-Y., 2008. Zircon U-Pb ages, Hf and O isotopes constrain the crustal architecture of the ultrahigh-pressure Dabie orogen in China. Chemical Geology 253, 222.

Zheng, Y.F., 2009. Fluid regime in continental subduction zones: petrological insights from ultrahigh-pressure metamorphic rocks. Journal of the Geological Society 166, 763-782.

Zheng, Y.F., Fu, B., Gong, B., Li, L., 2003. Stable isotope geochemistry of ultrahigh pressure metamorphic rocks from the Dabie-Sulu orogen in China: implications for geodynamics and fluid regime. Earth-Sci. Rev. 62, 105-161.

Zheng, Y.F., Gao, T.S., Wu, Y.B., Gong, B., Liu, X.M., 2007. Fluid flow during exhumation of deeply subducted continental crust: zircon U-Pb age and O-isotope studies of a quartz vein within ultrahigh-pressure eclogite. J. Metamorph. Geol. 25, 267-283.

Zheng, Y.F., Zhang, S.B., Zhao, Z.F., Wu, Y.B., Li, X.H., Li, Z.X., Wu, F.Y., 2007. Contrasting zircon Hf and O isotopes in the two episodes of Neoproterozoic granitoids in South China: Implications for growth and reworking of continental crust. Lithos 96, 127-150.

CHAPTER II

THE ORIGIN AND RESPONSE OF ZIRCON IN ECLOGITE TO METAMORPHISM DURING THE MULTI-STAGE EVOLUTION OF THE HUWAN SHEAR ZONE, CHINA: INSIGHTS FROM LU-HF AND U-PB ISOTOPIC AND TRACE ELEMENT GEOCHEMISTRY.

1. Abstract

The Huwan Shear Zone (HSZ) is an eclogite bearing transpressive wrench zone located along the Shangdan Suture that juxtaposes the Paleozoic Qinling and Mesozoic Hong'an-Dabie orogenic terrains. The region preserves a complex history that bridges the gap between adjacent orogenic terrains. Simultaneous in-situ trace element, U–Th–Pb and Lu–Hf isotope analysis of zircon grains from samples of the Xiongdian and Sujiahe eclogite identify a late Carboniferous to early Permian period of high pressure metamorphism, ca. 283 to 306 Ma. Zircon grains are observed to respond to metamorphic overprint via a two stage process: (1) An initial prograde stage of fluid catalyzed interface coupled dissolution-reprecipitation, involving exsolution of a non-ideal solid solution thorite ($ThSiO_4$) end member and loss of highly incompatible components (LREE and Pb), (2) A second stage of coupled zircon dissolution, coarsening, and new rim growth in equilibrium with garnet at high pressure conditions.

We identify Proterozoic whole rock Sm-Nd and zircon grain Lu-Hf isotopic evidence which challenges the traditional interpretation that the Xiongdian and Sujiahe eclogite formed in response to early Paleozoic mantle melting and oceanic crust generation. We argue the Huwan Shear Zone contains no conclusive evidence of early/middle Paleozoic oceanic crust, but rather Proterozoic crustal components analogous to those found in the Northern Qinling Terrain and

associated with formation of the Shangdan Suture. We present a simpler geodynamic model involving continuous convergence and accretion of terrains onto the southern margin of the North China Block during the Paleozoic Qinling and Mesozoic Dabie orogenies.

2. Introduction:

Zircon is ubiquitous accessory mineral in crustal lithologies and typically a residual phase during processes associated with crustal recycling and continental evolution. Zircon's ability to concentrate U whilst rejecting Pb (Watson et al., 1997) makes it a particularly important geochronometer and its robust crystalline lattice is effective at preventing intra element diffusion or structural breakdown up to the most extreme crustal temperatures and pressures (Cherniak and Watson, 2003; Cherniak 2010).

High grade metamorphic terrains associated with continental subduction and orogenesis are witness to the most extreme geodynamic processes acting upon the earth's crust. For such environments, zircon is commonly the only available phase that can preserve geochronological information to constrain specific dates for peak metamorphic conditions and rates of subduction and exhumation (E.g. Liati and Gebauer, 1999; Rubatto et al., 1999; Hermann et al., 2001; Rubatto and Hermann, 2003; Wan et al., 2005; Liu et al., 2006; Rubatto and Hermann, 2007ab; Harley et al., 2007; Liu and Liou, 2011).

It has been proposed that zircon grains in eclogites and other high grade metamorphic rocks require a catalyzing hydrous fluid phase to facilitate new growth or recrystallization, and thus record dehydration metamorphic reactions associated with high to ultrahigh pressure (HP/UHP) tectonic events (e.g. Corfu et al., 2003; Rubatto and Hermann, 2003, 2007ab; Breeding et al., 2004ab; Rubatto et al., 2008; Wu et al., 2006, 2007). The ability to constrain the timing of

fluid production during high grade metamorphism is an important step in understanding metamorphic PTt paths and consequently the geodynamics of orogenic mountain belts (e.g. Peacock, 1987, 1990, 1993; Williams et al., 1996: Leech et al., 2001; Breeding et al., 2004a; Spinelli and Wang, 2009). Understanding the response of zircon and conditions responsible for generation of U-Pb dates during high grade metamorphic processes, however, is a particularly challenging endeavor. The identification of key features that link zircon growth or recrystallization to specific metamorphic conditions requires a detailed geochemical and petrological investigation of both analyzed zircon grains and their host rock.

For our study, we focus on the extensive Central China orogenic belt (Fig. 1). Geochronological exploration across the Hong'an, Dabie and Sulu HP/UHP metamorphic terrains in the eastern portion of the belt identifies an unambiguous history of Triassic HP/UHP metamorphism during continental collision between the South China Block (SCB) and North China Block (NCB) (see review in Zhang et al., 2009). In contrast, however, geochronological evidence from the Qinling and Tongbai terrains in the western portion of the belt have produced evidence for an earlier Paleozoic timing of collision between the SCB and NCB (e.g. Kröner et al., 1993). Bridging the gap between Paleozoic and Mesozoic orogenic events now relies upon accurately unraveling the complex metamorphic and geodynamic histories for a number of thin and highly deformed transpressive wrench zones, or shear zones, located along the Shangdan Suture, which marks the suture between the SCB and NCB, and the northern extent of Triassic HP/UHP metamorphism.

To help understand the origin and response of zircon to metamorphism in this orogenic belt, we present whole rock compositional and Sr-Nd isotopic data combined with in-situ measurements of zircon trace element concentrations and U-Pb and Lu-Hf isotopes for four samples located in the western portion of the Huwan Shear Zone (HSZ), a complex mélange of

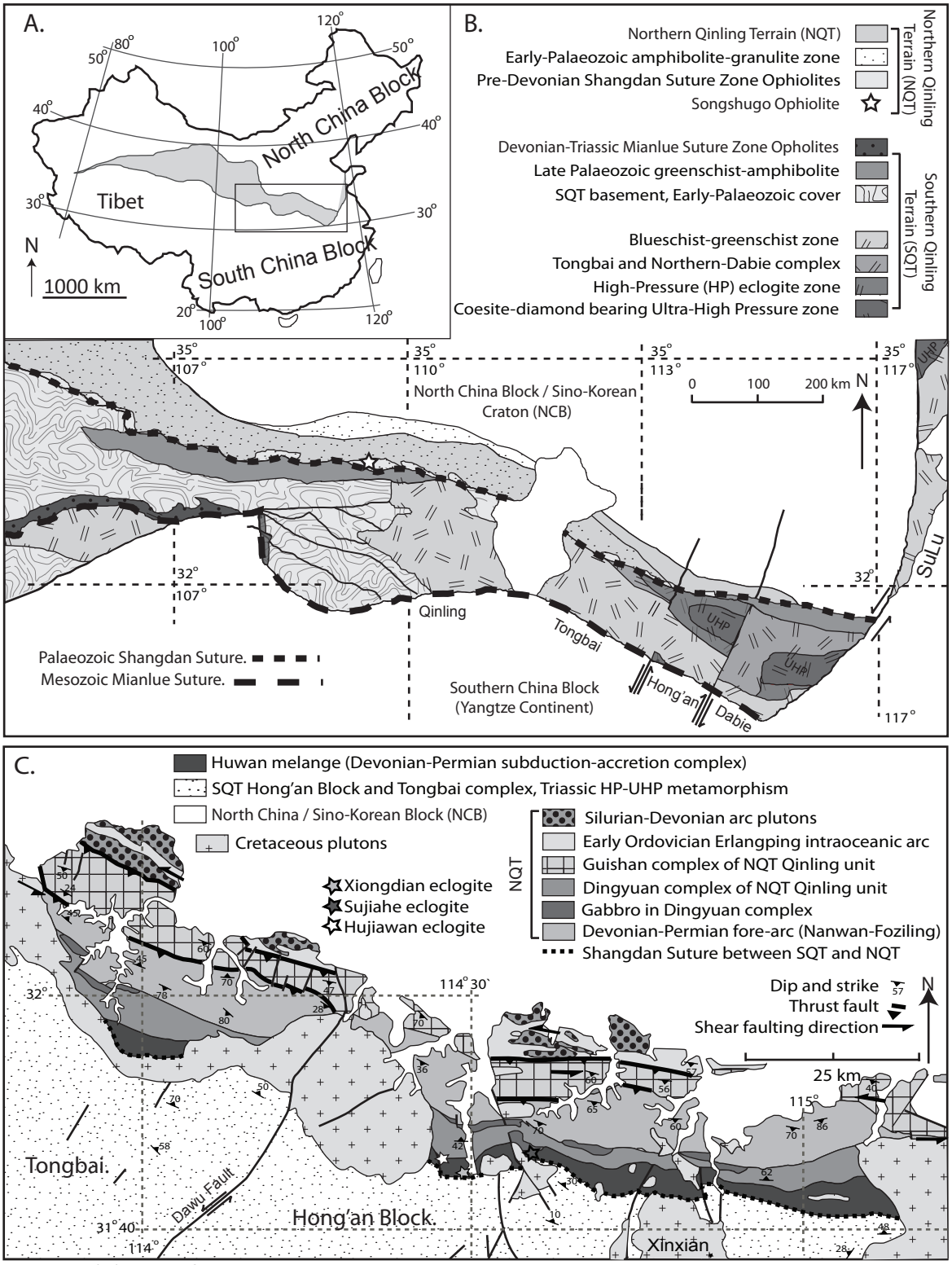

Figure 1: (A) Map of China, the grey shaded region represents the extensive Paleozoic-Mesozoic central China orogenic belt. (B) General tectonic map of the Qinling-Tongbai-Hong'an-Dabie-Sulu Mesozoic metamorphic belt and Southern and Northern Qinling Terrains: After Liu et al., 2010; Dong et al., 2008, 2011: (C) Geological map of Tongbai-Hong'an Mesozoic metamorphic-orogenic belt including the Huwan Shear Zone and sample locations (after Ratschbacher et al., 2006). See Ratschbacher et al., (2003, 2006) for detailed lithological descriptions.

meta lithologies situated between the northern margin of the Hong'an block and associated with construction of the Shangdan Suture zone (Fig. 1c. e.g. Ratschbacher et al., 2006). This information will be used to a critically evaluate geochemical and geodynamic models developed using the Huwan Shear Zone, and expand upon prior tectonic interpretations (e.g. Meng and Zhang, 1999, 2000; Ayers et al., 2002; Ratschbacher et al., 2006; Wu et al., 2009; Cheng et al., 2009, 2010).

3. Geological setting and samples:

The Huwan Mélange (Ratschbacher et al. 2006) or Huwan Shear Zone (HSZ) (Sun et al., 2002) forms a complex 5-10 km belt of mylonitized and elongated blocks of high pressure/low temperature eclogite (HP/LT), gabbro, marble, and quartzite within a matrix of argillic schists (Fu et al., 2002, Ratschbacher et al., 2006). Eclogites occur as massive outcrops with no obvious lithological contacts or occasionally as layers and lenses surrounded by metasediments (e.g. Wu et al., 2009). Peak metamorphism has been constrained to pressures of 1.4 to 2.1 GPa and temperatures of 540°C to 730°C, followed by a retrograde greenschist- to amphibolite-facies overprint at ~0.6 GPa and 530°C to 685°C (Fu et al., 2002; Liu et al 2004b; Ratschbacher et al. 2006; Cheng et al., 2009, 2010).

The HSZ is currently proposed to sit between the Mesozoic HP/UHP Hong'an block portion of the Southern Qinling Terrain (SQT) to its south (e.g. Wu et al., 2006), and the early to middle Paleozoic Northern Qinling Terrain (NQT) to the north (Fig. 1b) (e.g. Meng and Zhang 1999, 2000; Ratschbacher et al., 2003, 2006; Wu et al., 2009; Cheng et al., 2009; Dong et al., 2011). Early to Middle Paleozoic U-Pb zircon dates in eclogites from the HSZ suggest the region participated in the early Paleozoic Qinling orogeny (e.g. Meng and Zhang 1999, 2000; Wu et al.,

2009; Wang et al., 2011; Dong et al., 2011), involving collision between the NQT and SQT, with exhumation cooling ages and structural deformation patterns indicating the HSZ to have been an active component during Triassic orogenic events, involving collision of the SCB into the southern margin of the composite SQT-NQT-NCB (Eide and Liou 2000; Ratschbacher et al.. 2006: Wu et al., 2006, 2009; Liu et al., 2008; Cheng et al., 2009, 2010).

Owing to this transitional geographical and geochronological position between Paleozoic and Mesozoic orogenic terrains, the HSZ is particularly important for unraveling the timing and nature of protracted events that occurred between the SCB and NCB (e.g. Meng and Zhang, 1999; Ratschbacher et al., 2003, 2006). Attempts to understand the origin of this region and place it within the context of the disparate orogenic terrains, however, have proved particularly difficult. Firstly, complex whole rock elemental and isotopic geochemical trends reported for eclogites from Xiongdian have led to a number of different tectonic designations for their protoliths, including Paleotethyan oceanic crust (Gao et al. 2002; Fu et al., 2002; Wu et al., 2009; Cheng et al., 2009, 2010), Neoproterozoic continental crust (Hacker et al., 2000; Liu et al., 2004b), and late Proterozoic island arc crust (Li et al., 2001). Secondly, Integrating structural and field based relationships with metamorphic Pressure Temperature time (PTt) information in these highly deformed, high grade metamorphic regions has proved particularly challenging (e.g. Jahn et al., 2005; Ratschbacher et al., 2006; Cheng et al., 2009; Dong et al., 2011). U-Pb zircon dates alone have been proposed to record high grade metamorphic events that spread over 200 Myr, from the Silurian to the Triassic (Jian et al., 2000, 2001; Sun et al., 2002; Wu et al., 2009; Cheng et al., 2009).

We focus on two eclogite units located within the western portion of the HSZ. The Xiongdian eclogite unit is a complex and petrologically banded formation and also the largest eclogite unit within the HSZ (Sun et al., 2002). Our Xiongdian eclogite samples all contain fresh

garnet and omphacite, abundant rutile and apatite, and accessory quartz, zircon, pyrite, calcite and chlorite. Our sample from the Sujiahe eclogite is a retrograded foliated quartz eclogite containing fragmented garnet porphyroblasts with abundant amphibole and chlorite interspersed within a fine grained and heavily retrograded matrix with accessory calcite, rutile, and zircon.

4. Analytical methods

4.1. Whole rock Major and Trace Element analysis:

Whole rock major and trace element concentrations were measured at the State Key Laboratory of Continental Dynamics, Northwest University, Xi'an, China. Major element oxide concentrations were measured by XRF using fused glass disks and a Rigaku RIX 2100 spectrometer. Trace element concentrations were determined using an Agilent 7500a ICP-MS after acid digestion of samples in a Teflon bomb. Analyses of USGS rock standards (BCR-2, BHVO-1 and AGV-1) are reported in Appendix. A, and indicate a precision and accuracy of better than 5% for major elements and 10% for trace elements and REE. Results are reported in Table. 1.

4.2. Sr and Nd isotopic analysis

Whole rock Sm-Nd and Rb-Sr isotopic compositions were measured at the State Key Laboratory of Continental Dynamics, Northwest University, Xi'an, China, using a multi-collector ICP-MS (Nu Plasma). Analytical precisions of isotope ratio measurements are given as ± 2σ. Separation of Rb, Sr, Sm and Nd was completed using a routine two column ion-exchange technique. Analytical precisions of isotope ratio measurements are given as ± 2σ. Sr isotopic

ratios were corrected for mass fractionation relative to $Sr^{86}/Sr^{88} = 0.1194$. BCR-2 standard yielded an $^{87}Sr/^{86}Sr$ ratio of 0.704959 ± 36 and $^{143}Nd/^{144}Nd$ ratio of 0.512613 ± 9, compared with its reported $^{87}Sr/^{86}Sr$ ratio of 0.704958 and $^{143}Nd/^{144}Nd$ ratio of 0.512633 (Raczek et al., 2003). The measured $^{143}Nd/^{144}Nd$ ratios were normalized against $^{146}Nd/^{144}Nd = 0.7219$. For calculation of Depleted mantle model ages ($T[Nd]_{DM}$), we use a Sm^{147} decay constant of 6.54×10^{-12} $year^{-1}$ (Lugmair and Marti, 1978), and depleted mantle values $^{147}Sm/^{144}Nd = 0.2137$ and $^{143}Nd/^{144}Nd = 0.51315$ from Chen and Jahn (1998). For calculation of εNd values, we use CHUR values of $^{147}Sm/^{144}Nd = 0.1966$ and $^{143}Nd/^{144}Nd = 0.512646$ from Wasserburg et al. (1981). The results are reported in Table. 1.

Table. 1. Major, trace element, and Sr-Nd isotopic compositions of eclogite samples.
Major elements are reported as wt.% oxides and trace elements as ppm.

Location	Xiongdian	Xiongdian	Xiongdian	Sujiahe
Sample	HXD20	HXD98-7	HXD98-8	SJH1
SiO_2 (wt.%)	45.87	46.11	51.08	53.81
TiO_2	1.18	1.16	0.87	1.00
Al_2O_3	17.15	16.12	13.64	15.32
TFe_2O_3	16.65	17.61	10.82	9.93
MnO	0.13	0.20	0.17	0.22
MgO	4.77	5.33	7.45	5.94
CaO	10.83	11.64	10.65	8.72
Na_2O	1.72	2.27	3.52	2.54
K_2O	0.37	0.08	0.57	1.07
P_2O_5	0.11	0.08	0.09	0.23
LOI	0.76	0.01	0.83	0.91
Total	99.54	100.61	99.02	99.69
Li (ppm)	32.85	-	-	8.96
Be	0.28	0.27	0.62	0.85
Sc	40.46	51.95	55.98	19.97
V	-	458	324	217
Cr	187	223	245	222
Co	158	46	76	68
Ni	73.69	60.51	113.70	81.76
Cu	29.57	33.92	163.70	51.04
Zn	91.71	87.86	89.00	94.37

Table. 1. Continued.

Ga	19.75	15.76	15.95	15.76
Ge	1.57		1.91	2.02
Rb	21.36	3.33	17.10	33.20
Sr	256	292	209	227
Y	15.27	13.78	19.90	35.15
Zr	14.88	17.27	28.00	115.66
Nb	0.84	1.19	4.05	12.83
Cs	1.97	0.50	1.47	1.09
Ba	31	25	180	341
La	1.66	1.58	4.31	25.52
Ce	4.31	3.78	9.85	52.69
Pr	0.70	0.62	1.46	6.21
Nd	4.10	3.27	7.13	26.02
Sm	1.47	1.24	2.26	5.48
Eu	0.59	0.54	0.85	1.30
Gd	1.97	1.72	2.56	5.50
Tb	0.38	0.33	0.53	0.86
Dy	2.49	2.24	3.13	5.14
Ho	0.56	0.51	0.69	1.12
Er	1.57	1.53	1.89	3.26
Yb	1.52	1.60	2.07	3.52
Lu	0.23	0.24	0.29	0.55
Hf	0.56	0.71	0.94	2.87
Ta	0.22	0.39	0.36	0.71
Pb	7.75	0.39	0.36	9.28
Th	0.06	0.32	0.72	7.12
U	0.08	0.02	0.71	1.84

$^{87}Rb/^{86}Sr$	0.241571	0.235570
$^{87}Sr/^{86}Sr$	0.706622	0.711852
2s	0.000013	0.000025
$^{147}Sm/^{144}Nd$	0.216608	0.127210
$^{143}Nd/^{144}Nd$	0.512954	0.512129
2s	0.000004	0.000008
$T[Nd]_{DM}$ (Ma)	-10671	1794
εNd[t=0]	6.0	-10.1

4.3. Zircon extraction and Cathodoluminescence (CL) imaging:

Eclogite samples were crushed and zircon grains extracted using conventional magnetic and heavy liquid techniques, then hand picked using binocular microscopes. Individual grains

were mounted in epoxy resin and inner domains exposed by polishing. CL imaging was performed at the State Key Laboratory of Continental Dynamics, Northwest University, using a Quanta 400 FEG high resolution emission field environmental scanning electron microscope connected to a Gatan Mono CL3+ system.

4.4. Zircon Trace Element and U-Th-Pb isotope analysis:

In-situ zircon analyses were performed using a GeoLas 2005 laser-ablation system equipped with a 193 nm ArF-excimer laser at Northwest University, Xi'an, China. The energy density was 15–20 J/cm^2, repetition rate 10 Hz, and laser power 100 mJ/pulse. Data were collected during 80 seconds of ablation, following approximately 30 seconds of background counting.

Trace element and U-Th-Pb isotope analyses were performed using an ELAN6100 DRC (Dynamic Reaction Cell) ICP-MS, following the procedures described by Yuan et al. (2004). The spot diameter for each analysis was 30 μm. Helium was used as the carrier gas to enhance the transport efficiency of ablated material, and was mixed with argon before entering the ICP to maintain stable and optimum excitation conditions. Zircon 91500 was used as the reference standard, which has a recommended $^{206}Pb/^{238}U$ age of 1065.4 ± 0.6 Ma (Wiedenbeck et al., 1995). Common Pb was corrected for using the EXCEL program ComPbCorr#3_151 for analyses with common ^{206}Pb > 1%, by assuming the observed $^{206}Pb/^{238}U$, $^{207}Pb/^{235}U$ and $^{208}Pb/^{232}Th$ ratios for a discordant zircon analysis can be accounted for by a combination of lead loss at a defined time (Andersen, 2002). U–Pb dates were calculated using the ISOPLOT program (Ludwig, 2003). U-Th-Pb isotopic and age data is reported in in Table. 2a. Trace element concentrations are reported in Table. 2b, and 1σ error values for zircon trace element analyses are reported in Appendix. B.

Table. 2a. Zircon U and Th concentration, U-Pb isotopic ratios and ages.

Analysis	Location	Th (ppm)	U (ppm)	Th/U	Ratios						Ages (Ma)					
					$^{207}Pb/^{206}Pb$	1σ	$^{207}Pb/^{235}U$	1σ	$^{206}Pb/^{238}U$	1σ	$^{207}Pb/^{206}Pb$	1σ	$^{207}Pb/^{235}U$	1σ	$^{206}Pb/^{238}U$	1σ
Sujiahe																
SJH1-01.1	rim	2.7	127.7	0.021	0.05492	0.00198	0.36070	0.01303	0.04763	0.00107	409	78	313	10	300	7
SJH1-01.2	core	56.7	80.4	0.705	0.05661	0.00203	0.52061	0.01868	0.06670	0.00151	476	78	426	12	416	9
SJH1-02.1	mantle	2.0	106.6	0.018	0.06108	0.00250	0.40701	0.01655	0.04832	0.00113	642	86	347	12	304	7
SJH1-02.2	core	68.9	110.9	0.621	0.05738	0.00255	0.38373	0.01692	0.04850	0.00116	506	95	330	12	305	7
SJH1-03.1	mantle	0.7	220.8	0.003	0.05190	0.00258	0.34510	0.01694	0.04822	0.00119	281	110	301	13	304	7
SJH1-03.2	rim	1.0	235.3	0.004	0.06076	0.00376	0.37677	0.02296	0.04497	0.00121	631	128	325	17	284	7
SJH1-04.1	core	55.4	81.0	0.683	0.05714	0.00410	0.48333	0.03408	0.06134	0.00177	496	151	400	23	384	11
SJH1-04.2	mantle	1.2	208.2	0.006	0.05432	0.00425	0.36732	0.02822	0.04903	0.00149	384	167	318	21	309	9
SJH1-05.1	core	35.4	188.9	0.187	0.05718	0.00500	0.48008	0.04117	0.06088	0.00197	498	182	398	28	381	12
SJH1-05.2	rim	3.0	73.5	0.041	0.06651	0.00672	0.43445	0.04305	0.04737	0.00168	822	198	366	30	298	10
SJH1-06.1	core	80.7	91.6	0.880	0.06752	0.01000	1.22163	0.17778	0.13119	0.00632	854	281	811	81	795	36
SJH1-06.2	rim	2.6	79.3	0.032	0.05386	0.00883	0.33301	0.05370	0.04484	0.00235	365	333	292	41	283	15
SJH1-07.1	core	670.6	1581.5	0.424	0.06614	0.01182	1.78170	0.31336	0.19533	0.01111	811	335	1039	114	1150	60
SJH1-07.2	rim	1.5	96.6	0.016	0.05534	0.01103	0.37113	0.07279	0.04863	0.00304	426	392	321	54	306	19
SJH1-09.1	core	552.6	572.5	0.965	0.06582	0.01409	1.35142	0.28514	0.14888	0.01001	801	394	868	123	895	56
SJH1-09.2	mantle	0.9	226.0	0.004	0.05172	0.01318	0.34498	0.08677	0.04837	0.00383	273	498	301	66	305	24
SJH1-10.1	mantle	8.4	99.9	0.084	0.05393	0.01494	0.46137	0.12628	0.06203	0.00533	368	527	385	88	388	32
SJH1-10.2	rim	1.2	96.1	0.012	0.05371	0.01613	0.33446	0.09933	0.04516	0.00420	359	565	293	76	285	26
SJH1-12.1	core	320.8	273.2	1.174	0.05829	0.01892	0.53939	0.17338	0.06710	0.00673	540	586	438	114	419	41
SJH1-12.2	rim	0.5	20.6	0.026	0.06508	0.02311	0.46843	0.16487	0.05219	0.00570	777	610	390	114	328	35
Xiongdian																
HXD98-7-01.1		0.018	2.4	0.007	0.21199	0.01412	1.74305	0.10887	0.05962	0.00202	2921	104	1025	40	373	12
HXD98-7-01.2		0.3	27.8	0.009	0.07742	0.00323	0.49278	0.02042	0.04616	0.00108	1132	81	407	14	291	7
HXD98-7-02		1.3	1.9	0.712	0.14631	0.01521	1.15861	0.11624	0.05742	0.00211	2303	168	781	55	360	13
HXD98-7-03		0.0023	0.7	0.003	0.23426	0.04545	1.38103	0.25135	0.04275	0.00315	3081	280	881	107	270	20
HXD98-7-04		28.5	172.0	0.166	0.05394	0.00169	0.36763	0.01161	0.04942	0.00109	369	69	318	9	311	7
HXD98-7-05		12.1	76.7	0.157	0.05438	0.00235	0.36461	0.01564	0.04862	0.00112	387	94	316	12	306	7
HXD98-8-01.1		3.4	221.7	0.015	0.05423	0.00180	0.36980	0.01232	0.04946	0.00109	380	73	320	9	311	7

Table. 2a. Continued.

HXD98-8-01.2	3.3	224.0	0.015	0.05581	0.00182	0.38042	0.01245	0.04943	0.00109	445	71	327	9	311	7
HXD98-8-02.1	803.9	504.7	1.593	0.05375	0.00141	0.49960	0.01333	0.06741	0.00145	361	58	411	9	421	9
HXD98-8-03.1	941.8	482.9	1.950	0.05996	0.00153	0.55019	0.01440	0.06655	0.00144	602	54	445	9	415	9
HXD98-8-03.2	1.3	76.8	0.017	0.05374	0.00194	0.37100	0.01347	0.05007	0.00113	360	79	320	10	315	7
HXD98-8-04.1	0.3	141.0	0.002	0.05497	0.00169	0.37626	0.01174	0.04964	0.00110	411	67	324	9	312	7
HXD98-8-05.1	4.3	275.0	0.015	0.05232	0.00148	0.36393	0.01057	0.05044	0.00111	299	63	315	8	317	7
HXD98-8-06.1	0.4	78.8	0.005	0.05246	0.00231	0.36346	0.01597	0.05024	0.00118	306	97	315	12	316	7
HXD-20-01.1	5.5	19.8	0.275	0.07781	0.00414	0.67108	0.03547	0.06254	0.00164	1142	102	521	22	391	10
HXD-20-01.2	22.9	72.3	0.317	0.08040	0.00246	0.64570	0.02049	0.05824	0.00138	1207	59	506	13	365	8
HXD-20-02.1	12.3	33.5	0.367	0.06441	0.00248	0.59934	0.02349	0.06748	0.00163	755	79	477	15	421	10
HXD-20-02.2	16.8	49.2	0.341	0.05184	0.00339	0.43206	0.02805	0.06043	0.00162	279	143	365	20	378	10
HXD-20-03.1	0.0065	0.0516	0.126	0.54360	0.12387	40.2293	8.07757	0.53666	0.07538	4364	298	3776	199	2770	316
HXD-20-03.2	2.9	5.9	0.491	0.23070	0.02398	1.62151	0.15630	0.05097	0.00247	3057	157	979	61	321	15
HXD-20-04	335.0	734.3	0.456	0.05444	0.00131	0.44523	0.01167	0.05930	0.00137	389	53	374	8	371	8
HXD-20-05	0.6	13.5	0.044	0.08901	0.00747	0.65504	0.05385	0.05337	0.00167	1404	153	512	33	335	10
HXD-20-06	5.6	35.8	0.157	0.06819	0.00348	0.47908	0.02437	0.05095	0.00133	874	102	397	17	320	8
HXD-20-06a	2.4	38.8	0.061	0.07425	0.00304	0.56856	0.02355	0.05553	0.00137	1048	80	457	15	348	8
HXD-20-07.1	46.1	260.9	0.177	0.05752	0.00155	0.39818	0.01149	0.05020	0.00118	511	59	340	8	316	7
HXD-20-07.2	30.6	286.8	0.107	0.06461	0.00171	0.45744	0.01297	0.05134	0.00120	762	55	383	9	323	7
HXD-20-08	12.3	417.7	0.029	0.05339	0.00143	0.36589	0.01049	0.04970	0.00116	345	59	317	8	313	7
HXD-20-09	45.3	112.5	0.403	0.05463	0.00173	0.48555	0.01608	0.06445	0.00153	397	69	402	11	403	9
HXD-20-10.1	8.1	38.2	0.213	0.05242	0.00274	0.36985	0.01942	0.05116	0.00129	304	115	320	14	322	8
HXD-20-10.2	2.6	29.7	0.088	0.05728	0.00386	0.39611	0.02658	0.05014	0.00135	502	142	339	19	315	8
HXD-20-11.1	2.0	14.5	0.136	0.05341	0.00456	0.43126	0.03657	0.05855	0.00163	346	182	364	26	367	10
HXD-20-11.2	1.1	18.0	0.062	0.10134	0.00656	0.67771	0.04321	0.04849	0.00138	1649	115	525	26	305	9
HXD-20-12.1	0.4	1.4	0.282	0.09231	0.02512	1.06061	0.28338	0.08331	0.00514	1474	444	734	140	516	31
HXD-20-12.2	1.0	3.2	0.321	0.14721	0.02748	1.18112	0.21129	0.05818	0.00362	2314	289	792	98	365	22
HXD-20-13	8.6	69.0	0.124	0.05460	0.00206	0.44747	0.01737	0.05943	0.00145	396	82	376	12	372	9
HXD-20-14	18.9	62.1	0.304	0.05275	0.00221	0.36611	0.01564	0.05033	0.00124	318	92	317	12	317	8
HXD-20-16.1	2.8	25.0	0.111	0.06934	0.00456	0.54813	0.03570	0.05732	0.00161	909	130	444	23	359	10

Table. 2a. Continued.

HXD-20-18	1.7	6.9	0.243	0.09152	0.01312	0.73008	0.10266	0.05784	0.00231	1457	251	557	60	363	14
HXD-20-16.2		0.1		0.63581	0.08991	31.2051	3.76880	0.35588	0.03350	4592	190	3526	119	1963	159
HXD-20-17	8.6	408.7	0.021	0.05509	0.00161	0.45179	0.01410	0.05947	0.00142	416	64	379	10	372	9
HXD-20-19.1	11.3	33.2	0.339	0.05628	0.00347	0.46103	0.02843	0.05940	0.00159	463	132	385	20	372	10
HXD-20-19.2	9.5	22.7	0.418	0.06519	0.00440	0.52459	0.03530	0.05835	0.00159	780	136	428	24	366	10
HXD-20-20.1	21.3	90.9	0.235	0.06395	0.00231	0.51258	0.01923	0.05812	0.00143	740	75	420	13	364	9
HXD-20-20.2	27.0	189.5	0.143	0.05906	0.00215	0.38611	0.01460	0.04740	0.00116	569	77	332	11	299	7
HXD-20-21.1	6.7	24.0	0.280	0.06414	0.00448	0.56938	0.03953	0.06436	0.00183	746	141	458	26	402	11
HXD-20-21.2	4.0	12.3	0.321	0.11284	0.00908	0.62505	0.04739	0.04016	0.00154	1846	139	493	30	254	10

Table. 2b. In-situ zircon Rare Earth Element concentrations in ppm

Sujiahe	**La**	**Ce**	**Pr**	**Nd**	**Sm**	**Eu**	**Gd**	**Tb**	**Dy**	**Ho**	**Er**	**Tm**	**Yb**	**Lu**
SJH1-01.1		0.278	0.0038	0.101	0.190	0.140	1.33	0.38	3.07	0.74	2.19	0.36	2.62	0.43
SJH1-01.2	0.0009	11.050	0.0340	0.441	0.958	0.312	4.59	1.69	20.55	8.26	40.11	9.67	103.63	22.00
SJH1-02.1	0.0010	0.288	0.0036	0.071	0.207	0.117	1.13	0.37	3.15	0.92	3.53	0.77	7.97	1.76
SJH1-02.2	0.0032	7.130	0.0318	0.624	1.352	0.326	6.86	2.48	29.27	11.76	56.01	12.73	131.64	27.93
SJH1-03.1		0.145	0.0016	0.004	0.076	0.098	0.94	0.56	8.26	3.73	19.07	4.89	56.08	13.00
SJH1-03.2		0.236		0.050	0.103	0.082	0.97	0.44	6.19	2.96	16.10	4.38	51.80	12.92
SJH1-04.1	0.0163	7.640	0.1920	2.530	3.880	0.831	15.38	5.15	55.96	20.87	89.15	18.72	175.27	34.28
SJH1-04.2		0.333	0.0014	0.027	0.172	0.150	1.53	0.61	6.77	2.57	11.52	2.67	28.69	6.12
SJH1-05.1	0.0241	2.950	0.0278	0.212	0.343	0.159	1.59	0.56	6.26	2.60	13.19	3.35	39.92	9.90
SJH1-05.2	0.0012	0.264	0.0075	0.118	0.286	0.166	1.41	0.39	3.00	0.71	2.06	0.34	3.06	0.57
SJH1-06.1	0.0158	6.950	0.1420	2.040	2.850	0.593	11.33	3.57	37.66	13.39	55.33	11.12	101.74	19.83
SJH1-06.2		0.276	0.0020	0.057	0.198	0.166	1.29	0.32	2.17	0.45	1.20	0.17	1.26	0.19
SJH1-07.1	0.0054	4.200	0.1170	2.280	5.860	0.482	32.75	11.02	107.57	33.03	117.50	21.44	179.45	31.29
SJH1-07.2	0.0196	0.278	0.0327	0.235	0.195	0.079	0.82	0.26	2.22	0.62	1.96	0.35	2.92	0.51

Table. 2b. Continued.

SJH1-09.1	0.0638	26.620	0.3810	4.860	6.080	0.829	19.53	5.50	50.59	16.42	64.05	12.88	116.64	22.04
SJH1-09.2		0.080	0.0021	0.028	0.138	0.080	0.99	0.45	5.90	2.32	10.71	2.35	23.87	4.96
SJH1-10.1		1.369	0.0005	0.028	0.046	0.053	0.35	0.15	2.12	1.04	6.04	1.73	23.10	6.59
SJH1-10.2	0.0012	0.154	0.0011	0.042	0.090	0.057	0.61	0.17	1.27	0.28	0.79	0.13	1.18	0.21
SJH1-12.1	0.0382	22.380	0.4830	6.270	8.920	1.380	30.79	9.66	103.31	37.86	164.82	34.19	323.07	63.54
SJH1-12.2	0.0980	0.286	0.0432	0.296	0.186	0.100	0.84	0.38	4.78	1.84	7.61	1.60	15.40	3.23
Xiongdian														
HXD98-7-01.1		0.004	0.0005	0.010	0.008	0.008	0.09	0.08	1.57	0.92	5.77	1.60	19.52	4.94
HXD98-7-01.2	0.0010	0.051		0.005	0.029	0.020	0.25	0.14	2.71	1.49	9.16	2.59	32.51	8.66
HXD98-7-02		1.146	0.0130	0.241	0.661	0.763	6.00	2.69	38.66	18.75	96.85	22.13	209.28	35.41
HXD98-7-03		0.003	0.0006	0.003	0.037	0.033	0.41	0.30	4.73	1.79	5.94	0.91	6.54	0.97
HXD98-7-04	0.0049	8.540	0.0169	0.426	1.083	0.576	5.09	1.96	24.69	11.17	57.69	14.55	168.32	38.97
HXD98-7-05	0.0008	3.720	0.0114	0.242	0.882	0.568	7.44	3.48	51.72	25.58	133.93	32.61	353.11	81.92
HXD98-8-01.1	0.0030	0.841	0.0042	0.107	0.374	0.296	2.99	1.45	21.27	10.03	53.92	13.69	154.72	36.00
HXD98-8-01.2		0.837	0.0010	0.078	0.358	0.330	3.31	1.64	23.34	10.73	57.97	14.68	165.34	38.65
HXD98-8-02.1	1.7760	233.1	5.3400	55.850	42.490	19.850	105.15	22.73	178.75	49.14	156.04	25.23	206.34	36.61
HXD98-8-02.2		2.211	0.0024	0.064	0.072	0.040	0.45	0.15	2.07	0.90	4.71	1.27	16.37	4.38
HXD98-8-03.1	4.6600	396.63	9.6800	81.820	51.600	22.620	105.03	21.67	161.58	44.46	151.27	28.15	269.55	57.22
HXD98-8-03.2		0.984	0.0032	0.034	0.052	0.051	0.50	0.24	3.84	1.97	11.89	3.25	39.95	9.77
HXD98-8-04.1		0.060	0.0006	0.024	0.030	0.034	0.50	0.33	5.81	3.12	17.59	4.62	52.31	12.20
HXD98-8-05.1		1.068	0.0040	0.111	0.453	0.334	3.87	1.84	27.94	14.15	78.29	20.02	229.32	54.17
HXD98-8-06.1		0.037	0.0013	0.027	0.071	0.091	1.33	1.08	20.58	11.60	67.75	17.45	192.63	43.57
HXD-20-01.1		4.890	0.0098	0.166	0.514	0.265	3.78	1.80	25.04	11.47	60.47	14.65	164.14	39.16
HXD-20-01.2		5.240	0.0057	0.173	0.570	0.299	4.78	2.16	29.69	13.85	72.54	17.74	196.12	47.17
HXD-20-02.1		2.430	0.0036	0.083	0.201	0.182	1.82	0.85	12.36	5.85	31.66	8.30	99.49	26.26
HXD-20-02.2		3.620	0.0032	0.104	0.492	0.217	2.49	1.18	16.30	7.71	39.55	10.15	117.57	29.27
HXD-20-03.1		0.002				0.005	0.03	0.02	0.34	0.19	0.81	0.15	1.04	0.19

Table. 2b. Continued.

HXD-20-04		9.890	0.0080	0.163	0.163	0.109	0.70	0.24	2.57	0.94	4.53	1.05	12.24	2.99
HXD-20-05		0.122	0.0011	0.012	0.046	0.024	0.29	0.17	2.81	1.64	9.07	2.34	27.43	6.97
HXD-20-06	0.0015	2.370	0.0044	0.112	0.441	0.245	3.83	1.75	24.08	11.22	57.23	13.55	146.90	35.40
HXD-20-06a		1.083	0.0017	0.051	0.044	0.191	0.13	0.03	0.25	0.08	0.26	0.07	0.59	0.11
HXD-20-07.1	0.0012	1.990	0.0059	0.118	0.293	0.248	1.50	0.62	7.30	3.09	13.43	2.61	25.85	5.92
HXD-20-07.2		2.170	0.0019	0.054	0.110	0.123	0.84	0.33	3.95	1.59	7.32	1.57	17.44	4.39
HXD-20-08	0.0016	1.690	0.0008	0.025	0.129	0.086	1.66	0.81	12.72	6.28	33.43	7.99	85.39	19.38
HXD-20-09		12.880	0.0172	0.344	1.144	0.468	8.64	3.84	51.93	22.87	114.70	27.25	284.48	62.63
HXD-20-10.1		3.390	0.0096	0.176	0.476	0.259	3.18	1.43	19.24	8.65	44.30	10.47	112.51	26.71
HXD-20-10.2		1.233	0.0019	0.035	0.160	0.110	1.34	0.61	8.50	3.68	18.88	4.45	46.32	10.60
HXD-20-11.1	0.0014	1.610	0.0021	0.124	0.334	0.229	4.51	2.51	39.81	19.09	95.06	20.69	200.90	42.10
HXD-20-11.2		0.320	<0.0033	0.009	0.015	0.036	0.19	0.11	1.61	0.69	3.42	0.79	8.27	1.93
HXD-20-12.1		3.680	0.0065	0.120	0.492	0.213	4.13	1.78	24.52	11.24	58.78	14.00	152.47	35.63
HXD-20-12.2		1.910	0.0038	0.061	0.276	0.141	1.70	0.84	11.91	5.63	30.07	7.30	80.86	20.22
HXD-20-13		2.550	0.0046	0.104	0.367	0.210	2.86	1.16	16.36	7.61	40.90	10.12	113.49	27.93
HXD-20-14		1.840	0.0050	0.069	0.123	0.114	1.30	0.58	8.79	4.30	23.93	6.33	77.47	20.82
HXD-20-16.1		1.261	0.0071	0.050	0.149	0.122	1.18	0.53	7.08	3.19	16.93	4.20	46.88	11.42
HXD-20-16.2		0.001	0.0006	0.018		0.001	0.04	0.03	0.84	0.45	1.86	0.34	2.77	0.48
HXD-20-17		0.692	0.0083	0.126	0.323	0.143	1.47	0.49	4.34	1.33	5.34	1.14	11.35	2.51
HXD-20-18	0.0057	0.519	0.0041	0.022	0.033	0.038	0.28	0.21	2.55	1.28	6.26	1.66	18.82	4.90
HXD-20-19.1		3.570	0.0064	0.125	0.342	0.182	2.24	1.01	13.93	6.54	36.12	9.27	106.80	27.14
HXD-20-19.2	0.0071	4.230	0.0094	0.227	0.448	0.254	3.93	1.82	25.38	11.49	60.72	14.97	167.66	40.31
HXD-20-20.1		3.030	0.0064	0.154	0.644	0.345	5.63	2.39	33.93	15.37	80.37	18.74	199.44	45.00
HXD-20-20.2	0.0071	1.610	0.0211	0.219	0.511	0.232	2.56	0.82	8.78	3.15	13.41	2.79	26.07	5.78
HXD-20-21.1		2.270	0.0052	0.075	0.228	0.141	1.80	0.80	11.45	5.31	28.14	7.15	84.89	21.96
HXD-20-21.2		2.440	0.0042	0.096	0.196	0.110	2.06	0.85	12.12	5.69	30.12	7.54	85.69	21.11

4.5. Zircon Lu–Hf isotope analysis:

Lu-Hf isotopic analyses were performed using a Nu plasma high-resolution (HR) Multi-Collector (MC)-ICPMS, following the procedures described by Yuan et al. (2008). The spot diameter for each analysis was 44 μm and Helium was used as carrier gas. Isobaric interference of ^{176}Lu on ^{176}Hf was corrected by measuring the intensity of the interference-free ^{175}Lu isotope and using a $^{176}Lu/^{175}Lu$ ratio of 0.02669 to calculate $^{176}Lu/^{177}Hf$ ratios. Correction for the isobaric interference of ^{176}Yb on ^{176}Hf involved measuring the interference-free ^{172}Yb and ^{173}Yb during the analysis and calculating a mean βYb value from ^{172}Yb and ^{173}Yb (Woodhead et al., 2004; Iizuka and Hirata, 2005) using the recommended $^{176}Yb/^{172}Yb$ ratio of 0.5886 (Chu et al., 2002). Zircon 91500 was used as the reference standard, with a recommended $^{176}Hf/^{177}Hf$ ratio of 0.282306 ± 10 (Woodhead et al., 2004). For calculation of εHf values and mantle melting model ages, we use a ^{176}Lu decay constant of 1.867×10^{-11} $year^{-1}$ (Soderlund et al., 2004), with initial chondritic reservoir (CHUR) ratios $^{176}Hf/^{177}Hf$= 0.282785 and $^{176}Lu/^{177}Hf$ = 0.0336 from Bouvier et al. (2008), and depleted mantle [DM] $^{176}Hf/^{177}Hf$ = 0.28325 and $^{176}Lu/^{177}Hf$ = 0.0384, from Vervoort and Blichert-Toft (1999). Errors in εHf and $T[Hf]_{DM}$ and values were calculated on the basis of analytical errors, but much larger and poorly constrained errors may be associated with the $T[Hf]_{DM}$ model ages due to errors with the reference model (Zheng et al., 2005). The results are reported in Table. 2c with 2σ errors.

Table. 2c. Zircon Lu-Hf isotopic data. For $\varepsilon Hf_{(t)}$ values, (t) = U-Pb age.

Sample Name	$^{176}Hf/^{177}Hf$	2σ	$^{176}Yb/^{177}Hf$	2σ	$^{176}Lu/^{177}Hf$	2σ	εHf	$T[Hf]_{DM}$	2σ
Sujiahe									
SJH1-01.1	0.282327	0.000019	0.000313	0.000006	0.000009	0.000000	-11	1273	26
SJH1-01.2	0.282738	0.000020	0.011481	0.000203	0.000471	0.000008	6	719	27
SJH1-02.1	0.282542	0.000021	0.001310	0.000040	0.000057	0.000002	-2	980	28
SJH1-02.2	0.282584	0.000020	0.013548	0.000100	0.000547	0.000004	-2	934	27
SJH1-03.1	0.282748	0.000016	0.005963	0.000432	0.000234	0.000016	3	700	22
SJH1-04.1	0.282848	0.000020	0.014080	0.000043	0.000543	0.000001	9	565	29
SJH1-04.2	0.282763	0.000018	0.002771	0.000040	0.000129	0.000002	4	677	25
SJH1-05.1	0.282456	0.000028	0.000257	0.000025	0.000009	0.000001	-5	1097	39
SJH1-06.1	0.282548	0.000019	0.001352	0.000029	0.000062	0.000001	8	971	26
SJH1-06.2	0.282354	0.000016	0.000174	0.000007	0.000005	0.000000	-11	1235	22
SJH1-07.1	0.282315	0.000015	0.014395	0.000107	0.000492	0.000004	7	1304	21
SJH1-07.2	0.282560	0.000015	0.000217	0.000011	0.000006	0.000000	-3	955	20
SJH1-09.1	0.282322	0.000016	0.014818	0.000064	0.000543	0.000003	2	1297	22
SJH1-09.2	0.282302	0.000016	0.008642	0.000317	0.000319	0.000012	-12	1317	22
SJH1-10.1	0.282695	0.000016	0.001847	0.000019	0.000097	0.000001	4	771	22
SJH1-10.2	0.282543	0.000017	0.000644	0.000015	0.000028	0.000001	-4	978	23
SJH1-12.1	0.282685	0.000017	0.017693	0.000317	0.000698	0.000011	4	796	23
Xiongdian									
HXD98-8-01.2	0.282678	0.000040	0.010561	0.000171	0.000485	0.000008	1	258	17
HXD98-8-02.1	0.282581	0.000016	0.004052	0.000137	0.000175	0.000005	-5	929	22
HXD98-8-02.2	0.282553	0.000014	0.001536	0.000057	0.000073	0.000002	-1	965	19
HXD98-8-03.2	0.282434	0.000040	0.002056	0.000026	0.000091	0.000001	-7	424	17
HXD98-8-04.1	0.282833	0.000015	0.005203	0.000061	0.000243	0.000003	7	1083	38
HXD98-8-05.1	0.282895	0.000014	0.018693	0.000073	0.000873	0.000004	9	963	24
HXD98-8-06.1	0.282888	0.000025	0.021088	0.000330	0.000960	0.000014	9	392	14
HXD-98-7-04	0.282960	0.000015	0.011407	0.000023	0.000532	0.000001	11	409	21
HXD-98-7-05	0.283076	0.000013	0.023161	0.000261	0.001069	0.000012	15	249	19
HXD20-02.2	0.282678	0.000022	0.009959	0.000052	0.000470	0.000002	3	802	55
HXD20-04	0.282243	0.000023	0.002007	0.000019	0.000091	0.000001	-13	1129	55
HXD20-08	0.283057	0.000014	0.004119	0.000116	0.000165	0.000005	15	270	20
HXD20-09	0.282965	0.000011	0.018232	0.000153	0.000762	0.000006	13	405	15
HXD20-10.1	0.282974	0.000012	0.007994	0.000175	0.000361	0.000007	12	387	17
HXD20-10.2	0.282994	0.000015	0.003259	0.000057	0.000133	0.000003	12	357	21
HXD20-11.1	0.283068	0.000012	0.019421	0.000161	0.000767	0.000006	16	581	21
HXD20-13	0.282950	0.000012	0.013447	0.000117	0.000630	0.000006	12	504	19
HXD20-14	0.282942	0.000010	0.008137	0.000099	0.000389	0.000005	11	432	14
HXD20-17	0.282555	0.000017	0.001420	0.000039	0.000061	0.000002	-2	801	30
HXD20-19.1	0.282972	0.000010	0.010485	0.000116	0.000504	0.000006	13	1389	32
HXD20-20.1	0.282474	0.000028	0.008995	0.000220	0.000393	0.000009	-5	516	36

5. Results:

5.1. Whole rock geochemistry

5.1.1. Major Element geochemistry:

Using the Total Alkali vs. silica classification (Lebas et al., 1989: Fig. 2a), our Xiongdian samples plot as basaltic with lower SiO_2 contents than other published Xiongdian analyses, which can range up to Basaltic Andesite and Andesite (Li et al 2001; Jahn et al., 2005; Cheng et al., 2009). Our Xiongdian samples also have higher TiO_2 wt.% relative to other published values (Fig. 2b). Our single sample of eclogite from the village of Sujiahe, sample SJH1, is similar in many ways to our Xiongdian eclogite samples, except for a slightly higher SiO_2 concentration (SiO_2 = 53.8 wt.%) and lower TiO_2 wt.%, plotting within the Basaltic Andesite field (Fig. 2a).

For our three Xiongdian eclogite samples, MgO wt.% correlates positively with SiO_2 and Na_2O and negatively with TiO_2, Al_2O_3, TFe_2O_3, and CaO wt.% (Fig. 2b). Including other published Xiongdian analyses (Li et al., 2001; Jahn et al., 2005; Cheng et al., 2009), however, causes these trends to disappear into scatter (Fig. 2b), making it unclear whether primary igneous processes and/or secondary chemical alteration during weathering and metamorphism produced their final compositions, or even if our Xiongdian samples are genetically related to those from other studies (Li et al., 2001; Jahn et al., 2005; Cheng et al., 2009).

5.1.2. Trace element Geochemistry

Sample SJH1 contains elevated Large Ion Lithophile Elements (LILE) concentrations, reduced HFSE contents (Fig. 3), and a two part chondrite normalized REE profile (Fig. 4), with a large negative slope between La and Eu and a low slope between Gd and Lu.

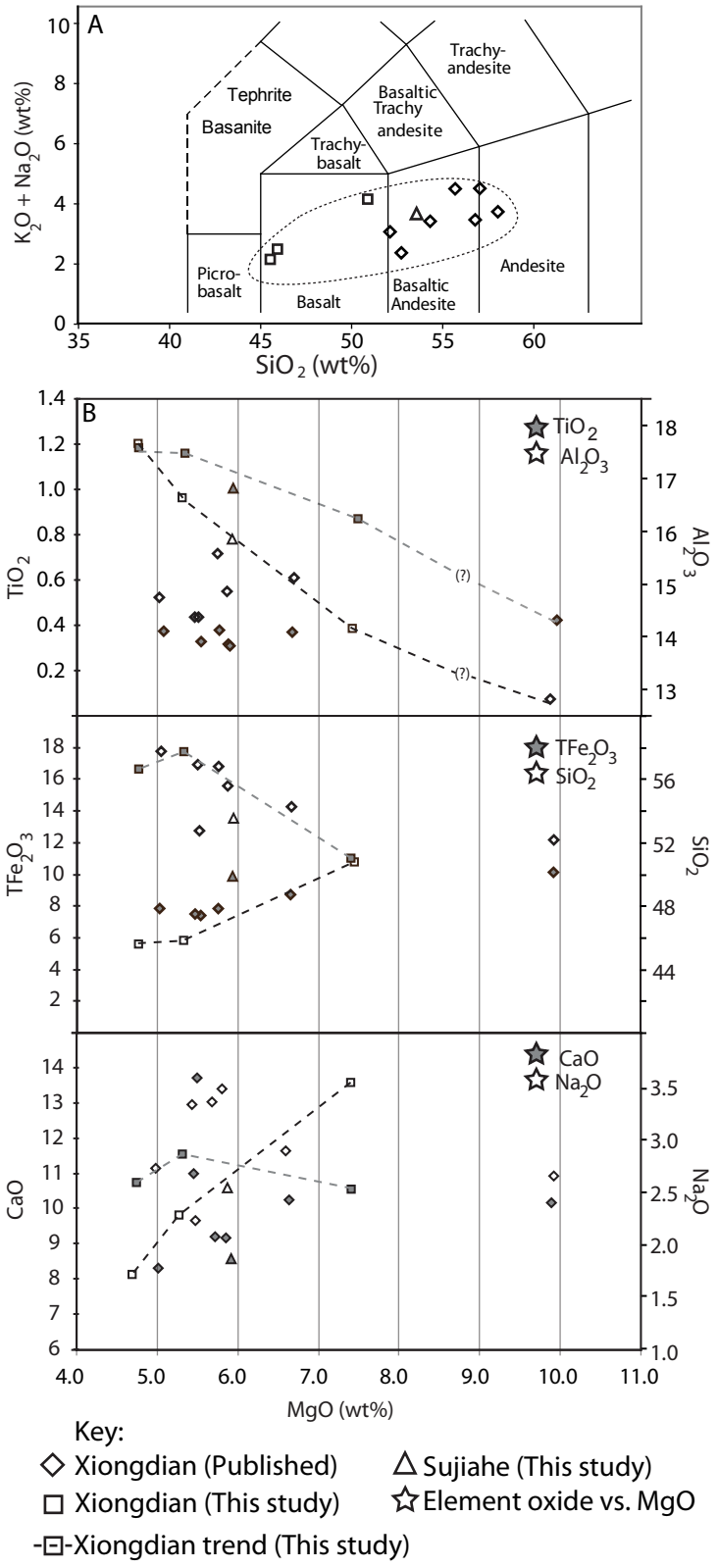

Figure 2: (A). Total-Alkali vs. Silica diagram. (B). MgO vs. TiO_2, Al_2O_3, SiO_2 TFe_2O_3, CaO and Na_2O. Trend lines connect our three Xiongdian eclogite samples.

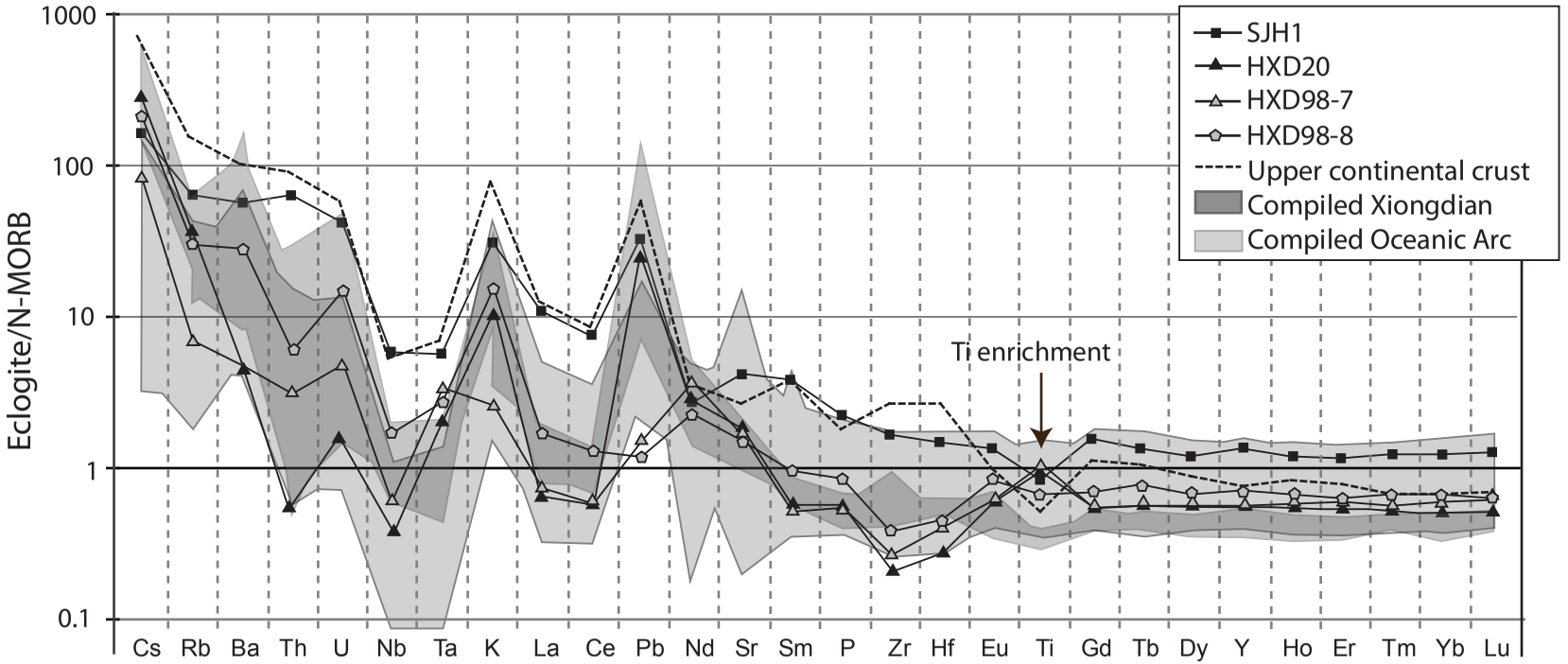

Figure 3: Eclogite trace-element profiles normalized to MORB (Sun and McDonough, 1989). Compiled oceanic arc field data from Elliott et al., (1997) and Pearce et al., (1995) with the average upper-continental crust composition from Rudnick and Gao (2003).

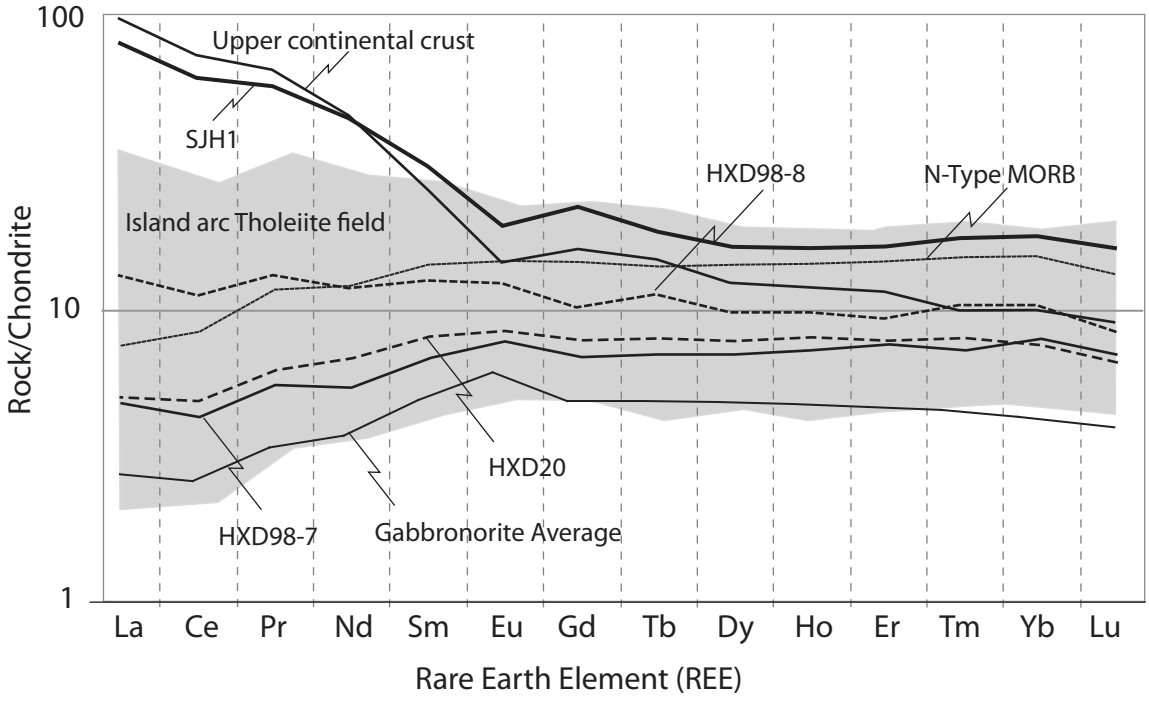

Figure 4: Chondrite normalized REE profiles for samples from Xiongdian and Sujiahe eclogite. Upper crustal values are from Rudnick and Gao (2003). Island Arc field uses data from Elliott et al. (1997) and Pearce et al. (1995). Gabbronorite average is from Greene et al. (2006).

Similar LILE enrichments and HFSE depletions are observed for our Xiongdian analyses (Fig. 3). However, among published data sets LILE contents show an order of magnitude variation. HFSE for our Xiongdian eclogites are also highly variable, but show a consistent depletion relative to MORB (Fig. 3), especially for Zr and Hf (Li et al., 2001; Jahn et al., 2005; Cheng et al., 2009). More interestingly, unlike previously published analyses, samples HXD20 and HXD-98-7 display positive Ti peaks (Fig. 3). All Xiongdian eclogite samples display either MORB or island arc tholeiite-like, flat or slightly LREE depleted profiles (Fig. 4), with little variability in REE contents between samples. Cr and Ni contents for our samples are the lowest yet recorded for the Xiongdian eclogite and similar to primitive MORB values (i.e. Klein, 2003).

5.1.3. Sr and Nd isotopes:

Sample SJH1 has a $^{143}Nd/^{144}Nd$ ratio of 0.512129±8 and a $^{87}Sr/^{86}Sr$ ratio of 0.711852±25, with an $\varepsilon Nd_{[T=0]}$ value of -10.1 and ancient $T[Nd]_{DM}$ model age of 1.8 Ga and (Fig. 5ab). In contrast, our Xiongdian sample HXD20 has a notably more primitive isotopic composition, with a $^{143}Nd/^{144}Nd$ ratio of 0.512954±4 and $^{87}Sr/^{86}Sr$ ratio of 0.706622±13, a characteristic feature of all Xiongdian eclogite analyses and used as evidence for an oceanic crust protolith (e.g. Fu et al., 2002; Wu et al., 2009; Cheng et al., 2009). Relative to other published analyses, our sample HXD20 contains the most primitive $^{143}Nd/^{144}Nd$ ratio, which along with the other published analyses display a spread in $^{143}Nd/^{144}Nd$ and $^{87}Sr/^{86}Sr$ ratios that is outside the level of diversity expected for a single isotopic source (Fig. 5a). A $^{147}Sm/^{144}Nd$ ratio of 0.2166 for sample HXD20 yields an $\varepsilon Nd_{[T=0]}$ value of +6.0(Fig. 5a), but fails to generate a reasonable $T[Nd]_{DM}$ model age (= -10671 Ma).

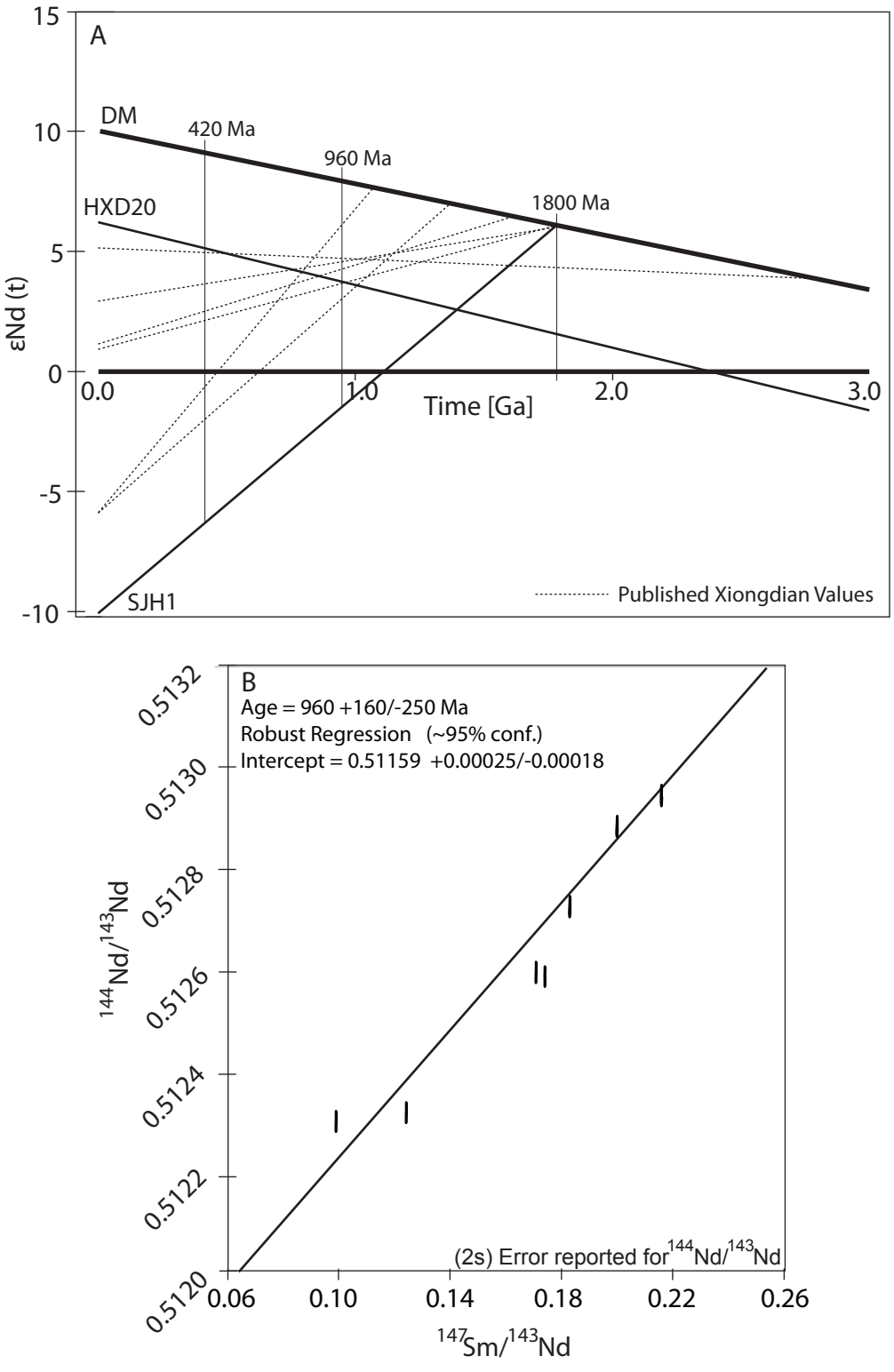

Figure 5: (A) εNd (t) vs. time (Ga). Published Xiongdian analyses from Fu et al. (2002); Li et al. (2001); Jahn et al. (2005); Cheng et al. (2009). (B) $^{143}Nd/^{144}Nd$ vs. $^{147}Sm/^{144}Nd$ for published Xiongdian analyses. Errorchron age calculated using Isoplot (Ludwig, 2003).

5.2. Zircon results

5.2.1 Zircon textures

Zircon grains in sample SJH1 are subhedral, displaying rounded external habits with aspect ratios typically 1:1, and not exceeding ~1:3. All grains are colorless, transparent, and average 200-300 μm in length. CL images clearly display core domains and secondary alteration or over growth textures (Fig. 6a). Zircon core regions contain a mix of preserved oscillatory zoned domains, bright or dark zoning free domains, or complex convolute zoning with abundant inclusions. All cores are separated from secondary outer domains by a convolute boundary, indicative of resorption prior to rim growth.

To aid clarity when discussing the behavior of zircon for sample SJH1, we use textural and geochemical observations to divide our zircon analyses into (1) igneous domains for preserved igneous components, (2) secondary domains that are discussed to represent recrystallized zircon domains, and (3) rim domains that display evidence of growth in equilibrium with garnet. The details concerning these designations are discussed below.

Zircon grains from samples HDX20, HXD98-7, and HXD98-8 are typically euhedral to anhedral with aspect ratios 1:1, and not exceeding ~1:2 (Fig. 6b). All grains are colorless, transparent, and average 50 -100μm in length. CL images display complex textures with internal grain areas containing a mix of bright to dark CL grey scale that display (1) unzoned (Fig. 6ab), (2) complex diffuse or convolute zonation with inclusions (Fig. 6bd), or (3) sectoral zoning (Fig. 6bcg). For some grains (Fig. 6be), small (<50μm) black inclusions apparently define the center of the grain. Rims are typically thin bands of intermediate grey shade, with weak convolute to concentric zoning or unzoned.

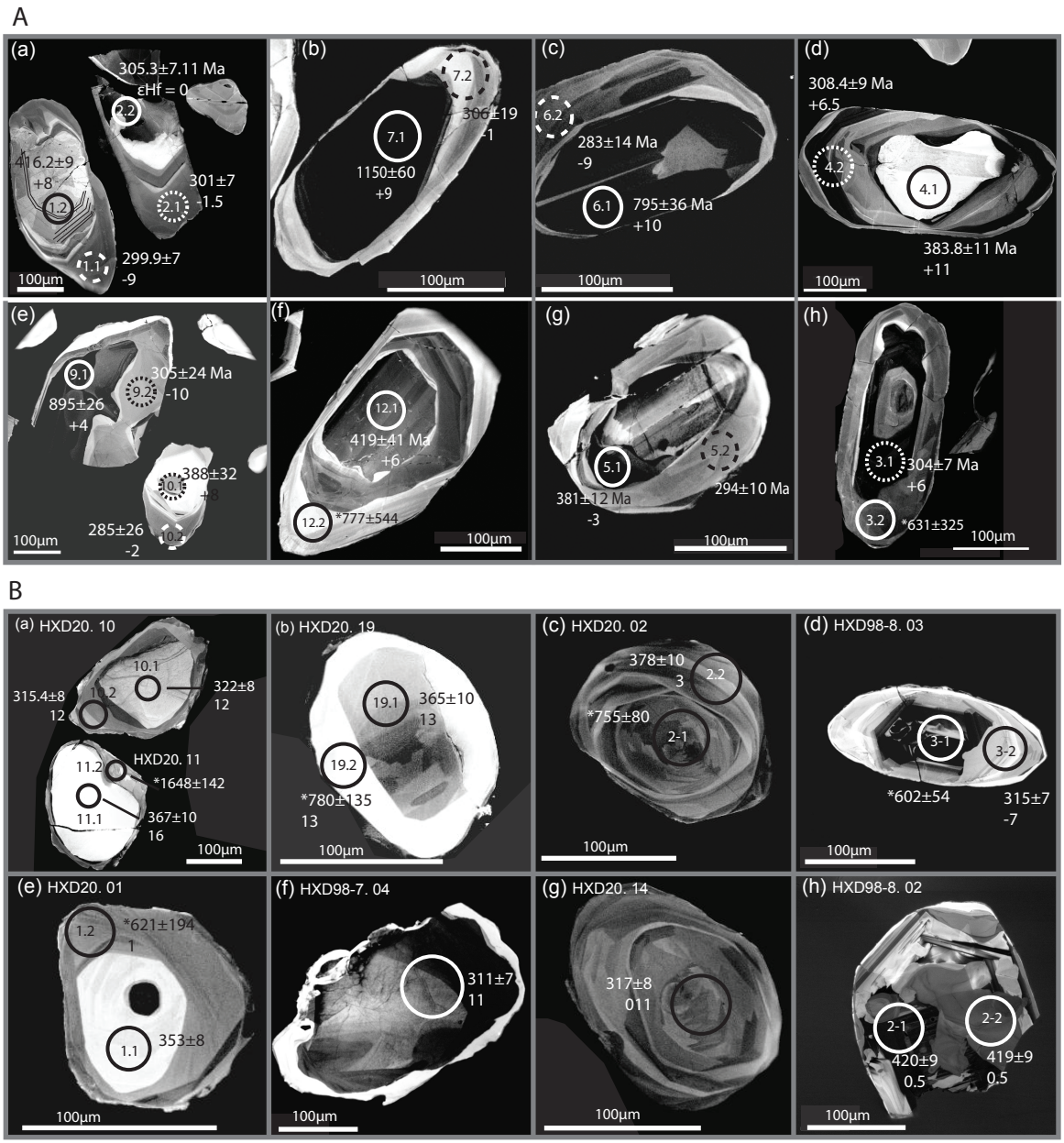

Figure 6: Cathode luminescence images of zircons from sample (A.a-h) SJH1 and (B.a-h) Xiongdian samples. Circles represent analysis spot locations with analysis number included. For Figure 6(A), finely dashed circles represent secondary-domain analyses, while coarse dashed circles represent rims; all other circles represent igneous domain analyses. Labels located next to circles are $^{206}Pb/^{238}U$ age (Ma), where * = $^{207}Pb/^{206}Pb$ age for discordant grains, and εHf (t=U-Pb).

5.2.2. Zircon U-Pb geochronology

Eighteen concordant U-Pb analyses are reported for 10 grains from sample SJH1 (Table. 2a). Igneous domain analyses yield $^{238}U/^{206}Pb$ dates between 1150 ± 60 and 305 ± 7 Ma (Fig. 7a). Two igneous domain analyses, with dates at 416 ± 9 and 418 ± 41 Ma, display evidence of igneous zoning. Secondary domains and rim domains contain much younger $^{238}U/^{206}Pb$ dates that range from 308 ± 9 to 282 ± 14 Ma, with one secondary domain analysis recording a date of 388±32 Ma. Using the Unmix function of Isoplot for Excel (Ludwig, 2003), we identify three main age peaks at 301±3 (±2s) Ma, 383±8 Ma and 416±9 Ma (Fig 7a).

Forty seven U-Pb isotope analyses were performed on 31 grains extracted from Xiongdian eclogite samples HXD20 (32 analyses, 20 grains, 15 concordant dates), HXD98-7 (6 analyses, 5 grains, 2 concordant dates), and HXD98-8 (9 analyses, 6 grains, 8 concordant dates) (Table. 2b). Despite apparent preservation of simple core alteration/secondary domain relationships (Fig. 6b), there are no clear correlations between analysis location and $^{238}U/^{206}Pb$ date. Unmix (Ludwig, 2003) age populations include three main age peaks at 313±2 (±2s) Ma, 367±3 Ma and 414±5 Ma (Fig. 7b).

Comparing our Xiongdian and Sujiahe eclogite zircon U-Pb dates to other published reports (Fig. 7cd), we identify five age peaks between 420 and 300 Ma, which overlap between eclogite locations and suggest similar Paleozoic to Mesozoic geodynamic histories, the nature of which will be discussed in detail later.

5.2.3. Sujiahe Zircon trace elements:

Igneous domain analyses for grains from SJH1 contain Th contents of 35 to 321 ppm, while secondary domain and rim analyses overlap with notably reduced concentrations of 0.74 to 8.4 ppm. U contents for the three domains overlap, with the lowest average recorded in

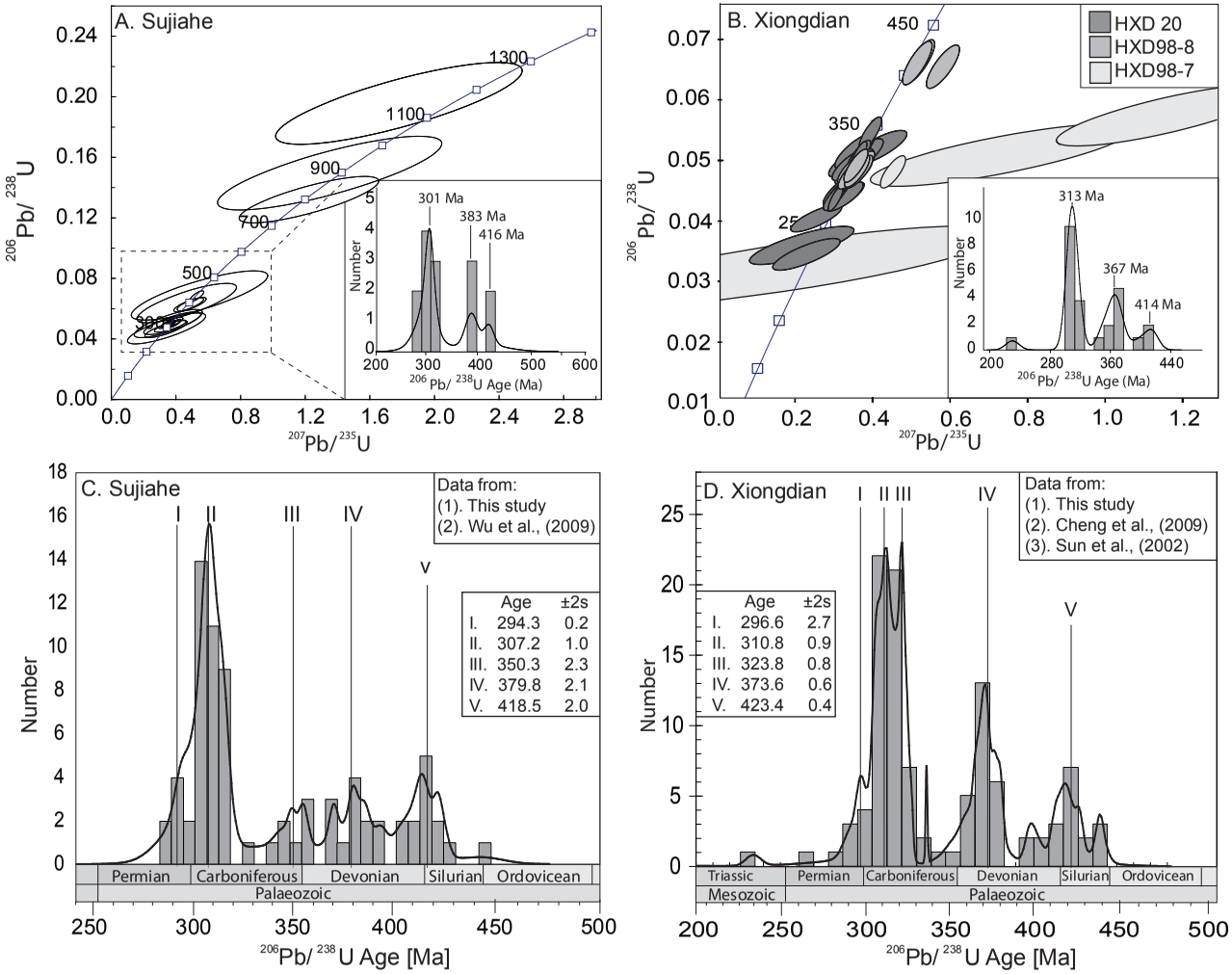

Figure 7: Zircon Concordia diagram for zircon analyses for samples from (a) Sujiahe and (b) Xiongdian. Inset diagrams are plots of $^{206}Pb/^{238}U$ age probability density for our samples. Figures (c: Sujiahe) and (d: Xiongdian) are probability density plots that include our samples and those from the other studies (Sun et al., 2002; Wu et al., 2009; Cheng et al., 2009). Age peaks are calculated using the un-mix function of Isoplot for Microsoft Excel (Ludwig, 2003).

zircon rim analyses (94.6 ppm, n=5). Th/U ratios for igneous domain analyses are all >0.1 (Th/U = 0.18 to 1.17), while secondary domain and rim Th/U ratios are lower by one to two orders of magnitude, reflecting their relative Th depletion (secondary domain Th/U = 0.018 to 0.003, rim Th/U = 0.011 to 0.032).

Rare earth element (REE) contents (Table. 2a) for igneous domain analyses are elevated relative to other domains, with positively trending profiles (Fig. 8a), a low average $(Sm/Lu)_N$ ratio of 0.023, and negative Eu anomalies, indicating crystallization from a melt that experienced plagioclase fractionation (e.g. Murali et al 1983).

Secondary domains contain reduced REE contents relative to igneous domains, with positively trending MREE and HREE profiles and steeper gradients (Fig. 8a) that yield a lower average $(Sm/Lu)_N$ ratio of 0.006, with one analysis at 0.019. Secondary domain LREE contents are depleted by an order of magnitude relative to igneous domain analyses while Eu anomalies are negligible, reflecting the lack of plagioclase control.

Rim domain analyses display flat HREE profiles indicating the "garnet effect" on HREE uptake in zircon (Fig. 8a) (Rubatto, 2002; Hermann and Rubatto, 2003; Rubatto and Hermann, 2007ab). LREE and MREE are notably depleted in rim domains relative to igneous domains, but overlap with those from secondary domains. The flat HREE profile gradient is further reflected in $(Sm/Lu)_N$ ratios, which yield an elevated average of 0.11, with Eu anomalies again negligible and overlapping with secondary domain analyses.

5.2.4. Xiongdian Zircon trace elements

Zircon trace element concentrations are highly variable and show no correlations when plotted against one another. U contents in zircon vary over an order of magnitude, while Th contents vary over three orders of magnitude (U = 12.3 to 734 ppm, Th = 0.35 to 804 ppm). Th/U ratios for all analyses can be broadly divided into two groups, those <0.02 (n=9) and those

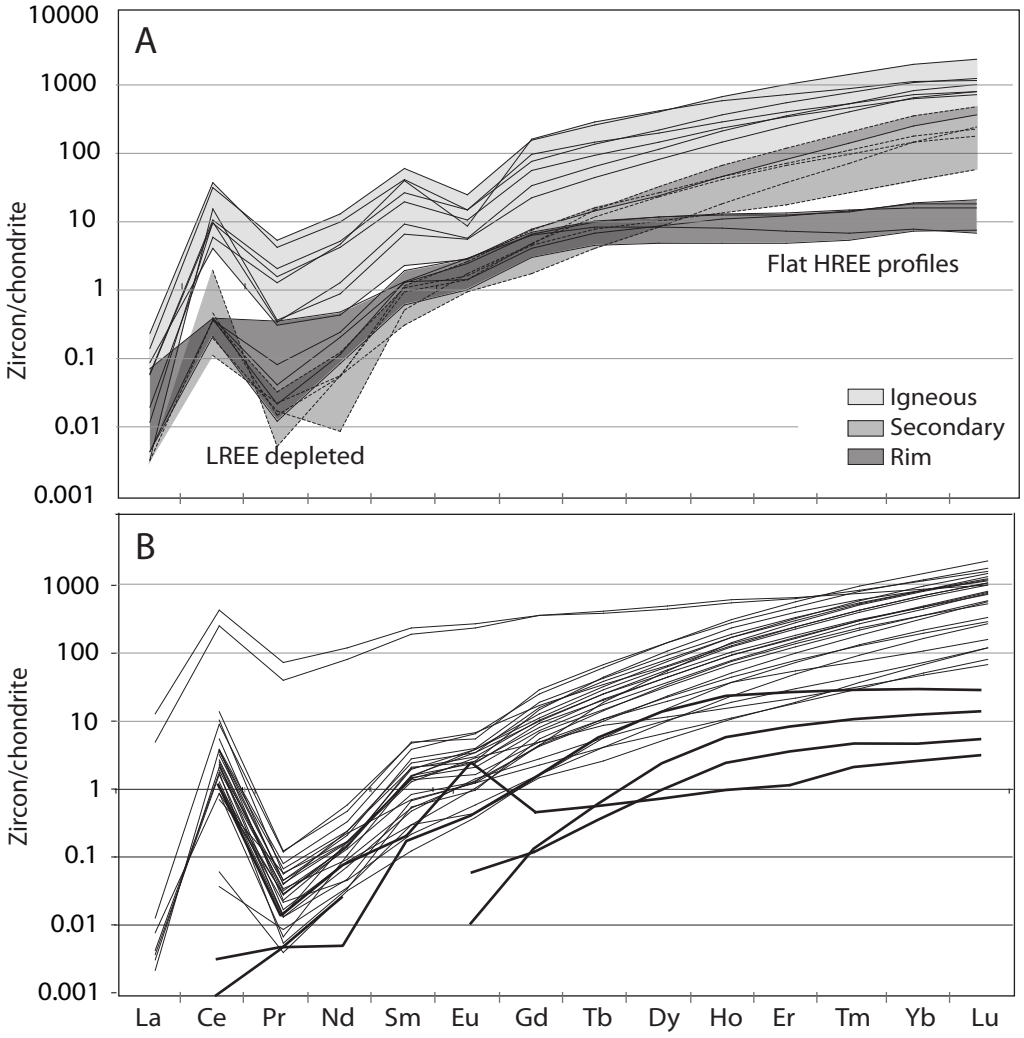

Figure 8: Chondrite normalized zircon REE contents for grains from (A) sample SJH1 and (B) Xiongdian samples.

>0.1 (n=16). While this may allow for a simple differentiation between those thought to represent magmatic and metamorphic domains, there is no correlation between Th/U ratio, textural domain/backscattered electron intensity, and U-Pb date.

The majority of Xiongdian zircon analyses (Table. 2a) contain La concentrations close to or below detection limits (Fig. 8b), negligible Eu anomalies, with the remaining REE displaying over two orders of magnitude variation between analyses. Two core/inner domain analyses, HXD98-8 2.1 (Concordant $^{206}Pb/^{238}U$ age = 420±9 Ma) and 3.1 (Discordant, $^{207}Pb/^{206}Pb$ age = 602±54 Ma), display notably elevated L-MREE, Th and P contents with high Th/U ratios of 1.6 to 1.9 (Fig 6Bdh and 8a). We also observe four analyses (HXD-20-03.1, HXD-20-06a, HXD-20-16.2, and HXD98-7-03) that display apparently flat HREE profiles and contain low U, Th, Pb and REE concentrations and Th/U ratios. These analyses, however, yielded grossly discordant U-Pb dates

5.2.5 Zircon Lu-Hf isotopes:

Seventeen Lu-Hf isotopic analyses were performed on previously dated domains in nine zircon grains from sample SJH1 (Table. 2c). Igneous, secondary domain, and rim domains all contain a wide range of $^{176}Hf/^{177}Hf$ ratios (Fig. 9a), with igneous domains covering both the upper and lower limits. $^{176}Hf/^{177}Hf$ ratios between igneous and secondary domains on single grains are practically identical. In cases where single grains have both igneous and secondary domain or rim domain $^{176}Hf/^{177}Hf$ analyses, rim domains display a notably different ratio. This diversity is reflected further in $\varepsilon Hf_{(T=U\text{-}Pb)}$ values that range from +10 to -11 (Fig. 9b). $^{176}Hf/^{177}Hf$ ratios show no correlation with REE contents or trace element ratios (i.e. Th/U).

$^{176}Lu/^{177}Hf$ ratios vary by two orders of magnitude between igneous and secondary domains. Igneous domain analyses are characterized by $^{176}Lu/^{177}Hf$ ratios > 0.000471, although two analyses contain reduced ratios of 0.000062 and 0.000009. Zircon secondary and rim

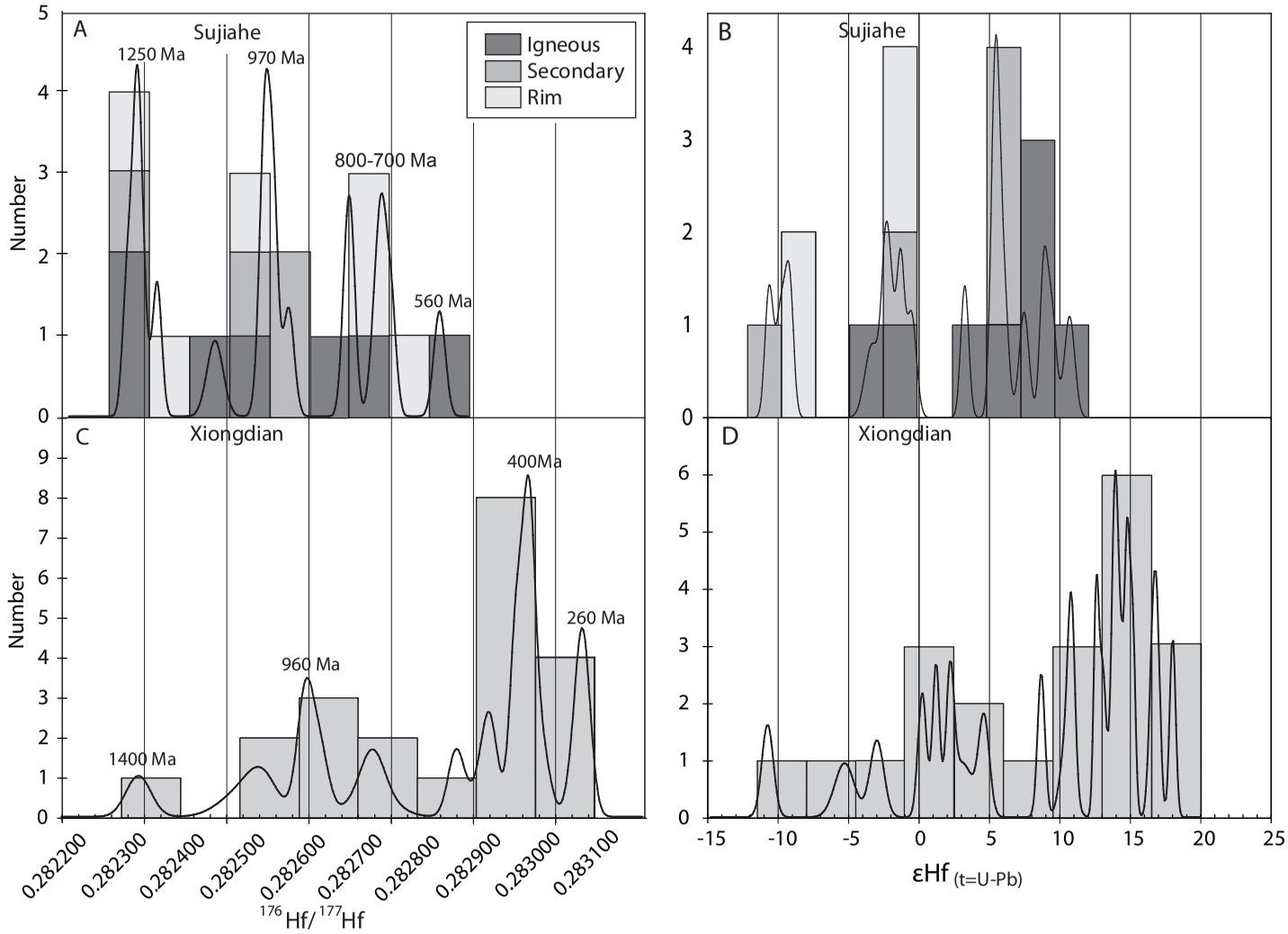

Figures 9.(ac): Probability density plot of zircon $^{176}Hf/^{177}Hf$ for grains from sample (a) SJH1 and (c) Xiongdian eclogite. Ages with peaks represent $T[Hf]_{DM}$ ages. Figures 9. (bd): Probability density plot of εHf(t=U-Pb) for grains from sample (b) SJH1 and (d) Xiongdian eclogite. Sujiahe zircon analyses are divided into igneous, secondary and rim-domains.

domain analyses contain lower $^{176}Lu/^{177}Hf$ ratios < 0.000319, with an average of 0.000012 recorded in zircon rim domains.

Twenty one Lu-Hf isotopic analyses were performed on previously dated core and alteration/secondary domains of eighteen zircon grains from samples HXD20, 98-8, and 98-7 from Xiongdian (Table. 2c). $^{176}Hf/^{177}Hf$ and $^{176}Lu/^{177}Hf$ display a wide range of 0.282243 to 0.283076 (Fig. 9c) and 0.000061 to 0.001069, respectively. Further diversity is reflected in $\varepsilon Hf_{(T=U\text{-}Pb)}$ values that range widely from +18 to -11 (Fig. 9d). A probability plot of $^{176}Hf/^{177}Hf$ (Fig. 9c) shows a distribution skewed to lower values, i.e. less radiogenic. No correlation is observed between $^{176}Hf/^{177}Hf$ and U-Pb dates or trace element ratios.

6. Discussion:

6.1 The origin and nature of the Xiongdian eclogite protolith:

Published studies propose the Xiongdian eclogite to have a protolith representing early to middle Paleozoic Paleotethyan oceanic crust that formed though mixing of a depleted mantle (DM) melt and an unspecified arc or crustal component (Li et al., 2001; Fu et al., 2002; Wu et al., 2009; Cheng et al., 2009; Liu et al., 2010). These interpretations are in part supported by enriched LILE signatures (Fig. 3), flat LREE profiles (Fig. 4) and primitive $^{143}Nd/^{144}Nd$ isotopic ratios (Li et al., 2001; Fu et al., 2002; Sun et al., 2002; Cheng et al., 2009). Ti/V ratios of 10 to 16 plot within the field for island arc tholeiites (Shervais 1982), while Cr and Ni contents range from MORB like up to those observed for ultra-mafic bodies (i.e. Cr = 1118 to 187 ppm), complicating a simple oceanic or ocean arc origin (Jahn 1998; Li et al., 2001; Fu et al.. 2002; Jahn et al., 2005; Cheng et al., 2009; this study).

Unlike previously published analyses, our samples HXD-20 and HXD-98-7 display an elevated TiO_2 wt.% and V concentration, suggestive of Fe-Ti oxide accumulation and an origin involving lower crustal cumulate processes (Jahn 1998; Zhang et al., 2006; Liu et al., 2007; Tang et al., 2007; Liu et al., 2005, 2008). A cumulate model is also supported, in part, by the enriched Cr and Ni concentrations and Cr/Ni ratios that range from 2.1 up to 6.4 (Jahn 1998), although a relationship between Ti and Cr or Ni concentration is not clear. SiO_2 values, however, range from 46 to 58 wt.% and exceed those observed for typical MORB (e.g. SiO_2 ~50±1 wt.%: Klein, 2003), and appear less typical of simple mafic mantle melt cumulates (i.e. <<47 wt.% SiO_2 for Fe-Ti oxide bearing Gabbro: Shellnutt et al., 2009).

6.1.1. Metasomatic vs. magmatic processes:

Similar complex geochemical signatures have been observed for other eclogites within the Dabie Sulu orogenic belt by Jahn (1998), who comments on the complexity of banded eclogite formations as representing a mix of magmatic and metamorphic processes, and metasomatic alteration. The role of metasomatic fluids and the redistribution of geochemical components during continental subduction have particularly important implications for the behavior of mineral phases within a rock (e.g. Zhao et al., 2007), including zircon (Xia et al., 2010), and the generation of apparent arc signatures for an oceanic MORB protolith. The composition of aqueous metasomatic fluids typically become progressively enriched in Si, Al, Na, K, LILE and LREE, and remain largely depleted in M-HREE, HFSE, Fe, Mg, Ca, Cr and Ni as conditions approach the second critical end point, i.e. moving from a siliceous aqueous fluid to a hydrous granitic melt (e.g. Manning 2004; Kessel et al., 2005; Hermann et al., 2006; Zhao et al., 2007). The diverse values of SiO_2 wt.% for the Xiongdian eclogite, however, show no clear relationship with fluid mobile or immobile components.

In contrast to its primitive looking $^{143}Nd/^{144}Nd$ ratio (0.512954), the $^{87}Sr/^{86}Sr$ ratio (0.706622) of sample HXD20 appears more isotopically enriched or evolved. This Sr isotopic shift was first discussed by Fu et al. (2002), who interpreted whole rock oxygen, strontium and hydrogen isotopes to record hydrothermal alteration prior to metamorphism. Similar complex geochemical and isotopic trends have been observed in regions of mixed cumulates and melt dykes in the mantle to ocean arc crust transition zone (e.g Benn et al., 1988). These regions are identified in a number of accreted and layered ophiolite terrains that contain dunites, chromitites, wehrlites, troctolites, pyroxenites, gabbronorites and gabbros which occur on scales of meters to ~1 km (e.g Benn et al., 1988; Greene et al., 2006; Piccardolow and Guarnieri, 2011).

Orthopyroxene rich gabbronorites in such regions have been reported to contain elevated SiO_2 contents, primitive MORB like and greater Cr, Ni and MgO contents, and high $^{87}Sr/^{86}Sr$ ratio in contrast to a MORB like $^{143}Nd/^{144}Nd$ ratio (Juteau et al., 1988; Van der Laan et al., 1992; Lachize et al., 1996; Python and Ceuleneer, 2003; Nonnette et al., 2005; Koepke et al., 2009; Piccardolow and Guarnieri, 2011). These features have been interpreted to indicate that melt evolution followed the hydrous and oxidized calk alkaline differentiation trend, characterized by silica enrichment at constant FeO/MgO due to substantial crystallization of Fe-rich ferromagnesian phases (i.e. magnetite, Ti-magnetite, Ti-pargasite, etc.) in the early stages of fractional crystallization. In this regard, the Xiongdian eclogite body appears to record a complex geochemical system, most likely involving an evolving response to phase equilibria changes during hydrous melting, melt-rock reactions and fractional crystallization in the middle to lower oceanic/ocean arc crust.

6.2. The origin and nature of the Sujiahe eclogite protolith:

Our Sujiahe eclogite sample SJH1, in contrast to the Xiongdian eclogites, clearly contains major element and trace element signatures, particularly REE profiles (Fig. 4), typical of both continental arc magmas and the average upper crustal composition (Rudnick and Gao, 2003) (Fig. 3). These features are common to eclogites and other metalithologies throughout the SQT and SCB (Bryant et al., 2004; Zhao et al., 2008, and references therein).

As noted in Figure 3, HFSE in our sample are depleted relative to LILE. While this may initially suggest melting processes in an arc environment, Zr and Hf contents for sample SJH1 overlap with those typical of MORB (Klein 2003), as do Cr and Ni contents which are typically depleted in arc volcanics. In this regard, the protolith for sample SJH1 may have been generated not by processes associated with a continental arc environment, but by decompression mantle melting and crustal assimilation.

6.3. Constraints from whole rock Sm-Nd isotopes:

Focusing on Xiongdian whole rock Sm-Nd isotopes, as previously mentioned, the observation of primitive $^{143}Nd/^{144}Nd$ ratios and MORB like REE profiles (Fig. 4) have been collectively used as evidence in support of a middle Paleozoic Paleotethyan oceanic protolith (Fu et al., 2002; Wu et al., 2008; Cheng et al., 2009, 2010). As discussed in Wu et al., (2009), eclogites in the north west HSZ occur as layers or lenses in sediments and may represent tectonic fragments of an ophiolite complex formed in a continental marginal setting.

$T[Nd]_{DM}$ model ages (1.0 to 2.8 Ga) and $\varepsilon Nd_{(t=420\ Ma)}$ values (-1.7 to 5.0), reported for the Xiongdian eclogite have been explained as simply reflecting assimilation of more evolved continental material during emplacement and cooling. An important feature of our Xiongdian eclogite HXD20 is its $^{147}Sm/^{144}Nd$ ratio, which is greater than the $^{147}Sm/^{144}Nd$ ratio accepted to

represent the Depleted Mantle (e.g. DePaolo and Wasserburg, 1979: Chen and Jahn, 1998). This feature precludes our ability to calculate a meaningful $T[Nd]_{DM}$ model age for sample HXD20 and implies that our Xiongdian eclogite sample will follow a near parallel evolution path to the DM and yield an apparently "primitive" Nd isotopic composition irrespective of its timing of formation. While a $^{147}Sm/^{144}Nd$ ratio greater than the DM could suggest an episode of post-crystallization Sm/Nd fractionation (i.e. metasomatism during metamorphism), we identify a linear correlation ($R^2 = 0.97$) between $^{143}Nd/^{144}Nd$ and $^{147}Sm/^{144}Nd$ for data collected from published Xiongdian reports (Fig. 5b).

An attempt to calculate a Sm-Nd isochron for this correlation using a model I algorithm in the Isoplot program (Ludwig, 2003) produced a MSWD value of 15, implying an errorchron relationship where the observed scatter is not a result of their analytical uncertainties alone. Considering we are using only whole rock isotopic data, which by itself has a limited range in isotopic diversity, and also because the data is compiled from a number of different sources, this result should not be unexpected. Using a robust regression algorithm in Isoplot, which makes no assumptions concerning the origin or the distribution of scatter by fitting the data points about a correlation line, a whole rock Sm-Nd age of 960 ($^{+160}/_{-260}$) Ma is calculated for compiled Xiongdian eclogite data.

This ca. 960 ($^{+160}/_{-250}$) Ma errorchron provides support, along with overlapping zircon U-Pb age peaks and $^{87}Sr/^{86}Sr$ isotopic signatures, for the hypothesis that these Xiongdian eclogite studies have sampled a Proterozoic cogenetic igneous body. This hypothesis, however, requires the Xiongdian eclogite to have remained closed to Sm/Nd fractionation upon initial emplacement and crystallization. Using the intercept and gradient of the errorchron relationship, the source of the Xiongdian eclogite would have had an enriched $^{143}Nd/^{144}Nd$ ratio

(i.e. 0.511590) and $^{147}Sm/^{144}Nd$ ratio (i.e. 0.2458) at the timing of melting (i.e. analogous to an uplifted garnet peridotite-harzburgite: Dicken 2005).

In contrast to the Xiongdian eclogite, Sm-Nd isotopic ratios for our Sujiahe sample yield a Paleoproterozoic $T[Nd]_{DM}$ age of 1.8 Ga, which is consistent with Proterozoic $T[Nd]_{DM}$ model ages between 1.8 to 2.5 Ga for metamorphic rocks across the Yangtze continent (e.g. Chen and Jahn, 1998; Ma et al., 2000; Bryant et al., 2004). This evidence supports inclusion of SJH1 as either a portion of Paleoproterozoic continental crust or a younger mantle melt significantly contaminated by Paleoproterozoic or older continental crust. In either case, however, these whole rock geochemical and isotopic observations provide no support for the presence of a Silurian/Devonian basin underlain by oceanic crust as advocated by Wu et al. (2009).

6.4. The origin of zircon:

6.4.1. Xiongdian eclogite.

Zircon grains from the Xiongdian eclogite have received considerable attention owing to its designation as Paleotethyan oceanic crust. Previously published analyses of Xiongdian eclogite zircon grains display a number of overlapping characteristics, a lack of clear magmatic cores with oscillatory zonation, unclear relationships between U-Pb dates and trace element patterns (i.e. REE profiles and Th/U ratios), and a tri modal distribution in U-Pb dates (Fig. 7d). The lack of typical magmatic zircon features or a correlation between trace element composition and U-Pb dates has been suggested to represent the effect of sub-solidus zircon recrystallization during metamorphism or evidence for assimilation and recrystallization of a heterogeneous crustal detrital component (Sun et al., 2002; Jahn et al., 2005; Wu et al., 2009; Liu et al., 2009).

A late Silurian to early Devonian U-Pb age peak has been proposed to record timing of melt emplacement and crystallization, supporting the Paleotethyan crust protolith model (Sun et al., 2002; Cheng et al., 2009; Liu et al., 2009). The presence of two analyses with L-MREE enrichments, elevated Th and U concentrations, and magmatic Th/U ratios (e.g. Rubatto 2002) (Fig. 8b), one of which contains a concordant 420.5±9 Ma U-Pb age, represents either a mixed analysis involving LREE-, U-, and Th-rich inclusions (i.e. monazite), and/or crystallization from an evolved LREE enriched melt component (e.g. Belousova et al., 2006).

Our Xiongdian eclogite samples contain between 15 and 28 ppm Zr. This would appear to favor Zr to have been taken up largely during crystallization of amphibole and clinopyroxene, preventing zircon saturation or extensive zircon crystallization during cooling of a mafic oceanic crust protolith. In this case, assimilation of detrital crustal zircon grains may explain the origin of zircon in the Xiongdian eclogite protolith. This model, however, is not favored if we accept the Sm-Nd isotopic evidence for no external addition of components. For either case, due to the lack of textural evidence for preserved igneous cores, pre metamorphic trace element signatures, or an obvious initial U-Pb zircon age peak (our peak at 414.4±5.1 Ma is an average of 3 analyses), we are presented with no clear U-Pb zircon constraints from which to confidently evaluate the timing or nature of protolith formation for the Xiongdian eclogite.

Our zircon Hf-isotope analyses display a number of features similar to those presented by Liu et al. (2009): i.e. a dominantly positive distribution of εHf(t) with values up to ~20, and a relatively continuous distribution of $T[Hf]_{DM}$ ages from Carboniferous (Liu et al,. 2009) or Permian (our data) up to 950-1000 Ma with isolated ancient $T[Hf]_{DM}$ ages between 1350-1400 Ma. These features were interpreted by Liu et (2009) as consistent with a protolith model involving late Silurian/Early Devonian depleted mantle melting, crustal Hf isotopic contamination, and formation of the Paleotethyan oceanic crust. Due to the notably depleted

whole rock Hf concentration for our Xiongdian eclogite samples (0.56 to 0.94 ppm Hf), assimilation of a small volume of ancient crustal Hf from a continental source could reasonably explain the observed zircon Lu-Hf isotopic distribution patterns for our study and that of Liu et al. (2009).

As mentioned above, however, the exceptionally low whole rock Zr concentrations for our Xiongdian eclogite samples do not favor a simple model involving saturation and precipitation of zircon from an Hf-isotope contaminated Silurian/Early Devonian depleted mantle melt (e.g. Zheng et al., 2006). Also, it is generally accepted that zircon grains precipitated from a melt contaminated with ancient Hf will contain $T[Hf]_{DM}$ ages older than their respective U-Pb ages. While this relationship is largely observed in our Xiongdian eclogite zircon analyses, we also report a number of grains that show the opposite trend, involving $T[Hf]_{DM}$ ages that are younger than their respective U-Pb dates, an unusual feature that cannot be easily explained by assimilation of crustal Hf during fractional crystallization of a melt. An origin involving crustal contamination to explain the rather large spread in zircon $^{176}Hf/^{177}Hf$ ratios, $T[Hf]_{DM}$ ages and εHf values (Fig. 9), is also somewhat inconsistent with our observation that whole rock analyses plot on a Sm-Nd errorchron, implying insignificant addition of Nd through contamination and hybridization.

Without the presence of zircon to control the Hf budget, Hf becomes distributed into minerals where it is not a major structural component and where $^{176}Lu/^{177}Hf$ ratios are greater than those observed in zircon. Over time the $^{176}Hf/^{177}Hf$ ratios of these minerals increase at a rate proportional to their $^{176}Lu/^{177}Hf$ ratios resulting in $^{176}Hf/^{177}Hf$ ratios that no longer represent the initial $^{176}Hf/^{177}Hf$ ratios of the minerals, whole rock, or the melt source. Partitioning experiments and natural observations indicate that clinopyroxene, ilmenite and amphibole contain most of the Zr and Hf in low pressure mafic rocks, while pargasite, titanite, rutile,

garnet, and zircon control the Zr and Hf budget at high pressures (e.g. Spandler et al., 2003; Greene et al., 2006; Miller et al., 2007; Slama et al., 2007; Piccardo and Guarnieri, 2011). Consumption of these minerals during metamorphism or metasomatism would liberate radiogenic Hf, which would be then incorporated during growth of metamorphic zircon.

Provided with enough time and a number of separate minerals with different $^{176}Lu/^{177}Hf$ ratios, the zircon Hf isotopic composition of grains will display a heterogeneous mix involving multiple Hf sources, each with different $^{176}Hf/^{177}Hf$ ratios (e.g. Slama et al., 2007). Despite the lack of U-Pb zircon dates greater than 420 Ma, a Sm-Nd isotope errorchron ca. 960 $^{+160}/_{-250}$ Ma and Proterozoic $T[Hf]_{DM}$ ages (i.e. 800 to 1100 Ma) support the Xiongdian eclogite protolith to have existed since ~1.0 Ga. This would also provide an adequate period of time for Hf-isotope heterogeneity to develop, assuming zircon saturation was not attained during initial magmatic processes but instead associated with a secondary thermal event ca. 420 Ma.

6.4.2. Sujiahe:

For their two Sujiahe samples, Wu et al. (2009) identify U-Pb age peaks associated with igneous cores (i.e. concentric zonation) at 420±7 Ma (sample 07XX07 n=6) and 411±11 Ma (sample 07XX08 n=4), and interpret these late Silurian to early Devonian dates as representing mantle melting and protolith emplacement. Similar to the observations of Liu et al (2009), in-situ Lu-Hf and U-Pb isotopic analyses for zircon grains from these samples display a broad unimodal distribution in $^{176}Hf/^{177}Hf$ ratios and $T[Hf]_{DM}$ ages, with a prominently positive εHf(t = 420 and 410 Ma) values.

For our sample we identify only two concordant late Silurian U-Pb dates, at 416±9Ma and 419±40 Ma, both taken from igneous domains that contain magmatic REE profiles (Fig. 8a) and Th/U ratios of 0.7 and 1.7 (i.e. Rubatto, 2002), respectively. The presence of Proterozoic

igneous domain U-Pb dates (794±36 Ma, 894±56 Ma, and 1150±60 Ma) with similar magmatic Th/U ratios, and REE profiles that overlap with the younger analyses, however, makes it unclear whether or not the two late Silurian dates do indeed record Protolith formation.

Zircon $^{176}Hf/^{177}Hf$ ratios and $T[Hf]_{DM}$ ages for sample SJH1 display notably different patterns to those described above, containing only Proterozoic $T[Hf]_{DM}$ ages that define three main peaks, with an initial peak ca. 1.25 Ga. This pattern, however, is similar in many respects to Sujiahe sample 07XX07 reported by Wu et al. (2009), which contains both a distribution in $T[Hf]_{DM}$ ages centered towards a Proterozoic 950±100 Ma average, but also a number of grains with Early Paleozoic to Mesoproterozoic U-Pb dates, 527±Ma to 1439±4 Ma. These ancient U-Pb dates are proposed to be variably discordant xenocrystic cores, while the zircon Lu-Hf isotopic composition is interpreted as evidence for oceanic crust that incorporated more evolved crustal component(s).

While our zircon Lu-Hf isotopic data does not rule out assimilation of ancient crustal Hf and xenocrystic zircon grains, an interesting relationship is observed for analyses SJH1-07.1, SJH1-06.1 and SJH1-12.1, which contain overlapping U-Pb dates and $T[Hf]_{DM}$ ages ca. 1150 Ma, 800 Ma and 420 Ma, respectively. The $T[Hf]_{DM}$ ages for these analyses also align with the tri modal distribution in $T[Hf]_{DM}$ ages observed for the remaining population. While the presence of such geochronological features would appear to suggest sample SJH1 contains three mantle melt contributions (ca. 1150, 800, and 420 Ma), it is difficult to reconcile a model of repeated juvenile Hf addition without significant protolith host rock reworking and melting. The most reasonable solution for our observed $T[Hf]_{DM}$ age distribution is new zircon growth at ca. 800 and 420 Ma in response to secondary metamorphic events involving release of Hf sourced from a separate host rock phase which had a $^{176}Lu/^{177}Hf$ similar to the DM (e.g. Gerdes and Zeh, 2009).

In this regard, we observe very limited evidence that supports a late Silurian to early Devonian emplacement of a mantle melt. The $T[Hf]_{DM}$ age peak of 1.25 Ga (Fig. 10a) and single U-Pb date at 1.15 Ga are consistent with Proterozoic $T[Nd]_{DM}$ ages recorded across the SQT (e.g. Gao et al., 1996; Ratschbacher et al., 2003) and SCB (e.g. Chen and Jahn, 1998; Ma et al., 2000; Ling et al., 2003; Bryant et al., 2004; Ratschbacher et al., 2006; Hacker et al., 2006; Zheng et al., 2006; Zhao et al., 2008; Wang et al., 2010). Further to this, a whole rock $T[Nd]_{DM}$ age of 1.8 Ga favors the isotopic composition of source components responsible for SJH1 protolith to have formed >1.0 Ga, i.e. 1.25 Ga and 1.8 Ga.

6. 5. Proterozoic to Paleozoic origin and evolution of the HSZ:

For sample SJH1, Proterozoic Hf and Nd DM melting model ages at 1.25 Ga and 1.8 Ga, respectively, overlap with DM melting model ages and zircon U-Pb dates reported throughout the SCB and SQT (e.g. Bryant et al., 2004; Zhang et al., 2006; Zhao et al., 2008), and NQT (e.g. Diwu et al., 2012). The generation of these discrepancies, between zircon Hf and whole rock Nd isotopic systems are proposed to represent a two stage crustal evolution model for the SCB (Zheng et al., 2006), i.e. primary emplacement of Paleoproterozoic zircon undersaturated mantle melts, followed by secondary generation of zircon saturated melts through anatexis of these mafic crustal components during the Neoproterozoic. We favor this two stage model to explain the isotopic features recorded in sample SJH1 and designate our sample as having been present prior to Phanerozoic events recorded between the NCB and SCB.

The occurrence of middle Paleozoic to Mesozoic Paleotethyan Ocean in the HSZ is largely based on the interpretation that the Xiongdian eclogite represents a fragment of oceanic crust created in the Silurian Devonian (e.g. Fu et al., 2002; Ratschbacher et al., 2003, 2006; Wu et al., 2009; Cheng et al., 2009, 2010; Liu et al., 2009, 2011). In contrast to this interpretation,

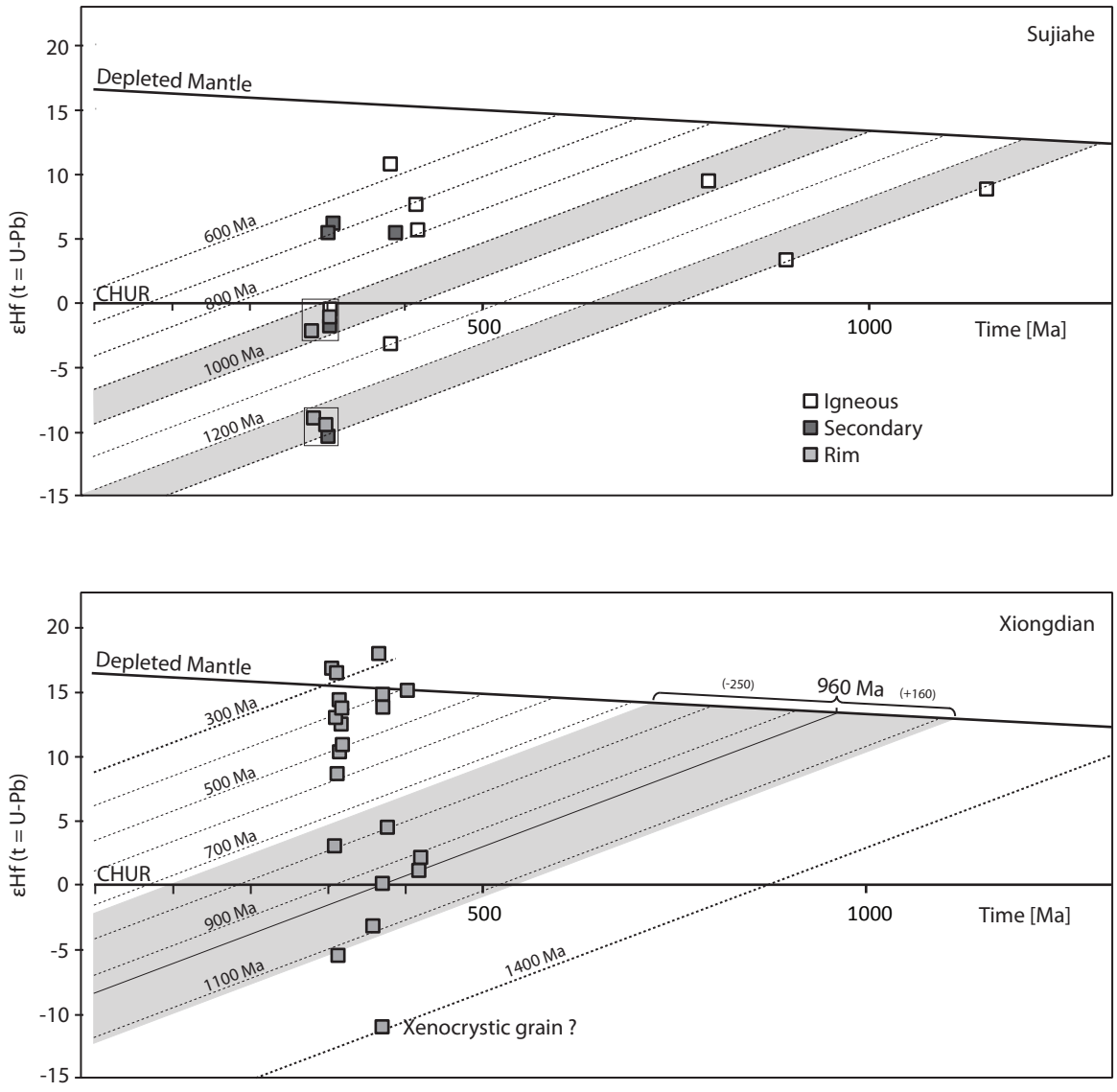

Figure 10: (a) εHf (t = $^{238}U/^{206}Pb$) vs. time for analyses from Sujiahe eclogite sample SJH1. Shaded grey domains represent Proterozoic T[Hf]DM age peaks. (b) εHf (t = $^{238}U/^{206}Pb$) vs. time for analyses from Xiongdian eclogite samples. Shaded grey domain represents the 960 Ma Sm-Nd errorchron with +160 and -250 Ma errors. Depleted Mantle evolution trends are calculated with values from Vervoort and Blichert-Toft, (1999). CHUR evolution trends are calculated using values from Bouvier et al. (2008).

we identify Neoproterzoic $T[Hf]_{DM}$ ages (ca. 800 to 1100 Ma) and a 960 $^{+160}/_{-250}$ Ma Sm-Nd errorchron age, which together provides evidence for a Neoproterozoic timing, ca. ~1.0 Ga, of oceanic arc crust protolith formation.

A Neoproterozoic timing of oceanic crust production between the SCB and NCB is consistent with similar observations for the Qinling Group of the NQT (Fig. 1c), located immediately north of the HSZ. This group is host to a number of Neoproterozoic gneisses, granodiorites and gabbros, including the Grenvillian Songshugou ophiolite (Fig. 1b), with a formation age of 1030±46 Ma (Dong et al., 2008), and the back arc basin N-MORB type metabasalts of the Kuanping Group, with a formation age of 943Ma (Dong et al., 2008; Diwu et al., 2010). These features suggest the HSZ contains a mélange of Proterozoic continental and oceanic blocks compiled from the NQT and possibly SQT, and associated with events that can be traced west along the Shangdan Suture.

7. The behavior of zircon during HP/LT metamorphism:

7.1. Zircon recrystallization during Carboniferous metamorphism:

7.1.1. Sujiahe eclogite.

For sample SJH1, zircon secondary domains (Fig. 6a) contain positively trending REE profiles (Fig. 8a), $^{176}Hf/^{177}Hf$ ratios identical to their respective Igneous domains (when present), extreme Th depletion, and reduced Th/U ratios (<0.1) and LREE contents. These features are consistent with in-situ (i.e. solid state) metamorphic recrystallization via interface coupled dissolution-reprecipitation, involving no redistribution or transport of zircon structural components (e.g. Tomaschek et al., 2003; Geisler et al., 2007; Chen et al 2010).

During interface coupled dissolution-reprecipitation, a mobile hydrous component catalyzes the dissolution of zircon domains that have an elevated solubility owing to radiation damage (i.e. metamictization), increased strain with accumulation of plastic crystal micro-structures (Timms et al., 2006; Reddy et al., 2006, 2009 element contents (see review in Geisler et al., 2007). Following dissolution, co-precipitation of crystalline zircon, distinguished as secondary domains or rims on igneous cores, represents the inwardly penetrating reaction front that was migrating toward the grain interior. The newly precipitated zircon domains display lower concentrations of incompatible elements (i.e. LREE) and Th, which is concentrated into Thorite inclusions that represent unmixing of a non-ideal solid solution end member, but retains the original composition of compatible components (i.e. HREE) and ideal solid solution end member such as Hf, and thus original $^{177}Hf/^{176}Hf$ ratios (e.g. Hoskin and Black, 2000; Tomaschek et al., 2003; Breeding et al., 2004b; Geisler et al., 2007; Martin et al., 2008; Rubatto et al., 2008; Chen et al., 2010; Ferriss et al., 2010).

It appears reasonable to suggest our SJH1 secondary domains recrystallized in response to prograde metamorphic events ca. 315-305 Ma (i.e. age peak II, Fig 7c) (e.g. Hoskin and Black, 2000; Tomaschek et al., 2003; Breeding et al., 2004b; Geisler et al., 2007; Martin et al., 2008; Rubatto et al., 2008; Chen et al., 2010). Recrystallization was likely triggered by fluids produced during devolatilization reactions crossing the blueschist or amphibolite to eclogite facies transition (Selverstone et al., 1992; Peacock, 1993; Giaramita and Sorensen, 1994; Poli and Schmidt, 1995; Schmidt and Poli, 1998; Becker et al., 2000; Spandler and Hermann, 2006; Bebout, 2007).

7.1.2. Xiongdian Eclogite.

For our Xiongdian eclogite samples, $^{177}Hf/^{176}Hf$ ratios and REE profiles remain effectively identical or unchanged between different domains within single zircon grains. The presence of REE profiles with insignificant Eu inflections, prominent positive Ce peaks, and steep LREE to HREE gradients overlap with zircon secondary domains for sample SJH1, and support our Xiongdian zircon ages to also reflect in-situ recrystallization during metamorphism, except involving a mechanism that appears to only reset U-Pb ages and not lead to loss or redistribution of other components (e.g. Corfu et al., 2003; Geisler et al., 2007; Chen et al., 2010).

For Xiongdian zircon grains HXD98-8-02 and HXD98-8-03, their LREE, U, and Th enriched core domains are coupled to external domains that contain significantly lower REE and Th contents, and steeper REE profile gradients, typical of the prominent population. This indicates coupled interface dissolution-precipitation to have impacted at least some zircon grains in our Xiongdian eclogite samples, if not all. Interestingly, because these REE features are observed for zircon domains that date back to ca. 419 Ma (i.e. HXD98-8-02.2), recrystallization appears to have begun by at least the Devonian.

7.2: Zircon and eclogite facies equilibrium:

7.2.1. Sujiahe eclogite.

Zircon rim domains for grains from sample SJH1 contain notably flat HREE profiles, depleted HREE contents, and different Lu-Hf isotopic compositions relative to their respective igneous or secondary domain analyses. These features indicate cogenetic growth of zircon and

garnet during HP metamorphism ca. 306-282 Ma (age peak I. Fig. 7c) (Rubatto, 2002; Hermann and Rubatto, 2003; Rubatto and Hermann, 2007ab; Chen et al., 2010: Gerdes and Zeh, 2009).

The ancient ca. 950 Ma and 1250 Ma $T[Hf]_{DM}$ ages recorded in zircon rim domains (Fig. 10a) implies consumption of the preexisting zircon population. An issue, however, concerning the dissolution and transport of Zr (and Hf) required for zircon growth is demonstrated in zircon/fluid and trace element/fluid solubility experiments, which highlight the insoluble and immobile nature of crystalline zircon and Zr in hydrous metamorphic fluids (Ayers and Watson, 1991; Kessel et al., 2005; Kovalenko and Ryzhenko, 2009; Ayers et al., 2012), and appear to make LT/HP sub solidus hydrothermal fluid zircon dissolution and Zr and Hf transport a highly limited process (e.g. Zeh et al.. 2010).

Alternatively, the experimental work of Ayers et al. (2003) showed that when no other major source of Zr is available, quartzite hosted zircon grains develop secondary domains through Ostwald ripening at the expense of the internal zircon population. These features were observed only during experimental runs involving addition of a hydrous component, consistent with proposed mechanisms of zircon growth during HP/UHP metamorphism where a fluid phase is required for Zr diffusion or advection (Corfu et al., 2003; Wu et al., 2006).

This mechanism of metamorphic zircon coarsening through consumption of the protolith zircon population appears consistent with the overlapping Hf-isotope composition of igneous, secondary domain, and rim domains (Fig. 9a and 10a). Interestingly, rim domains display LREE and Th concentrations, and Th/U ratios, which overlap with features proposed to have been generated by dissolution-reprecipitation of secondary domains. It remains unclear though, whether dissolution-reprecipitation occurred prior to or was a mechanism coupled to coarsening and rim formation. It is also possible, although not entirely necessary, that coarsening could have been aided by the coupled processes of metamictization and

accumulation of high energy sites during synmetamorphic intracrystalline strain produced a zircon population thermodynamically susceptible to dissolution and Ostwald ripening (Dempster et al., 2008; Vonlanthen et al., 2012).

A model involving zircon coarsening is consistent with natural and experimental observations, where, after the formation of eclogite, any free fluid produced during the transition from blueschist or amphibolite to eclogite facies is either lost from the system and/or becomes reconsumed into higher pressure hydrous phases (i.e. chlorite, lawsonite, chloritoid, zoisite, clinozoisite, phengite, paragonite, and apatite: e.g. Austrheim, 1987; Carswell, 1990; Poli and Schmidt, 1997, Schmidt and Poli, 1998; 2002; Jamtveit and Austrheim, 2010). Sporadic aqueous fluid production may still occur during the HP/UHP stage, however, due to their host rock bimodal garnet omphacite mineralogy, they will be effectively prevented from developing an inter-connected network due to high wetting (dihedral) angles (e.g. Watson and Lupulescu, 1993; Mibe et al., 2003). This limitation in both fluid volume and transport scale leads us to favor a fluid assisted coarsening mechanism involving micron scale diffusion of Zr for new growth, rather than zircon dissolution and Zr advection with fluid transport.

7.2.2. Xiongdian eclogite.

Unlike zircon grains from SJH1, the production of precise geochronological information for the Xiongdian eclogite has been a long standing problem, hindering our ability to reconstruct tectonic events preceding the final Mesozoic suturing (e.g. see review in Jahn et al., 2005). We report no analyses with both concordant U-Pb dates and flat HREE profiles that represent an equilibrium relationship with garnet (e.g. Rubatto and Hermann, 2007b). Also, our Xiongdian samples lack U-Pb zircon dates that fall into the range defined by zircon rim domains from sample SJH1, only secondary domains and older.

In contrast, Sun et al. (2002) report flat HREE profiles, garnet inclusions and U-Pb dates that span 322 to 290 Ma recorded in zircon secondary domains for grains extracted from a quartz eclogite Xiongdian sample. From these analyses, an average age of ca. 309 Ma (i.e. age peak II. Fig 7d) was proposed to represent the timing of peak HP metamorphism (Sun et al., 2002). While this age range compares well to rim domain analyses from our Sujiahe eclogite sample and those reported by Wu et al. (2009), Sun et al., (2002) also report zircon inner domain analyses with flat HREE profiles and dates that span 323 to 373 Ma, making it unclear when HP metamorphism began and the number of metamorphic events recorded by the Xiongdian eclogite.

The presence of garnet inclusions in Xiongdian eclogite zircon secondary domains has also been reported by Cheng et al. (2009), but similar to our work they also report no flat HREE profiles. The cause of this lack of "garnet effect" is unclear, but may be in part explained by their zircon rims appearing as thin bands, which for our study were often too thin to perform analyses. Alternatively, these secondary domains may instead represent in-situ dissolution–reprecipitation reaction zones and not new growth.

Geochronological studies for the garnet grains themselves yield even further ambiguity. Ye et al. (1993) report a 422±67 Ma garnet whole rock Sm-Nd Isochron age, while Cheng et al., (2009) and Cheng et al., (2010) report garnet Lu–Hf and Sm–Nd isochron ages of 271.3±5.3 Ma and 252.5±5 Ma, respectively. As discussed by Cheng et al., (2009), garnet porphyroblasts in the Xiongdian eclogite display a two stage history and clear core rim relationship involving inclusion rich cores surrounded by sharply defined inclusion free idiomorphic rims. The compositions of the garnet inclusions in zircon are comparable to those of the garnet cores, and represent a distinct earlier stage of garnet growth discontinuous to the rim domains that produce whole rock garnet Lu-Hf and Sm-Nd isochrons of ca. 270 Ma.

From their zircon U-Pb analyses, Cheng et al. (2009) interpret a 315±5 Ma age cluster as the initial timing of garnet growth. We also record a zircon U-Pb age peak at 313±2 Ma (Fig. 7b) and agree this relates to similar Carboniferous metamorphic events recorded in eclogites from Sujiahe (i.e. age peak II. Fig. 7cd). However, we do not completely agree that this age necessarily represents the timing of initial garnet growth, but rather prograde fluid migration and recrystallization, as discussed above.

8. Tectonic and geodynamic implications:

Mattauer et al., (1985) proposed that following the Paleozoic Qinling orogeny and closure of the Prototethyan ocean, continued convergence between the SQT and NQT/NCB block involved purely intra-continental shallow crustal deformation of the SQT up until the Mesozoic, with the SQT at this time representing a passive margin that developed along the northern margin of the SCB in response to Proterozoic opening of the Prototethyan Ocean. Such a model implies that oceanic subduction along the Shangdan Suture had effectively ceased by ca. 420 to 400 Ma (Fig. 11ab). Advancement of this model, however, has been limited due to the lack of early to middle Paleozoic dates in the SQT, and the rarity of metamorphic ages between 400 Ma to 325-315 Ma for lithologies in the NQT and SQT to constrain the nature of events occurring during this time.

In contrast, studies on meta lithologies from the HSZ have identified a wealth of dates to adequately fill this gap (Fig. 7cd) (Jian et al., 2000, 2001; Xu et al., 2000; Li et al., 2001; Sun et al., 2002; Wu et al., 2009; Cheng et al., 2009; Liu et al., 2009, 2011), leading to advancement of an alternative model (e.g. Wu et al., 2009; Cheng et al,. 2009, 2010; Liu et al., 2009, 2011), which invokes multiple, rapid Wilson Cycle like switches involving, (1) convergence between the

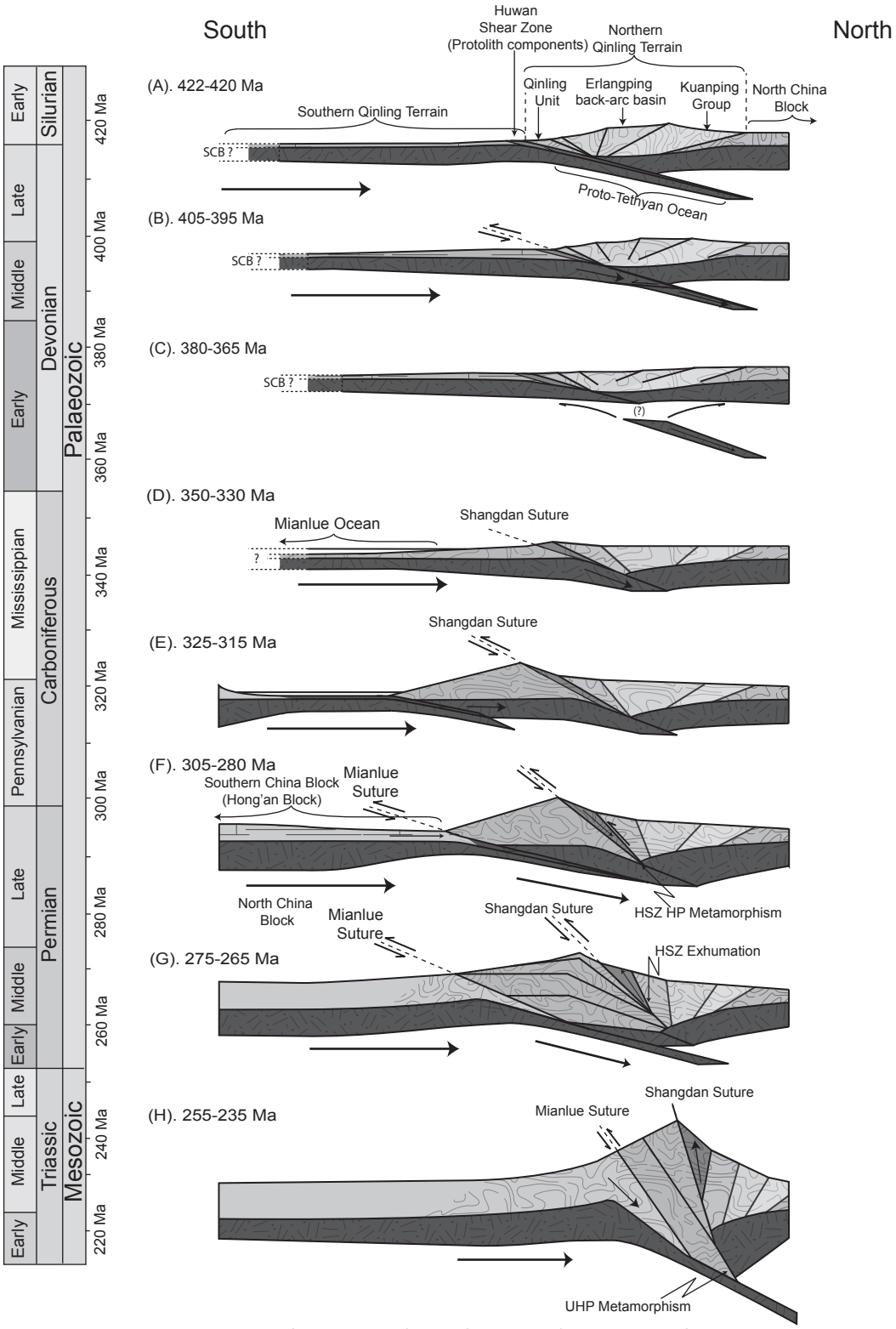

Figure 11: Tectonic evolution of the SQT (Hong'an block). See text for detailed description. Although depicted in Fig 11 as a separate tectonic unit, it is important to note that the HSZ is a mélange of eclogite components from the SQT and NQT that were brought together sequentially throughout the Paleozoic evolution of the Qinling region, and finally amalgamated into a Shear Zone during the Mesozoic collision between the SCB and SQT-NQT-NCB.

SQT/SCB and NQT-NCB during the Silurian Qinling Orogeny, (2) late Silurian/early Devonian divergence and rifting between the SQT and SCB and ocean basin (Paleotethyan or Mianlue ocean) formation up until the late Carboniferous, and (3) a final reversal back to convergence and ocean basin consumption associated with northward subduction beneath the southern margin of the SQT that is ultimately terminated by the Triassic collision between the SCB and SQT/NQT/NCB, and formation of a second suture, the Mianlue Suture (Meng and Zhang 1999, 2000; Wu et al., 2009; Cheng et al., 2009, 2010; Liu et al., 2009, 2011). The main discriminating factor between the two models is the proposed intermediate stage of divergence and ocean basin formation between ca. 440 and 420 Ma (Li et al., 2001; Sun et al., 2002; Wu et al., 2009; Cheng et al., 2009).

8.1. Formation and evolution of the Huwan Shear Zone:

As previously discussed, we consider our eclogite samples to be likely associated with the NQT and represent Proterozoic crust that was juxtaposed together during early Paleozoic Qinling orogenic events, which are more prominently defined west along the Shangdan Suture zone. If this reinterpretation is correct, evidence for Paleotethyan oceanic crust in the HSZ becomes exceedingly scarce and the position of the Shangdan Suture lies along the southern boundary of the HSZ.

It is important to note that we do not discredit the presence of a Paleotethyan or Mianlue ocean basin that separated the SQT and SCB and was subsequently subducted during the Paleozoic, only that evidence for its existence is not recorded in the HSZ. In this regard, we favor the HSZ to record a model similar to that first proposed by Mattauer et al., (1985), involving continued convergence during the Paleozoic following the Qinling orogen and

formation of the Shangdan Suture, rather than a period of late Silurian/early Devonian rifting and ocean basin formation.

Focusing on our zircon U-Pb age distributions, a picture is emerging from the NQT where metamorphic lithologies and late Silurian/early Devonian dates are interpreted to record a prolonged period of crustal accretion associated with Prototethyan Ocean subduction and arc magmatism (i.e. Erlangping arc: Fig 1c) ca. 450 to 490 Ma, followed by prompt (i.e. Δ10 to 25 Myr) crustal reworking with migmatization and granulite facies metamorphism (e.g. Kroner et al., 1993; Ratschbacher et al., 2006; Dong et al., 2008, 2011; Wang et al., 2011b, Zhu et al., 2011; Liu et al., 2012; Diwu et al., 2012). The two oldest non Proterozoic U-Pb dates for sample SJH1, 420.5±8.77 Ma and 419±8.74 Ma (Fig. 7a), are for zircons that contain textural evidence of magmatic growth (Fig. 6A,af), supporting another significant thermal event at ca. 420 Ma, in addition to the Neoproterozoic magmatism (age peak V. Figs. 7c and 7d). We interpret these ages as likely representing the final stages of ocean basin closure and initial stages of the Qinling orogeny between the NQT and SQT, which occurred sequentially between ca. 420-400 Ma (see reviews in Dong et al., 2011).

A 420-350 Ma spread in phengite $^{39}Ar/^{40}Ar$ dates, reported by Xu et al., (2000) for samples collected from the HSZ, indicate this period to have been dominated by cooling, tectonic exhumation and thinning (Fig. 11c). As discussed above, trace element analyses of zircon domains associated with these ages (Peak IV: Fig. 7cd) appear to indicate a period of recrystallization, possibly in response to infiltration of low temperature retrograde metamorphic fluids (e.g. 250–600°C: Rubatto et al., (2008), and references there in).

During this time, it remains unclear in the Eastern portion of the belt whether the southern margin of the SQT represented an extended passive margin attached to the northern margin of the SCB (i.e. Mattauer et al., 1985), or whether the SQT had previously split away from

the SCB and was separated by the Mianlue ocean, as it is proposed to be in the western portion (Fig. 11d). Attempts to trace the Mianlue suture zone eastward towards the Hong'an and Dabie terrains have proved particularly difficult (e.g. Li et al,. 2007, 2009, 2011; Dong et al., 2011). Many authors favor the eastward extension of the Mianlue suture to lie along the southern margin of the Hong'an-Dabie HP/UHP terrains (Fig. 1b) (e.g. Meng and Zhang 1999; Li et al,. 2007; Dong et al., 2011), however, this does not necessarily mean the Mianlue ocean extended as far east as the Hong'an-Dabie blocks. In either case, northward convergence of the SQT into the NQT-NCB is thought to have continued up to the mid Carboniferous and accommodated via intra-continental shortening, southward syn-metamorphic back thrusting, and crustal thickening with further accretionary wedge development (Fig. 11d) (Mattauer et al., 1985; Ratschbacher et al., 2006).

By ca. 325-315 Ma (i.e. age peak III: Fig. 7d), the HSZ and other units along the Shangdan suture record evidence of extensive lateral strike slip deformation (Fig. 11e: e.g. Mattauer et al., 1985; Ratschbacher et al., 2003, 2006). This period of time is especially well represented in eclogites from the HSZ where U-Pb ages are concentrated between 325 to 280 Ma (Fig. 7cd). Using the age peaks in Figures 7dc, we propose initiation of deep burial in the HSZ to have occurred ca. 325 Ma at the earliest (Age peak III: Fig 7d), reaching the eclogite facies realm between ca. 315 to 305 Ma (Age peaks II: Fig. 7cd), followed by Carboniferous Permian HP metamorphism between ca. 305 to 280 Ma (Fig. 11f) (e.g. Wu et al., 2009). We interpret this final HP pulse in activity along the Shangdan Suture to potentially relate to lateral stress associated with subduction and closure of the Mianlue Ocean in the western portion of the belt and/or intra-continental shortening of the SQT had reached its limit as convergence between the SCB and SQT-NQT-NCB had begun.

During the final stages of ocean basin closure, it is proposed that the geometry of oceanic subduction changed, with clockwise rotation of the SCB as it approached the southern margin of the SQT (e.g. Liu et al., 2005; Li et al., 2007). As a result of this geometric reorganization, continent-continent collision occurred first along the eastern margin of the SQT (Fig 11f), where UHP deformation was subsequently concentrated and Mesozoic overprint extensive. Post peak retrograde metamorphism and exhumation of the Xiongdian and Sujiahe eclogites to upper crustal levels likely occurred ca. 275-265 Ma (Fig. 11g), potentially involving accretion into the hanging wall and uplift with continued convergence between the SQT and SCB. In the Xiongdian eclogite, late Permian to early Triassic whole rock/Garnet Lu-Hf and Sm-Nd isochron ages ca. 270-253 Ma (Cheng et al., 2009, 2010) suggest the HSZ was involved in a complex coupled interplay between progressive convergence, burial and exhumation during the final stages of convergence between the SCB and SQT-NQT-NCB (Fig. 1b and Fig. 11h). Muscovite cooling ages across the HSZ range from ca. 267 Ma (Niu et al., 1994) to ca. 206 Ma (Webb et al., 1999), and structural deformation fabric (i.e. mylonitization) has been dated at ca. 235 Ma to 195 Ma (Ratschbacher et al., 2006).

9. Summary and Conclusions:

The Huwan Shear Zone is one of a number of thin and highly deformed transpressive shear zones associated with formation of the Shangdan Suture. Studies using eclogites from the HSZ have produced a spectrum of in-situ U-Pb zircon dates to reconstruct their metamorphic evolution and probe the ability of zircon to record high grade metamorphism.

The origins of zircon in our samples represent a two stage process associated with crustal evolution processes rather than crustal growth and addition of juvenile mantle melt components.

Analysis of zircon grains from a sample of Sujiahe eclogite detail a clear response to eclogite facies metamorphic overprint (Table. 3), in support of the observations of Wu et al., (2009). We identify three types of zircon, based on their geochemical and textural features: (1) preserved igneous components, (2) secondary domains, which represents igneous zircon recrystallized via coupled interface dissolution-reprecipitation during in-situ hydrothermal fluid infiltration and prograde metamorphism, and (3) rim domains that display an equilibrium growth relationship with garnet, and thus records HP metamorphic conditions.

Analyses of zircon grains from samples of the Xiongdian eclogite yield a somewhat more ambiguous response to metamorphic events (Table. 3). Unlike sample SJH1 from Sujiahe, we do not observe any zircon domains of clear igneous origin, limiting our ability to constrain a subsequent response to high grade metamorphism. Analyses of different spots on single grains identify a prominent history involving in-situ zircon recrystallization and U-Pb age resetting without considerable loss or redistribution of other components. We also do not observe any evidence of an equilibrium relationship with HP garnet, new growth, or generation of dates associated with SJH1 zircon rim domains, indicating either a lack of reaction during HP metamorphism, or a lack of sufficient rim growth during metamorphism for micro analysis.

By presenting revised Protolith models which favor the Xiongdian eclogite to be Neoproterozoic (ca. 1.0 Ga) lower oceanic arc crust and the Sujiahe eclogite to be a hybrid between recycled 1.25 Ga and 1.8 Ga juvenile crustal components, we effectively remove any conclusive evidence for early/middle Paleozoic oceanic crust in the HSZ.

We propose the HSZ to contain a mélange of Proterozoic crustal components analogous to those found in the Northern Qinling Terrain. These components were brought together by events associated with formation of the Shangdan Suture zone and transpressive deformation during a protracted Paleozoic Mesozoic period of convergence and accretion along the southern margin the NCB.

Table. 3. Summary data and interpretations for eclogite-hosted zircon analyses.

Sample	SJH1	SJH1	SJH1	Xiongdian
Domain	Core	Mantle	Rim	All
U-Pb dates	1150-305 Ma	388-304 Ma	306-282 Ma	420-234 Ma
CL Zonation	Mottled, anisotropic and or oscillatory zonation patterns.	Mottled, anisotropic and or discontinuous zonation patterns.	Mottled, anisotropic and or discontinuous zonation patterns.	Mottled, anisotropic, discontinuous and or sector zonation patterns.
REE profile	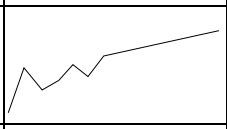			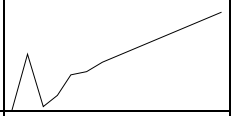
HREE/MREE: Average [Gd/Lu]N	21.2	63.4	2.7	86
MREE/LREE: Average [Gd/Nd]N	19	163	31	57
Eu anomaly	Yes: Negative	Negligible	Negligible	Negligible
Range: U (ppm)	1581-80	226-99	128-73	734-12
Average :U (ppm)	373	172	95	187
Range: Th (ppm)	670-35	8.3-0.7	2.9-1.1	803-0.3
Average :Th (ppm)	230	2.6 (Th depletion)	2.2 (Th depletion)	56
Th/U ratios	>0.18	<0.03	<0.04	1.59-0.002 Average 0.21
Lu/Hf ratio Average 10^{-4}	420	167	12	439
Lu-Hf ratio Range	698-9	361-57	28-5	1069-61
$^{177}Hf/^{176}Hf$ ratio	Variable	Same as core	Different to core	Highly variable
Summary:	Magmatic Variable Pb-loss Multiple melt events	Dissolution-Reprecipitation. Thorite exsolution.	New-zircon growth at HP conditions. Equillibrium with garnet	Dissolution-Reprecipitation.

10. References:

Andersen, T., 2002. Correction of common lead in U-Pb analyses that do not report 204Pb. Chemical Geology 192, 59.

Austrheim, H., 1987. Eclogitization Of Lower Crustal Granulites By Fluid Migration Through Shear Zones. Earth And Planetary Science Letters 81, 221-232.

Ayers, J.C., DeLaCruz, K., Miller, C., Switzer, O., 2003. Experimental study of zircon coarsening in quartzite (+/-) H2O at 1.0 GPa and 1000°C, with implications for geochronological studies of high-grade metamorphism. American Mineralogist 88, 365-376.

Ayers, J.C., Dunkle, S., Gao, S., Miller, C.F., 2002. Constraints on timing of peak and retrograde metamorphism in the Dabie Shan Ultrahigh-Pressure Metamorphic Belt, east-central China, using U-Th-Pb dating of zircon and monazite. Chemical Geology 186, 315.

Ayers, J.C., Watson, E.B., 1991. Solubility Of Apatite, Monazite, Zircon, And Rutile In Supercritical Aqueous Fluids With Implications For Subduction Zone Geochemistry. Philosophical Transactions Of The Royal Society Of London Series A-Mathematical Physical And Engineering Sciences 335, 365-375.

Ayers J.C., Zhang L., Luo Y., Peters T., 2012. Zircon and Baddeleyite Solubility in Alkaline Aqueous Fluids at Upper Crustal Conditions. Submitted

Bebout, G.E., 2007. Metamorphic chemical geodynamics of subduction zones. Earth and Planetary Science Letters 260, 373-393.

Becker, H., Jochum, K.P., Carlson, R.W., 2000. Trace element fractionation during dehydration of eclogites from high-pressure terranes and the implications for element fluxes in subduction zones. Chemical Geology 163, 65.

Belousova, E.A., Griffin, W.L., O'Reilly, S.Y., 2006. Zircon crystal morphology, trace element signatures and Hf isotope composition as a tool for petrogenetic modelling: Examples from Eastern Australian granitoids. Journal Of Petrology 47, 329-353.

Benn, K., Nicolas, A., Reuber, I., 1988. Mantle—crust transition zone and origin of wehrlitic magmas: Evidence from the Oman ophiolite. Tectonophysics 151, 75-85.

Bouvier, A., Vervoort, J.D., Patchett, P.J., 2008. The Lu-Hf and Sm-Nd isotopic composition of CHUR: Constraints from unequilibrated chondrites and implications for the bulk composition of terrestrial planets. Earth and Planetary Science Letters 273, 48.

Breeding, C.M., Ague, J.J., Brocker, M., 2004a. Fluid-metasedimentary rock interactions in subduction-zone melange: Implications for the chemical composition of arc magmas. Geology 32, 1041-1044.

Breeding, C.M., Ague, J.J., Grove, M., Rupke, A.L., 2004b. Isotopic and chemical alteration of zircon by metamorphic fluids: U-Pb age depth-profiling of zircon crystals from Barrow's garnet zone, northeast Scotland. American Mineralogist 89, 1067-1077.

Bryant, D.L., Ayers, J.C., Gao, S., Miller, C.F., Zhang, H., 2004. Geochemical, age, and isotopic constraints on the location of the Sinoâ€“Korean/Yangtze Suture and evolution of the Northern Dabie Complex, east central China. Geological Society of America Bulletin 116, 698-717.

Carswell, D.A., 1990. Eclogites and the eclogite facies: definitions and classification. In: Carswell, D.A. (Ed.), Eclogite Facies Rocks. Blackie, Glasgow, pp. 1– 14. Published in the USA by Chapman & Hall, New York.

Chen, J., Jahn, B.-m., 1998. Crustal evolution of southeastern China: Nd and Sr isotopic evidence. Tectonophysics 284, 101.

Chen, R.-X., Zheng, Y.-F., Xie, L., 2010. Metamorphic growth and recrystallization of zircon: Distinction by simultaneous in-situ analyses of trace elements, U-Th-Pb and Lu-Hf isotopes in zircons from eclogite-facies rocks in the Sulu orogen. Lithos 114, 132.

Cheng, H., DuFrane, S.A., Vervoort, J.D., Nakamura, E., Zheng, Y.-F., Zhou, Z., 2010. Protracted oceanic subduction prior to continental subduction: New Lu-Hf and Sm-Nd geochronology of oceanic-type high-pressure eclogite in the western Dabie orogen. American Mineralogist 95, 1214-1223.

Cheng, H., King, R.L., Nakamura, E., Vervoort, J.D., Zheng, Y.-F., Ota, T., Wu, Y.-B., Kobayashi, K., Zhou, Z.-Y., 2009. Transitional time of oceanic to continental subduction in the Dabie orogen: Constraints from U-Pb, Lu-Hf, Sm-Nd and Ar-Ar multichronometric dating. Lithos 110, 327.

Cherniak, D.J., 2010. Diffusion in Accessory Minerals Zircon, Titanite, Apatite, Monazite and Xenotime, in: Zhang, Y.X.C.D.J. (Ed.), Diffusion in Minerals and Melts, 827-869.

Cherniak, D.J., Watson, E.B., 2003. Diffusion in zircon, in: Hanchar, J.M.H.P.W.O. (Ed.), Zircon. 113-143.

Chu, N.-C., Taylor, R.N., Chavagnac, V., Nesbitt, R.W., Boella, R.M., Milton, J.A., German, C.R., Bayon, G., Burton, K., 2002. Hf isotope ratio analysis using multi-collector inductively coupled plasma mass spectrometry: an evaluation of isobaric interference corrections. Journal of Analytical Atomic Spectrometry 17, 1567.

Corfu, F., Hanchar, J.M., Hoskin, P.W.O., Kinny, P., 2003. Atlas of Zircon Textures. Reviews in Mineralogy and Geochemistry 53, 469-500.

Dempster, T.J., Martin, J.C., Shipton, Z.K., 2008. Zircon dissolution in a ductile shear zone, Monte Rosa granite gneiss, northern Italy. Mineral Mag 72, 971-986.

Depaolo, D.J., Wasserburg, G.J., 1979. Neodymium isotopes in flood basalts from the Siberian Platform and inferences about their mantle sources. Proceedings of the National Academy of Sciences of the United States of America 76, 3056-3060.

Dickin, A.P., 1995. Radiogenic Isotope Geology. 490 pp. Cambridge Univ. Press, Cambridge,

Diwu, C.R., Sun, Y., Liu, L.A., Zhang, C.L., Wang, H.L., 2010. The disintegration of Kuanping Group in North Qinling orogenic belts and Neo-proterozoic N-MORB. Acta Petrologica Sinica 26, 2025-2038.

Diwu, C., Sun, Y., Zhang, H., Wang, Q., Guo, A., Fan, L., 2012. Episodic tectonothermal events of the western North China Craton and North Qinling Orogenic Belt in central China: Constraints from detrital zircon U–Pb ages. Journal of Asian Earth Sciences 47, 107-122

Dong, Y.-P., Zhou, M.-F., Zhang, G.-W., Zhou, D.-W., Liu, L., Zhang, Q., 2008. The Grenvillian Songshugou ophiolite in the Qinling Mountains, Central China: Implications for the tectonic evolution of the Qinling orogenic belt. Journal of Asian Earth Sciences 32, 325.

Dong, Y., Zhang, G., Neubauer, F., Liu, X., Genser, J., Hauzenberger, C., 2011. Tectonic evolution of the Qinling orogen, China: Review and synthesis. Journal of Asian Earth Sciences 41, 213.

Eide, E.A., Liou, J.G., 2000. High-pressure blueschists and eclogites in Hong'an: a framework for addressing the evolution of high- and ultrahigh-pressure rocks in central China. Lithos 52, 1.

Elliott, T., Plank, T., Zindler, A., White, W., Bourdon, B., 1997. Element transport from slab to volcanic front at the Mariana arc. J. Geophys. Res. 102, 14991.

Ferriss, E.D.A., Ewing, R.C., Becker, U., 2010. Simulation of thermodynamic mixing properties of actinide-containing zircon solid solutions. American Mineralogist 95, 229-241.

Fu, B., Zheng, Y.-F., Touret, J.L.R., 2002. Petrological, isotopic and fluid inclusion studies of eclogites from Sujiahe, NW Dabie Shan (China). Chemical Geology 187, 107.

Gao, S., Y. Qiu, W. Ling, N. J. McNaughton, B. Zhang, G. Zhang, Z. Zhang, Z. Zhong, Z. and S. Suo 2002. SHRIMP single zircon U-Pb geochronology of eclogites from Yingshan and Xiongdian. Copyright © 2011 China University of Geosciences. Published by Elsevier B.V. All rights reserved Journal of China University of Geoscience, p. 558.

Gao, S., Zhang, B.-R., Wang, D.-P., Ouyang, J.-P., Xie, Q.-L., 1996. Geochemical evidence for the Proterozoic tectonic evolution of the Qinling Orogenic Belt and its adjacent margins of the North China and Yangtze cratons. Precambrian Research 80, 23.

Geisler, T., Schaltegger, U., Tomaschek, F., 2007. Re-equilibration of zircon in aqueous fluids and melts. Elements 3, 43-50.

Gerdes, A., Zeh, A., 2009. Zircon formation versus zircon alteration -- New insights from combined U-Pb and Lu-Hf in-situ LA-ICP-MS analyses, and consequences for the

interpretation of Archean zircon from the Central Zone of the Limpopo Belt. Chemical Geology 261, 230.

Giaramita, M.J., Sorensen, S.S., 1994. Primary fluids in low-temperature eclogites: evidence from two subduction complexes (Dominican Republic, and California, USA). Contributions to Mineralogy and Petrology 117, 279.

Greene, A.R., DeBari, S.M., Kelemen, P.B., Blusztajn, J., Clift, P.D., 2006. A Detailed Geochemical Study of Island Arc Crust: the Talkeetna Arc Section, South-Central Alaska. Journal of Petrology 47, 1051-1093.

Hacker, B.R., Ratschbacher, L., Webb, L., McWilliams, M.O., Ireland, T., Calvert, A., Dong, S.W., Wenk, H.R., Chateigner, D., 2000. Exhumation of ultrahigh-pressure continental crust in east central China: Late Triassic-Early Jurassic tectonic unroofing. Journal Of Geophysical Research-Solid Earth 105, 13339-13364.

Hacker, B.R., Wallis, S.R., Ratschbacher, L., Grove, M., Gehrels, G., 2006. High-temperature geochronology constraints on the tectonic history and architecture of the ultrahigh-pressure Dabie-Sulu Orogen. Tectonics 25.

Harley, S.L., Kelly, N.M., Moller, A., 2007. Zircon behaviour and the thermal histories of mountain chains. Elements 3, 25-30.

Hermann, J., Rubatto, D., 2003. Relating zircon and monazite domains to garnet growth zones: age and duration of granulite facies metamorphism in the Val Malenco lower crust. Journal Of Metamorphic Geology 21, 833-852.

Hermann, J., Rubatto, D., Korsakov, A., Shatsky, V.S., 2001. Multiple zircon growth during fast exhumation of diamondiferous, deeply subducted continental crust (Kokchetav Massif, Kazakhstan). Contributions To Mineralogy And Petrology 141, 66-82.

Hermann, J., Spandler, C., Hack, A., Korsakov, A.V., 2006. Aqueous fluids and hydrous melts in high-pressure and ultra-high pressure rocks: Implications for element transfer in subduction zones. Lithos 92, 399-417.

Hoskin, P.W.O., Black, L.P., 2000. Metamorphic zircon formation by solid-state recrystallization of protolith igneous zircon. Journal of Metamorphic Geology 18, 423-439.

Iizuka, T., Hirata, T., 2005. Improvements of precision and accuracy in in situ Hf isotope microanalysis of zircon using the laser ablation-MC-ICPMS technique. Chemical Geology 220, 121.

Jahn, B.M., 1998. Geochemical and isotopiccharacteristics of UHPeclogites and ultramaficrocks of the Dabie orogen: implications for continental subduction and collisional tectonics. In: Hacker, B., Liou, J.G. (Eds.), When Continents Collide: Geodynamics and Geochemistry of Ultrahigh-Pressure Rocks. Kluwer Acad. Publishers, Dordrecht, The Netherlands.

Jahn, B.-m., Liu, X., Yui, T.-F., Morin, N., Coz, M., 2005. High-pressure/ultrahigh-pressure eclogites from the Hong'an Block, East-Central China: geochemical characterization, isotope disequilibrium and geochronological controversy. Contributions to Mineralogy and Petrology 149, 499.

Jamtveit, B., Austrheim, H., 2010. Metamorphism: The Role of Fluids. Elements 6, 153-158.

Jian, P., Liu, D.Y., Yang, W.R., Williams, I.S., 2000. Petrographic and SHRIMP studies of zircons from the Caledonian Xiongdian Eclogite, northwestern Dabie Mountains. Acta Geologica Sinica-English Edition 74, 766-773.

Jian, P., Liu, D.Y., Yang, W.R., Williams, I.S., 2001. SHRIMP dating of zircons from the Caledonian Xiongdian eclogite, western Dabie Mountains, China. Chinese Science Bulletin 46, 77-79.

Juteau, T., Ernewein, M., Reuber, I., Whitechurch, H., Dahl, R., 1988. Duality of magmatism in the plutonic sequence of the Sumail Nappe, Oman. Tectonophysics 151, 107.

Kessel, R., Schmidt, M.W., Ulmer, P., Pettke, T., 2005. Trace element signature of subduction-zone fluids, melts and supercritical liquids at 120-180 km depth. Nature 437, 724-727.

Klein, E.M., Heinrich, D.H., Karl, K.T., 2003. Geochemistry of the Igneous Oceanic Crust, Treatise on Geochemistry. Pergamon, Oxford, p. 433.

Koepke, J., Schoenborn, S., Oelze, M., Wittmann, H., Feig, S.T., Hellebrand, E., Boudier, F., Schoenberg, R., 2009. Petrogenesis of crustal wehrlites in the Oman ophiolite: Experiments and natural rocks. Geochemistry Geophysics Geosystems 10.

Kovalenko, N., Ryzhenko, B., 2009. Comparative study of the solubility of zircon and baddeleyite. Geochemistry International 47, 405.

Kröner, A., Zhang, G.W., Sun, Y., 1993. Granulites in the Tongbai Area, Qinling Belt, China: Geochemistry, petrology, single zircon geochronology, and implications for the tectonic evolution of eastern Asia. Tectonics 12, 245.

Lachize, M., Lorand, J.P., Juteau, T., 1996. Calc-alkaline differentiation trend in the plutonic sequence of the Wadi Haymiliyah section, Haylayn massif, Semail ophiolite, Oman. Lithos 38, 207-232.

Lebas, M.J., 1989. Nephelinitic And Basanitic Rocks. Journal Of Petrology 30, 1299-1312.

Leech, M.L., 2001. Arrested orogenic development: eclogitization, delamination, and tectonic collapse. Earth and Planetary Science Letters 185, 149.

Li, S.G., Huang, F., Nie, Y.H., Han, W.L., Long, G., Li, H.M., Zhang, S.Q., Zhang, Z.H., 2001. Geochemical and geochronological constraints on the suture location between the North and South China blocks in the Dabie Orogen, Central China. Physics and Chemistry of the Earth, Part A: Solid Earth and Geodesy 26, 655.

Li, X.-H., Li, Z.-X., Li, W.-X., Liu, Y., Yuan, C., Wei, G., Qi, C., 2007. U-Pb zircon, geochemical and Sr-Nd-Hf isotopic constraints on age and origin of Jurassic I- and A-type granites from central Guangdong, SE China: A major igneous event in response to foundering of a subducted flat-slab? Lithos 96, 186.

Li, S., Kusky, T.M., Liu, X., Zhang, G., Zhao, G., Wang, L., Wang, Y., 2009. Two-stage collision-related extrusion of the western Dabie HP-UHP metamorphic terranes, central China: Evidence from quartz c-axis fabrics and structures. Gondwana Research 16, 294.

Li, S., Kusky, T.M., Zhao, G., Liu, X., Wang, L., Kopp, H., Hoernle, K., Zhang, G., Dai, L., 2011. Thermochronological constraints on two-stage extrusion of HP/UHP terranes in the Dabie-Sulu orogen, east-central China. Tectonophysics 504, 25.

Liati, A., Gebauer, D., 1999. Constraining the prograde and retrograde P-T-t path of Eocene HP rocks by SHRIMP dating of different zircon domains: inferred rates of heating, burial, cooling and exhumation for central Rhodope, northern Greece. Contributions to Mineralogy and Petrology 135, 340.

Ling, W., Gao, S., Zhang, B., Li, H., Liu, Y., Cheng, J., 2003. Neoproterozoic tectonic evolution of the northwestern Yangtze craton, South China: implications for amalgamation and break-up of the Rodinia Supercontinent. Precambrian Research 122, 111.

Liu, F.L., Liou, J.G., 2011. Zircon as the best mineral for P-T-time history of UHP metamorphism: A review on mineral inclusions and U-Pb SHRIMP ages of zircons from the Dabie-Sulu UHP rocks. Journal of Asian Earth Sciences 40, 1.

Liu, X., Jahn, B.-m., Liu, D., Dong, S., Li, S., 2004. SHRIMP U-Pb zircon dating of a metagabbro and eclogites from western Dabieshan (Hong'an Block), China, and its tectonic implications. Tectonophysics 394, 171.

Liu, X., Wei, C., Li, S., Dong, S., Liu, J., 2004. Thermobaric structure of a traverse across western Dabieshan: implications for collision tectonics between the Sino-Korean and Yangtze cratons. Journal of Metamorphic Geology 22, 361.

Liu, S., Steel, R., Zhang, G., 2005. Mesozoic sedimentary basin development and tectonic implication, northern Yangtze Block, eastern China: record of continent-continent collision. Journal of Asian Earth Sciences 25, 9.

Liu, D., Jian, P., Kröner, A., Xu, S., 2006. Dating of prograde metamorphic events deciphered from episodic zircon growth in rocks of the Dabie-Sulu UHP complex, China. Earth and Planetary Science Letters 250, 650.

Liu, Y.-H., Yang, H.-J., Shau, Y.-H., Meng, F., Zhang, J., Yang, J., Xu, Z., Yu, S.-C., 2007. Compositions of high Fe-Ti eclogites from the Sulu UHP metamorphic terrane, China: HFSE decoupling and protolith characteristics. Chemical Geology 239, 64.

Liu, X.C., Wu, Y.B., Wang, J., Peng, M., Jiao, W.F., 2009. Zircon U-Pb age recording couple subduction of oceanic and continental eclogites in the Huwan shear zone, western

Dabie Mountains, and its geodynamic implications. Acta Petrologica Sinica 25, 2209-2223.

Liu, X.C., Wu, Y.B., Gao, S., Wang, J., Peng, M., Gong, H.J., Liu, Y.S., Yuan, H.L., 2011. Zircon U–Pb and Hf evidence for coupled subduction of oceanic and continental crust during the Carboniferous in the Huwan shear zone, western Dabie orogen, central China. Journal of Metamorphic Geology 29, 233.

Liu, X.C., Jahn, B.M., Hu, J., Li, S.Z., Liu, X., Song, B., 2011. Metamorphic patterns and SHRIMP zircon ages of medium-to-high grade rocks from the Tongbai orogen, central China: implications for multiple accretion/collision processes prior to terminal continental collision. J. Metamorph. Geol. 29, 979-1002.

Liu, X., Li, S., Suo, Y., Liu, X., Dai, L., Santosh, M., 2012. Structural analysis of the northern Tongbai Metamorphic Terranes, Central China: Implications for Paleozoic accretionary process on the southern margin of the North China Craton. Journal of Asian Earth Sciences.

Ludwig, K.R., 2003. User's manual for Isoplot 3.00. A geochronological Toolkit for Microsoft Excel. . Berkeley Geochronology Center, Berkeley, California.

Lugmair, G.W., Marti, K., 1978. Lunar initial 143Nd/144Nd: Differential evolution of the lunar crust and mantle. Earth and Planetary Science Letters 39, 349.

Ma, C., Ehlers, C., Xu, C., Li, Z., Yang, K., 2000. The roots of the Dabieshan ultrahigh-pressure metamorphic terrane: constraints from geochemistry and Nd-Sr isotope systematics. Precambrian Research 102, 279.

Manning, C.E., 2004. The chemistry of subduction-zone fluids. Earth And Planetary Science Letters 223, 1-16.

Martin, L.A.J., Duchêne, S., Deloule, E., Vanderhaeghe, O., 2008. Mobility of trace elements and oxygen in zircon during metamorphism: Consequences for geochemical tracing. Earth and Planetary Science Letters 267, 161.

Mattauer, M., Matte, P., Malavieille, J., Tapponnier, P., Maluski, H., Xu, Z.Q., Lu, Y.L., Tang, Y.Q., 1985. Tectonics Of The Qinling Belt - Buildup And Evolution Of Eastern Asia. Nature 317, 496-500.

Meng, Q.R., Zhang, G.W., 1999. Timing of collision of the North and South China blocks: Controversy and reconciliation. Geology 27, 123-126.

Meng, Q.R., Zhang, G.W., 2000. Geologic framework and tectonic evolution of the Qinling orogen, central China. Tectonophysics 323, 183-196.

Mibe, K., Yoshino, T., Ono, S., Yasuda, A., Fujii, T., 2003. Connectivity of aqueous fluid in eclogite and its implications for fluid migration in the Earth's interior. J. Geophys. Res. 108, 2295.

Miller, C., Zanetti, A., Thoni, M., Konzett, J., 2007. Eclogitisation of gabbroic rocks: Redistribution of trace elements and Zr in rutile thermometry in an Eo-Alpine subduction zone (Eastern Alps). Chemical Geology 239, 96-123.

Murali, A.V., Parthasarathy, R., Mahadevan, T.M., Das, M.S., 1983. Trace element characteristics, REE patterns and partition coefficients of zircons from different geological environments- A case study on Indian zircons. Geochimica Et Cosmochimica Acta 47, 2047-2052.

Niu, B., Fu, Y., Liu, Z., Ren, J., Chen, W., 1994. Main tectonothermal events and 40Ar/39Ar dating of the Tongbai–Dabie Mts. Acta Geoscientia Sinica, pp. 20-34.

Nonnotte, P., Ceuleneer, G., Benoit, M., 2005. Genesis of andesitic-boninitic magmas at mid-ocean ridges by melting of hydrated peridotites: Geochemical evidence from DSDP Site 334 gabbronorites. Earth and Planetary Science Letters 236, 632.

Peacock, S.M., 1987. Thermal Effects Of Metamorphic Fluids In Subduction Zones. Geology 15, 1057-1060.

Peacock, S.M., 1990. Fluid Processes In Subduction Zones. Science 248, 329-337.

Peacock, S.M., 1993. The Importance Of Blueschist -] Eclogite Dehydration Reactions In Subducting Oceanic-Crust. Geological Society Of America Bulletin 105, 684-694.

Pearce, J.A., Baker, P.E., Harvey, P.K., Luff, I.W., 1995. Geochemical Evidence for
Subduction Fluxes, Mantle Melting and Fractional Crystallization Beneath the South Sandwich Island Arc. Journal of Petrology 36, 1073-1109.

Piccardo, G.B., Guarnieri, L., 2011. Gabbro-norite cumulates from strongly depleted MORB melts in the Alpine-Apennine ophiolites. Lithos 124, 200.

Poli, S., Schmidt, M.W., 1995. H20 Transport And Release In Subduction Zones - Experimental Constraints On Basaltic And Andesitic Systems. Journal of Geophysical Research-Solid Earth 100, 22299-22314.

Poli, S., Schmidt, M.W., 1997. The high-pressure stability of hydrous phases in orogenic belts: an experimental approach on eclogite-forming processes. Tectonophysics 273, 169-184.

Poli, S., Schmidt, M.W., 2002. Petrology of subducted slabs. Annual Review Of Earth And Planetary Sciences 30, 207-235.

Python, M., Ceuleneer, G., 2003. Nature and distribution of dykes and related melt migration structures in the mantle section of the Oman ophiolite. Geochem. Geophys. Geosyst. 4, 8612.

Raczek, I., Jochum, K.P., Hofmann, A.W., 2003. Neodymium and Strontium Isotope Data for USGS Reference Materials BCR-1, BCR-2, BHVO-1, BHVO-2, AGV-1, AGV-2, GSP-1, GSP-2 and Eight MPI-DING Reference Glasses. Geostandards Newsletter 27, 173.

Ratschbacher, L., Franz, L., Enkelmann, E., Jonckheere, R., Pörschke, A., Hacker, B.R., Dong, S., Zhang, Y., 2006. The Sino-Korean–Yangtze suture, the Huwan detachment, and the Paleozoic–Tertiary exhumation of (ultra)high-pressure rocks along the Tongbai-Xinxian-Dabie Mountains. Geological Society of America Special Papers 403, 45-75.

Ratschbacher, L., Hacker, B.R., Calvert, A., Webb, L.E., Grimmer, J.C., McWilliams, M.O., Ireland, T., Dong, S.W., Hu, J.M., 2003. Tectonics of the Qinling (Central China): tectonostratigraphy, geochronology, and deformation history. Tectonophysics 366, 1-53.

Reddy, S.M., Timms, N.E., Hamilton, P.J., Smyth, H.R., 2009. Deformation-related microstructures in magmatic zircon and implications for diffusion. Contributions To Mineralogy And Petrology 157, 231-244.

Reddy, S.M., Timms, N.E., Trimby, P., Kinny, P.D., Buchan, C., Blake, K., 2006. Crystal-plastic deformation of zircon: A defect in the assumption of chemical robustness. Geology 34, 257-260.

Rubatto, D., 2002. Zircon trace element geochemistry: partitioning with garnet and the link between U-Pb ages and metamorphism. Chemical Geology 184, 123-138.

Rubatto, D., Gebauer, D., Compagnoni, R., 1999. Dating of eclogite-facies zircons: the age of Alpine metamorphism in the Sesia-Lanzo Zone (Western Alps). Earth And Planetary Science Letters 167, 141-158.

Rubatto, D., Hermann, J., 2003. Zircon formation during fluid circulation in eclogites (Monviso, Western Alps): Implications for Zr and Hf budget in subduction zones. Geochimica et Cosmochimica Acta 67, 2173-2187.

Rubatto, D., Hermann, J., 2007. Experimental zircon/melt and zircon/garnet trace element partitioning and implications for the geochronology of crustal rocks. Chemical Geology 241, 38-61.

Rubatto, D., Hermann, J., 2007. Zircon behaviour in deeply subducted rocks. Elements 3, 31-35.

Rubatto, D., Muntener, O., Barnhoorn, A., Gregory, C., 2008. Dissolution-reprecipitation of zircon at low-temperature, high-pressure conditions (Lanzo Massif, Italy). American Mineralogist 93, 1519-1529.

Rudnick, R.L., Gao, S., Heinrich, D.H., Karl, K.T., 2003. Composition of the Continental Crust, Treatise on Geochemistry. Pergamon, Oxford, p. 1.

Schmidt, M.W., Poli, S., 1998. Experimentally based water budgets for dehydrating slabs and consequences for arc magma generation. Earth And Planetary Science Letters 163, 361-379.

Selverstone, J., Franz, G., Thomas, S., Getty, S., 1992. Fluid Variability In 2-Gpa Eclogites As An Indicator Of Fluid Behavior During Subduction. Contributions To Mineralogy And Petrology 112, 341-357.

Shellnutt, J.G., Zhou, M.-F., Zellmer, G.F., 2009. The role of Fe-Ti oxide crystallization in the formation of A-type granitoids with implications for the Daly gap: An example from the Permian Baima igneous complex, SW China. Chemical Geology 259, 204.

Shervais, J.W., 1982. Ti-V plots and the petrogenesis of modern and ophiolitic lavas. Earth And Planetary Science Letters 59, 101-118.

Sláma, J., Košler, J., Pedersen, R., 2007. Behaviour of zircon in high-grade metamorphic rocks: evidence from Hf isotopes, trace elements and textural studies. Contributions to Mineralogy and Petrology 154, 335.

Soderlund, U., Patchett, P.J., Vervoort, J.D., Isachsen, C.E., 2004. The 176Lu decay constant determined by Lu-Hf and U-Pb isotope systematics of Precambrian mafic intrusions. Earth and Planetary Science Letters 219, 311.

Spandler, C., Hermann, J., 2006. High-pressure veins in eclogite from New Caledonia and their significance for fluid migration in subduction zones. Lithos 89, 135-153.

Spandler, C., Hermann, J., Arculus, R., Mavrogenes, J., 2003. Redistribution of trace elements during prograde metamorphism from lawsonite blueschist to eclogite facies; implications for deep subduction-zone processes. Contributions To Mineralogy And Petrology 146, 205-222.

Spinelli, G.A., Wang, K., 2009. Links between fluid circulation, temperature, and metamorphism in subducting slabs. Geophys. Res. Lett. 36, L13302.

Sun, S.S., McDonough, W.F., 1989. Chemical and isotopic systematics of oceanic basalts: implications for mantle composition and processes. In: Saunders, A.D., Norry, M.J. (Eds.), Magmatism in the ocean basins. : Special Publications. Geological Society, London, pp. 313–345.

Sun, W., Williams, I.S., Li, S., 2002. Carboniferous and Triassic eclogites in the western Dabie Mountains, east-central China: evidence for protracted convergence of the North and South China Blocks. Journal of Metamorphic Geology 20, 873.

Tang, H.-F., Liu, C.-Q., Nakai, S.i., Orihashi, Y., 2007. Geochemistry of eclogites from the Dabie-Sulu terrane, eastern China: New insights into protoliths and trace element behaviour during UHP metamorphism. Lithos 95, 441.

Timms, N.E., Kinny, P.D., Reddy, S.M., 2006. Enhanced diffusion of Uranium and Thorium linked to crystal plasticity in zircon. Geochemical Transactions 7.

Tomaschek, F., Kennedy, A.K., Villa, I.M., Lagos, M., Ballhaus, C., 2003. Zircons from Syros, Cyclades, Greece - Recrystallization and mobilization of zircon during high-pressure metamorphism. Journal Of Petrology 44, 1977-2002.

van der Laan, S. R., R. J. Arculus, J. A. Pearce, and B. J. Murton (1992)), Petrography, mineral chemistry, and phase relations of the basement boninite series of Site 786, Izu-Bonin forearc. In Proc. ODP, Sci. Results, vol. 125 eddited by P. Fryer, et al., pp. 171-201, College Station, TX (Ocean Drilling Program))

Vervoort, J.D., Blichert-Toft, J., 1999. Evolution of the depleted mantle: Hf isotope evidence from juvenile rocks through time. Geochimica et Cosmochimica Acta 63, 533.

Vonlanthen, P., Fitz Gerald, J.D., Rubatto, D., Hermann, J., 2012. Recrystallization rims in zircon (Valle d'Arbedo, Switzerland): An integrated cathodoluminescence, LA-ICP-MS, SHRIMP, and TEM study. American Mineralogist 97, 369-377.

Wan, Y., Li, R., Wilde, S.A., Liu, D., Chen, Z., Yan, L., Song, T., Yin, X., 2005. UHP metamorphism and exhumation of the Dabie Orogen, China: Evidence from SHRIMP dating of zircon and monazite from a UHP granitic gneiss cobble from the Hefei Basin. Geochimica et Cosmochimica Acta 69, 4333.

Wang, F., Chen, F., Siebel, W., Li, S.-Q., Peng, P., Zhai, M.-G., 2011a. Zircon U-Pb geochronology and Hf isotopic composition of the Hongqiyingzi Complex, northern Hebei Province: New evidence for Paleoproterozoic and late Paleozoic evolution of the northern margin of the North China Craton. Gondwana Research 20, 122.

Wang, X.L., Jiang, S.Y., Dai, B.Z., Griffin, W.L., Dai, M.N., Yang, Y.H., 2011b. Age, geochemistry and tectonic setting of the Neoproterozoic (ca 830 Ma) gabbros on the southern margin of the North China Craton. Precambrian Research 190, 35-47.

Wang, Q., Wyman, D.A., Li, Z.-X., Bao, Z.-W., Zhao, Z.-H., Wang, Y.-X., Jian, P., Yang, Y.-H., Chen, L.-L., 2010. Petrology, geochronology and geochemistry of ca. 780 Ma A-type granites in South China: Petrogenesis and implications for crustal growth during the breakup of the supercontinent Rodinia. Precambrian Research 178, 185.

Wang, X.M., Liou, J.G., Maruyama, S., 1992. Coesite-Bearing Eclogites From The Dabie Mountains, Central China - Petrogenesis, P-T Paths, And Implications For Regional Tectonics. Journal Of Geology 100, 231-251.

Wasserburg, G.J., Jacousen, S.B., DePaolo, D.J., McCulloch, M.T., Wen, T., 1981. Precise determination of Sm/Nd ratios, Sm and Nd isotopic abundances in standard solutions. Geochimica Et Cosmochimica Acta 45, 2311-2323.

Watson, E.B., Lupulescu, A., 1993. Aqueous Fluid Connectivity And Chemical-Transport In Clinopyroxene-Rich Rocks. Earth And Planetary Science Letters 117, 279-294.

Watson, E.B., Cherniak, D.J., Hanchar, J.M., Harrison, T.M., Wark, D.A., 1997. The incorporation of Pb into zircon. Chemical Geology 141, 19-31.

Webb, L.E., Hacker, B.R., Ratschbacher, L., McWilliams, M.O., Dong, S., 1999. Thermochronologic constraints on deformation and cooling history of high- and ultrahigh-pressure rocks in the Qinling-Dabie orogen, eastern China. Tectonics 18, 621.

Wiedenbeck, M., AllÉ, P., Corfu, F., Griffin, W.L., Meier, M., Oberli, F., Quadt, A.V., Roddick, J.C., Spiegel, W., 1995. Three natural zircon standards for U-Th-Pb, Lu-Hf, trace element and REE analyses. Geostandards Newsletter 19, 1.

Williams, I.S., Buick, I.S., Cartwright, I., 1996. An extended episode of early Mesoproterozoic metamorphic fluid flow in the Reynolds Range, central Australia*. Journal of Metamorphic Geology 14, 29.

Woodhead, J., Hergt, J., Shelley, M., Eggins, S., Kemp, R., 2004. Zircon Hf-isotope analysis with an excimer laser, depth profiling, ablation of complex geometries, and concomitant age estimation. Chemical Geology 209, 121.

Wu, Y.B., Gao, S., Gong, H.J., Xiang, H., Jiao, W.F., Yang, S.H., Liu, Y.S., Yuan, H.L., 2009. Zircon U-Pb age, trace element and Hf isotope composition of Kongling terrane in the Yangtze Craton: refining the timing of Palaeoproterozoic high-grade metamorphism. Journal Of Metamorphic Geology 27, 461-477.

Wu, Y.-B., Hanchar, J.M., Gao, S., Sylvester, P.J., Tubrett, M., Qiu, H.-N., Wijbrans, J.R., Brouwer, F.M., Yang, S.-H., Yang, Q.-J., Liu, Y.-S., Yuan, H.-l., 2009. Age and nature of eclogites in the Huwan shear zone, and the multi-stage evolution of the Qinling-Dabie-Sulu orogen, central China. Earth and Planetary Science Letters 277, 345.

Wu, Y.-B., Zheng, Y.-F., Zhao, Z.-F., Gong, B., Liu, X., Wu, F.-Y., 2006. U-Pb, Hf and O isotope evidence for two episodes of fluid-assisted zircon growth in marble-hosted eclogites from the Dabie orogen. Geochimica et Cosmochimica Acta 70, 3743.

Xia, Q.X., Zheng, Y.F., Hu, Z.C., 2010. Trace elements in zircon and coexisting minerals from low-T/UHP metagranite in the Dabie orogen: Implications for action of supercritical fluid during continental subduction-zone metamorphism. Lithos 114, 385-412.

Xu, B., Grove, M., Wang, C., Zhang, L., Liu, S., 2000. 40Ar/39Ar thermochronology from the northwestern Dabie Shan: constraints on the evolution of Qinling-Dabie orogenic belt, east-central China. Tectonophysics 322, 279.

Xu, S.T., Okay, A.I., Ji, S.Y., Sengor, A.M.C., Wen, S., Liu, Y.C., Jiang, L.L., 1992. Diamond From The Dabie-Shan Metamorphic Rocks And Its Implication For Tectonic Setting. Science 256, 80-82.

Ye, B.D., Jiang, P., Xu, J., Cui, F., Li, Z., and Zhang, Z., 1993, The Sujiahe terrane collage belt and its constitution and evolution along the northern hillslope of the Tongbai–Dabie orogenic belt: Press of China University of Geoscience, Wuhan, p. 66-67.

Yuan, H., Gao, S., Liu, X., Li, H., Günther, D., Wu, F., 2004. Accurate U-Pb Age and Trace Element Determinations of Zircon by Laser Ablation-Inductively Coupled Plasma-Mass Spectrometry. Geostandards and Geoanalytical Research 28, 353.

Yuan, H.-L., Gao, S., Dai, M.-N., Zong, C.-L., Günther, D., Fontaine, G.H., Liu, X.-M., Diwu, C., 2008. Simultaneous determinations of U-Pb age, Hf isotopes and trace element compositions of zircon by excimer laser-ablation quadrupole and multiple-collector ICP-MS. Chemical Geology 247, 100.

Zeh, A., Gerdes, A., Will, T.M., Frimmel, H.E., 2010. Hafnium isotope homogenization during metamorphic zircon growth in amphibolite-facies rocks: Examples from the Shackleton Range (Antarctica). Geochimica et Cosmochimica Acta 74, 4740.

Zhang, R.Y., Liou, J.G., Ernst, W.G., 2009. The Dabie-Sulu continental collision zone: A comprehensive review. Gondwana Research 16, 1-26.

Zhang, Z.M., Liou, J.G., Zhao, X.D., Shi, C., 2006. Petrogenesis of Maobei rutile eclogites from the southern Sulu ultrahigh-pressure metamorphic belt, eastern China. Journal of Metamorphic Geology 24, 727.

Zhao, Z.-F., Zheng, Y.-F., Wei, C.-S., Chen, F.-K., Liu, X., Wu, F.-Y., 2008. Zircon U-Pb ages, Hf and O isotopes constrain the crustal architecture of the ultrahigh-pressure Dabie orogen in China. Chemical Geology 253, 222.

Zhao, Z.F., Zheng, Y.F., Chen, R.X., Xia, Q.X., Wu, Y.B., 2007. Element mobility in mafic and felsic ultrahigh-pressure metamorphic rocks during continental collision. Geochimica Et Cosmochimica Acta 71, 5244-5266.

Zheng, Y.F., Wu, Y.B., Zhao, Z.F., Zhang, S.B., Xu, P., Wu, F.Y., 2005. Metamorphic effect on zircon Lu-Hf and U-Pb isotope systems in ultrahigh-pressure eclogite-facies metagranite and metabasite. Earth and Planetary Science Letters 240, 378-400.

Zheng, Y.-F., Zhao, Z.-F., Wu, Y.-B., Zhang, S.-B., Liu, X., Wu, F.-Y., 2006. Zircon U-Pb age, Hf and O isotope constraints on protolith origin of ultrahigh-pressure eclogite and gneiss in the Dable orogen. Chemical Geology 231, 135-158.

Zhu, X.-Y., Chen, F., Li, S.-Q., Yang, Y.-Z., Nie, H., Siebel, W., Zhai, M.-G., 2011. Crustal evolution of the North Qinling terrain of the Qinling Orogen, China: Evidence from detrital zircon U-Pb ages and Hf isotopic composition. Gondwana Research 20, 194.

CHAPTER III

ZIRCON U-Pb AND Lu-Hf ISOTOPIC CONSTRAINTS ON FLUID ACTIVITY IN THE CRUST DURING CONTINENTAL SUBDUCTION PROVIDED BY A TONALITE GNEISS FROM THE LUOTIAN DOME, CENTRAL CHINA.

1. Abstract

To help understand the behavior of zircon and the evolution of the Northern Dabie Complex (NDC) during continental subduction, we present whole-rock geochemical and Sr-Nd isotopic data with in-situ zircon U-Pb and Lu-Hf isotopic and trace-element analyses for an amphibole-bearing tonalite gneiss from the Luotian Dome in the NDC. A whole-rock rare earth-element profile is similar to that of upper continental crust and major-element composition is consistent with a tonalite protolith. Elevated whole-rock trace-element concentrations indicate the addition of Nb, Ta, Th, and U to the igneous source or metamorphic protolith. A Palaeoproterozoic whole-rock Nd-isotope depleted-mantle melting model age of 2.1 Ga is consistent with reported values for the NDC.

Zircon Hf-isotope depleted-mantle model ages (T[Hf]DM) range from 1.85 - 1.2 Ga. Variable $^{176}Hf/^{177}Hf$ are interpreted to result from internal recycling of Hf from phases such as garnet (i.e. high Lu/Hf ratio) and incorporation during metamorphic zircon growth. Despite having Proterozoic Hf isotope signatures, zircon grains display no U-Pb dates greater than 309 Ma or Pb-Pb dates that exceed 420 Ma, suggesting either zircon grains were not present until the Phanerozoic, or secondary processes significantly impacted their original Proterozoic composition. Melting and protolith formation likely occurred during a Meso- to

Palaeoproterozoic stage of extension and crustal melting, which is characteristic of the Yangtze continent.

While previously published NDC zircon ages are predominantly Cretaceous, zircon grains in our sample record Triassic continental subduction of the NDC with a primary U-Pb age peak at 210 Ma. Zircon domains with older U-Pb ages (i.e. 234-280 Ma) display a number of flat to concave upwards M-HREE profiles and LREE contents up to 30 times chondrite. For the remaining zircon population, U-Pb dates, Lu-Hf isotopes and REE profiles record metamorphic in-situ recrystallization catalyzed by internally derived fluids with expulsion of incompatible elements (i.e. Pb and LREE) and retention of compatible elements (i.e. Hf).

We favor the interpretation that the NDC experienced only high-pressure (<2.5 GPa) conditions during peak metamorphism, followed by extensive retrograde amphibolite facies metamorphism during exhumation. The spread in zircon T[Hf]DM ages observed across the Dabie orogen has been used to support models of continental subduction for the Dabie Orogen. However, without a detailed understanding of the pre-subduction crustal structure and origin of zircon within separate lithologies, the distribution of zircon T[Hf]DM ages reported for analyzed samples is unlikely to provide constraints upon the nature of processes operating during continental subduction.

2. Introduction

Zircon is a ubiquitous and refractory accessory mineral observed in a wide variety of crustal rocks and one of the most important tools for exploring the evolving chemical and physical nature of the earth's crust (e.g. Watson and Harrison 2005; Valley et al., 2005; Condie et al., 2009, 2011; Liu and Liou 2011). The ability of zircon to concentrate U^{+4} and Th^{+4} during

growth whilst rejecting Pb^{+2} makes the mineral a highly precise geochronometer for dating activation and evolution of ancient geochemical systems (Cherniak et al., 1997; Watson et al., 1997; Cherniak and Watson 2001; Davis et al., 2003; Hanchar and Watson 2003). Further, experimental investigations have shown crystalline zircon to display low aqueous solubility (e.g. Ayers and Watson 1991) and negligible volume diffusional loss of constituents, particularly those used for geochronology, over a wide range of crustal metamorphic P-T conditions (e.g. Cherniak and Watson 2003; Cherniak 2010).

Zircon grains extracted from high and ultra-high pressure metamorphic (HPM/UHPM) lithologies associated with the uplifted and exposed roots of orogenic mountain belts have been shown to contain evidence for growth during deep tectonic processes, including inclusions of the ultra-high pressure index minerals coesite and diamond (e.g. Tabata et al., 1998; Ye et al., 2000; Liu et al., 2001, 2002; Song et al., 2005; Zhang et al., 2006a), and flat heavy rare earth element (HREE) chondrite-normalized profiles characteristic of growth in equilibrium with garnet in the eclogite facies (Rubatto 2002; Herman and Rubatto 2003; Rubatto and Herman 2007ab). Using zircon grains to constrain the dates and rates of these events, however, remains largely dependent upon accurate characterization of the geochemical environment of zircon growth or modification.

Growing evidence suggests metamorphic fluids can profoundly affect zircon's geochronological system during high-grade metamorphism (e.g. Williams et al., 1996; Rubatto and Hermann 2003; Wu et al., 2006, 2009; Zhao et al., 2006; Geisler et al., 2007; Zheng et al., 2007). Understanding the link between zircon dates and high-pressure fluid-rock interactions, however, has proved a challenging endeavor. Numerous studies report a high degree of textural, geochemical and isotopic complexity associated with the development of secondary overprint or growth domains in zircon grains (e.g. Carson et al., 2002; Breeding et al., 2004;

Bomparola et al,. 2007; Martin et al., 2008; Chen et al., 2010; Sheng et al., 2011). Despite progress, important questions persist concerning the nature of fluids produced during metamorphism and our ability to date these events using the complex textural and geochemical trends observed in zircon.

In this paper, we combine bulk-rock geochemical and Sr-Nd isotopic data with in-situ zircon trace-element and U-Pb-Lu-Hf isotopic data for an amphibole-bearing tonalite gneiss collected within the Northern Dabie Complex to better understand the origin and evolving behavior of zircon during fluid-rock interaction associated with deep continental subduction and exhumation.

3. Geological setting and Geochronological issues:

The Dabie Mountains, situated in central-east China (Fig. 1), represent a portion of the exhumed and exposed roots of a Mesozoic East-West trending orogenic belt that formed during a protracted sequence of events involving the subduction of Yangtze continental crust to mantle depths (~125 km: Xu et al., 1992) beneath the North China, or Sino-Korean, craton (e.g. Zhang et al., 2009; Liou et al., 2009). Four distinct fault-bounded metamorphic terrains have been identified within the region, which, from north to south, include (1) the North Huaiyang zone, (2) the Northern Dabie Complex (NDC), (3) the Central Dabie zone (CDZ), and (4) the Southern Dabie low-temperature zone (SDZ) (e.g. Bryant et al., 2004; Liu et al 2011ab).

UHPM was initially discovered in the CDZ owing to the occurrence of in-situ diamond and coesite (Okay et al., 1989; Xu et al., 1992), and indicated continental subduction had reached peak conditions of >2.8 GPa and 700-850°C during the Triassic (e.g. Ames et al., 1996; Rowley et al., 1997; Hacker et al., 1998; Zheng et al., 2004, 2006; Tang et al., 2008). In the past

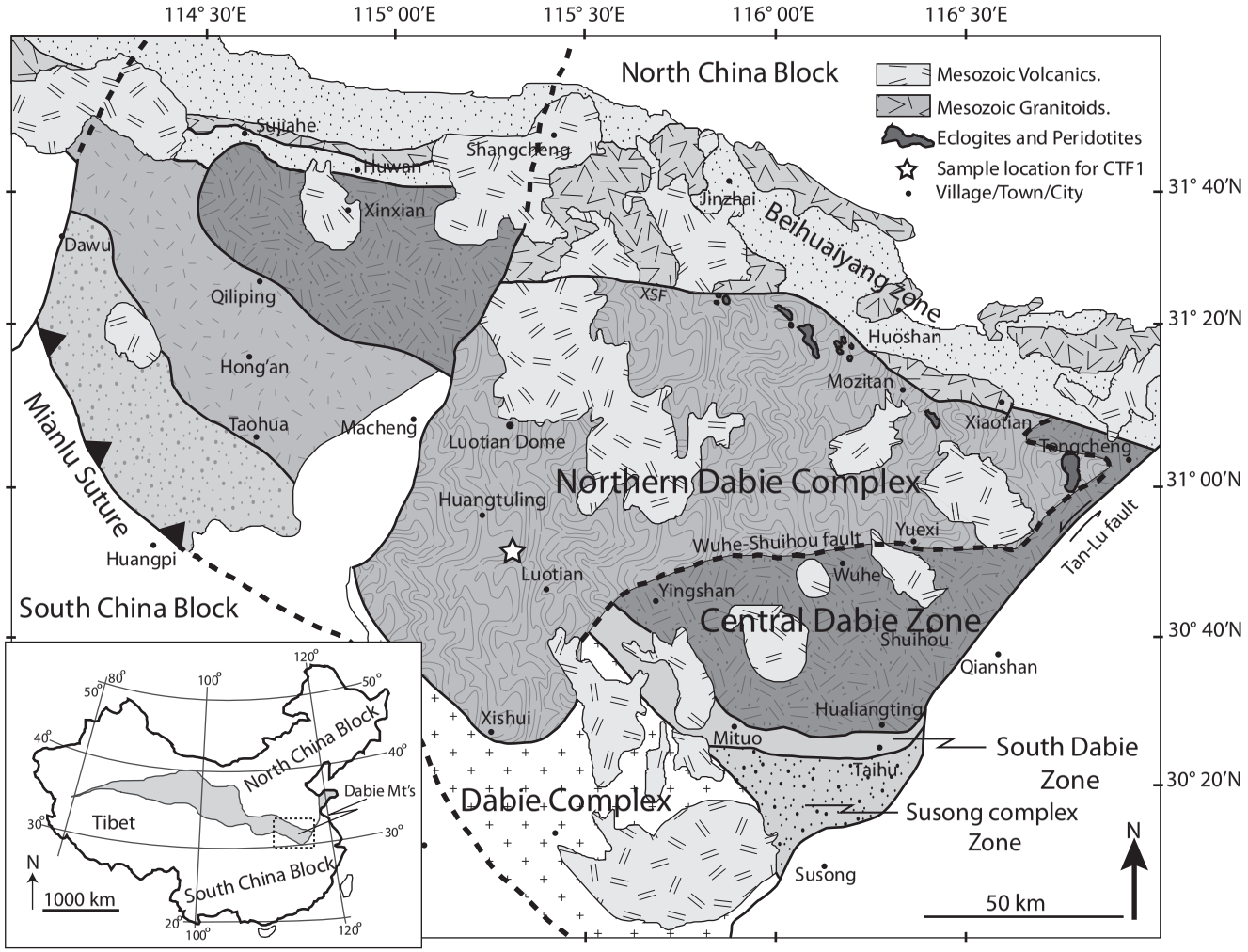

Figure. 1: Schematic tectonic map of the Dabie orogen, with inset showing the location of this area within China. For the insert map of China, the grey shaded region represents the extensive Paleozoic-Mesozoic central China orogenic belt, which includes, from west to east, the Qaidam, Qilian, Wudang, Qinling, Tongbai, Hong'an, Dabie and Su-Lu orogenic blocks. Compiled after Bryant et al (2004), Zhao et al., (2008) and Liu et al., (2011a).

few years detailed textural, geochemical, and mineral-inclusion analyses have been used to identify possible evidence of Triassic UHPM in the adjacent high-temperature NDC (Xu et al., 2003, 2005; Liu et al., 2007ab; 2011ab; Tong et al., 2011). Some studies propose that UHPM conditions were in fact attained in the NDC, but evidence is scarce because of extensive thermal overprinting and the rarity of mafic-ultramafic lithologies that preserve UHP phases better than felsic lithologies during retrograde metamorphism (e.g. Koons and Thompson 1985).

Studies published two decades ago first speculated the NDC may have experienced UHPM (e.g. Wang and Liou 1991; Li et al. 1993; see review in Tsai and Liou 2000). However, without conclusive evidence of UHPM, subsequent models proposed the NDC to represent a High Temperature (HT) post-collisional extensional magmatic terrain produced during the early Cretaceous (Hacker et al 1998), or a Triassic HP core of an anticlinal dome structure that extends beneath the UHP CDZ within the South China block (Bryant et al., 2004). The recent claim of UHPM conditions in the NDC (Xu et al., 2003, 2005; Liu et al., 2007ab; 2011ab) has led to reevaluation of the Dabie orogen crustal architecture and the nature of continental subduction-exhumation processes recorded in the CDZ and NDC (e.g. Zhao et al 2008; Liu et al., 2007, 2011ab).

The NDC is characterized by an abundance of felsic orthogneiss bodies that are intruded by voluminous post-collisional Cretaceous granitic bodies (e.g. Ma et al., 2000; Bryant et al., 2004; Zhao et al., 2008). Rare mafic and ultra-mafic lenses of amphibolite, granulite, meta-peridotite, and retrograded eclogite are interspersed with orthogneiss and banded tonalites located along the northern and southern boundaries, (Bryant et al 2004; Liu et. al, 2007, 2011ab, and references there in).

Our attention is focused upon a retrograded gneiss outcrop of the ChetangFan formation (N30°51.055', E115°19.181'), located within the Luotian dome (Fig. 1), a deeply

eroded structure located within the southern portion of the NDC near its border with the CDZ. Our sample is a fine- to medium-grained amphibole-bearing gneiss with no conclusive evidence for the occurrence or preservation of garnet or omphacite. Petrographic observations showed abundant green hornblende, augite, and strained interstitial quartz containing linear trails of small fluid inclusions, coarse-grained and zoned plagioclase grains and accessory titanite, zircon, apatite and Fe-Mg oxides with patches of fine grained matrix material.

4. Analytical Methods:

4.1. Whole-rock Major and Trace-Element analysis:

Whole-rock major and trace element concentrations were measured at the State Key Laboratory of Continental Dynamics, Northwest University, Xi'an, China. Major element oxide concentrations were measured by XRF using fused glass disks and a Rigaku RIX 2100 spectrometer. Trace element concentrations were determined using an Agilent 7500a ICP-MS after acid digestion of samples in a Teflon bomb. Analyses of USGS rock standards (BCR-2, BHVO-1 and AGV-1) indicate a precision and accuracy of better than 5% for major elements and 10% for trace elements and REE. Results are reported in Table. 1.

4.2. Sr and Nd isotopic analysis

Whole-rock Nd–Sr isotopic compositions were measured at the State Key Laboratory of Continental Dynamics, Northwest University, Xi'an, China, using a multi-collector ICP-MS (Nu Plasma). Analytical precisions of isotope ratio measurements are given as ± 2σ errors. Separation of Rb, Sr, Sm and Nd was completed using a routine two-column ion-exchange technique. Analytical precisions of isotope ratio measurements are given as ± 2σ. Sr isotopic

Table. 1. Major, trace element, and Sr-Nd isotopic composition of eclogite samples. Major elements are reported as wt.% oxides and trace elements as ppm.

Oxide	CTF1	CTF1R
SiO_2	63.3	63.2
TiO_2	0.71	0.71
Al_2O_3	13.6	13.6
TFe_2O_3	4.45	4.45
MnO	0.15	0.15
MgO	2.05	2.03
CaO	9.8	9.8
Na_2O	3.44	3.43
K_2O	0.87	0.86
P_2O_5	0.22	0.21
LOI	1.05	1.06
Total	99.8	99.6
Trace elements		
Li	8.1	7.6
Be	6.3	6.3
Sc	11	11
V	74	75
Cr	24	26
Co	110	109
Ni	21	22
Cu	4.1	4.7
Zn	102	101
Ga	17	17
Ge	1.63	1.68
Rb	32	32
Sr	391	393
Y	32	33
Zr	57	51
Nb	60	61
Cs	1.06	1.05
Ba	151	156
La	29	31
Ce	53	55
Pr	6.1	6.3
Nd	23	24
Sm	4.7	4.9
Eu	1.06	1.08
Gd	4.6	4.6
Tb	0.75	0.77
Dy	4.6	4.6
Ho	1	1.01

Table. 1. Continued.

Er	2.9	3
Tm	0.49	0.5
Yb	3.29	3.36
Yb	3.29	3.36
Lu	0.50	0.51
Hf	2.26	2.12
Ta	12.5	12.8
Pb	14.7	14.5
Th	51.3	50.8
U	9.0	8.9
Nb/Ta	4.8	4.8
Zr/Hf	25.5	24.2
Nb/Zr	1.05	1.20
$^{87}Rb/^{86}Sr$	0.29684	0.29735
$^{87}Sr/^{86}Sr$	0.713358	0.713321
2s	25	10
$^{147}Sm/^{144}Nd$	0.11882	0.12058
$^{143}Nd/^{44}Nd$	0.511839	0.511850
2s	10	8
$Nd_{(DM)}$ Ma	2097	2120

ratios were corrected for mass fractionation relative to $^{86}Sr/^{88}Sr$ = 0.1194. BCR-2 standard yielded an $^{87}Sr/^{86}Sr$ of 0.704959 ± 36 and $^{143}Nd/^{144}Nd$ of 0.512613 ± 9, compared with its reported $^{87}Sr/^{86}Sr$ of 0.704958 and $^{143}Nd/^{144}Nd$ of 0.512633 (Raczek et al., 2003). Measured $^{143}Nd/^{144}Nd$ were normalized against $^{146}Nd/^{144}Nd$ = 0.7219. For calculation of Depleted-mantle model ages ($Nd_{(DM)}$), we used a ^{147}Sm decay constant of 6.54 × 10-12 $year^{-1}$ (Lugmair and Marti, 1978), and depleted-mantle values $^{147}Sm/^{144}Nd$ = 0.2137 and $^{143}Nd/^{144}Nd$ = 0.51315 from Chen and Jahn (1998). The results are reported in Table. 1.

4.3. Zircon extraction and imaging:

The CTF1 sample was crushed and zircon grains extracted using conventional magnetic and heavy-liquid techniques, then hand-picked using binocular microscopes. Individual grains were mounted in epoxy-resin and inner-domains exposed by polishing. CL imaging was

performed at the State Key Laboratory of Continental Dynamics, Northwest University, using a Quanta 400 FEG high resolution field emission environmental scanning electron microscope connected to a Gatan Mono CL3+ system. Back scattered electron images were collected at Vanderbilt University using a Tescan Vega 3LM scanning electron microscope connected to an Oxford X-Max 50mm Silicon Drift Detector for collection of Energy-dispersive X-rays (EDS).

4.4. Zircon Trace-Element and U-Th-Pb isotope analysis:

In-situ zircon analyses were performed using a GeoLas 2005 laser-ablation system equipped with a 193 nm ArF-excimer laser at Northwest University, Xi'an, China. The energy density was 15–20 J/cm^2, repetition rate 10 Hz, and laser power 100 mJ/pulse. Data were collected during 80 seconds of ablation, following approximately 30 seconds of background counting.

Trace-element and U-Th-Pb isotope analyses were performed using an ELAN6100 DRC (Dynamic Reaction Cell) ICP-MS, following the procedures described by Yuan et al. [2004]. The spot diameter for each analysis was 30 μm. Helium was used as the carrier gas to enhance the transport efficiency of ablated material, and was mixed with argon before entering the ICP to maintain stable and optimum excitation conditions. Zircon 91500 was used as the reference standard, which has a recommended $^{206}Pb/^{238}U$ age of 1065.4 ± 0.6 Ma [Wiedenbeck et al., 1995]. Common Pb was corrected for using the EXCEL program ComPbCorr#3_151 for analyses with common ^{206}Pb > 1% of total ^{206}Pb (Andersen, 2002). U–Pb dates were calculated using the ISOPLOT program [Ludwig, 2003]. U-Th-Pb isotopic and age data is reported in Table. 2a. Trace element concentrations are reported in Table. 2b, and 1σ error values for zircon trace element analyses are reported in Appendix. C.

Table. 2a. Zircon U-Pb isotopic ratios and ages. U and Th contents are ppm.

Analysis	Location	Th (ppm)	U (ppm)	Th/U	$^{238}U/^{206}Pb$	1σ	$^{207}Pb/^{206}Pb$	1σ	$^{207}Pb/^{235}U$	1σ	$^{206}Pb/^{238}U$	1σ	$^{207}Pb/^{206}Pb$	1σ	$^{207}Pb/^{235}U$	1σ	$^{206}Pb/^{238}U$	1σ
CTF1-01.1	core	18.3	435.6	0.042	29.8	0.61	0.050	0.0012	0.229	0.0057	0.034	0.00069	175	57	210	5	213	4
CTF1-01.2	rim	1.9	246.4	0.008	35.8	0.75	0.050	0.0015	0.193	0.0057	0.028	0.00058	208	68	180	5	177	4
CTF1-02.1	core	8.5	286.2	0.030	29.3	0.60	0.050	0.0013	0.238	0.0060	0.034	0.0007	217	58	217	5	217	4
CTF1-03.1	mantle	12.2	233.8	0.052	27.4	0.57	0.070	0.0018	0.352	0.0092	0.037	0.00076	289	101	232	8	226	5
CTF1-03.2	core	96.8	615.4	0.157	24.9	0.51	0.055	0.0013	0.306	0.0071	0.040	0.00082	419	51	271	6	254	5
CTF1-04.1	Dark core	257.6	2067	0.125	22.7	0.46	0.050	0.0011	0.303	0.0067	0.044	0.0009	187	51	269	5	278	6
CTF1-05.1	core	28.6	512.7	0.056	20.4	0.42	0.051	0.0012	0.345	0.0080	0.049	0.00101	237	53	301	6	309	6
CTF1-06.1	mantle	11.4	330.5	0.035	30.2	0.62	0.051	0.0013	0.235	0.0061	0.033	0.00068	258	58	214	5	210	4
CTF1-06.2	mantle	14.1	299.6	0.047	30.1	0.63	0.051	0.0013	0.235	0.0061	0.033	0.00069	256	58	214	5	211	4
CTF1-07.1	core	317.9	651.6	0.488	24.7	0.51	0.055	0.0013	0.306	0.0071	0.040	0.00083	408	50	271	6	255	5
CTF1-07.2	rim	859.8	1621	0.530	27.0	0.55	0.052	0.0012	0.266	0.0061	0.037	0.00076	289	51	240	5	235	5
CTF1-08.1	Core	54.0	479.7	0.113	31.9	0.66	0.050	0.0013	0.217	0.0056	0.031	0.00065	205	59	199	5	199	4
CTF1-09.1	mantle	7.3	134.1	0.054	30.9	0.66	0.057	0.0019	0.256	0.0085	0.032	0.00069	248	102	207	7	204	4
CTF1-10.1	Dark core	59.0	1136	0.052	22.7	0.47	0.051	0.0012	0.308	0.0072	0.044	0.00091	225	53	273	6	279	6
CTF1-11.1	Dark core	1215	6002	0.202	33.4	0.69	0.051	0.0012	0.210	0.0048	0.030	0.00062	236	51	194	4	190	4
CTF1-12.1	Dark core	561.3	4154	0.135	34.0	0.71	0.050	0.0012	0.203	0.0048	0.029	0.00061	197	53	187	4	187	4
CTF1-13.1	Dark core	635.9	2376	0.268	22.5	0.47	0.050	0.0012	0.305	0.0071	0.044	0.00092	186	53	270	6	280	6
CTF1-13.2	Mantle	1.6	223.0	0.007	35.5	0.74	0.051	0.0015	0.198	0.0059	0.028	0.00059	235	67	183	5	179	4
CTF1-14.2	Rim	10.8	240.2	0.045	32.4	0.68	0.052	0.0014	0.223	0.0061	0.031	0.00065	303	61	205	5	196	4
CTF1-15.1	core	11.4	133.2	0.086	33.4	0.72	0.058	0.0020	0.238	0.0083	0.030	0.00065	299	107	197	7	189	4
CTF1-15.2	rim	13.1	139.6	0.094	42.5	1.01	0.085	0.0041	0.276	0.0129	0.024	0.00056	167	193	145	11	143	3
CTF1-16.1	Core	39.4	359.9	0.110	32.4	0.68	0.049	0.0014	0.208	0.0060	0.031	0.00065	137	66	192	5	196	4
CTF1-16.2	Rim	28.6	440.0	0.065	37.0	0.78	0.045	0.0013	0.167	0.0050	0.027	0.00057			157	4	172	4
CTF1-17.1	Dark core	607.0	1689	0.359	22.8	0.48	0.051	0.0012	0.307	0.0076	0.044	0.00092	223	56	272	6	277	6
CTF1-17.2	Mantle	1.5	223.6	0.007	35.4	0.77	0.054	0.0017	0.211	0.0068	0.028	0.00061	382	70	195	6	180	4
CTF1-18.1	core	13.9	481.4	0.029	30.2	0.64	0.052	0.0014	0.239	0.0065	0.033	0.0007	294	60	217	5	210	4
CTF1-19.1	core	44.1	365.5	0.121	30.5	0.65	0.052	0.0015	0.234	0.0069	0.033	0.0007	276	66	214	6	208	4

Table. 2b. In-situ zircon Rare Earth Element concentrations in ppm.

Analysis	Location	La	Ce	Pr	Nd	Sm	Eu	Gd	Tb	Dy	Ho	Er	Tm	Yb	Lu
CTF1-01.1	core	0.01	26.10	0.02	0.43	0.78	0.45	3.12	0.81	7.09	2.22	8.29	1.59	15.42	3.33
CTF1-01.2	rim	0.02	0.51	0.01	0.05	0.12	0.06	0.50	0.14	1.37	0.42	1.60	0.31	2.83	0.60
CTF1-02.1	core	0.004	16.40	0.01	0.25	0.37	0.22	1.58	0.43	4.30	1.36	5.27	1.03	10.19	2.18
CTF1-03.1	mantle	b.d	13.81	0.04	0.93	1.43	0.79	5.11	1.38	12.82	4.12	15.90	3.17	29.99	6.27
CTF1-03.2	core	5.02	29.97	2.07	11.87	3.24	1.11	6.07	1.24	9.70	2.56	8.19	1.41	12.36	2.27
CTF1-04.1	Dark core	0.01	21.33	0.12	1.97	4.87	2.55	20.94	5.43	45.51	12.89	41.75	6.78	53.73	9.36
CTF1-05.1	core	0.004	36.14	0.07	1.12	1.61	0.96	5.70	1.43	12.48	3.83	14.50	2.75	26.02	5.64
CTF1-06.1	mantle	0.05	15.48	0.07	0.75	1.10	0.63	4.19	1.14	10.95	3.59	13.49	2.62	24.60	5.11
CTF1-06.2	mantle	0.07	14.70	0.09	1.21	1.59	0.89	5.91	1.62	15.04	4.85	19.13	3.72	34.33	6.95
CTF1-07.1	core	4.82	36.19	2.32	17.33	6.67	1.90	5.53	0.84	5.21	1.36	4.66	0.87	7.98	1.67
CTF1-07.2	rim	10.79	97.60	5.92	48.84	16.99	4.68	14.13	1.95	10.83	2.43	7.04	1.15	10.07	2.00
CTF1-08.1	Sector core	0.01	7.72	0.04	0.47	0.68	0.35	2.23	0.49	4.16	1.25	4.48	0.81	7.05	1.49
CTF1-09.1	mantle	0.01	8.49	0.01	0.14	0.29	0.17	1.16	0.36	3.29	1.11	4.62	0.90	8.73	1.82
CTF1-10.1	Dark core	0.12	8.14	0.10	1.06	1.55	0.97	8.47	2.46	21.68	6.33	21.46	3.49	28.69	5.16
CTF1-11.1	Dark core	0.35	29.95	0.35	4.53	5.99	2.87	24.60	7.11	71.03	24.97	107.59	24.87	274.20	65.10
CTF1-12.1	Dark core	1.43	14.12	0.27	1.59	0.96	0.59	4.01	1.33	14.16	5.48	24.80	5.53	58.78	13.02
CTF1-13.1	Dark core	0.56	120.81	2.16	27.49	24.91	10.61	48.94	8.42	52.12	11.15	31.17	4.94	41.17	8.01
CTF1-13.2	Mantle	b.d	0.44	0.002	0.03	0.10	0.07	0.58	0.14	1.36	0.42	1.58	0.31	2.69	0.57
CTF1-14.2	Rim	0.05	11.24	0.06	0.88	1.35	0.68	4.27	1.10	9.88	3.13	11.93	2.38	21.91	4.67
CTF1-15.1	core	0.01	2.23	0.01	0.04	0.09	0.04	0.38	0.10	0.91	0.30	1.22	0.26	2.44	0.58
CTF1-15.2	rim	0.71	2.60	0.07	0.36	0.15	0.11	0.51	0.12	1.40	0.42	1.78	0.36	3.34	0.70
CTF1-16.1	Core	0.003	6.04	0.02	0.49	0.72	0.32	1.83	0.40	3.67	1.02	3.51	0.64	5.82	1.19
CTF1-16.2	Rim	0.15	3.61	0.06	0.49	0.54	0.28	1.50	0.36	3.15	0.92	4.10	0.94	10.72	2.58
CTF1-17.1	Dark core	0.21	89.29	0.57	7.25	8.12	3.60	18.19	3.13	20.18	4.45	12.50	1.88	15.40	2.97
CTF1-17.2	Mantle	0.17	0.52	0.04	0.31	0.22	0.10	0.61	0.16	1.49	0.43	1.61	0.31	2.72	0.54
CTF1-18.1	core	0.002	24.22	0.01	0.30	0.49	0.29	1.74	0.49	4.59	1.43	5.27	1.04	9.87	2.10
CTF1-19.1	core	b.d	5.37	0.01	0.21	0.40	0.26	1.70	0.47	4.19	1.24	4.24	0.80	7.01	1.36

4.5. Zircon Lu–Hf isotope analysis:

Lu-Hf isotopic analyses were performed using a Nu plasma high-resolution (HR) Multi-Collector (MC)-ICPMS, following the procedures described by Yuan et al. (2008). The spot diameter for each analysis was 44 μm and Helium was used as carrier gas. Isobaric interference of ^{176}Lu on ^{176}Hf was corrected by measuring the intensity of the interference-free ^{175}Lu isotope and using a ^{176}Lu/^{175}Lu ratio of 0.02669 to calculate ^{176}Lu/^{177}Hf ratios. Correction for the isobaric interference of ^{176}Yb on ^{176}Hf involved measuring the interference-free ^{172}Yb and ^{173}Yb during the analysis and calculating a mean βYb value from ^{172}Yb and ^{173}Yb (Woodhead et al., 2004; Iizuka and Hirata, 2005) using the recommended ^{176}Yb/^{172}Yb ratio of 0.5886 [Chu et al., 2002]. Zircon 91500 was used as the reference standard, with a recommended ^{176}Hf/^{177}Hf ratio of 0.282306 ± 10 (Woodhead et al., 2004). ^{176}Lu/^{177}Hf ratios are very low, making the contribution from post-crystallization radiogenic ingrowth of ^{176}Hf negligible. For calculation of εHf values and mantle-melting model ages (here after referred to as T[Hf]DM ages), we use a ^{176}Lu decay constant of 1.867×10^{-11} year^{-1} (Soderlund et al., 2004), with initial chondritic reservoir (CHUR) ratios ^{176}Hf/^{177}Hf= 0.282785 and ^{176}Lu/^{177}Hf = 0.0336 from Bouvier et al. (2008), and depleted mantle (DM) ^{176}Hf/^{177}Hf = 0.28325 and ^{176}Lu/^{177}Hf = 0.0384, from Vervoort and Blichert-Toft (1999). To compare our data with similar reports from the Dabie Orogen we also calculate εHf(t=750 Ma) values assuming a 750 Ma timing for initial zircon growth (i.e. calculating both CHUR and our Lu-Hf analysis for t = 750 Ma: Zheng et al., 2006). ƐHf(t=750 Ma) values were proposed by Zheng et al. (2006) as a means to evaluate the role of magma mixing or crustal residence for generating zircon Hf-isotopic heterogeneity associated with crustal recycling and zircon growth c. 750 Ma. Errors in εHf and T[Hf]DM and values were calculated on the basis of analytical errors, but much larger and poorly constrained errors may be associated with the T[Hf]DM model ages due to errors with the reference model (Zheng et al., 2005). The results are reported in Table. 2c.

Table. 2c. Zircon Lu-Hf isotopic data.

Analysis	Location	$^{176}Hf/^{177}Hf$	2σ	$^{176}Yb/^{177}Hf$	2σ	$^{176}Lu/^{177}Hf$	2σ	ε(t=U-Pb)	$T_{(DM)}$ Ga	1σ
CTF1-01.1	core	0.282272	19	0.002754	20	0.000110	1	-15	1351	26
CTF1-01.2	rim	0.282144	21	0.000556	26	0.000022	1	-21	1521	28
CTF1-02.1	core	0.282280	25	0.001555	10	0.000065	1	-15	1338	34
CTF1-03.2	core	0.281903	24	0.001578	61	0.000061	3	-28	1850	33
CTF1-04.1	Dark core	0.282190	16	0.003414	66	0.000115	2	-17	1463	21
CTF1-05.1	core	0.282077	22	0.003672	51	0.000143	3	-20	1618	30
CTF1-06.1	mantle	0.281921	36	0.002643	77	0.000109	3	-28	1827	48
CTF1-06.2	mantle	0.282334	20	0.003009	50	0.000113	2	-13	1266	27
CTF1-07.1	core	0.282368	19	0.000784	15	0.000030	1	-11	1218	26
CTF1-08.1	Sector core	0.282359	15	0.000884	14	0.000035	1	-13	1230	20
CTF1-10.1	Dark core	0.282273	15	0.002889	12	0.000102	1	-14	1349	20
CTF1-11.1	Dark core	0.282218	15	0.019799	98	0.000886	5	-18	1454	20
CTF1-12.1	Dark core	0.281960	18	0.004948	93	0.000206	3	-27	1779	24
CTF1-13.1	Dark core	0.282288	15	0.001448	72	0.000057	3	-13	1327	21
CTF1-13.2	Mantle	0.282286	12	0.000225	4	0.000009	0	-16	1329	16
CTF1-14.2	Rim	0.281992	19	0.000479	17	0.000021	1	-26	1728	26
CTF1-16.1	Core	0.282378	13	0.000782	14	0.000032	1	-12	1204	18
CTF1-16.2	Rim	0.282345	12	0.001160	11	0.000049	1	-14	1250	16
CTF1-17.1	Dark core	0.282292	17	0.001988	11	0.000074	0	-13	1322	23
CTF1-17.2	Mantle	0.282283	11	0.000201	5	0.000008	0	-16	1332	15
CTF1-18.1	core	0.282328	17	0.002126	23	0.000086	1	-13	1273	23
CTF1-19.1	core	0.282387	11	0.000503	6	0.000020	0	-11	1191	15

5. Results:

5.1. Whole rock geochemistry

Our sample CTF1 contains 63 wt.% SiO_2 and CIPW Hypersthene-normative composition typical of tonalite or dacite (Fig. 2a) (e.g. Rollinson 1993; Tatsumi and Eggins 1995). Our tonalite sample also appears strongly metaluminous (A/CNK = 0.56) with an elevated CaO and relatively low K_2O and Na_2O content (Fig. 2b), and calcic with a low MgO and Fe_2O_3 (e.g. Frost et al., 2001).

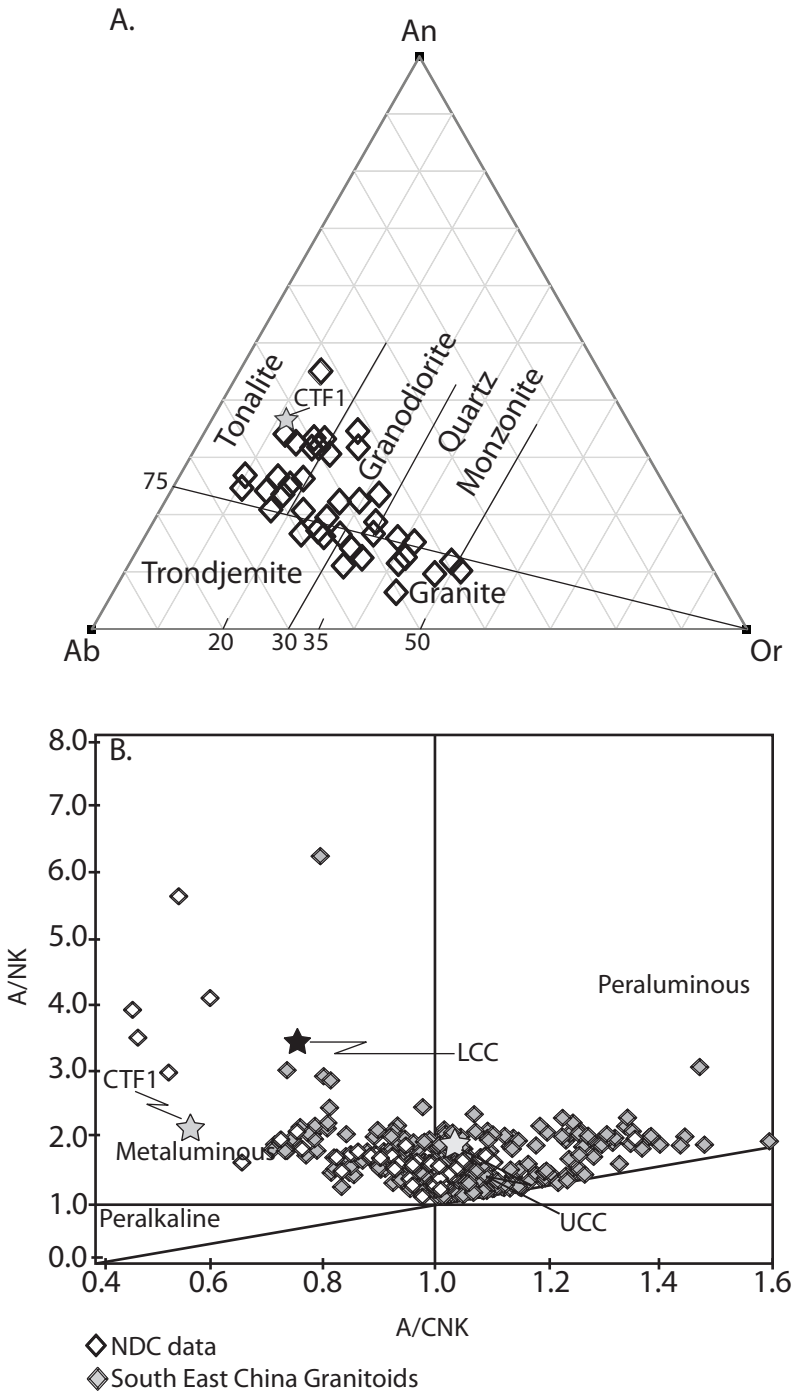

Figure. 2. (A) Granitic classification in terms of normative anorthite (An), albite (Ab), and orthoclase (Or). Fields defined by Barker, (1979). NDC data are compiled from Zheng et al., (1999), Zhang et al., (2000), Ma et al., (2000), and Bryant et al. (2004). UCC, MCC, and LCC refer to Upper, Middle, and Lower Continental Crust averages, respectively, from Rudnick and Gao (2003). After Zhao et al., (2008). (B) Shand's Index diagram for classification of granitoids (Maniar and Piccolli 1989). Northern Dabie Complex (NDC) data from Ma et al., (2000) and Bryant et al., (2004). South East China Granitoid data from Chen et al., (2002), Zhang et al., (2002), Wang et al., (2007), Zhao et al., (2008), Zhang et al., (2008), Huang et al., (2008), He et al., (2011) and Qi et al., (2011).

Based on a primitive-mantle normalized plot (Fig. 3a), our sample shares many features with the upper-continental crust average (Rudnick and Gao, 2003) and intra-oceanic arc tonalites that are representative of other granitoids found across SE China. The high field strength elements (HFSE) U, Th, and Nb plot notably above normalized values for the UCC, with Ta anomalously enriched (Fig. 3a). For the remaining HFSE, Ti contents are about equal to the UCC average, whilst Zr and Hf are depleted relative to the LREE and display values similar to those observed in arc magmas (Fig. 3a).

Chondrite-normalized REE profiles (Fig. 3b) display steep negative trends that parallel the UCC average and Archean tonalite-trondhjemite-granodiorite (TTG) suites (e.g. the Kongling Gneiss: Ma et al., 2000). In contrast, the flat M-HREE profile is similar in both concentration and gradient to oceanic basalts (i.e. MORB), intra-oceanic arc tonalites and the UCC, except with a slight enrichment in the HREE's Tm, Yb and Lu (Fig. 3c).

Whole-rock Rb-Sr and Sm-Nd isotopes were measured using sample CTF1 along with a repeat analysis. An average of these two analyses yields an $^{87}Sr/^{86}Sr$ ratio of 0.713340 and $^{87}Rb/^{86}Sr$ 0.2971, with a $^{143}Nd/^{144}Nd$ ratio of 0.511845 and $^{147}Sm/^{144}Nd$ ratio of 0.1197. Individual ratios for each analysis are reported in Table. 1. Sm-Nd isotope ratios yield a Depleted Mantle model age (here after referred to as T[Nd]DM) of 2.1 Ga and a present day ƐNd(t=0 Ga) value of -15.5.

5.2. Zircon results:

5.2.1 Zircon textures:

CL images of zircon grains show interior domains with complex sector zonation patterns and, with the possible exceptions of CTF1-02 and CTF1-16, lack clear visible oscillatory zoning characteristic of igneous cores (Fig. 4a). Interior domains also contain a mix of strongly

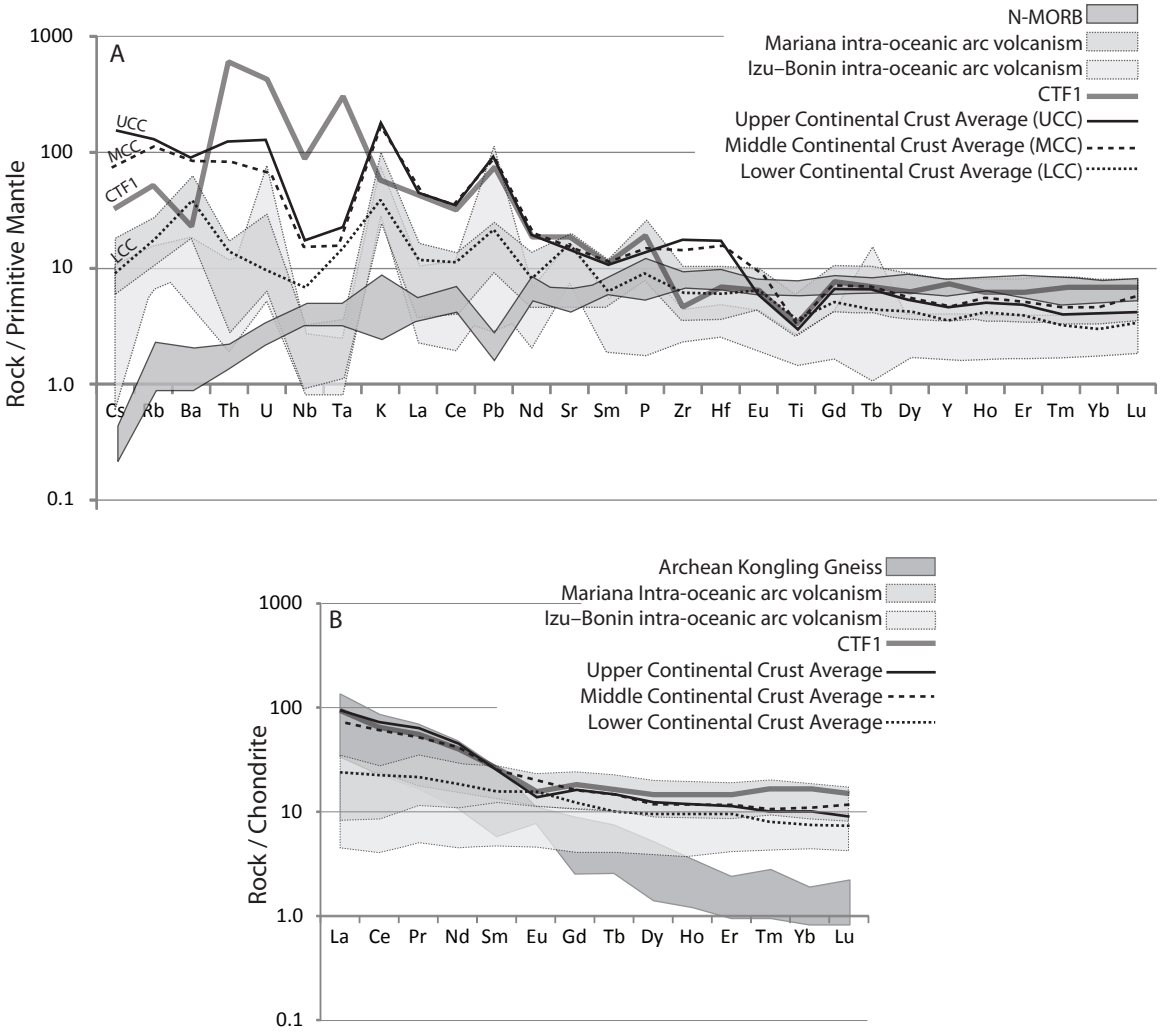

Figure. 3. (a) Primitive mantle (Sun and Mcdonough, 1989) normalized whole-rock geochemical profiles. N-MORB data from Hofmann (1988), Sun and McDonough (1989), Hart et al., (1999) and Niu et al (1999). Mariana intra-oceanic arc volcanism data from Elliott et al., (1997). Izu–Bonin intra-oceanic arc volcanism data from Ishizuka et al (2006). Continental Crust Averages from Rudnick and Gao (2003). (b) Chondrite normalized REE profiles. Archean Kongling Gneiss data from (Ma et al., 2000). Mariana intra-oceanic arc volcanism data from Elliott et al., (1997). Izu–Bonin intra-oceanic arc volcanism data from Ishizuka et al (2006). Continental Crust Averages from Rudnick and Gao (2003).

contrasting light-grey to dark sectors (e.g., grain CTF1-16 in Fig. 4a). Larger grains (~>150 µm) typically include at least two main inner-domains, separated by convolute or rounded boundaries. Thin (<10 µm) bright rims of variable thickness sometimes fill embayments (e.g., grains CTF1- 10 and -17). Mineral inclusions and parallel linear fractures are observed in CL images for a number of grains (i.e. Grain CTF1-01, -05, -15: Fig. 4a). In some grains BSE images show radial fractures surrounding homogeneous interior domains (U and/or Th rich domains), porous textures with small mineral inclusions/voids, and thin discontinuous overgrowths with quartz and titanite inclusions (Fig. 4b I-III) identified using Energy-dispersive X-ray (EDS) spectra. Mineral inclusions were observed in ~10% of the grains. Quartz inclusions were associated with zircon interiors whilst titanite was typically found in the exterior regions. (U,Th)SiO_4 inclusions (bright grains labeled UTh in Fig. 4b VI-VII) are surrounded by radial cracks and some appear to be connected to external (U,Th)SiO_4 grains via cracks in zircon exterior regions (e.g., Fig. 4b IV).

5.2.2. Zircon U-Pb geochronology:

Twenty seven U-Pb and trace-element analyses were performed on nineteen grains from sample CTF1 (Table. 2ab). We report U-Pb ages as $^{206}Pb/^{238}U$ with 2σ errors, unless otherwise stated. We observe no correlation between analysis location, textural domain, or $^{206}Pb/^{238}U$ age. U-Pb analyses yield a heterogeneous population of normal (i.e.$^{207}Pb/^{206}Pb$ date > $^{206}Pb/^{238}U$ dates) and reverse (i.e. $^{207}Pb/^{206}Pb$ date < $^{206}Pb/^{238}U$ dates) discordant dates with a 91% to 108% spread in discordance (I.e. % = [$^{207}Pb/^{235}U$ age] / [$^{206}Pb/^{238}U$ age] x 100). $^{238}U/^{206}Pb$ ages range between 143±3 Ma and 309±6 Ma (Fig. 5ab), with minor peaks at 279±5 Ma (n=3), 255±7 Ma (n=2), and a single analysis at 309±6 Ma observed using a $^{206}Pb/^{238}U$ age probability density plot (Fig. 5b). The highest peak occurs at 210±3 Ma (n=6), and grades into a poorly

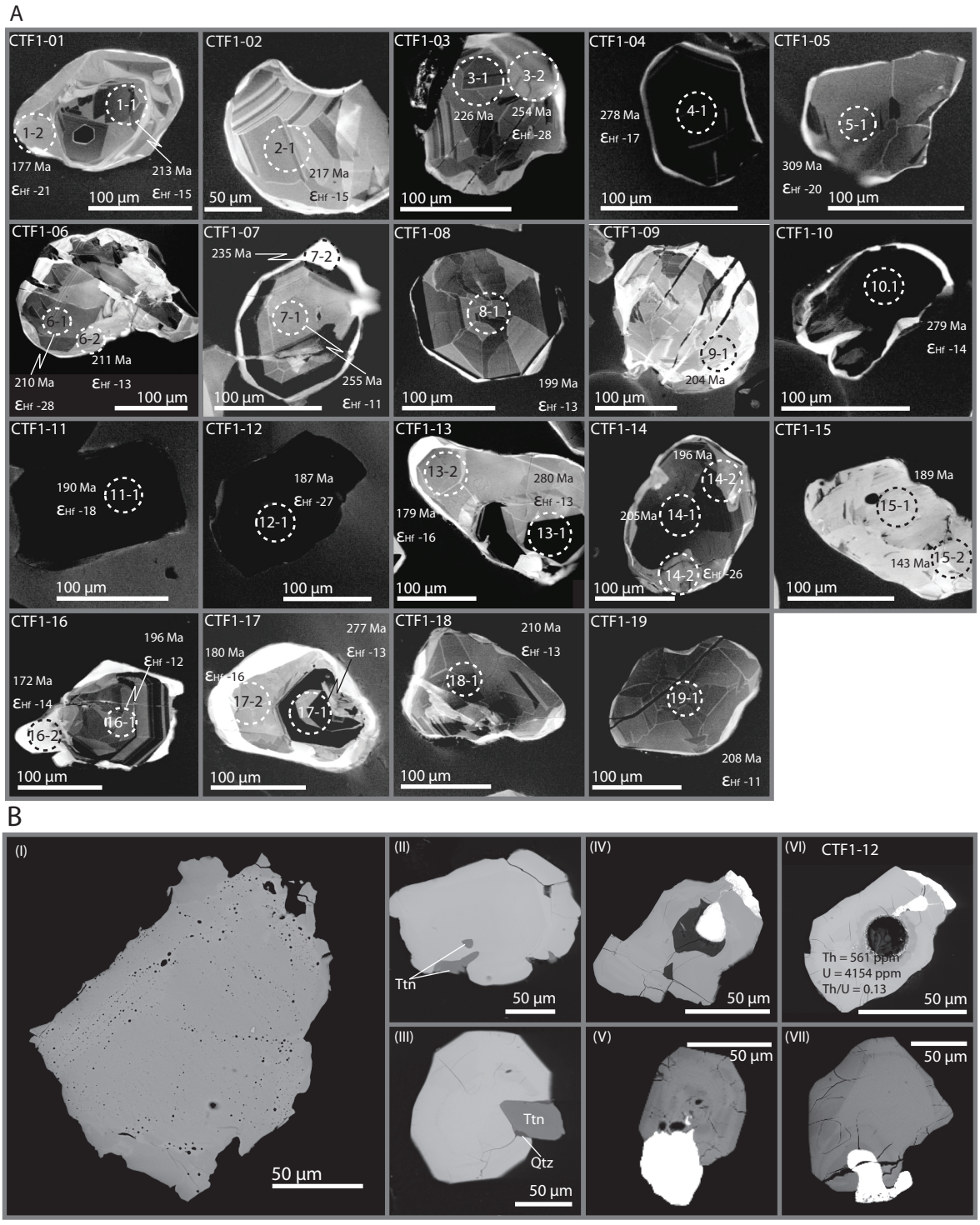

Figure. 4. (a) Cathodoluminescence (CL) zircon images. Circles represent location of Laser Ablation analyses and grains are annotated with ^{206}Pb-^{235}U ages and εHf(t=U-Pb) values. (b) Back Scattered Electron (BSE) images for select zircon grains showing inclusions of titanite (Ttn), quartz (Qtz), and a Th-U silicate phases (UTh: white).

defined or composite peak between 189±8 and 197±9 Ma, and a final young peak c. 177±4 Ma (Fig. 5b).

5.2.3. Zircon trace-elements:

On a chondrite normalized REE plot (Fig. 6a), most zircon analyses display positively trending profiles with large positive Ce anomalies (Fig. 6a). A small subset of analyses displays nearly flat profiles with small Ce anomalies (Fig. 6a). Overall, La_N values vary by almost four orders of magnitude, with the remaining LREE ranging over three orders of magnitude and the M-HREE two orders of magnitude. Eu anomalies are insignificant for all analyses. Zircon grains from CTF1 contain a wide range in U and Th concentrations (Fig. 6b), spanning up to three orders of magnitude (i.e. U = 6001 to 133 ppm, Th = 1214 to 1.47 ppm).

5.2.4. Zircon Lu-Hf isotopes:

Twenty two Lu-Hf isotopic analyses were performed on seventeen grains from sample CTF1 (Table. 2c). $^{176}Hf/^{177}Hf$ ratios range from 0.281903 to 0.282387 (Fig. 7a). The distribution of $^{176}Hf/^{177}Hf$ ratios displays a single well-defined peak at 0.282285 with a tail that extends up to 0.282387 (Fig. 7a). ƐHf(t=U-Pb) and εHf(t=750 Ma) values range from -11 to -28 and +1 to -16, respectively (Fig. 7b). T[Hf]DM ages range from c. 1190 to 1850 Ma with a non-Gaussian distribution that includes a peak at 1.3 Ga and tail that extends to older values (Fig. 7c).

6. Protolith composition and relationship to crustal recycling processes:

Our metaluminous tonalite gneiss sample (Fig. 2a) has a low K content (0.9 wt% K_2O at 63 wt % SiO_2) similar to modern low-K tonalites, for example, from the Izu-Bonin-Mariana (IBM)

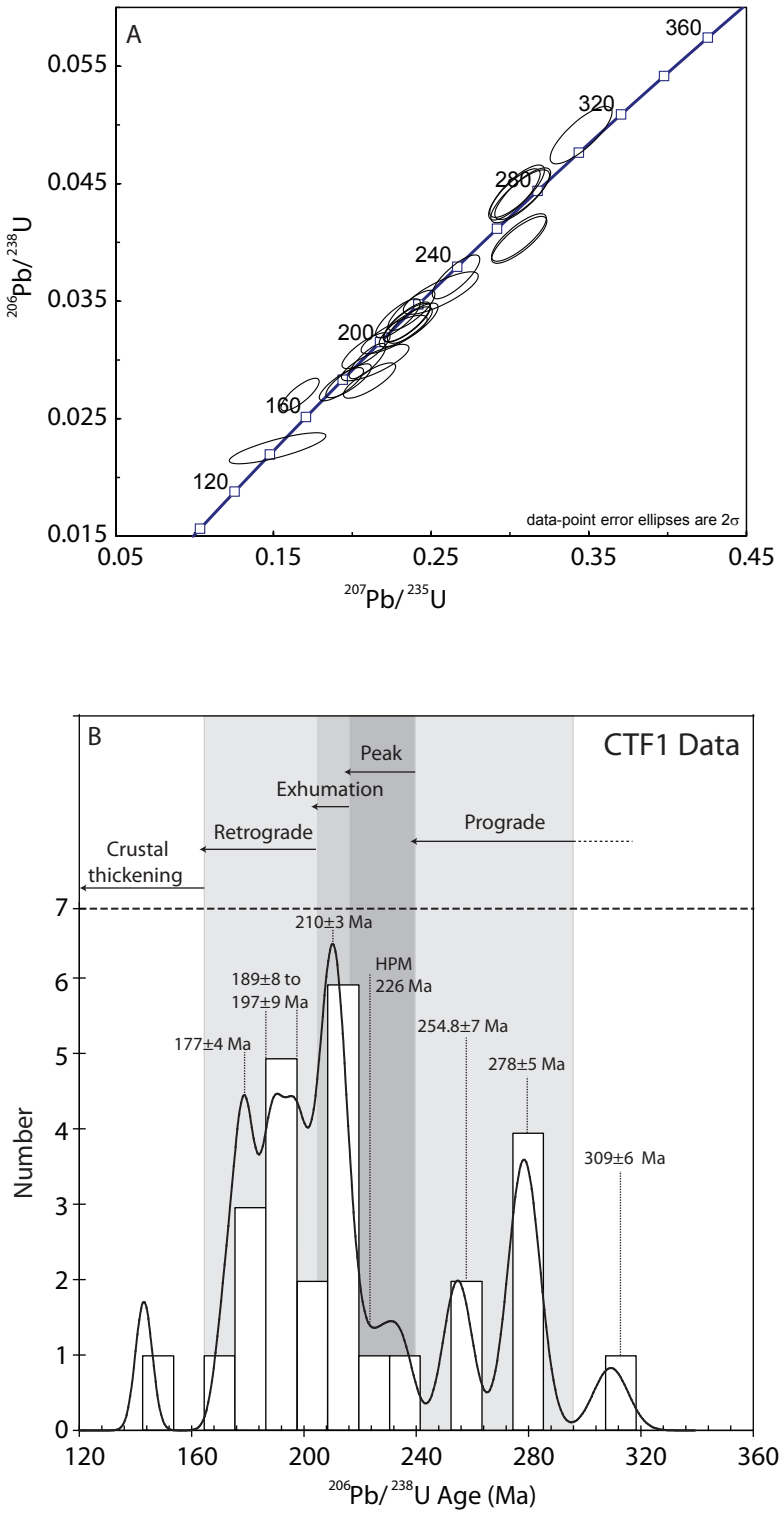

Figure. 5. (a) Zircon U-Pb Concordia diagram. (b) Probability density plot of $^{206}Pb/^{238}U$ ages, annotated with representative stage of continental subduction and metamorphism (see text for discussion of stages).

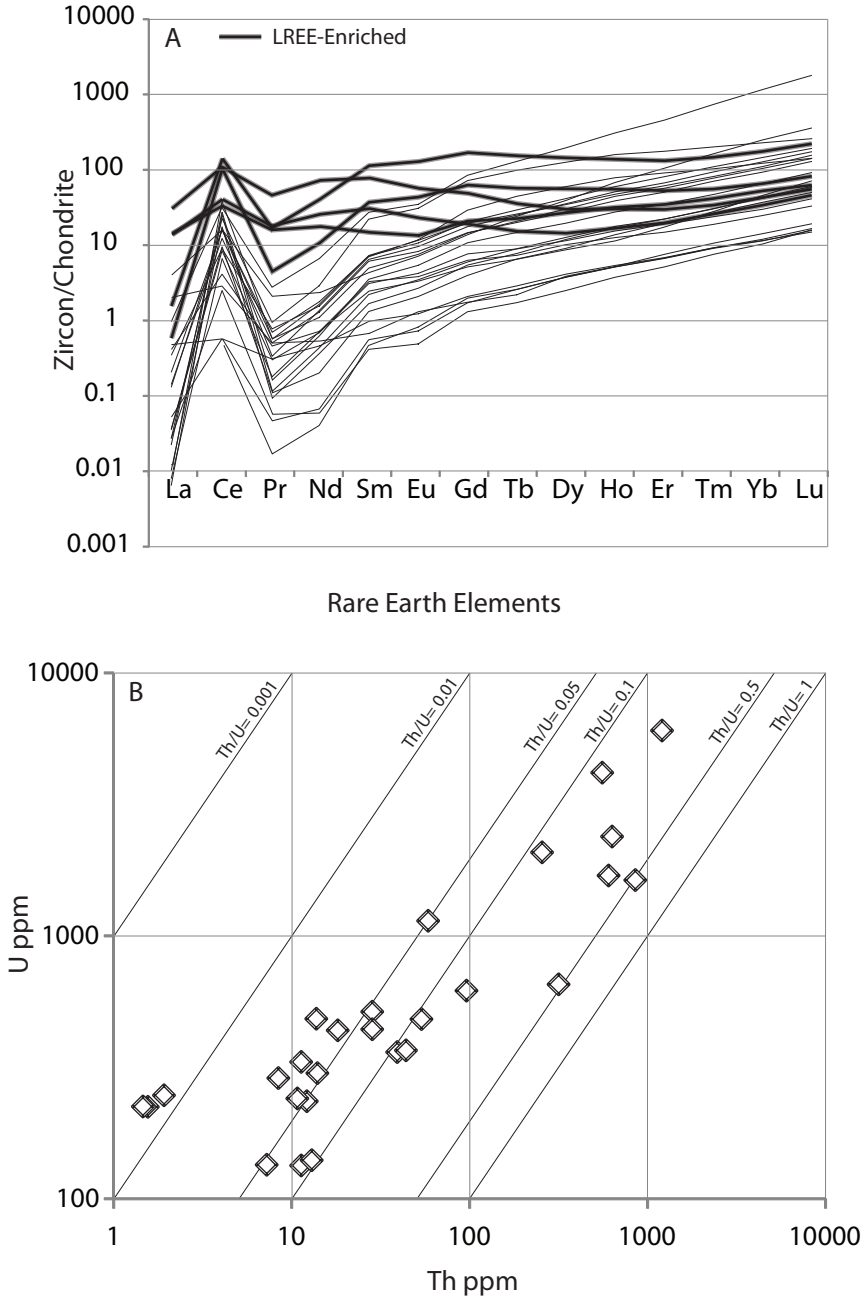

Figure. 6. (a) Chondrite normalized zircon REE profiles. Note LREE enriched and flat to concave upwards profiles. (b) Plot of U vs. Th with axes in Logarithmic form, annotated with lines representing Th/U values.

arc (e.g. Kimura et al., 2002). Compared to continental tonalites from south China, our sample has one of the lowest K_2O and highest CaO contents, more in line with a less evolved lithology, i.e., mafic rocks and the lower continental crust average (53.4 wt% SiO_2: Rudnick and Gao 2003).

Across south China, Neoproterozoic and Palaeoproterozoic continental granitoid bodies are associated with recycling of the Archean Yangtze Craton, and represent important periods of continental crust construction and crustal distillation (e.g. Ma et al., 2000; Chen et al 2002; Zhang et al., 2006b, 2008; Li et al., 2003; Huang et al., 2006; Zhao et al., 2008; Qi et al., 2011). In the NDC, extensive Proterozoic rifting and granitoid generation has been overprinted by post-collisional collapse of the Dabie Mountains during the Cretaceous, producing a region dominated by Cretaceous granitoids (e.g. Hacker et al., 1998; Bryant et al., 2004). For our sample, a T[Nd]DM model age of ~2.1 Ga is consistent to other NDC studies (e.g. Chen and Jahn, 1998; Ma et al., 2000; Bryant et al., 2004), and support its protolith to also have formed during the Palaeoproterozoic, despite the lack of U-Pb dates that exceed 309 Ma (see below for discussion on the origin of zircon grains).

6.1. HFSE fractionation:

Ti and the HFSE element pair Zr-Hf show depletions relative to the LREE (Fig. 3a), consistent with the characteristic trends observed for the continental crust (Rudnick and Gao, 2003), IBM arc tonalites and SE China Granitoids (Fig. 3a). In contrast, compared to the average crustal compositions of Rudnick and Gao (2003), IBM arc tonalites and a majority of SE China Granitoids, we observe a primitive-mantle trace-element normalized profile where two HFSE pairs, Nb-Ta, and Th-U (Fig. 3a), are notably enriched. The magnitude of this enrichment is 2-10 times greater than the most trace-element enriched granites from the Northern Dabie Complex

(i.e. SiO_2> 73 wt%), with the highest Nb and Ta values reported for granodiorites and TTG-like rocks from South China.

Furthermore, we observe an unusually low Nb/Ta of 4.8 relative to those for typical magmatic crustal components and processes (i.e. Nb/Ta > 12–13: Barth et al., 2000), and a low Zr/Hf of 25 relative to arc tonalites of comparable SiO_2 wt.% (i.e. Zr/Hf > 30–35) (Fig. 8a). Likewise, a Nb/Zr ratio of 1.05 is anomalously high compared to tonalites and granitoids from the NDC, SE China and IBM arc, whose Nb/Zr ratios do not exceed 0.50 with an average of 0.07, and the UCC average of 0.06 (Fig. 8b) (Rudnick and Gao 2003). This large gap between Nb/Zr ratios provides evidence for the enrichment of Nb, Ta, U, and Th, and fractionation of Zr from Hf.

Typical magmatic fractionation processes are not thought to lead to extensive fractionation of Nb from Ta, nor Nb and Ta from Zr and Hf (Green 1995; Dostal and Chatterjee 2000), nor is the addition or presence of flux components (i.e. halogens, P, Li, B, H_2O) (e.g. Linnen 1998; Van Lichtervelde et al., 2010). The most likely mechanism for HFSE fractionation would involve the preferential in-situ retention of Zr and Hf in a residual and immobile solid phase (i.e. zircon, baddelyite, or zirconolite) during infiltration of a fluid in which Nb-Ta and U-Th remain fluid compatible at high concentrations. As noted by Rubin et al. (1993), the mobility or immobility of Zr and Hf during infiltration of an F-rich metasomatic fluid is a function of the solubility of their source phases; for example, they propose aegirine and arfvedsonite in an alkaline amphibolite could have liberated Zr upon fluid dissolution whilst zircon remained residual, suffering only moderate alteration. It is also important to note that because we present only one sample of 4-5 kg of rock from a single formation, we cannot entirely rule out any unusual trace-element features as those resulting from sampling bias.

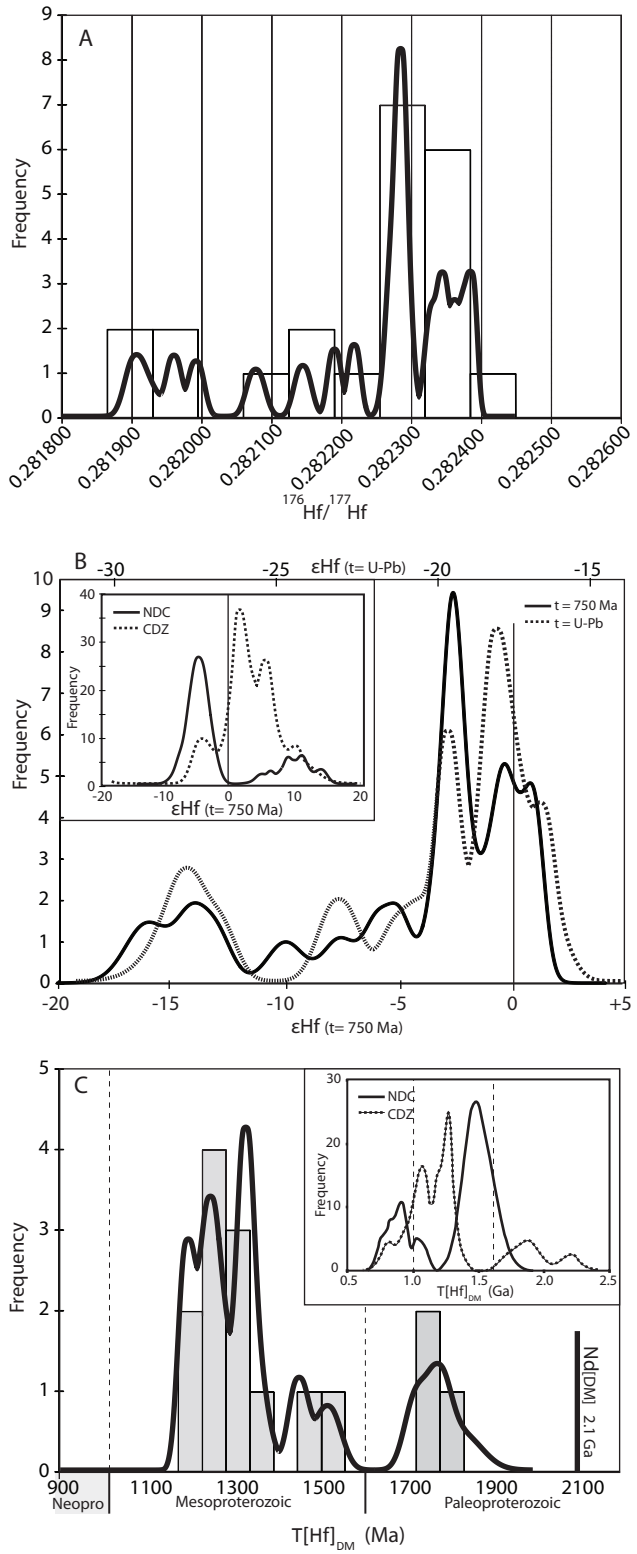

Figure. 7. (a) Plot of zircon $^{176}Hf/^{177}Hf$ ratio probability density. (b) Plot of zircon ¬εHf(t=U-Pb) and εHf(t=750 Ma) probability density. Inset plot displays the results of compiled analyses of εHf(t=750) from rocks across the NDC and CDZ; data from Zheng et al., (2005, 2006) and Zhao et al. (2008) for comparison to our εHf(t=750 Ma) values. (c) Plot of zircon $T[Hf]_{DM}$ model age probability density with whole-rock $T[Nd]_{DM}$ model age. Inset plot after Zhao et al. (2008).

7. The origin of zircon:

Unlike other NDC zircon geochronological studies (e.g., Bryant et al., 2004), we observe no Precambrian zircon ages, with prominent peaks occurring only at times proposed to represent continental subduction and exhumation (Fig. 5b). Furthermore, we observe no conclusive textural or geochemical evidence of an initial magmatic growth stage. Zircon analyses with U-Pb dates >234 Ma (Proposed later to record prograde events) contain two types of REE profiles. Firstly, LREE depleted (i.e. [La]N <0.33 to 0.01) with no Eu anomalies, large Ce anomalies, and positively trending M-HREE profiles. Secondly, LREE enriched (i.e. [La]N >0.5 to 29.4) with no Eu anomalies, small Ce anomalies and flat to mildly upward-concave M-HREE profiles (Fig. 6a). M-HREE patterns similar to those of the second group have been observed for zircon grains in equilibrium with garnet (Rubatto and Hermann. 2007). The occasional observation of titanite inclusions within zircon suggests it too may have been an important co-precipitating phase and played a role in controlling zircon REE profiles. Experimental measurement of REE partitioning between titanite and silicate melts identifies a parabola that peaks at Sm and favors uptake of the MREE (Prowatke and Klemme, 2006). Mineral-matrix measurements of REE partitioning between titanite (i.e. sphene) and silicate melts identifies a parabola that peaks at Sm and favors significant uptake of the L-MREE relative to zircon (Colombini et al., 2011). Although we chose zircon analysis spots free from observable mineral inclusions (Fig. 4a), we cannot rule out the possibility that sub-micron titanite inclusions were sampled during analysis, leading to an artificial enrichment in LREE. However, this explanation seems unlikely because we were able to remove anomalous analytical cycles from the time-resolved analyses.

U contents for igneous zircon grains are typically <1000 ppm (Parrish and Noble 2003), increasing to levels >>1000 ppm for some grains from granitoids, granites and other high U magmatic environments (e.g. Belousova et al., 2002; Hoskin and Schaltegger 2003). The elevated actinide concentrations observed in a number of CTF1 zircon interior domains (>1000 ppm and up to 6000 ppm: Fig. 6b) argues against simple crystallization from a typical tonalitic melt, but potentially through the involvement of an actinide enriched component.

For zircon grains on which we could perform both internal and external domain analyses, two groups can be identified; Firstly, group (1) grains that contain interior and exterior domains with similar and overlapping REE profiles, U, Th and total Pb concentrations, and Th/U and $^{176}Lu/^{177}Hf$ ratios. Secondly, group (2) grains that contain exterior domains with 1 to 2 orders of magnitude lower concentrations of REE, U, Th, and total Pb, and lower Th/U and $^{176}Lu/^{177}Hf$ ratios than their respective interior domains.

7.1. Lu-Hf Isotopes:

Focusing upon grains that were large enough to allow analysis from two spot locations, U-Pb isotopic trends appear to be decoupled from trends observed for the Lu-Hf isotopes, indicating they are recording different processes. Within our analyzed zircon population we observe two grains out of five that display intra-grain Hf isotopic variation, grains CTF1-01 and -06. For these two grains $^{176}Lu/^{177}Hf$ and Th/U ratios and REE contents decrease by an order of magnitude from the interior to the exterior domain, features typical for grains with magmatic cores and metamorphic rims (e.g. Wu et al., 2009). The CL image of grain CTF1-01 (Fig. 4a) shows a dark interior domain containing blocky-sector zoning, with a rounded-convolute boundary and an exterior domain with irregular lighter shades of grey. The U-Pb date of the inner-domain is older (213±4 Ma) than for the outer-domain (177±4 Ma), while T[Hf]DM ages

display the opposite trend, with an older outer domain (1521 Ma vs. 1350 Ma) and more negative εHf(t=U-Pb) value (-20 vs. -15), relative to its inner domain. Grain CTF1-06 has a particularly complex CL texture (Fig. 4a), containing an inner-region with mixed grouping of dark-grey regions and sector zones with parallel fractures. This interior region is surrounded by a patchy zoned and discontinuous lighter grey band of zircon. T[Hf]DM ages between spot locations show a trend opposite to those of grain CTF1-1, with an older T[Hf]DM age (1826 vs. 1266 Ma) and more negative Hf value (-28 vs. -13) for the complex inner-region. Interestingly, both interior and exterior domains record nearly identical U-Pb ages at c. 210 Ma, and nearly identical $^{176}Lu/^{177}Hf$ and Th/U ratios, U, Th and REE contents.

In contrast to the zircon grains described above, grains CTF1-13, -16, and -17 contain clearer interior-exterior CL texture relationships. As expected, U-Pb dates are older for interior domains than exterior domains. However, interior and exterior domains record similar $^{176}Hf/^{177}Hf$ ratios and T[Hf]DM model ages (Fig. 4a), supporting the disconnected behavior of the two isotopic systems.

The prominent Mesoproterozoic T[Hf]DM model age peak with a smaller contribution of Palaeoproterozoic ages (Fig. 7c) may suggest either an open system inheritance of older zircon grains from a heterogeneous source region or assimilation of older crustal Hf during anatexis; processes typically associated with crustal granitoid construction (e.g. Miller et al., 1988; Kemp et al., 2005; Siebel and Chen 2010). Alternatively, heterogeneous $^{176}Hf/^{177}Hf$ ratios recorded in zircon grains may develop under closed system conditions if growth was associated with secondary events that led to release of Hf residing in phases with significantly higher $^{176}Lu/^{177}Hf$ ratios. Of particular importance is the progressive breakdown of garnet because garnet concentrates Lu and has high and variable Lu/Hf ratios (i.e. ~1.0) and therefore can develop

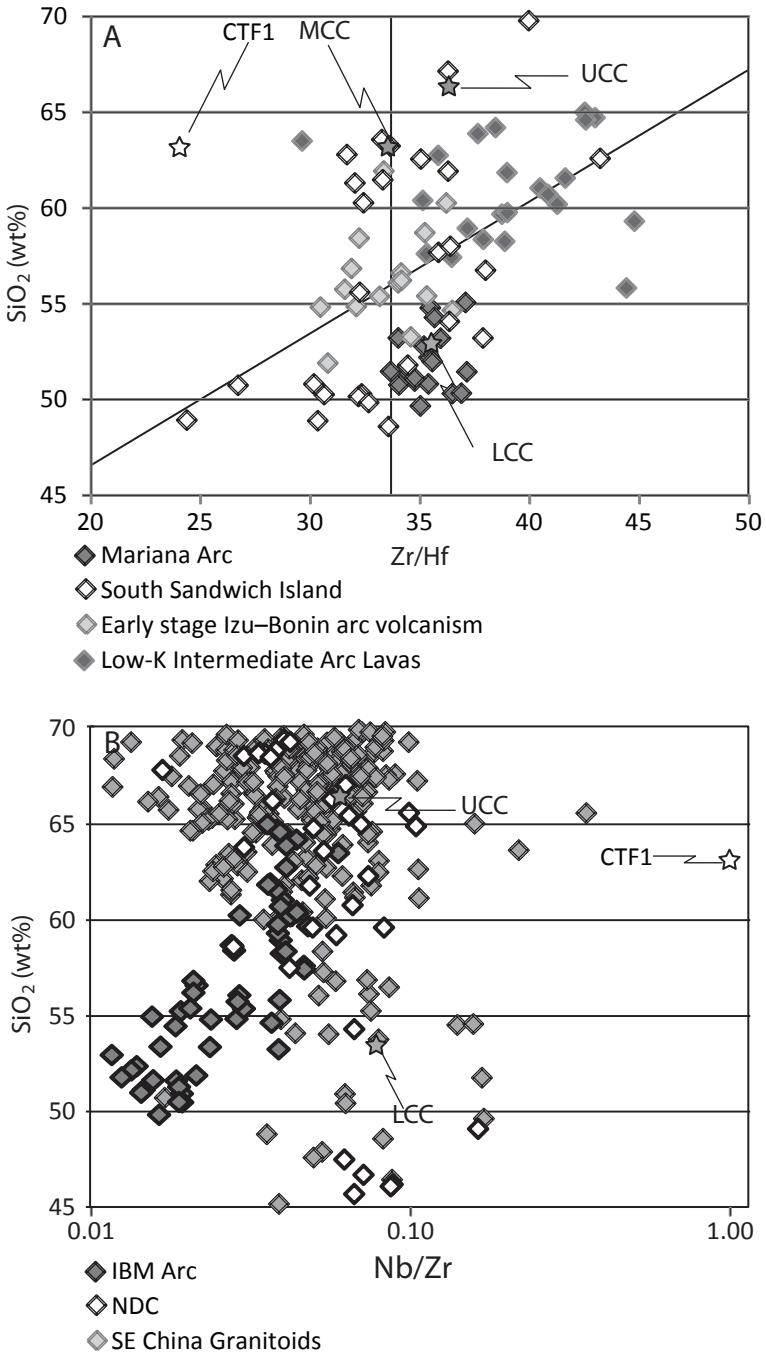

Figure. 8. (a) Plot of SiO_2 wt.% vs. Zr/Hf. Mariana intra-oceanic arc volcanism data from Elliott et al., (1997). South Sandwich Island arc data from Pearce et al., (1995), Izu–Bonin intra-oceanic arc volcanism data from Ishizuka et al (2006), Low-K Intermediate Arc Lava data from Kimura et al (2002). UCC, MCC, and LCC refer to Upper, Middle, and Lower Continental Crust averages, respectively, from Rudnick and Gao (2003). (b) Plot of SiO_2 wt.% vs. Nb/Zr. NDC data from Ma et al., (2000) and Bryant et al., (2004). South East China Granitoid data from Chen et al., (2002), Zhang et al., (2002), Wang et al., (2007), Zhao et al., (2008), Zhang et al., (2008), Huang et al., (2008), He et al., (2011) and Qi et al., (2011). IBM arc data from Ishizuka et al (2006) and Kimura et al (2002). UCC and LCC refer to Upper and Lower Continental Crust averages, respectively, from Rudnick and Gao (2003).

sufficiently high and variable $^{176}Hf/^{177}Hf$ ratios in only a few tens of Myr (e.g. Sláma et al., 2007; Valley et al., 2010; Peters et al., submitted).

The discrepancy between our measured 2.1 Ga bulk-rock T[Nd]DM age and the heterogeneous distribution in zircon T[Hf]DM dates (Fig. 7c) are features observed in other studies and proposed to represent a two-stage crustal evolution model for the Yangtze continent (Zheng et al., 2006; Zhao et al., 2008). Zheng et al. (2006) propose an initial stage involving melting of the primitive and depleted mantle during the Palaeoproterozoic with addition of mafic Zr-depleted juvenile crustal components (i.e. mafic arc mantle melts) that were incapable of precipitating zircon. Secondly, Neoproterozoic crustal recycling processes, c. 750 Ma, leads to melting of hydrated juvenile crustal components, granitoid formation, and the sub-solidus (?) release of Hf from phases with variable Lu/Hf that generate the observed heterogeneous zircon Hf-isotope compositions. Neoproterozoic zircon U-Pb dates, c. 750 Ma, are a prominent characteristic for crustal rocks from the Dabie orogen (e.g. Bryant et al., 2004; Zheng et al., 2006). The diverse $^{176}Hf/^{177}Hf$ isotope ratios we observe support the growth of zircon following a period of crustal residence involving Hf released from phases with Lu/Hf ratios >> zircon. However, the lack of zircon U-Pb dates greater than c. 309 Ma for our sample limits our ability to tie it specifically to the two-stage model presented by Zhang et al., (2006).

8. Discussion:

8.1. The nature and timing of multistage continental subduction and metamorphism of the Northern Dabie Complex:

Bryant et al., (2004) proposed that the NDC resided south of the CDZ prior to Triassic continental subduction and remained a physically coherent unit during subduction and that

therefore ultra-high pressure metamorphism was limited to the CDZ. The final juxtaposition of the NDC below the CDZ occurred largely during exhumation when the subducted UHPM CDZ was thrust over the HPM NDC. Following this stage of thrust stacking and crustal thickening, orogenic collapse and crustal extension led to Cretaceous granitoid magmatism, followed by uplift, doming, and exposure of the deeper HPM NDC.

Recently, Liu et al. (2007a) reported a single micro-diamond inclusion in a zircon grain from a tonalitic gneiss sample from the northern margin of the NDC as evidence for Triassic UHPM in the NDC. However, Zhang et al (2009) question the authenticity of this diamond inclusion, which compared to diamond inclusions from known UHP terrains, does not appear to be a typical high relief phase and cannot be distinguished from graphite and moissanite using Raman spectroscopy. Furthermore, U-Pb analysis of the diamond-bearing zircon domain yielded a 199±6 Ma date, which is inconsistent with all other reports on the timing of peak HPM or UHPM across the Dabie-Sulu orogenic belt. More recently, Liu et al., (2011a) reported a single relict coesite inclusion in zircon, distinguished from quartz by its higher relief and lower birefringence, from an eclogite sample collected from the Luotian Dome as evidence of UHPM (Fig. 9); however, Liu et al., (2011a) note that this inclusion may also be only quartz owing to the absence of a diagnostic coesite Raman spectrum peak. Other reports of UHPM in the NDC are limited to indirect mineral decompression textures, including quartz-pseudomorphs after coesite, orientated quartz rods in Clinopyroxene (CPX), Rutile + CPX + Amphibole + Apatite needles in garnet, and elevated F contents in apatite (Tsai and Liou 2000; Malaspina et al., 2006; Liu et al., 2011b). These decompression textures, however, are limited to eclogites either associated with peridotites (Tsai and Liou 2000; Malaspina et al., 2006) or rocks derived from under-plated mantle-derived lower crust (Liu et al., 2007b). These metamorphic lithologies are particularly rare in the NDC and it remains controversial whether they were in-situ or emplaced

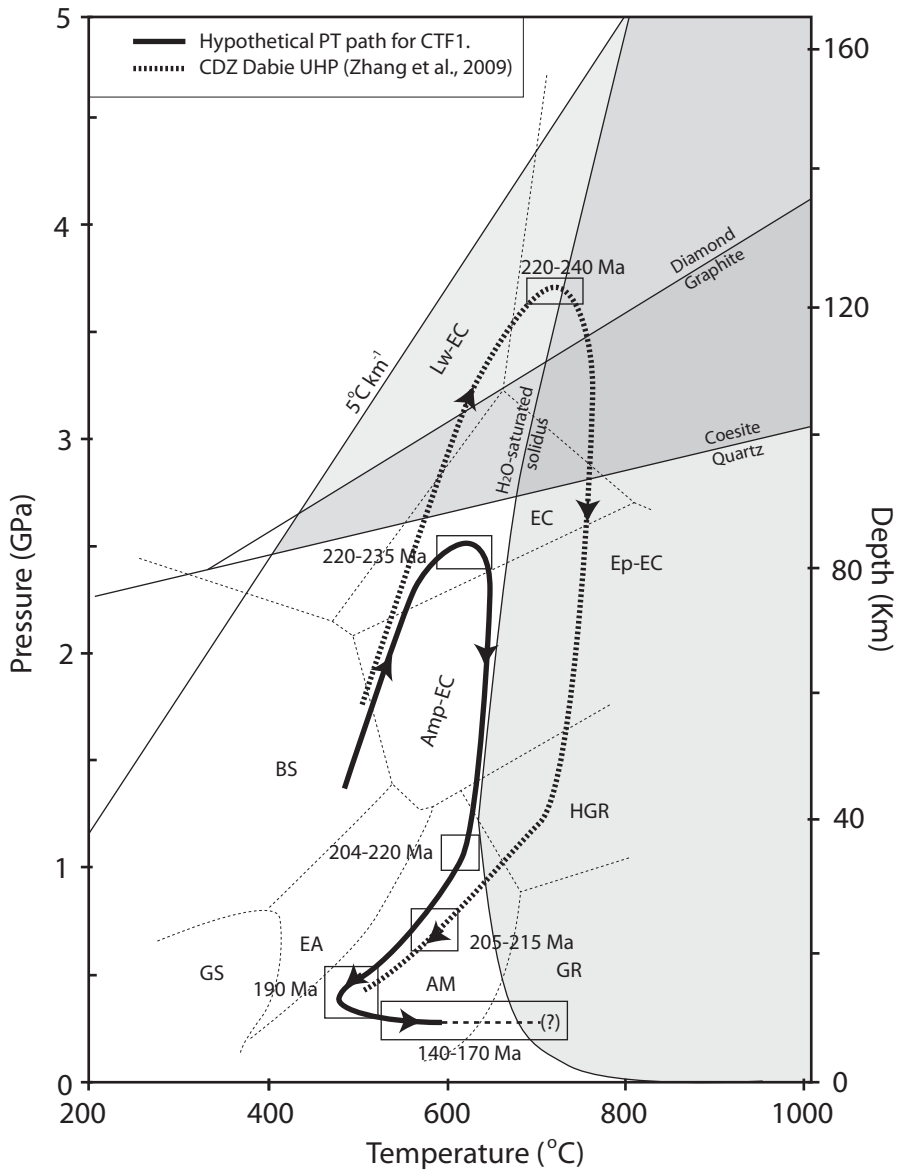

Figure. 9. Summary PTt metamorphic paths for HP/UHP eclogites and orthogneiss from the Dabie orogen and Luotian Dome, east central China, compiled after Zhang et al., (2009) and references therein. Metamorphic facies are labeled: granulite (GR), amphibolite (AM), epidote amphibolite (EA), blueschist schist (BS), greenschist (GS) and subdivision of the eclogite (EC) into amphibole (Amp) eclogite, epidote (Ep) eclogite, lawsonite (Lw) eclogite.

during continental subduction, and thus, whether or not their peak conditions are the rule or the exception for the NDC (e.g. Liu et al., 2005; Zhang et al., 2009; Liou et al., 2009).

Across the Dabie-Sulu orogenic terrain, peak UHPM is proposed to have been attained between c. 230 to 220 Ma (e.g. Fig. 9), with a precursor UHPM event recorded in the CDZ c. 244 to 235 Ma (e.g. Ayers et al., 2002; Hacker et al 2006). For the Luotian Dome, U-Pb analysis of zircon domains containing (U)HP metamorphic index-minerals (i.e. coesite(?)-quartz, garnet, rutile) displayed a 227 Ma to 222 Ma range with a weighted mean age of 226±3 Ma for peak metamorphism (Fig. 9: Liu et al., 2011a), suggesting a relatively consistent termination of HP/UHPM conditions across the orogenic belt, c. ~220 Ma (see reviews in Hacker et al., 2006; Zhang et al., 2009; Tong et al 2011).

Following peak HP/UHPM in the eclogite facies, rapid exhumation to amphibolite facies conditions between 220 Ma and 205 Ma is reported for the CDZ (Fig. 9) (e.g. Hacker et al., 2006). In contrast, it is proposed that mafic eclogites in the NDC experienced post-peak high pressure and high temperature metamorphism (i.e. >750°C: Malaspina et al., 2006; Tong et al., 2011). Mineral equilibria define an eclogite to granulite facies exhumation path based on the occurrence of othopyroxene, plagioclase, spinel and cordierite in CPX-garnet symplectites and coronas around garnet in rare mafic rocks in the NDC (Xu et al., 2000; Tsai and Liou 2000; Malaspina et al., 2006; Liu et al., 2007b; Tong et al., 2011). Similar to other orthogneiss samples from the NDC (e.g. Xie et al., 2010), we observe no evidence for UHPM or HP granulite-facies metamorphism. It remains unclear whether the retrograde overprint destroyed all evidence of HP/UHP and granulite facies metamorphism, or if these conditions are restricted to mafic/ultra-mafic outcrops located along the northern margin of the NDC as suggested by Bryant et al. (2004).

The Δ166 Myr range in U-Pb zircon dates recorded in our sample encapsulates the majority of prograde through peak and retrograde metamorphic events associated with the protracted evolution of the Dabie orogen (e.g. Hacker et al., 2006; Zhang et al., 2009; Liu and Liou 2011) (Fig. 5b). Despite this range, we observe only a limited number of zircon REE profiles with features that may represent an equilibrium relationship between zircon and garnet (Fig. 6a: i.e. flat HREE garnet signature: Rubatto 2002, Hermann and Rubatto 2003; Rubatto and Hermann 2007ab). These profiles are associated with U-Pb ages at 235 to 280 Ma and may represent a stage of zircon growth or recrystallization associated with prograde garnet growth.

As summarized in Fig. 5b, it remains unclear which ages to associate with the onset of prograde metamorphic events due to the presence of a single U-Pb date at c. 309 Ma and age peak at c. 278 Ma. The sporadic nature of dates older than c. 210 Ma indicates these to have either no geological meaning or to represent discrete events leading to continental subduction. Individual zircon $^{238}U/^{206}Pb$ ages at 235±5 and 226±5 Ma for our sample appear to reflect zircon growth or recrystallization at times corresponding to regional peak metamorphism, followed by our most prominent peak at 210±3 Ma (Fig. 9), conforming to the timing of widespread retrograde amphibolite-facies metamorphism in the CDZ (Ayers et al. 2002). While many of our measured zircon U-Pb ages correspond to the timing of regional retrograde metamorphism, we also observe a relatively continuous distribution of U-Pb ages extending down to 172 Ma. This age distribution suggests either a lack of discrete retrograde events at this location or the loss of Pb from these domains as thermal relaxation led to increasing temperatures during lower-crustal residence up until Cretaceous orogenic collapse and exhumation of the NDC.

8.2. The response of zircon to metamorphism during continental subduction:

The response of zircon to metamorphism is a particularly complex subject. Multiple metamorphic events can complicate interpretations of U-Pb geochronological dates and construction of metamorphic PTt paths. Sub-solidus in-situ recrystallization can completely remove or grossly distort evidence of original zircon formation (i.e. Gerdes and Zeh 2009; Putnis 2009; Chen et al., 2010). We consider this the most likely explanation for zircon U-Pb dates from sample CFT-1, which are considerably younger than zircon T[Hf]DM model ages.

8.2.1. Zircon alteration and resetting of U-Pb dates:

In most crustal environments, diffusion of Pb from crystalline zircon is an extremely slow process, and rates of U diffusion are even lower by up to four orders of magnitude (Cherniak and Watson 2001, 2003; Cherniak 2010). The generation of cracks and interconnected "fast" diffusion pathways during metamictization is commonly cited for enhancing the susceptibility of Pb to remobilization or leaching during hydrothermal alteration (e.g. Davis and Krogh 2001; Carson et al., 2002; Cherniak and Watson 2001, 2003; Cherniak 2010). The generation of dislocations, point defects and intra-grain crystallographic misorientations during crystal-plastic deformation of zircon in a low-temperature/high pressure metamorphic regime is also thought to enhance Pb loss (Mclaren et al., 1994; Reddy et al., 2006, Timms et al., 2006).

Separating analyses into those with prograde (i.e. >234 Ma), peak (226-234 Ma), and retrograde (<218 Ma) concordant U-Pb dates, all prograde domains have U concentrations > 500 ppm while all but two retrograde domains contain <500 ppm U. The exceptions are grains CTF-11 and -12 that contain the two highest U concentrations, 6001 and 4154 ppm, and record dates of 189 and 186 Ma, respectively. A similar pattern is observed for Th contents where prograde

domains typically contain ~100 to 1000 ppm Th and an average of ~500 ppm, whilst retrograde domains contain 1.5 to 50 ppm Th with an average of ~17 ppm.

Although we lack specific U-Pb isotopic evidence, bulk-rock Sm-Nd and zircon Lu-Hf isotopic evidence supports an initial Proterozoic timing of formation for our sample CTF1, consistent with other studies from the NDC (e.g. Bryant et al., 2004). If zircon grains first appeared during Proterozoic events, Pb loss during Mesozoic metamorphism was an efficient process (i.e. >90-100 %). Pb loss may have been greatly enhanced by a prior stage of metamictization in grains with grossly enriched U and Th contents (i.e. >1000 to 6000 ppm U). Fluids produced by prograde devolatilization reactions (e.g. Scambelluri and Philippot 2001; Manning et al., 2004) could progressively leach Pb from metamict domains until temperatures became high enough to anneal radiation damage, at which point radiogenic lead would begin to accumulate within zircon grains (e.g. Geisler et al., 2007; Carson et al., 2002).

8.2.2. In-situ Recrystallization:

Due to the high temperatures required to break down the zircon lattice under anhydrous conditions (i.e. >1400°C to 1673°C for crystalline zircon and >800°C to 950°C for fully metamict grains: e.g. Vaczi et al., 2009), a catalyzing hydrothermal component (either H+ or OH- ions) is required to overcome the thermodynamic barriers that would otherwise prevent zircon from recrystallizing during sub-solidus crustal metamorphism (e.g. Tole, 1984; Rubie, 1986; Shina et al., 1992; Ayers et al., 2003; Geisler et al., 2003ab, 2007; Salje and Zhang 2006; Carlson 2010). Fluid-aided zircon recrystallization typically affects grains, or regions within grains, where structural degradation or metastable non-ideal solid solutions have enhanced their solubility relative to pure crystalline zircon, and results in partial or complete U-Pb date resetting for the affected domains owing to the removal of incompatible radiogenic Pb (e.g. Geisler et al., 2007).

Group (1) zircon grains, which contain limited trace element differences between exterior and interior domains, appear to record a closed system recrystallization mechanism resulting in no significant extraction or redistribution of trace-elements, except highly incompatible elements (i.e. LREE). This process most likely involved a fluid catalyst (Mullin 2001; Geisler et al., 2007) and progressive re-attainment of structural integrity following a period of metamicitization or strain accumulation (e.g. Mezger and Krogstad, 1997; Hoskin and Black 2000; Nasdala et al., 2001; Geisler et al., 2007). At temperatures of ~200˚C to 350 °C, annealing of individual fission tracks occurs with the re-formation of disrupted bonds and reordering of neighboring atoms (e.g. Mezger and Krogstad, 1997; Hoskin and Black 2000; Cherniak and Watson, 2001; Nasdala et al., 2001). With the infiltration of a catalyzing hydrous fluid, other mechanisms become thermodynamically activated, i.e., annealing of cracks, cleavage surfaces, dislocations and diffusion of point defects with attainment of greater structural integrity during zircon recrystallization (e.g. Geisler et al., 2007).

In contrast, exterior domains of group (2) zircon grains display markedly lower trace element contents relative to interior domains, with a preferential loss of incompatible elements (i.e. LREE and Pb) and decreased less-compatible/more-compatible ratios, i.e., Th/U and Lu/Hf (Fig. 10a). These features are typical of a coupled-interface dissolution-reprecipitation recrystallization mechanism involving expulsion of non-ideal solid solutions (i.e. Th via thorite) and incompatible components (e.g. Geisler et al., 2007). In most natural systems, zircon contains five main tetragonal solid-solution end-members that are related by substitution of Hf^{+4} (hafnon), Th^{+4} (thorite or huttonite), or U^{+4} (coffinite) for Zr^{+4}, or the coupled substitution of Y^{+3} or REE^{+3} for Zr^{+4} and P^{+5} for Si^{+4} (xenotime) (Speer 1980; Hoskin and Schaltegger 2003; Forster 2006). Owing to the near identical chemical properties of Zr^{+4} and Hf^{+4}, Hafnon and Zircon form a complete solid-solution (e.g. Ramakrishnan et al., 1969), while REE, Th^{+4} and U^{+4} have limited

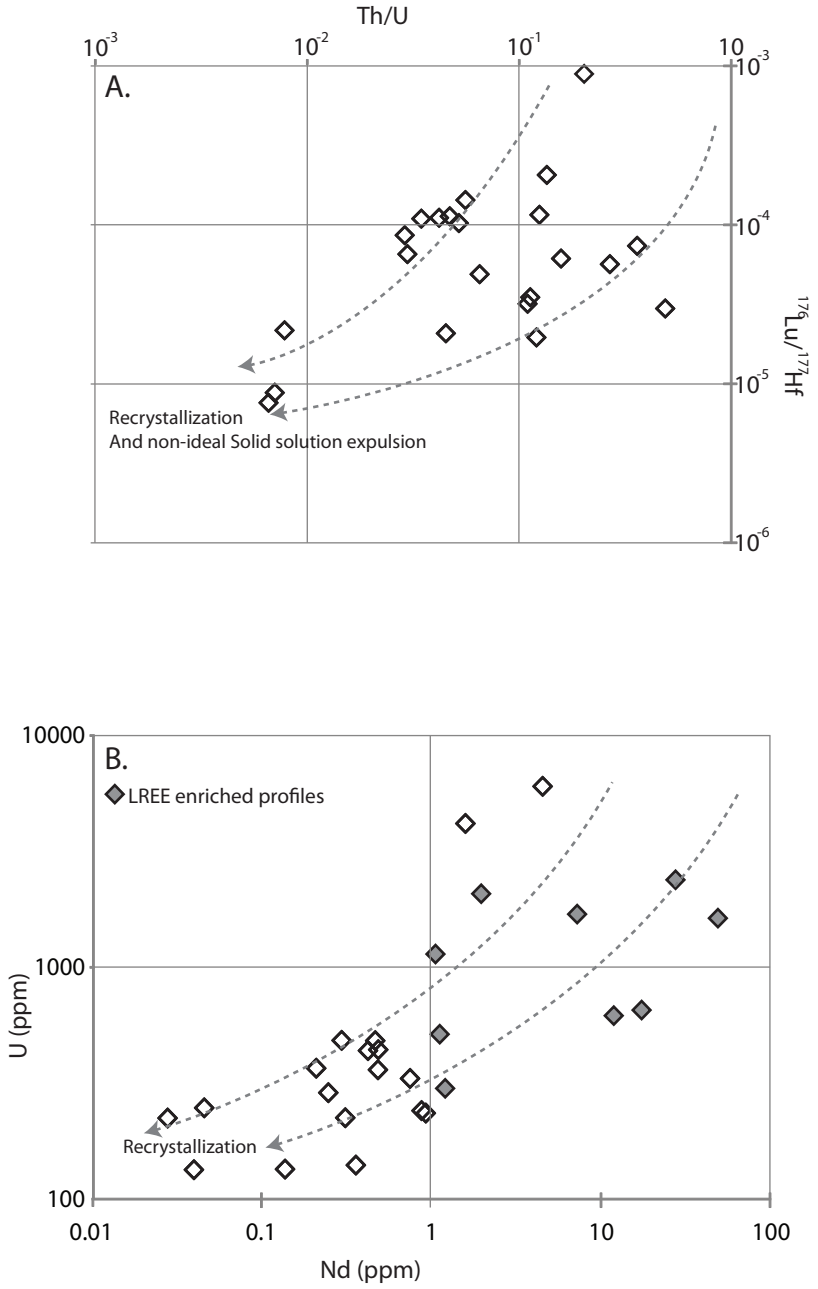

Figure. 10. (a) Plot of zircon Th/U ratio vs.$^{176}Lu/^{177}Hf$ ratio. (b) Plot of zircon U vs. Nd.

solubilities in zircon due to non-ideal solid solution effects (see reviews in Hoskin and Schaltegger 2003; Ferris et al., 2010). In the presence of a hydrothermal fluid catalyst, a zircon grain whose solubility has been enhanced through prior incorporation of these non-ideal solid-solution end-members will follow a recrystallization path involving either whole and/or partial dissolution followed by subsequent precipitation of an ideal solid-solution (e.g. Tomaschek et al, 2003; Geisler et al., 2007; Rubatto et al., 2008) that has a lower Gibbs free energy and is therefore more thermodynamically stable under the conditions of reaction (e.g. Prieto; 2009; Xia et al., 2009; Pollok et al., 2011). The expulsion of incompatible elements, development of inwardly penetrating reaction fronts now visible as arrested reaction fronts that were migrating toward grain interiors, and Th and U rich inclusions formed during this replacement process have been observed in natural samples and experimental charges (see summary in Tomaschek et al., 2003; Geisler et al., 2007; Rubatto et al., 2008; Soman et al., 2010).

In contrast to the behavior of trace elements that are incompatible in zircon during recrystallization, the original Hf isotope composition is preserved because Hf is so compatible in zircon, i.e., the zircon-hafnon solid solution is close to ideal (Förster 2006; Ferriss et al., 2010). What remains unclear is the fate of incompatible trace-element components liberated from the zircon lattice during dissolution-reprecipitation recrystallization. Similar to other reports (i.e. Tomaschek et al, 2003; Geisler et al., 2007; Rubatto et al., 2008), we observe zircon grains containing numerous micro-inclusions (Fig. 4b I) that may have formed during coupled dissolution-reprecipitation. We also observe a number of zircon grain BSE images which display 10-40 μm diameter Th and U silicate inclusions that may represent an arrested state of sub-solidus separation from the enclosing zircon grain, and are connected to the surface of the zircon grain via cracks and fractures (Fig. 4b. C-E).

8.2.3. Hydro-geodynamics and the role of zircon:

The large spread in zircon U-Pb dates in sample CTF-1 supports a process involving a highly spatially-limited and low-volume fluid or molecular water component associated with individual hydrous grain breakdown or fluid infiltration during metamorphism. The 210 Ma peak in U-Pb dates likely corresponds to a peak in fluid production during retrograde metamorphism that catalyzed zircon recrystallization.

A limitation, however, to using zircon dates from metamorphic rocks to reconstruct hydrologic processes during deep continental subduction is that without information about the pressure-temperature conditions at which recrystallization occurred, and recognizing that recrystallization may occur over wide ranges of P and T, its identification does not independently constrain the conditions at which fluids were present, an issue similar to that recently discussed by Sheng et al (2011). Furthermore, for zircon grains from our sample upon which only one analysis could be performed, there appear no clear [geochemical boundaries?] between the proposed end-member mechanisms of recrystallization. A moderately positive correlation observed for plots of Th/U vs. $^{176}Lu/^{177}Hf$ and Log[U] vs. Log[Nd] (Fig. 10ab) suggests a single recrystallization process where Th and Lu are fractionated from U and Hf, respectively.

8.3. U-Pb and Lu-Hf zircon constraints on the Dabie Orogen Architecture.

In a recent reevaluation of the pre-subduction crustal structure Zhao et al. (2008) presented zircon U-Pb and Lu-Hf isotopic data for a number of samples collected throughout the NDC and proposed the occurrence of two crustal layers. The first layer, which outcrops dominantly in the Northern portion of the NDC, is dominated by Triassic U-Pb metamorphic ages and Palaeoproterozoic Lu-Hf crustal ages. The second and lower layer outcrops dominantly in

the southern portion of the NDC (i.e. includes the towns of Macheng and Luotian: Fig. 1), and yields Cretaceous U-Pb metamorphic ages and Neo- to Mesoproterozoic crustal ages (Zhao et al., 2008; Liu et al., 2011a). Cretaceous granitoids are voluminous in the NDC and thought to be sourced from the lower-most crustal basement, which has an Archaean to Palaeoproterozoic Hf isotope composition (Nengzhong and Wu 2008; Zhao et al., 2011). Overlying all these layers is the CDZ, proposed to represent the mid-upper portion of the crust that is dominated by Neo- to Mesoproterozoic crust that experienced Triassic UHPM.

Zhao et al., (2008) and Zhao et al., (2011) favor an interpretation that the diachronous T[Hf]DM age distribution between the CDZ and northern NDC resulted from an initial vertically and chronologically stratified crustal architecture, and that both terranes experienced UHP metamorphism during continental subduction. To accommodate UHPM in the NDC, they suggested that the continental crust did not remain a single coherent unit, as in the case presented by Bryant et al. (2004). Rather, the middle (i.e. NDC) and upper (i.e. CDZ) crust layers detached from the lower crust at HPM conditions during subduction (e.g. Tang et al., 2006; Liu et al., 2007a; Zhao et al., 2008; Liu and Li 2008; Liu et al., 2011a). This lower-crustal detachment allowed the middle and upper crust to continue subducting to UHPM conditions. At peak UHPM conditions, the middle (NDC) and upper (CDZ) crust detached from one another, leading to a retrograde amphibolite exhumation path for the CDZ (Fig. 9), and a granulite to amphibolite exhumation path for the NDC.

While these newer models provide an explanation for the development of UHPM in the NDC (although as discussed previously, the evidence for this is very weak), a fundamental issue that remains unclear is what forces were driving continental subduction of the middle and upper crust after they detached from the lower crust. Detachment occurs when the buoyancy of low-

density felsic crust exceeds the tensile strength of the crust. Subduction of continental crust would not continue after detachment; only denser mafic lithologies would continue to be subducted. This becomes particularly difficult to understand when considering that according to the model of Zhao et al. (2008) the lower crust does not undergo UHPM, despite its juxtaposition between the lithospheric mantle and NDC, which are both subducting to UHPM conditions (Zhao et al., 2008).

Further, while it is thought that zircon U-Pb Triassic ages and Paleoproterozoic T[Hf]DM ages are limited to the northern border of the NDC, while zircon U-Pb Cretaceous ages and Neo- to Mesoproterozoic T[Hf]DM ages are characteristic of the southern NDC and CDZ (e.g. Zhao et al., 2008), our sample from the southern NDC contains Triassic to Jurassic zircon U-Pb dates (Fig. 5b) and a dominant Mesoproterozoic T[Hf]DM age peak, making it unclear which terrain to assign our sample based on zircon analyses (Fig. 7c). Xie et al. (2010) try to reconcile similar discrepancies by proposing that the Luotian dome contains an erosional remnant of the CDZ preserved in the NDC. If the Luotian Dome is indeed a deeply eroded structural dome, it is would seem impossible for it to contain erosional remnants of the stratigraphically overriding CDZ while other regions of the NDC exposed in areas outside the dome that are less deeply eroded do not. In this regard we see no reason why our sample is not part of the NDC and present a simpler model (Fig. 11) that does not require detachment of crustal layers prior to exhumation or unexposed lower-crustal tectonic slices as sources for Cretaceous granitoids (e.g. Zhao et al,. 2008; Liu et al., 2011a).

8.3.1 Geodynamic evolution of the Dabie orogen:

As previously discussed, there exists no clear evidence of Triassic UHPM in the NDC and on this basis we propose a model, which is an extension of that developed by Bryant et al.

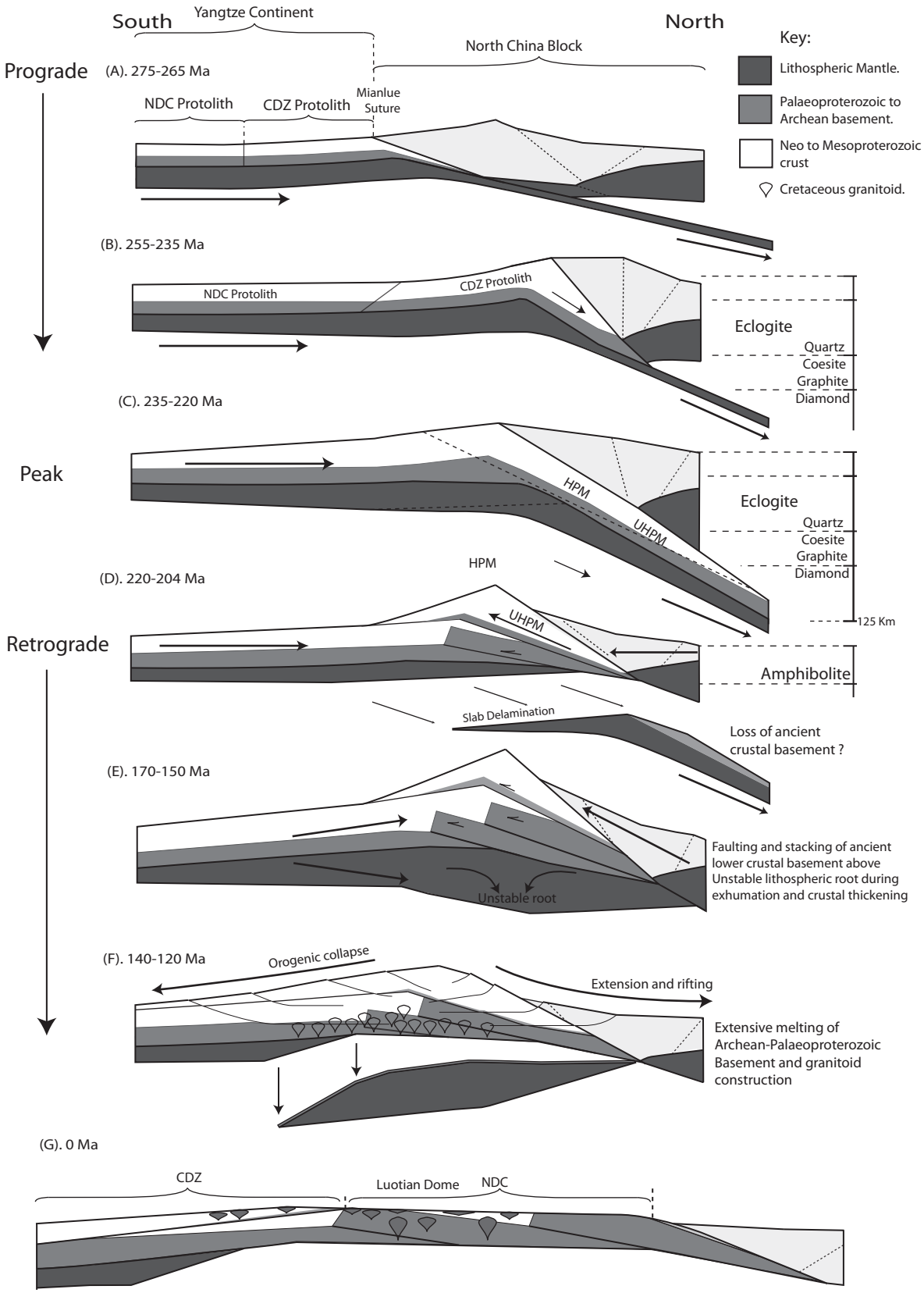

Figure. 11. (a-g) Tectonic evolution of the Dabie Orogen. After Bryant et al., (2004). See text for description.

(2004) and shows that with a simple pre-subduction chronologically stratified (top to bottom, young to old) Hf isotope crustal structure, as proposed by Zhao et al. (2008) and Zhao and Zheng (2009) (Fig. 11a), it is possible to produce the observed Hf isotope distribution (Fig. 11a-g) described by Zhao et al., (2008).

During subduction, the CDZ was situated north of the NDC and formed the leading edge of the slab that reached UHPM conditions c. 235-220 Ma (Fig. 11a-c). Following peak UHPM, the CDZ detached from the subducting slab and was rapidly exhumed and thrust over the NDC (Fig. 11d), which had only attained HP conditions, and the two began to exhume to shallower levels in the crust c. 220-204 Ma. Continental convergence and crustal thickening continued up until c. 140 Ma (Fig. 11d-e), after which orogenic collapse and lithospheric mantle delamination led to extension and input of heat into the lower crust (Fig. 11.f). This stage of crustal heating led to extensive crustal melting and granitoid construction in the NDC. The current crustal architecture of the Dabie orogen (Fig. 11g) represents the uplifted and eroded roots of this orogenic system, exposing crustal sections at the earth's surface with different Hf isotopic compositions, as represented by our sample and those reported by others (i.e. Zheng et al., 2006; Zhao et al., 2008).

9. Summary and conclusions:

Our sample from the Luotian dome has a tonalitic whole-rock geochemical composition typical of other orthogneisses in the NDC and throughout the Dabie orogen. A Palaeoproterozoic bulk-rock T[Nd]DM model age of 2.1 Ga, and Palaeo- to Mesoproterozoic 1.85-1.2 Ga distribution in zircon T[Hf]DM model ages, is consistent with the prevailing estimates of timing

of basement construction and cratonization recorded in the Yangtze craton (Zhao et al., 2008; Xiong et al., 2009).

While zircon Hf isotope heterogeneity may be attributed to crustal hybridization between Palaeo- to Neoproterozoic sources (implying a Neoproterozoic protolith age), we prefer an internal recycling of Hf involving breakdown of a phase with a Lu/Hf ratio~>1 such as garnet and incorporation of radiogenic Hf into newly grown zircon (implying a Paleoproterozoic protolith age).

Although depleted-mantle melting model ages (T[Nd]DM and T[Hf]DM) are all Proterozoic, zircon grains from our sample display no U-Pb dates greater than 309 Ma or Pb-Pb dates that exceed 420 Ma, suggesting either zircon was not present until the Phanerozoic, or Mesozoic metamorphism caused complete resetting of the zircon U-Pb system.

Zircon grains in our sample record the protracted Mesozoic prograde, peak, and retrograde evolution of the Dabie orogen and continental subduction of the Northern Yangtze continental margin. Within our zircon population, older analyses (i.e. U-Pb >234 Ma) contain the majority of elevated Th and U concentrations (up to 6000 ppm U), with a number of domains displaying flat to concave upwards M-HREE profiles and LREE contents up to 30 times chondrite. These features potentially suggest growth in equilibrium with garnet (to suppress the M-HREE REE-profile gradient: Fig. 6a), during either a prior stage of high-pressure crustal metamorphism or prograde continental subduction, and mixed analyses involving titanite inclusions that contain high levels of L-MREE. For the remaining zircon population, their U-Pb dates, Lu-Hf composition and REE profiles record a response to metamorphism involving fluid catalyzed in-situ recrystallization reactions and expulsion of incompatible geochemical components (i.e. Pb, LREE) and non-ideal solid-solutions (i.e. thorite). A U-Pb age peak at 210 Ma supports this to

have occurred largely during retrograde metamorphism associated with fluid-redistribution or infiltration during amphibolitization.

We favor the NDC to have experienced only high-pressure and retrograde-amphibolite metamorphism during continental subduction-exhumation, and show the spread in T[Hf]DM ages for our and other zircon studies across the Dabie orogen can be explained without invoking UHPM for the NDC and are unlikely to provide important constraints upon the geodynamic evolution of the Dabie orogen without a clear understanding of the pre-subduction crustal structure.

10. References:

Ames, L., Gaozhi, Z., & Baocheng, X., 1996. Geochronology and isotopic character of ultrahigh-pressure metamorphism with implications for collision of the Sino-Korean and Yangtze cratons, central China. Tectonics 15, 472-489.

Andersen, T., 2002. Correction of common lead in U-Pb analyses that do not report 204Pb. Chemical Geology, 192, 59-79.

Ayers, J.C., De La Cruz, K., Miller, C., & Switzer, O., 2003. Experimental study of zircon coarsening in quartzite +/- H2O at 1.0 GPa and 1000 degrees C, with implications for geochronological studies of high-grade metamorphism. American Mineralogist, 88, 365-376.

Ayers, J.C., Dunkle, S., Gao, S., & Miller, C.F., 2002. Constraints on timing of peak and retrograde metamorphism in the Dabie Shan Ultrahigh-Pressure Metamorphic Belt, east-central China, using U-Th-Pb dating of zircon and monazite. Chemical Geology, 186, 315-331.

Ayers, J.C., & Watson, E.B., 1991. Solubility Of Apatite, Monazite, Zircon, And Rutile In Supercritical Aqueous Fluids With Implications For Subduction Zone Geochemistry. Philosophical Transactions Of The Royal Society Of London Series A-Mathematical Physical And Engineering Sciences, 335, 365-375.

Barker, F.,1979. Trondhjemite: definition, environment and hypotheses of origin. In: Trondhjemites, Dacites and Related Rocks (ed. Barker, F.), pp. 1–12. Elsevier, Amsterdam.

Barth, M.G., McDonough, & W.F., Rudnick, R.L., 2000. Tracking the budget of Nb and Ta in the continental crust. Chemical Geology, 165, 197-213.

Belousova, E.A., Griffin, W.L., O'Reilly, S.Y., & Fisher, N.I., 2002. Igneous zircon: trace element composition as an indicator of source rock type. Contributions To Mineralogy And Petrology, 143, 602-622.

Bomparola, R.M., Ghezzo, C., Belousova, E., Griffin, W.L., & O'Reilly, S.Y., 2007. Resetting of the U–Pb Zircon System in Cambro-Ordovician Intrusives of the Deep Freeze Range, Northern Victoria Land, Antarctica. Journal of Petrology, 48, 327-364.

Bouvier, A., Vervoort, J.D., & Patchett, P.J., 2008. The Lu-Hf and Sm-Nd isotopic composition of CHUR: Constraints from unequilibrated chondrites and implications for the bulk composition of terrestrial planets. Earth and Planetary Science Letters, 273, 48-57.

Breeding, C.M., Ague, J.J., Grove, M., & Rupke, A.L., 2004. Isotopic and chemical alteration of zircon by metamorphic fluids: U-Pb age depth-profiling of zircon crystals from Barrow's garnet zone, northeast Scotland. American Mineralogist, 89, 1067-1077.

Bryant, D.L., Ayers, J.C., Gao, S., Miller, C.F., & Zhang, H., 2004. Geochemical, age, and isotopic constraints on the location of the Sino Korean/Yangtze Suture and evolution of the Northern Dabie Complex, east central China. Geological Society of America Bulletin, 116, 698-717.

Carlson, W.D., 2010. Dependence of reaction kinetics on H(2)O activity as inferred from rates of intergranular diffusion of aluminium. Journal of Metamorphic Geology. 28, 735-752.

Carson, C.J., Ague, J.J., Grove, M., Coath, C.D., & Harrison, T.M., 2002. U-Pb isotopic behaviour of zircon during upper-amphibolite facies fluid infiltration in the Napier Complex, east Antarctica. Earth and Planetary Science Letters, 199, 287-310.

Chen, B., Jahn, B.M., & Wei, C.J., 2002. Petrogenesis of Mesozoic granitoids in the dabie UHP complex, central china: trace element and Nd-Sr isotope evidence. Lithos, 60, 67-88.

Chen, J.F., & Jahn, B.M., 1998. Crustal evolution of southeastern China: Nd and Sr isotopic evidence. Tectonophysics, 284, 101-133.

Chen, R.-X., Zheng, Y.-F., & Xie, L., 2010. Metamorphic growth and recrystallization of zircon: Distinction by simultaneous in-situ analyses of trace elements, U-Th-Pb and Lu-Hf isotopes in zircons from eclogite-facies rocks in the Sulu orogen. Lithos, 114, 132-154.

Cherniak, D.J., 2010. Diffusion in Accessory Minerals Zircon, Titanite, Apatite, Monazite and Xenotime, in: Diffusion in Minerals and Melts (eds. Zhang, Y.X. & Cherniak, D.J.) pp. 827-869. Mineralogical Society of America, Saint Louis, Mo.

Cherniak, D.J., Hanchar, J.M., & Watson, E.B., 1997. Diffusion of tetravalent cations in zircon. Contributions To Mineralogy And Petrology, 127, 383-390.

Cherniak, D.J., & Watson, E.B., 2001. Pb diffusion in zircon. Chemical Geology, 172, 5-24.

Cherniak, D.J., & Watson, E.B., 2003. Diffusion in zircon, In: Zircon - Reviews in Mineralogy and Geochemistry (eds. Hanchar, J.M., & Hoskin, P.W.O.), pp. 113-143. Mineralogical Society of America, Saint Louis, Mo.

Chu, N.-C., Taylor, R.N., Chavagnac, V., Nesbitt, R.W., Boella, R.M., Milton, J.A., German, C.R., Bayon, G., & Burton, K., 2002. Hf isotope ratio analysis using multi-collector inductively coupled plasma mass spectrometry: an evaluation of isobaric interference corrections. Journal of Analytical Atomic Spectrometry, 17, 1567-1574.

Colombini, L., Miller, C., Gualda, G., Wooden, J., & Miller, J., 2011. Sphene and zircon in the Highland Range volcanic sequence (Miocene, southern Nevada, USA): elemental partitioning, phase relations, and influence on evolution of silicic magma. Contributions to Mineralogy And Petrology, 102, 29-50.

Condie, K.C., Belousova, E., Griffin, W.L., & Sircombe, K.N., 2009. Granitoid events in space and time: Constraints from igneous and detrital zircon age spectra. Gondwana Research, 15, 228-242.

Condie, K.C., Bickford, M.E., Aster, R.C., Belousova, E., & Scholl, D.W., 2011. Episodic zircon ages, Hf isotopic composition, and the preservation rate of continental crust. Geological Society of America Bulletin, 123, 951-957.

Davis, D.W., & Krogh, T.E., 2001. Preferential dissolution of 234U and radiogenic Pb from [alpha]-recoil-damaged lattice sites in zircon: implications for thermal histories and Pb isotopic fractionation in the near surface environment. Chemical Geology, 172, 41-58.

Davis, D.W., Krogh, T.E., & Williams, I.S., 2003. Historical Development of Zircon Geochronology. Reviews in Mineralogy and Geochemistry, 53, 145-181.

Dostal, J., & Chatterjee, A.K., 2000. Contrasting behaviour of Nb/Ta and Zr/Hf ratios in a peraluminous granitic pluton (Nova Scotia, Canada). Chemical Geology, 163, 207-218.

Farges, F., 1996. Does Zr-F ''complexation'' occur in magmas? Chemical Geology, 127, 253-268.

Elliott, T., Plank, T., Zindler, A., White, W., & Bourdon, B., 1997. Element transport from slab to volcanic front at the Mariana arc. Journal of Geophysical Research, 102, 14991-15019.

Ferriss, E.D.A., Ewing, R.C., & Becker, U., 2010. Simulation of thermodynamic mixing properties of actinide-containing zircon solid solutions. American Mineralogist, 95, 229-241.

Förster, H.J., 2006. Composition and origin of intermediate solid solutions in the system thorite-xenotime-zircon-coffinite. Lithos, 88, 35-55.

Frost, B.R., Barnes, C.G., Collins, W.J., Arculus, R.J., Ellis, D.J., & Frost, C.D., 2001. A Geochemical Classification for Granitic Rocks. Journal of Petrology, 42, 2033-2048.

Geisler, T., Pidgeon, R.T., Kurtz, R., van Bronswijk, W., & Schleicher, H., 2003a. Experimental hydrothermal alteration of partially metamict zircon. American Mineralogist, 88, 1496-1513.

Geisler, T., Rashwan, A.A., Rahn, M.K.W., Poller, U., Zwingmann, H., Pidgeon, R.T., Schleicher, H., & Tomaschek, F., 2003b. Low-temperature hydrothermal alteration of natural metamict zircons from the Eastern Desert, Egypt. Mineralogical Magazine, 67, 485-508.

Geisler, T., Schaltegger, U., & Tomaschek, F., 2007. Re-equilibration of zircon in aqueous fluids and melts. Elements, 3, 43-50.

Gerdes, A., & Zeh, A., 2009. Zircon formation versus zircon alteration -- New insights from combined U-Pb and Lu-Hf in-situ LA-ICP-MS analyses, and consequences for the interpretation of Archean zircon from the Central Zone of the Limpopo Belt. Chemical Geology, 261, 230-243.

Green, T.H., 1995. Significance of Nb/Ta as an indicator of geochemical processes in the crust--mantle system. Chemical Geology, 120, 347-359.

Hacker, B.R., Ratschbacher, L., Webb, L., Ireland, T., Walker, D., & Shuwen, D., 1998. U/Pb zircon ages constrain the architecture of the ultrahigh-pressure Qinling-Dabie Orogen, China. Earth and Planetary Science Letters, 161, 215-230.

Hacker, B.R., Wallis, S.R., Ratschbacher, L., Grove, M., & Gehrels, G., 2006. High-temperature geochronology constraints on the tectonic history and architecture of the ultrahigh-pressure Dabie-Sulu Orogen. Tectonics, 25. TC5006.

Hanchar, J.M., & Watson, E.B., 2003. Zircon saturation thermometry. In: Zircon - Reviews in Mineralogy and Geochemistry (eds. Hanchar, J.M., & Hoskin, P.W.O.), pp. 89-112. Mineralogical Society of America, Saint Louis, Mo.

Hermann, J., & Rubatto, D., 2003. Relating zircon and monazite domains to garnet growth zones: age and duration of granulite facies metamorphism in the Val Malenco lower crust. Journal of Metamorphic Geology. 21, 833-852.

Hart, S.R., Blusztajn, J., Dick, H.J.B., Meyer, P.S., & Muehlenbachs, K., 1999. The fingerprint of seawater circulation in a 500-meter section of ocean crust gabbros. Geochimica et Cosmochimica Acta, 63, 4059-4080.

He, Y., Li, S., Hoefs, J., Huang, F., Liu, S.-A., & Hou, Z., 2011. Post-collisional granitoids from the Dabie orogen: New evidence for partial melting of a thickened continental crust. Geochimica et Cosmochimica Acta, 75, 3815-3838.

Hofmann, A.W., 1988. Chemical differentiation of the Earth: the relationship between mantle, continental crust, and oceanic crust. Earth and Planetary Science Letters, 90, 297-314.

Hoskin, P.W.O., & Black, L.P., 2000. Metamorphic zircon formation by solid-state recrystallization of protolith igneous zircon. Journal of Metamorphic Geology, 18, 423-439.

Hoskin, P.W.O., & Schaltegger, U., 2003. The composition of zircon and igneous and metamorphic petrogenesis, In: Zircon - Reviews in Mineralogy and Geochemistry (eds. Hanchar, J.M., & Hoskin, P.W.O.), pp. 27-62. Mineralogical Society of America, Saint Louis, Mo.

Huang, J., Zheng, Y.-F., Zhao, Z.-F., Wu, Y.-B., Zhou, H.-B., & Liu, X., 2006. Melting of subducted continent: Element and isotopic evidence for a genetic relationship between Neoproterozoic and Mesozoic granitoids in the Sulu orogen. Chemical Geology, 229, 227-256.

Huang, X.-L., Xu, Y.-G., Li, X.-H., Li, W.-X., Lan, J.-B., Zhang, H.-H., Liu, Y.-S., Wang, Y.-B., Li, H.-Y., Luo, Z.-Y., & Yang, Q.-J., 2008. Petrogenesis and tectonic implications of Neoproterozoic, highly fractionated A-type granites from Mianning, South China. Precambrian Research, 165, 190-204.

Iizuka, T., & Hirata, T., 2005. Improvements of precision and accuracy in in situ Hf isotope microanalysis of zircon using the laser ablation-MC-ICPMS technique. Chemical Geology, 220, 121-137.

Ishizuka, O., Kimura, J.-I., Li, Y.B., Stern, R.J., Reagan, M.K., Taylor, R.N., Ohara, Y., Bloomer, S.H., Ishii, T., Hargrove Iii, U.S., & Haraguchi, S., 2006. Early stages in the evolution of Izu–Bonin arc volcanism: New age, chemical, and isotopic constraints. Earth and Planetary Science Letters, 250, 385-401.

Kemp, A.I.S., Wormald, R.J., Whitehouse, M.J., & Price, R.C., 2005. Hf isotopes in zircon reveal contrasting sources and crystallization histories for alkaline to peralkaline granites of Temora, southeastern Australia. Geology, 33, 797-800.

Kimura, J.-I., Yoshida, T., & Iizumi, S., 2002. Origin of Low-K Intermediate Lavas at Nekoma Volcano, NE Honshu Arc, Japan: Geochemical Constraints for Lower-Crustal Melts. Journal of Petrology, 43, 631-661.

Koons, P.O., & Thompson, A.B., 1985. Non-mafic rocks in the greenschist, blueschist and eclogite facies. Chemical Geology, 50, 3-30.

Li, S.G., Xiao, Y.L., Liou, D.L., Chen, Y.Z., Ge, N.J., Zhang, Z.Q., Sun, S.S., Cong, B.L., Zhang, R.Y., Hart, S.R., & Wang, S.S., 1993. Collision of the North China and Yangtze blocks and formation of coesite-bearing eclogites: Timing and processes. Chemical Geology, 109, 89-111.

Li, X.-H., Li, Z.-X., Ge, W., Zhou, H., Li, W., Liu, Y., & Wingate, M.T.D., 2003. Neoproterozoic granitoids in South China: crustal melting above a mantle plume at ca. 825 Ma? Precambrian Research, 122, 45-83.

Linnen, R.L., 1998. The solubility of Nb-Ta-Zr-Hf-W in granitic melts with Li and Li+F: Constraints for mineralization in rare metal granites and pegmatites. Economic Geology and The Bulletin Of The Society Of Economic Geologists, 93, 1013-1025.

Liou, J.G., Ernst, W.G., Zhang, R.Y., Tsujimori, T., & Jahn, B.M., 2009. Ultrahigh-pressure minerals and metamorphic terranes – The view from China. Journal of Asian Earth Sciences, 35, 199-231.

Liu, F.L., & Liou, J.G., 2011. Zircon as the best mineral for P-T-time history of UHP metamorphism: A review on mineral inclusions and U-Pb SHRIMP ages of zircons from the Dabie-Sulu UHP rocks. Journal of Asian Earth Sciences, 40, 1-39.

Liu, J., Ye, K., Cong, B., Shegnori, M., & Fan, H., 2001. Coesite inclusions in zircon from gneisses identified by laser Raman microspectrometer in ultrahigh pressure zone of Dabie Mountains, China. China Science Bulletin, 46, 1912-1916.

Liu, F.L., Xu, Z.Q., Liou, J.G., Katayama, I., Masago, H., Maruyama, S., & Yang, J.S., 2002. Ultrahigh-pressure mineral inclusions in zircons from gneissic core samples of the Chinese Continental Scientific Drilling Site in eastern China. European Journal of Mineralogy, 14, 499-512.

Liu, Y.-C., Li, S.-G., & Xu, S.-T., 2007a. Zircon SHRIMP U-Pb dating for gneisses in northern Dabie high T/P metamorphic zone, central China: Implications for decoupling within subducted continental crust. Lithos, 96, 170-185.

Liu, Y.C., Li, S.G., Gu, X.F., Xu, S.T., & Chen, G.B., 2007b. Ultrahigh-pressure eclogite transformed from mafic granulite in the Dabie orogen, east-central China. Journal of Metamorphic Geology, 25, 975-989.

Liu, Y.C., Li, S.G., Xu, S.T., Jahn, B.M., Zheng, Y.F., Zhang, Z.Q., Jiang, L.L., Chen, G.B., & Wu, W.P., 2005. Geochemistry and geochronology of eclogites from the northern Dabie Mountains, central China. Journal of Asian Earth Sciences, 25, 431-443.

Liu, Y.-C., Gu, X.-F., Li, S.-G., Hou, Z.-H., & Song, B., 2011a. Multistage metamorphic events in granulitized eclogites from the North Dabie complex zone, central China: Evidence from zircon U-Pb age, trace element and mineral inclusion. Lithos, 122, 107-121.

Liu, Y.-C., Gu, X.-F., Rolfo, F., & Chen, Z.-Y., 2011b. Ultrahigh-pressure metamorphism and multistage exhumation of eclogite of the Luotian dome, North Dabie Complex Zone (central China): Evidence from mineral inclusions and decompression textures. Journal of Asian Earth Sciences, 42, 607-617.

Ludwig, K.R., 2003. User's manual for Isoplot 3.00. A geochronological Toolkit for Microsoft Excel. Berkeley Geochronology Center, Berkeley, California.

Lugmair, G.W., & Marti, K., 1978. Lunar initial 143Nd/144Nd: Differential evolution of the lunar crust and mantle. Earth and Planetary Science Letters, 39, 349-357.

Ma, C., Ehlers, C., Xu, C., Li, Z., & Yang, K., 2000. The roots of the Dabieshan ultrahigh-pressure metamorphic terrane: constraints from geochemistry and Nd-Sr isotope systematics. Precambrian Research, 102, 279-301.

Malaspina, N., Hermann, J., Scambelluri, M., & Compagnoni, R., 2006. Multistage metasomatism in ultrahigh-pressure mafic rocks from the North Dabie Complex (China). Lithos, 90, 19-42.

Maniar, P.D., & Piccoli, P.M., 1989. Tectonic discrimination of granitoids. Geological Society of America Bulletin, 101, 635-643.

Manning, C.E., 2004. The chemistry of subduction-zone fluids. Earth and Planetary Science Letters, 223, 1-16.

Martin, L.A.J., Duchêne, S., Deloule, E., & Vanderhaeghe, O., 2008. Mobility of trace elements and oxygen in zircon during metamorphism: Consequences for geochemical tracing. Earth and Planetary Science Letters, 267, 161-174.

McLaren, A.C., Gerald, J.D.F., & Williams, I.S., 1994. The microstructure of zircon and its influence on the age determination from Pb/U isotopic ratios measured by ion microprobe. Geochimica et Cosmochimica Acta, 58, 993-1005.

Mezger, K., & Krogstad, E.J., 1997. Interpretation of discordant U-Pb zircon ages: An evaluation. Journal of Metamorphic Geology, 15, 127-140.

Miller, C.F., Watson, E.B., & Harrison, T.M., 1988, Perspectives on the source, segregation, and transport of granitoid magmas. Transactions of the Royal Society of Edinburgh, 79, 135-156

Nasdala, L., Wenzel, M., Vavra, G., Irmer, G., Wenzel, T., & Kober, B., 2001. Metamictisation of natural zircon: accumulation versus thermal annealing of radioactivity-induced damage. Contributions to Mineralogy and Petrology, 141, 125-144.

Nengzhong, L., & Wu, Y. B., 2008. Zircon U-Pb Age, Trace Element, and Hf Isotope Evidence for Paleoproterozoic Granulite-Facies Metamorphism and Archean Crustal Remnant in the Dabie Orogen. Journal of China University of Geosciences, 19, 110-134.

Niu, Y., Collerson, K.D., Batiza, R., Wendt, J.I., & Regelous, M., 1999. Origin of enriched-type mid-ocean ridge basalt at ridges far from mantle plumes: The East Pacific Rise at 11°20'N. Journal of Geophysical Research. 104, 7067-7087.

Okay, A.I., Xu, S.T., & Sengor, A.M.C., 1989. Coesite from The Dabie Shan Eclogites, Central China. European Journal of Mineralogy, 1, 595-598.

Parrish, R.R., & Noble, S.R., 2003. Zircon U-Th-Pb Geochronology by Isotope Dilution -- Thermal Ionization Mass Spectrometry (ID-TIMS). In: Zircon - Reviews in Mineralogy and Geochemistry (eds. Hanchar, J.M., & Hoskin, P.W.O.), pp. 183-213. Mineralogical Society of America, Saint Louis, Mo.

Pearce, J.A., Baker, P.E., Harvey, P.K., & Luff, I.W., 1995. Geochemical Evidence for Subduction Fluxes, Mantle Melting and Fractional Crystallization Beneath the South Sandwich Island Arc. Journal of Petrology, 36, 1073-1109.

Pollok, K., Putnis, C.V., & Putnis, A., 2011. Mineral replacement reactions in solid solution-aqueous solution systems: Volume changes, reactions paths and end-points using the example of model salt systems. American Journal of Science, 311, 211-236.

Prieto, M., 2009. Thermodynamics of Solid Solution-Aqueous Solution Systems. In. Thermodynamics and Kinetics of Water-Rock Interaction. Reviews in Mineralogy and Geochemistry (eds. Oelkers, E.H. & Schott, J.), pp 47-85. Mineralogical Society of America, Saint Louis, Mo.

Prowatke, S., & Klemme, S., 2006. Rare earth element partitioning between titanite and silicate melts: Henry's law revisited. Geochimica et Cosmochimica Acta, 70, 4997-5012.

Putnis, A., 2009. Mineral Replacement Reactions. In. Thermodynamics and Kinetics of Water-Rock Interaction. Reviews in Mineralogy and Geochemistry (eds. Oelkers, E.H. & Schott, J.), pp 87-124. Mineralogical Society of America, Saint Louis, Mo.

Qi, X., Zeng, L., Zhu, L., Hu, Z., & Hou, K., 2011. Zircon U-Pb and Lu-Hf isotopic systematics of the Daping plutonic rocks: Implications for the Neoproterozoic tectonic evolution of the northeastern margin of the Indochina block, Southwest China. Gondwana Research, 21, 180-193.

Raczek, I., Jochum, K.P., & Hofmann, A.W., 2003. Neodymium and Strontium Isotope Data for USGS Reference Materials BCR-1, BCR-2, BHVO-1, BHVO-2, AGV-1, AGV-2, GSP-1, GSP-2 and Eight MPI-DING Reference Glasses. Geostandards Newsletter, 27, 173-179.

Ramakrishnan, S.S., Gokhale, K.V.G.K., & Subbarao, E.C., 1969. Solid solubility in the system zircon - hafnon. Materials Research Bulletin, 4, 323-327.

Reddy, S.M., Timms, N.E., Trimby, P., Kinny, P.D., Buchan, C., & Blake, K., 2006. Crystal-plastic deformation of zircon: A defect in the assumption of chemical robustness. Geology, 34, 257-260.

Rollinson, H.R., 1993. Using Geochemical Data: Evaluation, Presentation, Interpretation. Longman Scientific and Technical, Essex, England

Rowley, D.B., Xue, F., Tucker, R.D., Peng, Z.X., Baker, J., & Davis, A., 1997. Ages of ultrahigh pressure metamorphism and protolith orthogneisses from the eastern Dabie Shan: U/Pb zircon geochronology. Earth and Planetary Science Letters, 151, 191-203.

Rubatto, D., 2002. Zircon trace element geochemistry: partitioning with garnet and the link between U-Pb ages and metamorphism. Chemical Geology, 184, 123-138.

Rubatto, D., & Hermann, J., 2003. Zircon formation during fluid circulation in eclogites (Monviso, Western Alps): Implications for Zr and Hf budget in subduction zones. Geochimica et Cosmochimica Acta, 67, 2173-2187.

Rubatto, D., & Hermann, J., 2007a. Zircon behaviour in deeply subducted rocks. Elements, 3, 31-35.

Rubatto, D., & Hermann, J., 2007b. Experimental zircon/melt and zircon/garnet trace element partitioning and implications for the geochronology of crustal rocks. Chemical Geology, 241, 38-61.

Rubatto, D., Muntener, O., Barnhoorn, A., & Gregory, C., 2008. Dissolution-reprecipitation of zircon at low-temperature, high-pressure conditions (Lanzo Massif, Italy). American Mineralogist, 93, 1519-1529.

Rubie, D.C., 1986. The catalysis of mineral reactions by water and restrictions on the presence of aqueous fluid during metamorphism. Mineralogical Magazine, 50, 399-415.

Rubin, J.N., Henry, C.D., & Price, J.G., 1993. The mobility of zirconium and other “immobile” elements during hydrothermal alteration. Chemical Geology, 110, 29-47.

Rudnick, R.L., Gao, S., Heinrich, D.H., & Karl, K.T., 2003. Composition of the Continental Crust, In. The Crust. Treatise on Geochemistry (ed. Rudnick, R.L.). pp. 1-64, Elsevier-Pergamon, Oxford.

Salje, E.K.H., & Zhang, M., 2006. Hydrous species in ceramics for the encapsulation of nuclear waste: OH in zircon. Journal of Physics: Condensed Matter, 18, L277-L281.

Scambelluri, M., & Philippot, P., 2001. Deep fluids in subduction zones. Lithos, 55, 213-227.

Sheng, Y.-M., Zheng, Y.-F., Chen, R.-X., Li, Q., & Dai, M., 2012, Fluid action on zircon growth and recrystallization during quartz veining within UHP eclogite: Insights from U–Pb ages, O–Hf isotopes and trace elements. Lithos. 136-139, 126-144.

Siebel, W., & Chen, F., 2010. Zircon Hf isotope perspective on the origin of granitic rocks from eastern Bavaria, SW Bohemian Massif. International Journal of Earth Sciences, 99, 993-1005.

Sinha, A.K., Wayne, D.M., & Hewitt, D.A., 1992. The Hydrothermal Stability Of Zircon - Preliminary Experimental And Isotopic Studies. Geochimica et Cosmochimica Acta, 56, 3551-3560.

Slama, J., Kosler, J., & Pedersen, R.B., 2007. Behaviour of zircon in high-grade metamorphic rocks: evidence from Hf isotopes, trace elements and textural studies. Contributions to Mineralogy and Petrology, 154, 335-356.

Söderlund, U., Patchett, P.J., Vervoort, J.D., & Isachsen, C.E., 2004. The 176Lu decay constant determined by Lu-Hf and U-Pb isotope systematics of Precambrian mafic intrusions. Earth and Planetary Science Letters, 219, 311-324.

Soman, A., Geisler, T., Tomaschek, F., Grange, M., & Berndt, J., 2010. Alteration of crystalline zircon solid solutions: a case study on zircon from an alkaline pegmatite from Zomba–Malosa, Malawi. Contributions to Mineralogy and Petrology, 160, 909-930.

Song, S.G., Zhang, L.F., Niu, Y.L., Su, L., Jian, P., & Liu, D.Y., 2005. Geochronology of diamond-bearing zircons from garnet peridotite in the North Qaidam UHPM belt, Northern Tibetan Plateau: A record of complex histories from oceanic lithosphere subduction to continental collision. Earth and Planetary Science Letters, 234, 99-118.

Speer, J.A., 1980. Zircon. Reviews in Mineralogy and Geochemistry, 5, 67-112.

Sun, S.-S., & McDonough, W.F., 1989. Chemical and isotopic systematics of oceanic basalts: implications for mantle composition and processes. Geological Society, London, Special Publications, 42, 313-345.

Tabata, H., Yamauchi, K., Maruyama, S., & Liou, J.G., 1998. Tracing the extent of a UHP metamorphic terrane: mineral-inclusion study of zircons in gneisses from the Dabieshan. In. When Continents Collide: Geodynamics and Geochemistry of Ultrahigh-Pressure Rocks (eds. Hacker, B.R., & Liou, J.G.), pp. 261–273. Kluwer Academic Publishers, Dordrecht.

Tang, J., Zheng, Y.-F., Wu, Y.-B., & Gong, B., 2006. Zircon SHRIMP U–Pb dating, C and O isotopes for impure marbles from the Jiaobei terrane in the Sulu orogen: Implication for tectonic affinity. Precambrian Research, 144, 1-18.

Tang, J., Zheng, Y.-F., Wu, Y.-B., Gong, B., Zha, X., & Liu, X., 2008. Zircon U-Pb age and geochemical constraints on the tectonic affinity of the Jiaodong terrane in the Sulu orogen, China. Precambrian Research, 161, 389-418.

Tatsumi, Y., & Eggins, S.M., 1995. Subduction Zone Magmatism. 211 pp. Blackwell, Cambridge.

Timms, N.E., Kinny, P.D., & Reddy, S.M., 2006. Enhanced diffusion of Uranium and Thorium linked to crystal plasticity in zircon. Geochemical Transactions, 7.

Tole, M.P., 1985. The Kinetics Of Dissolution Of Zircon (ZrSiO4). Geochimica et Cosmochimica Acta, 49, 453-458.

Tomaschek, F., Kennedy, A.K., Villa, I.M., Lagos, M., & Ballhaus, C., 2003. Zircons from Syros, Cyclades, Greece - Recrystallization and mobilization of zircon during high-pressure metamorphism. Journal of Petrology, 44, 1977-2002.

Tong, L., Jahn, B.-M., & Zheng, Y.-F., 2011. Diverse P-T paths of the northern Dabie complex in central China and its reworking in the early Cretaceous. Journal of Asian Earth Sciences, 42, 633-640.

Tsai, C.-H., & Liou, J.G., 2000. Eclogite-facies relics and inferred ultrahigh-pressure metamorphism in the North Dabie Complex, central-eastern China. American Mineralogist, 85, 1-8.

Vaczi, T., Nasdala, L., Wirth, R., Mehofer, M., Libowitzky, E., & Hager, T., 2009. On the breakdown of zircon upon "dry" thermal annealing. Contributions to Mineralogy and Petrology, 97, 129-138.

Valley, J., Lackey, J., Cavosie, A., Clechenko, C., Spicuzza, M., Basei, M., Bindeman, I., Ferreira, V., Sial, A., King, E., Peck, W., Sinha, A., & Wei, C., 2005. 4.4 billion years of crustal maturation: oxygen isotope ratios of magmatic zircon. Contributions to Mineralogy and Petrology, 150, 561-580.

Valley, P.M., Fisher, C.M., Hanchar, J.M., Lam, R., & Tubrett, M., 2010. Hafnium isotopes in zircon: A tracer of fluid-rock interaction during magnetite-apatite ("Kiruna-type") mineralization. Chemical Geology, 275, 208-220.

Van Lichtervelde, M., Holtz, F., & Hanchar, J.M., 2010. Solubility of manganotantalite, zircon and hafnon in highly fluxed peralkaline to peraluminous pegmatitic melts. Contributions to Mineralogy and Petrology, 160, 17-32.

Vervoort, J.D., & Blichert-Toft, J., 1999. Evolution of the depleted mantle: Hf isotope evidence from juvenile rocks through time. Geochimica et Cosmochimica Acta, 63, 533-556.

Wang, X.M., & Liou, J.G., 1991. Regional ultrahigh-pressure coesite-bearing eclogitic terrane in central China: Evidence from country rocks, gneiss, marble, and metapelite. Geology, 19, 933-936.

Wang, Q., Wyman, D.A., Xu, J.F., Jian, P., Zhao, Z.H., Li, C.F., Xu, W., Ma, J.L., & He, B., 2007. Early Cretaceous adakitic granites in the Northern Dabie Complex, central China: Implications for partial melting and delamination of thickened lower crust. Geochimica et Cosmochimica Acta, 71, 2609-2636.

Watson, E.B., Cherniak, D.J., Hanchar, J.M., Harrison, T.M., & Wark, D.A., 1997. The incorporation of Pb into zircon. Chemical Geology, 141, 19-31.

Watson, E.B., & Harrison, T.M., 2005. Zircon thermometer reveals minimum melting conditions on earliest Earth. Science, 308, 841-844.

Wiedenbeck, M., AllÉ, P., Corfu, F., Griffin, W.L., Meier, M., Oberli, F., Quadt, A.V., Roddick, J.C., & Spiegel, W., 1995. Three natural zircon standards for U–Th–Pb, Lu–Hf, trace element and REE analyses. Geostandards Newsletter, 19, 1-23.

Williams, I.S., Buick, I.S., & Cartwright, I., 1996. An extended episode of early Mesoproterozoic metamorphic fluid flow in the Reynolds Range, central Australia. Journal of Metamorphic Geology, 14, 29-47.

Woodhead, J., Hergt, J., Shelley, M., Eggins, S., & Kemp, R., 2004. Zircon Hf-isotope analysis with an excimer laser, depth profiling, ablation of complex geometries, and concomitant age estimation. Chemical Geology, 209, 121-135.

Wu, Y.B., Gao, S., Zhang, H.F., Yang, S.H., Liu, X.C., Jiao, W.F., Liu, Y.S., Yuan, H.L., Gong, H.J., & He, M.C., 2009. U-Pb age, trace-element, and Hf-isotope compositions of zircon in a quartz vein from eclogite in the western Dabie Mountains: Constraints on fluid flow during early exhumation of ultra high-pressure rocks. American Mineralogist, 94, 303-312.

Wu, Y.-B., Zheng, Y.-F., Zhao, Z.-F., Gong, B., Liu, X., & Wu, F.-Y., 2006. U-Pb, Hf and O isotope evidence for two episodes of fluid-assisted zircon growth in marble-hosted eclogites from the Dabie orogen. Geochimica et Cosmochimica Acta, 70, 3743-3761.

Xia, F., Brugger, J., Chen, G., Ngothai, Y., O'Neill, B., Putnis, A., Pring, A., 2009. Mechanism and kinetics of pseudomorphic mineral replacement reactions: A case study of the replacement of pentlandite by violarite. Geochimica et Cosmochimica Acta, 73, 1945-1969.

Xie, Z., Chen, J.F., & Cui, Y.R., 2010. Episodic growth of zircon in UHP orthogneisses from the North Dabie Terrane of east-central China: implications for crustal architecture of a collisional orogen. Journal of Metamorphic Geology, 28, 979-995.

Xiong, Q., Zheng, J., Yu, C., Su, Y., Tang, H., & Zhang, Z., 2009. Zircon U-Pb age and Hf isotope of Quanyishang A-type granite in Yichang: signification for the Yangtze continental cratonization in Paleoproterozoic. China Science Bulletin. 54, 436-446.

Xu, S., Liu, Y., Chen, G., Compagnoni, R., Rolfo, F., He, M., & Liu, H., 2003. New finding of micro-diamonds in eclogites from Dabie-Sulu region in central-eastern China. China Science Bulletin, 48, 988-994.

Xu, S.T., Liu, Y.C., Chen, G.B., Ji, S.Y., Ni, P., & Xiao, W.S., 2005. Microdiamonds, their classification and tectonic implications for the host eclogites from the Dabie and Su-Lu regions in central eastern China. Mineralogical Magazine, 69, 509-520.

Xu, S.T., Okay, A.I., Ji, S.Y., Sengor, A.M.C., Wen, S., Liu, Y.C., & Jiang, L.L., 1992. Diamond From The Dabie-Shan Metamorphic Rocks And Its Implication For Tectonic Setting. Science, 256, 80-82.

Ye, K., Yao, Y.P., Katayama, I., Cong, B.L., Wang, Q.C., & Maruyama, S., 2000. Large areal extent of ultrahigh-pressure metamorphism in the Sulu ultrahigh-pressure terrane of East China: new implications from coesite and omphacite inclusions in zircon of granitic gneiss. Lithos, 52, 157-164.

Yin, L., Pollard, P.J., Hu, S.X., & Taylor, R.G., 1995. Geologic and geochemical characteristics of the Yichun Ta-Nb-Li deposit, Jiangxi Province, South China. Economic Geology and The Bulletin Of The Society Of Economic Geologists, 90, 577-585.

Yuan, H., Gao, S., Liu, X., Li, H., Günther, D., Wu, F., 2004. Accurate U-Pb Age and Trace Element Determinations of Zircon by Laser Ablation-Inductively Coupled Plasma-Mass Spectrometry. Geostandards and Geoanalytical Research, 28, 353-370.

Yuan, H.-L., Gao, S., Dai, M.-N., Zong, C.-L., Günther, D., Fontaine, G.H., Liu, X.-M., & Diwu, C., 2008. Simultaneous determinations of U-Pb age, Hf isotopes and trace element compositions of zircon by excimer laser-ablation quadrupole and multiple-collector ICP-MS. Chemical Geology, 247, 100-118.

Zhang, H., Zhang, B., Zhong, Z., Gao, S., & Hu, S., 2000. Geochemistry of gneisses from Dabie complex and Tongbai complex in Qinling–Tongbai–Dabie orogenic Belt: implications for location of Yangtze–Sino-Korean suture. Journal of China University of Geosciences, 11, 392–405.

Zhang, H.F., Gao, S., Zhong, Z.Q., Zhang, B.R., Zhang, L., & Hu, S.H., 2002. Geochemical and Sr-Nd-Pb isotopic compositions of Cretaceous granitoids: constraints on tectonic framework and crustal structure of the Dabieshan ultrahigh-pres sure metamorphic belt, China. Chemical Geology, 186, 281-299.

Zhang, Z., Shen, K., Xiao, Y., Hoefs, J., & Liou, J.G., 2006a. Mineral and fluid inclusions in zircon of UHP metamorphic rocks from the CCSD-main drill hole: A record of metamorphism and fluid activity. Lithos, 92, 378-398.

Zhang, S.B., Zheng, Y.F., Wu, Y.B., Zhao, Z.F., Gao, S., & Wu, F.Y., 2006b. Zircon U-Pb age and Hf-O isotope evidence for Paleoproterozoic metamorphic event in South China. Precambrian Research, 151, 265-288.

Zhang, S.B., Zheng, Y.F., Zhao, Z.F., Wu, Y.B., Yuan, H.L., & Wu, F.Y., 2008. Neoproterozoic anatexis of Archean lithosphere: Geochemical evidence from felsic to mafic intrusions at Xiaofeng in the Yangtze Gorge, South China. Precambrian Research, 163, 210-238.

Zhang, R.Y., Liou, J.G., & Ernst, W.G., 2009. The Dabie-Sulu continental collision zone: A comprehensive review. Gondwana Research, 16, 1-26.

Zhao, Z., & Zheng, Y., 2009. Remelting of subducted continental lithosphere: Petrogenesis of Mesozoic magmatic rocks in the Dabie-Sulu orogenic belt. Science in China Series D: Earth Sciences, 52, 1295-1318.

Zhao, Z.F., Zheng, Y.F., Gao, T.S., Wu, Y.B., Chen, B., Chen, F.K., & Wu, F.Y., 2006. Isotopic constraints on age and duration of fluid-assisted high-pressure eclogite-facies recrystallization during exhumation of deeply subducted continental crust in the Sulu orogen. Journal of Metamorphic Geology, 24, 687-702.

Zhao, Z.F., Zheng, Y.F., Wei, C.S., & Wu, F.Y., 2011. Origin of postcollisional magmatic rocks in the Dabie orogen: Implications for crust-mantle interaction and crustal architecture. Lithos, 126, 99-114.

Zhao, Z.-F., Zheng, Y.-F., Wei, C.-S., Chen, F.-K., Liu, X., & Wu, F.-Y., 2008. Zircon U-Pb ages, Hf and O isotopes constrain the crustal architecture of the ultrahigh-pressure Dabie orogen in China. Chemical Geology, 253, 222-242.

Zheng, X., Jin, C., Zhai, M., & Shi, Y., 1999. Petrochemistry and tectonic background of the gray gneisses in north Dabie terrane (in Chinese with English abstract). Acta Petrologica Sinica, 15, 350–358.

Zheng, Y.F., Wu, Y.B., Chen, F.K., Gong, B., Li, L., & Zhao, Z.F., 2004. Zircon U-Pb and oxygen isotope evidence for a large-scale O-18 depletion event in igneous rocks during the Neoproterozoic. Geochimica et Cosmochimica Acta, 68, 4145-4165.

Zheng, Y.F., Gao, T.S., Wu, Y.B., Gong, B., & Liu, X.M., 2007. Fluid flow during exhumation of deeply subducted continental crust: zircon U-Pb age and O-isotope studies of a quartz vein within ultrahigh-pressure eclogite. Journal of Metamorphic Geology, 25, 267-283.

Zheng, Y.F., Zhao, Z.F., Wu, Y.B., Zhang, S.B., Liu, X.M., & Wu, F.Y., 2006. Zircon U-Pb age, Hf and O isotope constraints on protolith origin of ultrahigh-pressure eclogite and gneiss in the Dabie orogen. Chemical Geology, 231, 135-158.

CHAPTER IV

EXPERIMENTAL MEASUREMENT OF TRACE-ELEMENT PARTITIONING BETWEEN ZIRCON ($ZrSiO_4$) AND HYDROTHERMAL FLUIDS AT HIGH-PRESSURE (1.5 GPa) AND HIGH-TEMPERATURES (800-1000°C).

1. Abstract

We report the results of the first ever study to measure trace element partition coefficients between zircon and hydrothermal fluids though experimental synthesis and recrystallization of zircon. Experiments were run at high pressures (1.5 GPa) and temperatures (800-1000°C) using a standard piston cylinder apparatus to reproduce conditions at the base of the crust and during mountain building. Fluid compositions were quartz saturated and included distilled H_2O, 1m HCl, and 1m NaOH. Because Zr-rich phases behave as amphoteric solids, by altering the fluid pH we aim to characterize the effect of pH on zircon solubility and zircon/fluid partitioning. Sample capsules were constructed using a thick walled Ni open ended capsule lined with either gold or platinum. The Ni capsules were heat treated to generate a thin NiO layer that would buffer the oxygen fugacity of each run at NNO. The duration of our experiments varied from 24 hours to two weeks in order to monitor the time taken to reach equilibrium partitioning and also to grow zircon grains large enough for analysis using micro-analytical facilities.

Despite limitations in our ability to evaluate attainment of equilibrium, for a number of runs, measured partition coefficients for the trivalent Rare Earth elements (i.e. La-Lu: REE) have the characteristics expected for zircon, including positively trending $D_{REE}^{Zircon/fluid}$ values and prominent Ce anomalies. However, inconsistent partition coefficients for the pentavalent

cations P, Ta, and Nb suggest that not all trace elements attained partitioning equilibrium under the conditions of our experiments. Overall, partition coefficients are low, not exceeding ~10 for the most compatible elements (i.e. Yb, Lu, Y, Sc, Th, and U). Interestingly, ratios of $D^{zircon/fluid}_{Th}/D^{zircon/fluid}_{U}$ range from 0.3 to 2.7, suggesting zircon Th/U ratios of 10^{-2} to 10^{-3} for grains from metamorphic rocks result from loss of a thorite component during metamorphism.

2. Introduction:

Zircon (nominally $ZrSiO_4$) is a ubiquitous accessory mineral in Earth's crust, and one of the most important minerals available to study the geochemical and geodynamic evolution of the Earth. Zircon's use and fame as a geochronometer is tied to its robust crystalline lattice, which concentrates U whilst rejecting Pb (Watson et al., 1997), and is effective at preventing intra-element diffusion up to the most extreme crustal temperatures (see review in Cherniak and Watson, 2003; Cherniak 2010). Zircon is also a largely chemically and physically residual phase during crustal recycling, capable of preserving evidence of events prior to those that have immediately affected its host (e.g. Ayers and Watson 1991; Miller et al., 2003, 2007a; Rubatto and Hermann 2007; Hawkesworth et al., 2009; Claiborne et al., 2010). Evidence for sub-solidus hydrothermal growth and alteration of zircon can be found in HP/UHP rocks and veins associated with high grade metamorphism and mountain building. The occurrence of fluid, coesite and/or diamond inclusions in zircon support an important cogenetic relationship with metamorphic fluid production and suggest that zircon growth during HP/UHP metamorphism can provide a record of geochemical processes operating at peak or near-peak conditions (Becker et al., 1999; Widmer and Thompson, 2001; Liermann et al., 2003; Spandler et al., 2003;

Rubatto and Hermann, 2003; Jiang et al., 2005; Spandler and Hermann, 2006; Zheng et al., 2007; Glodney et al., 2008; Zhang et al., 2008; Wu et al., 2009; Zeh et al., 2010; Spandler et al., 2011).

Pure zircon is an orthosilicate where isolated $[SiO_4]^{-4}$ tetrahedra are connected by interstitial Zr cations, forming a tetragonal crystalline lattice. This simple lattice structure has two sites for cation substitution. Firstly, a tetragonal (Si) site, and secondly, a triangular dodecahedral (Zr) site (Speer, 1980). Common tetravalent cations that form a solid-solution relationship via Zr^{+4} substitution include Hf (Hafnon $HfSiO_4$), Th (Thorite $ThSiO_4$) and U (Coffinite $USiO_4$) (e.g. Hoskin and Schaltegger 2003; Ferriss et al., 2010). The incorporation of trivalent (e.g. REE, Ce^{+3}, Eu^{+3}, Y, Al, Cr, Sc, Mn) and pentavalent cations (e.g. P, Ta, Nb, V) is proposed to be achieved through coupled-substitution mechanisms (Eq. i), in a manner analogous to the Xenotime (YPO_4) substitution (Speer 1980; Finch et al., 2001; Hanchar et al., 2001; Hoskin and Schaltegger, 2003; Luo and Ayers, 2009). This may be achieved by substitution of one trivalent and one pentavalent cation for one Zr^{+4} and one Si^{+4}, but also for two Si^{+4} or two Zr^{+4} :

Eq. i. $$M^{+3} + N^{+5} = Zr^{+4} + Si^{+4}$$

Attempts to understand the origin of zircon and zircon overgrowths in metamorphic and hydrothermally altered rocks is an actively growing area of geochronology, but one limited by a lack of experimental trace element partitioning data for zircon under these conditions. Here we present the results of an experimental zircon/fluid partitioning study conducted at High/Ultra-High Pressure (1.5 GPa, 800-900°C) metamorphic conditions, and attempt to identify chemical characteristics indicative of zircon growth from a hydrothermal fluid.

3. Experimental and Analytical Procedures:

3.1. Starting materials.

Starting materials for zircon synthesis experiments consisted of finely powdered mixtures of high purity ZrO_2 (baddeleyite) and SiO_2 (quartz), mixed together in molecular proportions of 1:1, 1:2, or 1:3 molar to facilitate the reaction in Eq. ii. An XRD analysis of the starting powder identifies the presence of only quartz and baddeleyite (i.e. Zr and Si oxides and no zircon: Fig. 1a).

Eq. ii. $$ZrO_{2(xt)} + MSiO_{2(xt)} = ZrSiO_{4(xt)} + \ M - 1 \ SiO_{2(xt)}$$

[Where M represents the molecular proportion of SiO_2]

For zircon recrystallization experiments, individual grains of Mud Tank zircon (Hanchar and Hoskin 1998) were finely ground and grain fragments > ~20µm separated out using a settling column. Mud Tank zircon was chosen due to its low trace element content (Fig. 1b) and spatially homogeneous composition. Finely ground high purity SiO_2 was added to saturate the fluid in quartz during run completion (estimated using the solubility data and equations given in Manning, 1994).

For our synthesis experiments, Sc, and Hf were added to the starting material as powdered oxides, whilst for our recrystallization experiments, Hf and Sc were sourced from the Mud Tank zircon starting material. The trace elements La, Ce, Pr, Nd, Pm, Sm, Eu, Gd, Tb, Dy, Er, Tm, Yb, Lu, Hf, Y, Sc, Nb, Ta, Ti P, Th, and were added to the sample capsules via evaporation of GFS-Chemicals standard solutions (Fig. 1b). The compositions of starting materials used are reported in Table. 1.

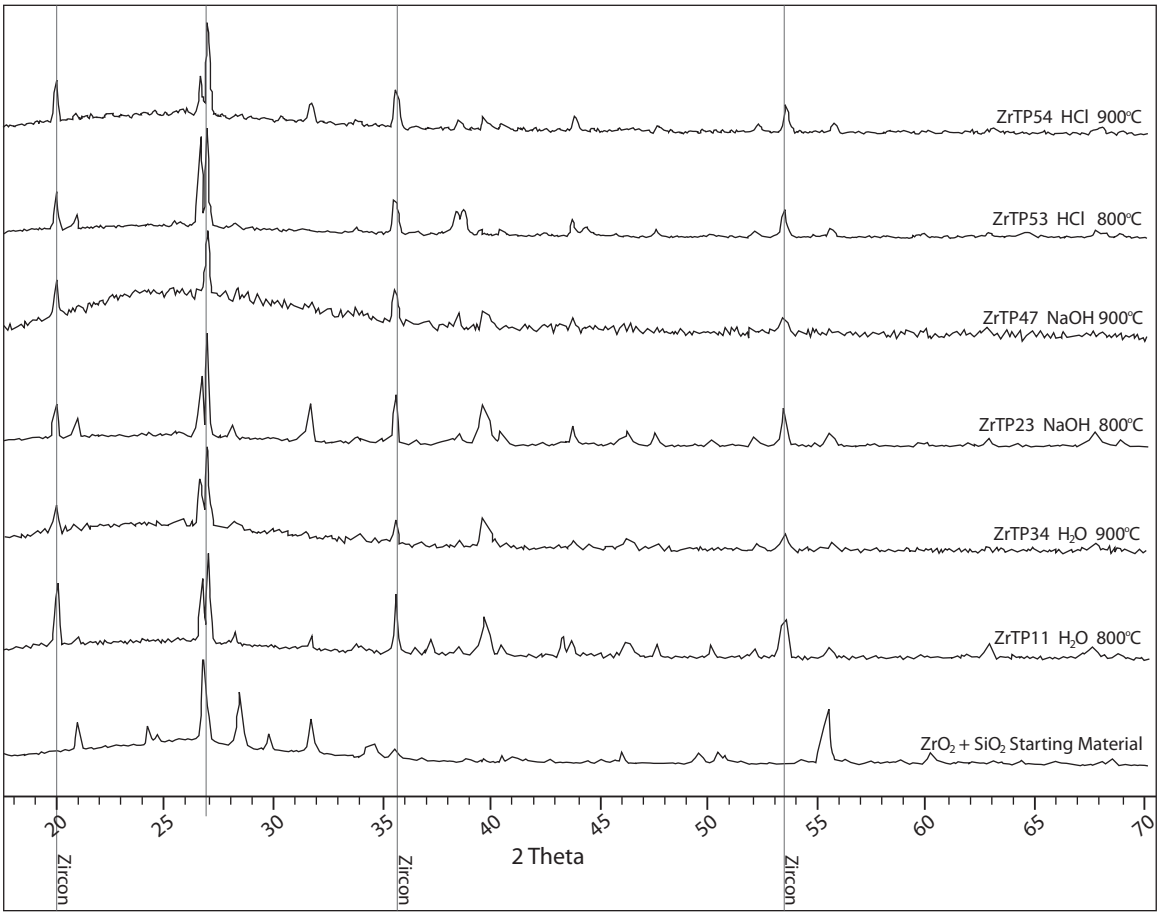

Figure. 1a. Plot of relative intensity vs. two Theta for select experimental runs and our starting material. Data was collected using the Scintag X-ray Powder Diffractometer at Vanderbilt University. Highlighted zircon lines represent peaks associated with zircon only. All other peaks represent either quartz, baddeleyite, zircon + quartz, and zircon +baddeleyite. Not the lack of zircon peaks in the starting material.

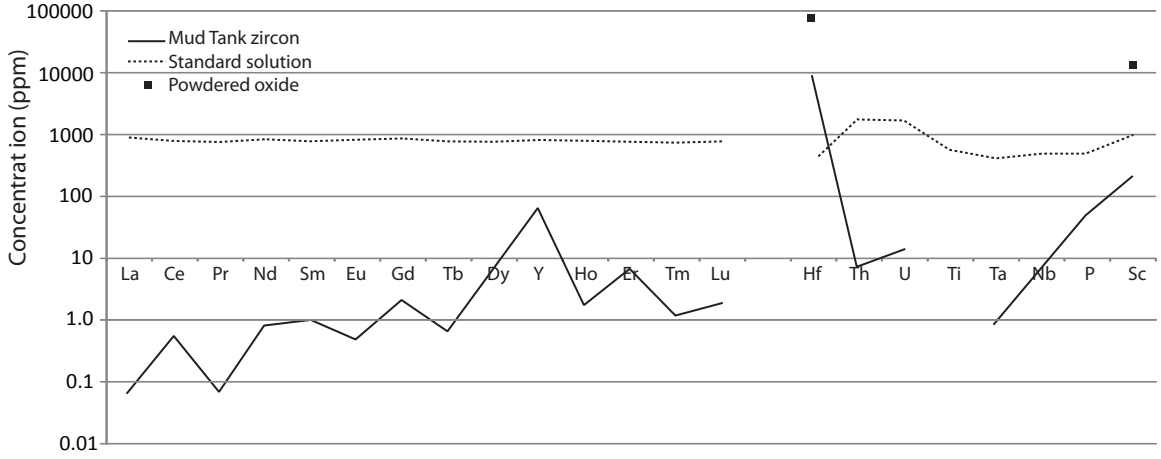

Figure. 1b. Concentration (ppm) of trace elements in the starting material for synthesis and recrystallization experiments.

Table. 1. Average Starting Material trace element concentrations (ppm). MT = Mud Tank zircon.

	MTZ grain	*1 SE*	*1 STDEV*	MTZ crushed	*1SE*	*1STDEV*	Doped fluid	*1 SE*	*1STDEV*	Oxide powders	*1 SE*	*1STDEV*
La	0.11	*0.03*	*0.07*	0.50	*0.13*	*0.22*	952	*23*	*43*	-	-	-
Ce	0.59	*0.06*	*0.09*	0.94	*0.18*	*0.24*	891	*30*	*50*	-	-	-
Pr	0.08	*0.03*	*0.02*	0.25	*0.09*	*0.05*	841	*23*	*37*	-	-	-
Nd	0.84	*0.27*	*0.06*	3.08	*0.75*	*0.72*	901	*36*	*33*	-	-	-
Sm	1.03	*0.23*	*0.31*	1.94	*0.68*	*0.65*	902	*33*	*76*	-	-	-
Eu	0.49	*0.09*	*0.17*	0.80	*0.23*	*0.20*	927	*30*	*46*	-	-	-
Gd	2.25	*0.32*	*0.78*	2.72	*0.91*	*0.64*	878	*38*	*25*	-	-	-
Tb	0.66	*0.06*	*0.04*	0.60	*0.14*	*0.17*	872	*24*	*43*	-	-	-
Dy	6.46	*0.42*	*0.52*	5.05	*0.77*	*1.25*	853	*26*	*43*	-	-	-
Y	69.48	*2.57*	*3.29*	46.49	*4.00*	*2.55*	947	*27*	*63*	-	-	-
Ho	1.77	*0.11*	*0.26*	1.16	*0.20*	*0.36*	883	*25*	*45*	-	-	-
Er	7.15	*0.40*	*0.79*	4.01	*0.62*	*1.34*	859	*27*	*39*	-	-	-
Tm	1.20	*0.09*	*0.23*	0.78	*0.15*	*0.27*	841	*23*	*49*	-	-	-
Lu	1.89	*0.12*	*0.21*	0.95	*0.17*	*0.25*	882	*27*	*46*	-	-	-
Hf	8731	*343*	*312*	6610	*849*	*454*	-	-	-	97893	*3066*	*4246*
Th	7.52	*0.36*	*1.09*	4.48	*0.38*	*0.80*	1897	*62*	*68*	-	-	-
U	14.01	*0.56*	*1.71*	9.65	*0.73*	*0.86*	1810	*49*	*37*	-	-	-
Ti	-	-	-	-	-	-	652	*142*	*80*	-	-	-
Ta	0.92	*0.08*	*0.12*	0.63	*0.15*	*0.14*	467	*12*	*26*	-	-	-
Nb	6.81	*0.29*	*0.30*	4.83	*0.45*	*0.66*	550	*14*	*30*	-	-	-
P	51.15	*21*	-	201	*402*	*55*	-	-	-	-	-	-
Sc	209	*7.58*	*5.92*	162	*10.82*	*15.31*	-	-	-	17687	*479*	*680*
Si	149581	*4798*	-	149581	*5076*	-	562423	*13354*		-	-	-
Zr	415006	*18124*	*2758*	284520	*31591*	*21103*	435131	*15699*	*17915*	-	-	-

To characterize the effect of pH on zircon solubility and zircon/fluid partitioning we used initial fluid compositions of distilled H_2O, 1m NaOH, or 1m HCl. NaOH was used due to the strong positive correlation between Zr-mineral solubility and hydroxyl concentration, which results from formation of Zr-hydroxide complexes (i.e. $Zr(OH)_4$) in the fluid (Tole 1985; Ayers et al., 2012). HCl was used because experimental evidence supports an enhanced Zr mobility and zircon solubility in HCl+H_2O fluids, leading to extensive zircon recrystallization when quartz saturated (Schmidt et al., 2006). The run conditions and fluids used are reported in Table. 2.

3.2. Experimental Sample Capsule:

Sample capsules consisted of an outer thick-walled open-ended nickel cylinder and an inner gold or platinum metal sleeve, constructed using the methods and dimensions outlined in Ayers et al., (1992 and 1997) (Fig. 2 and Fig. 3a.i). The nature of the thick-walled nickel cylinder is to maintain a relatively constant capsule geometry during the experimental run, preventing it from collapsing and expelling the fluid component.

An issue for high-temperature hydrothermal experiments is the progressive loss of fluid due to hydrogen diffusing through the inner-sleeve (Ayers et al., 1992). With progressive loss of hydrogen from the inner capsule, the oxygen fugacity (ƒO2) inside the inner capsule rises and constant partitioning equilibrium for multivalent cations cannot be attained; leading eventually to collapse of the capsule and failure of the run. To reduce the rate of hydrogen gas diffusion out of the capsule, nickel cylinders were pre-treated for ~24 hours at 1100°C to create a thin outer layer of nickel oxide prior to loading of the noble metal sleeve. Once hydrogen gas begins to diffuse through the inner sleeve it reacts with the NiO forming Ni and H_2O (Eq. iii).

Eq. iii. $$NiO_{(xt)} + H_{2(g)} = Ni_{(s)} + H_2O_{(aq)}$$

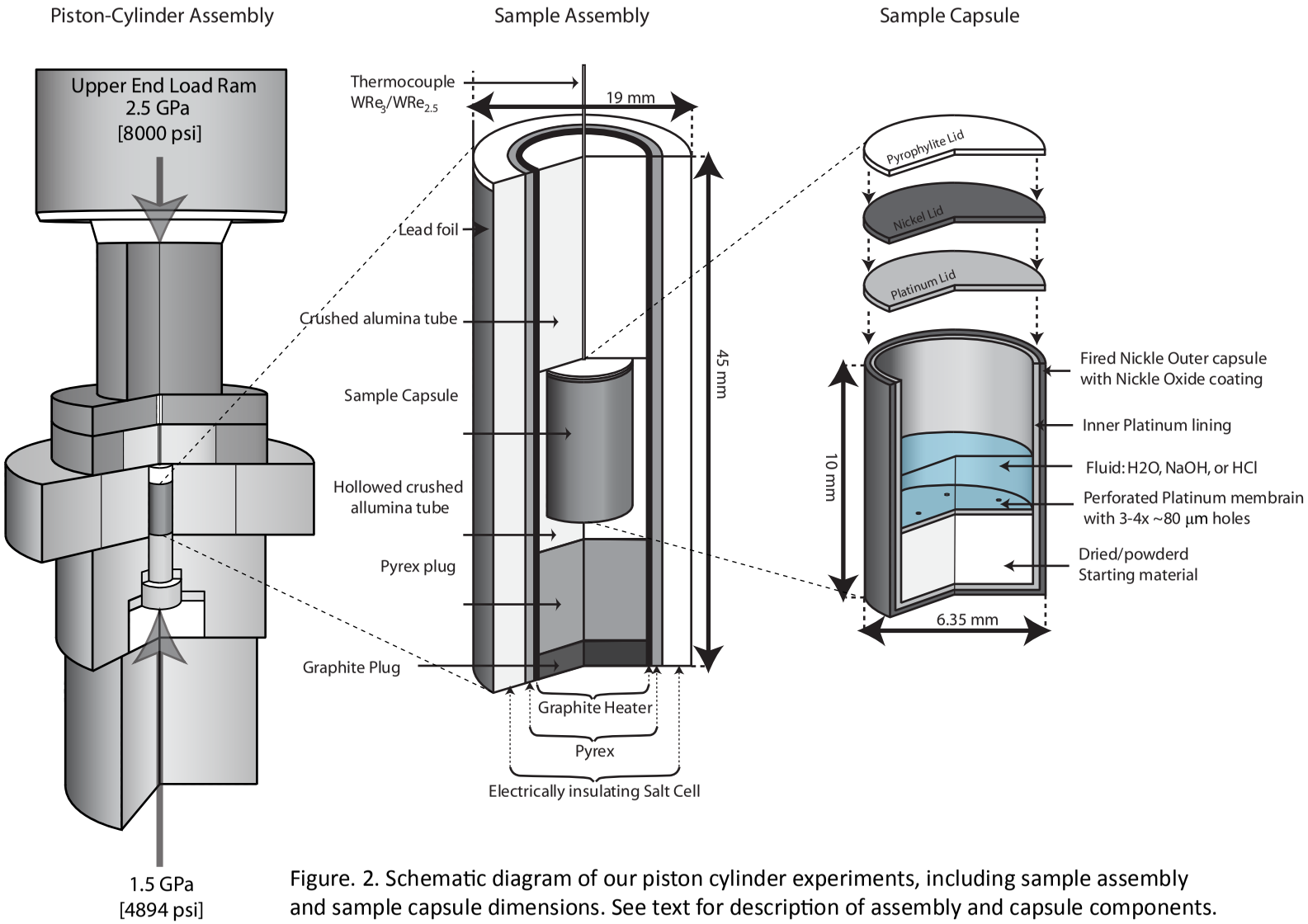

Figure. 2. Schematic diagram of our piston cylinder experiments, including sample assembly and sample capsule dimensions. See text for description of assembly and capsule components.

Table. 2. Experimental conditions, and starting material, fluid, and quenched solute weights for zircon synthesis and recrystallization runs.

Synthesis Experiements	Fluid	Time (Hr)	Temp (°C)	Pressure (Gpa)	Powder wt (g)	Fluid wt (g) before run	Fluid wt (g) After run	Quenched solute Wt. (g)	Solute g/1g fluid
ZrTP11	H_2O	168	800	1.5	0.023	0.038	0.032	0.003	0.097
ZrTP13	H_2O	72	800	1.5	0.021	0.032	0.029	0.011	0.387
ZrTP14	H_2O	24	800	1.5	0.019	0.033	0.026	0.007	0.288
ZrTP34	H_2O	96	900	1.5	0.025	0.027	0.018	0.006	0.330
ZrTP35	H_2O	96	900	1.5	0.024	0.031	0.021	0.008	0.405
ZrTP40	NaOH	168	800	1.5	0.021	0.030	0.014	0.003	0.184
ZrTP46	NaOH	72	800	1.5	0.027	0.025	0.021	0.008	0.358
ZrTP49	NaOH	96	900	1.5	0.020	0.028	0.016	0.008	0.511
ZrTP51	HCl	48	800	1.5	0.023	0.031	0.036	0.008	0.230
ZrTP52	HCl	48	800	1.5	0.020	0.027	0.023	0.005	0.216
ZrTP53	HCl	96	800	1.5	0.023	0.027	0.020	0.007	0.339
ZrTP54	HCl	72	900	1.5	0.022	0.032	0.028	0.005	0.178
Recrystallization Experiments									
ZrMT 02	H_2O	168	900	1.5	0.021	0.027	0.031	0.002	-
ZrMT 03	H_2O	168	800	1.5	0.020	0.030	0.025	-	-
ZrMT 05	H_2O	168	1000	1.5	0.027	0.031	0.025	0.002	-

By using an external source of water outside of the capsule we can buffer the hydrogen fugacity at the interface between the Ni/NiO capsule and inner-capsule, preventing development of a hydrogen concentration gradient. For our experiments we generated an external water source by the decomposition of pyrophyllite (Freda et al., 2001) [$Al_2Si_4O_{10}(OH)_2$], a hydrous aluminosilicate phase added above and below our sample capsule upon loading into the sample assembly. Once the fugacity of hydrogen is fixed outside of the inner capsule, the oxygen fugacity inside the capsule will be buffered at Nickel/Nickel oxide (NNO), preventing loss of fluid and maintaining equilibrium partitioning.

Once the Ni-NiO capsule has been lined with a noble metal sleeve, the open end of the sample capsule is ground and polished until both capsule and sleeve are flush; this results in creation of a tight seal with the lid upon addition of pressure during set up of the run. Before loading the sample the capsule is cleaned in an ultra-sonic bath using de-ionized water for ~5 minutes.

Using a hole punch, two small noble metal discs with a diameter of 6.3 mm are cut; one to be used for the sample capsule lid, and the other to create the inner-capsule perforated membrane, following the procedures outlined in Ayers et al., (1997). During the run, the perforated noble metal membrane allows attainment of chemical equilibrium throughout the capsule. Following run completion, cooling of the experiment forces any silica dissolved in the fluid to precipitate out as spheres of hydrous glass (Fig. 3a.ii), referred to as quenched solutes (QS), that extract any remaining dissolved trace elements. These quenched solutes, which form from fluid in the upper chamber, collect upon the upper surface of the membrane separating them from minerals and starting material in the lower chamber, and can be extracted from the upper chamber after completion of the run.

Prior to loading the powdered starting material, doped ICP-MS standard solutions are combined in a Teflon beaker and reduced in volume using a low-temperature setting on a hot plate. When the volume has been sufficiently reduced, the solution is transferred to the sample capsule, which then sits on the hot plate until the solution has evaporated. Upon complete evaporation, the sample capsule is left to cool for ~1 minute.

After cooling, ~0.02g of powdered starting material is weighed and carefully added to the base of the sample capsule. Next, the membrane is carefully pushed into the sample chamber until it rests on the powdered starting material. Finally, ~0.03g fluid is added to the top of the membrane and the capsule is carefully inserted into the sample assembly. Starting material and fluid weights are reported in Table. 2.

3.3. Experimental sample assembly:

The capsule is positioned within the assembly so that the upper chamber is located in the assembly hot spot to prevent crystallization of run products in the upper chamber and allow convective fluid homogenization to help attain chemical equillibrium (e.g. Schilling and Wunder 2004). The sample assembly is prepared using the methods and dimensions outlined in Ayers et al., (1992) and summarized in Fig. 2. Crushed alumina surrounding the capsule acts as a granular fluid under pressure and distributes pressure evenly on the capsule. The thin graphite tube acts as the furnace, producing heat via electrical resistance during the experimental run. The Pyrex tubing helps maintain the geometry of the sample assembly until it is heated in excess of >~600°c, when it becomes soft. The salt cells of compressed NaCl are added to the exterior of the sample assembly to prevent electrical conduction between the graphite furnace and the pressure vessel. Finally, a thin sheet of lead is wrapped around the assembly to lubricate the pressure vessel walls and aid removal of the assembly upon completion of the run.

3.4. Experimental set up:

The sample assembly is carefully inserted into the ¾" i.d. pressure vessel, which is then placed into the Piston Cylinder apparatus housed at Vanderbilt University (Fig. 2). Prior to addition of electrical current, force is added to the upper End Load Ram and ~0.6 GPa is slowly applied to the base of sample by advancing the piston into the cylinder. Upon addition of electrical current, the temperature is allowed to rise to 600°C when the Pyrex tubing becomes soft, after which additional pressure is added to the sample as temperature increases until the required conditions are attained. Pressure is kept constant during the run by manually adjusting the lower ram as needed.

Temperatures are measured using a $W_{97}Re_3/W_{75}Re_{25}$ thermocouple inserted axially into the assembly using high-purity alumina round four bore tubing (OD 0.063 inch, ID 0.016 inch) as shown in Fig. 2. The slot in the thermocouple plate is closed up with masking tape to help prevent oxidation of the thermocouple during the run. The temperature gradient across the sample capsule is expected to be ±10°C and no correction was made for the effect of pressure on measured temperature (Ayers et al., 1992).

3.5. Post-run preparation.

Upon completion of the experimental run, the capsule is extracted from the sample assembly, cleaned, and its Ni lid is removed. The platinum or gold lid of the capsule is pierced open and the capsule is placed in a 110°C oven to evaporate the fluid. The dried capsule is re-weighed to determine the final fluid weight, and then opened so that quenched solutes can be collected from the upper chamber. Once removed, the solutes are weighed and a small portion used to make grain mounts for observation with a polarizing microscope. Identification of

crystalline material, which would represent contamination from the lower chamber, would invalidate the run. For uncontaminated solutes, the remaining fraction is weighed, finely ground with 2 parts $LiBO_2$ and fused for five minutes at 1100°C into glass beads. The remaining capsule is impregnated with low-viscosity epoxy to preserve the lower-chamber components, sectioned lengthwise using a low-speed diamond-blade, mounted in epoxy with its quenched solute glass bead, and polished using standard polishing techniques until it is ready for imaging and analysis.

The weight of extracted quenched solutes varied between 1.3 mg to 8.5 mg (Table. 2), with an average of 5.3 mg, and produced $LiBO_2$ glass beads between 0.5 to 1 mm in diameter. An issue with our calculations of bulk fluid compositions is that all quenched solutes must be accounted for in order to yield the true magnitude of fluid trace element concentrations present during the run. Although care was taken to extract all quenched solutes available, this proved challenging for some of the more deformed capsules; which is in-part reflected in the variable quenched solutes weights. Furthermore, contamination with dark-green NiO powder, which occupied the region between the outer capsule and inner sleeve (Fig. 3a.i), occurred during quenched solutes extraction and was impossible to remove prior to quenched solutes weighing. Another feature that will affect the bulk-fluid concentration calculations is the difference in measured fluid volumes before and after each run. Calculated values of 12% to 56% fluid loss (equal to initial fluid weight minus final fluid weight) are observed for our experiments. While no clear evidence of NiO diffusion into the Nobel-metal inner-chamber was observed, we have no clear means to evaluate potential fluid loss by diffusion of H_2. These issues, however, affect only the absolute values of our estimated partition coefficients, not the relative values of partition coefficients (i.e., ratios of D values), which can be used to assess whether equilibrium was achieved during the run.

4. Analytical techniques:

4.1. Imaging:

Digital back-scattered electron (BSE) images of the lower chamber run products were obtained using a Hitachi S-4200 Scanning Electron Microscope at Vanderbilt University. Cathodoluminescence (CL) images were collected using a Cameca SX-50 electron microprobe (EPMA) at the University of Tennessee, Knoxville.

4.2. Phase identification:

Material from one half of each sectioned zircon synthesis experiment capsule was carefully removed from the lower chamber, finely ground with acetone, and transferred to a glass slide to make an "acetone smear" for powder XRD analysis. Experimental synthesis starting materials and run products were analyzed using a Scintag X-ray Powder Diffractometer at Vanderbilt University to allow for phase identification. The powder sample holder was a zero background Si510 plate, and the operation settings were 45 keV acceleration voltage at 40 mA tube current. Samples were scanned with Cu-Kα radiation from 18 to 60° 2θ at step intervals of 0.030 °/min (or 15 - 65° 2θ, 0.050°/min). DMS-NT search/match software with the ICDD database was used to match peak positions and intensities, along with Match! Software with the PDF-4 mineral database.

4.3. ICP-MS:

Compositional analyses of glass beads, sectioned lower chambers, and Mud Tank zircon starting material were completed using a Perkin Elmer Elan II DRC (Dynamic Reaction Cell) coupled with a New Wave 213 nm Nd:YAG laser located at Vanderbilt University. Argon gas was

used as the aerosol carrier to enhance transport efficiency. The laser was run with 15 J/cm^2 energy density using a repetition rate of 10 Hz. The beam diameter was 20 to 30 μm for analysis of lower chamber domains and 60-120 μm for analysis of glass solute beads and Mud Tank zircon. NIST 610 was used as the primary external standard while 612 and 614 were used as secondary standards. The minimum detection limits for trace-elements is typically 0.01 to 1 ppm for elements < 80 amu (atomic mass units), and 1 ppb for elements >80 amu, depending upon spot size and power setting (Kosler, 2001). Output data was processed using Glitter® is reported in Appendix. D – H.

5. Results

5.1. Image and Phase Analysis:

5.1.1. Zircon Synthesis experiments:

Capsule deformation during experiments made extraction of quenched solutes challenging but did not compromise the effectiveness of their membranes (Fig. 3a.i). Quenched solutes are typically small (<~1 μm) spheres of hydrous glass that often form globular clusters (Fig. 3a.ii), which for all successful runs appeared free from contamination of crystalline material from the lower chamber.

Optical images of sectioned lower chambers show a largely white/translucent-white crystalline mass with a coarse texture (Fig. 3a.iii). BSE and CL imaging clearly distinguishes large grey quartz crystals and a brighter Zr-phase (Fig. 3a.iv). For some runs, but not all, we were able to identify small (i.e. <5 μm) crystalline zircon grains (Fig. 3a.v), with the synthesis of zircon for all runs confirmed through XRD analysis: i.e. All run products yielded spectral peaks indicating

the presence of only quartz and zircon with some unreacted baddeleyite from the starting material (Fig. 1a).

Clumps or clusters of Zr-rich material 10 to 60 μm in diameter can be found throughout the lower chamber, with no obvious pattern to their distribution (Fig. 3a.vi). The interior regions of these clusters typically display EDS spectra where Zr peaks are considerably more prominent than Si peaks, and are interpreted to represent un-reacted starting material. Zircon occurs as thin (i.e. <5 μm) overgrowths on these clusters and yields an EDS spectra with Si and Zr peaks of roughly equal height. The small grain sizes and fine-scale intergrowths of zircon and unreacted starting material made it difficult to obtain clean analyses of zircon.

5.1.2. Zircon recrystallization experiments:

BSE images of crushed starting material show a mixture of small (i.e. ~1 μm) and larger (i.e. < 20 μm) angular zircon fragments (Fig. 3.bi). At 800°C (run ZrMT-03), complex inter-grain textures are observed using CL imaging, representing recrystallized zircon and possibly quenched solutes (Fig. 3b. ii). For our 900°C run (ZrMT-02), larger grains begin to display clear evidence of hydrothermal alteration and recrystallization with the development of inwardly penetrating reaction fronts (Fig. 3b.iii and 3b.iv). At 1000°C (ZrMT-05), complex textures are observed in CL and BSE images (Fig. 3b. v and iv) that show an extensive replacement of smaller crushed zircon fragments (i.e. Fig. 3b. i) with a homogenous grey recrystallized zircon matrix (Fig. 3b. vi). Larger grains for this run appear to be reduced in angularity and size (Fig. 3b.v and vi).

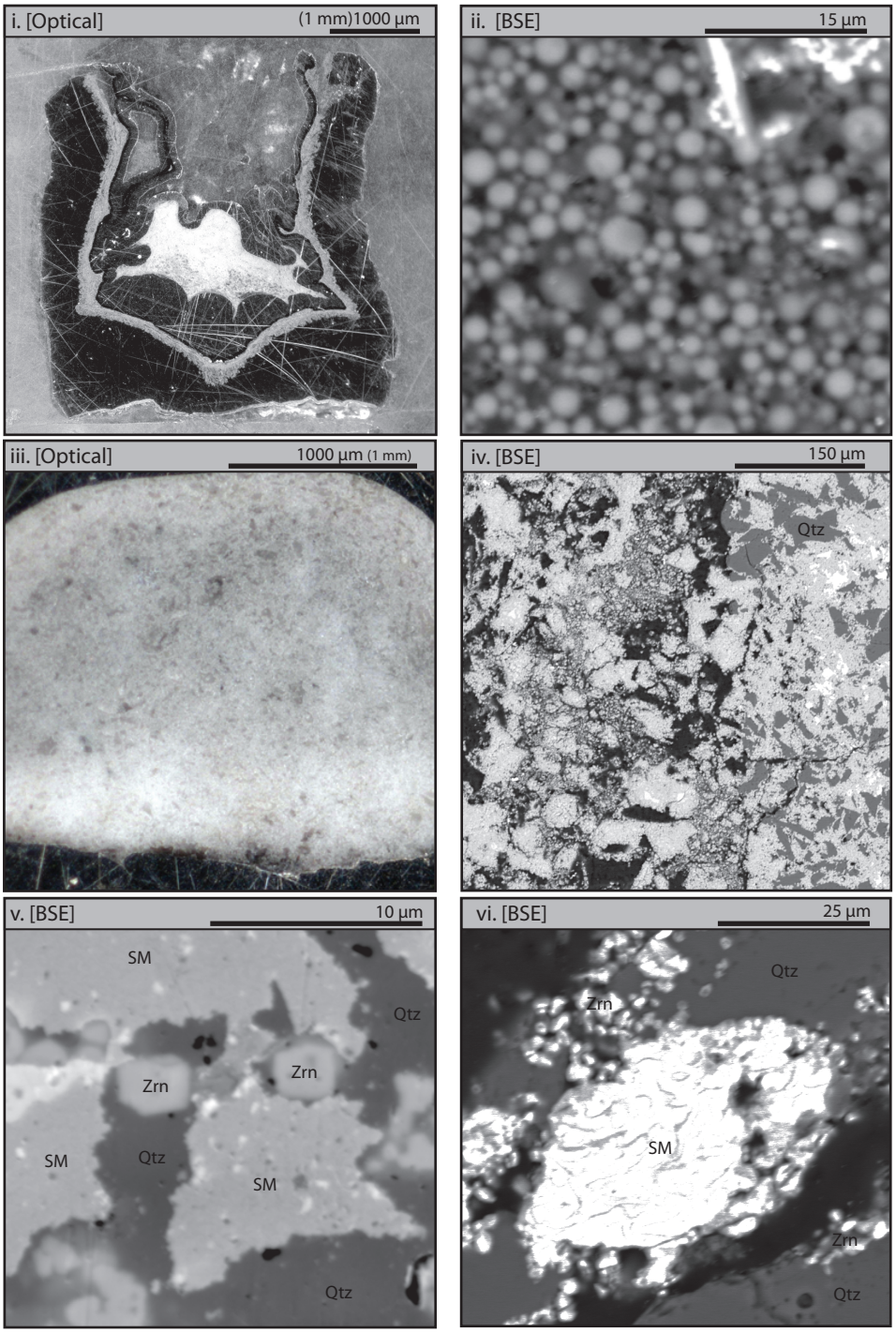

Figure. 3a. (i) Photograph of a sectioned capsule after an experimental run. Note the crystalline white lower chamber and presence of a light grey layer of NiO that separates the thick dark Ni outer capsule and dark thin inner capsule. (ii) Back Scattered Electron (BSE) image of quenched solutes extracted from the upper chamber after run completion. (iii) Optical microscope photograph of the crystalline lower chamber. Note the larger quartz grains. (iv) BSE image of the lower chamber after run completion. Note the large grey quartz grains, clumps of white starting material, and small (<5µm) zircon grains. (v) BSE image of individual zircon grains surrounded by quartz and unreacted starting material. Note the small zircon size.(vi) BSE image of a clump of unreacted starting material surrounded by small zircon grains and larger quartz grains.

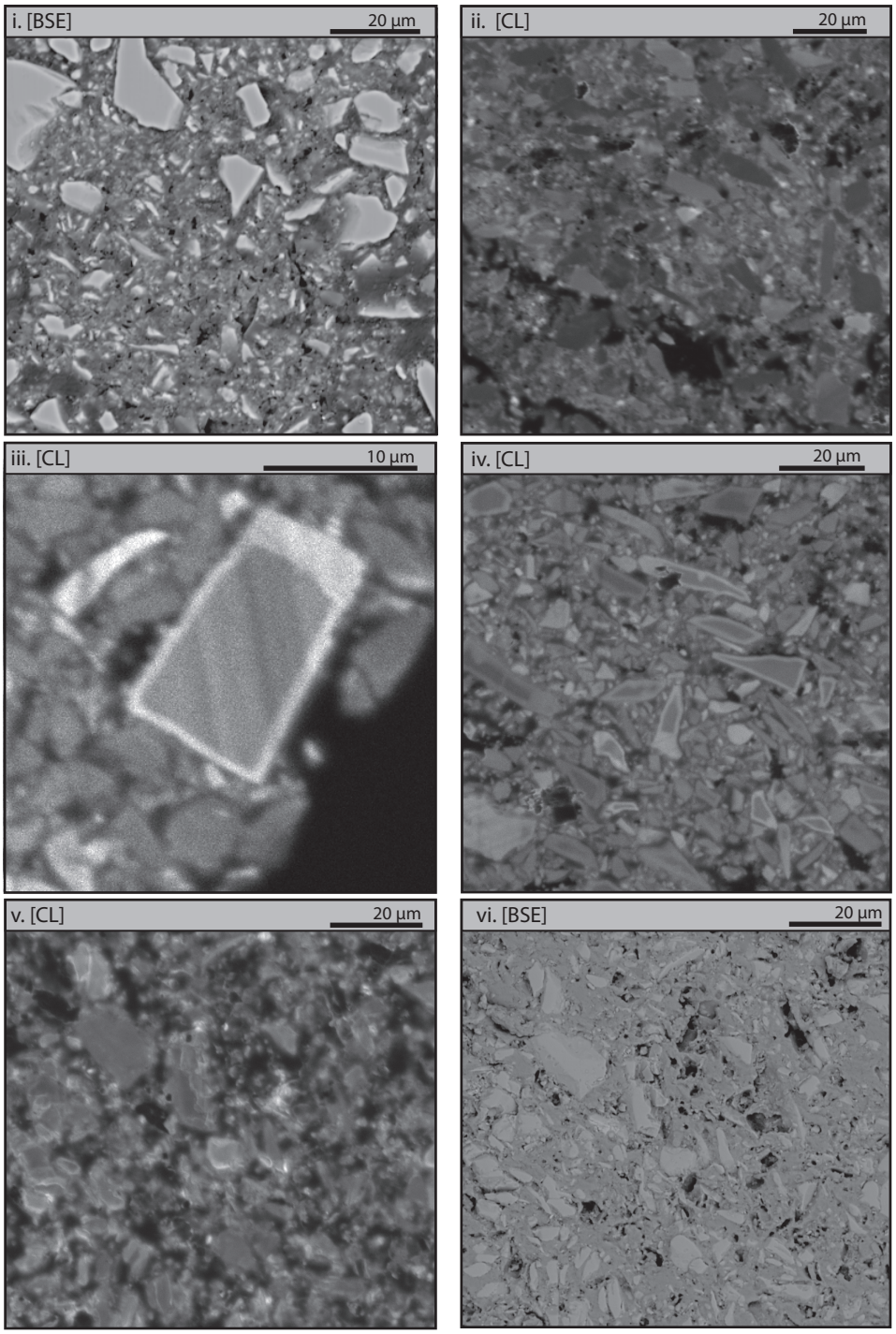

Figure. 3b. (i) CL image of crush Mud Tank zircon starting material. (ii) CL image of ZrMT 03 recrystallized zircon at 800°C. (iii) CL image of ZrMT 02 recrystallized zircon at 900°. Note the preservation of original zoning. (iv) CL image of ZrMT 02 recrystallized zircon at 900° Note the development of alteration rims on larger grains. (v) CL image and (vi) BSE images of ZrMT 05 recrystallized zircon at 1000°C.

5.2. Fluid composition:

5.2.1. Zircon Synthesis experiments:

EMP analysis of SiO_2 and ZrO_2 in the glass beads (i.e. QS + $LiBO_2$) yielded low totals ranging from 5.2 to 24.6 wt.% (Appendix. I). Despite efforts to minimize contamination, collected solutes often contained small fragments of Ni, Pt, and NiO. While metal fragments could be effectively identified and extracted, NiO grains could not. Runs that yielded low quenched solute weights were particularly sensitive to the the increased difficulty associated with accurate measurement and addition of exceedingly small amounts of $LiBO_2$.

LA-ICP-MS data was reduced using the SiO_2 wt.% reported for NIST -610, -612, and -614, and the EMP measured SiO_2 wt.% for each glass bead; i.e., Si was used as an internal standard. Si concentrations are subsequently normalized to values that assume the sum of SiO_2 and ZrO_2 concentrations in the quenched solutes equal 100 wt.% (Eq. iv); ideally eliminating or minimizing the impact of NiO contamination. The normalized quenched solute Si concentration values are then used to calculate the QS concentration of the remaining analyzed elements (Eq. v). Finally, the fluid composition is calculated using the concentration of each element in the QS, the weight of quenched solutes, and the weight of fluid for each run (Eq. vi). Fluid compositions for our zircon synthesis experiments are reported in Table. 3a.

Eq. iv. $$\boldsymbol{Si_{(QS)}} = \frac{\boldsymbol{100 \times Si_{(G)}}}{\boldsymbol{SiO_{2_{(G)}} + ZrO_{2_G}}}$$

Eq. v. $$\boldsymbol{C^i_{(QS)}} = \frac{\boldsymbol{Si_{(QS)}}}{\boldsymbol{Si_{(G)}}} \times \boldsymbol{C^i_{(G)}}$$

Eq. vi. $$\boldsymbol{C^{i}_{(Fl)}} = \frac{\boldsymbol{QS\ wt}}{\boldsymbol{Fluid\ wt}} \times \boldsymbol{C^{i}_{(QS)}}$$

Where $Si_{(QS)}$ is the concentration (ppm) of Si in the QS; $Si_{(G)}$ is the weighted mean Si concentration (ppm) in the glass; $SiO_{2(G)}$ and $ZrO_{2(G)}$ are wt.% values for each glass bead measured by EMP; $C^{i}_{(QS)}$, $C^{i}_{(G)}$ and $C^{i}_{(Fl)}$ are the concentrations (ppm) of trace-element i in the QS, glass, and final fluid, respectively (where Fluid wt = final weight H_2O + QS weight).

Multiple Laser ablation analyses across each glass bead record a homogeneous distribution of trace-elements. As shown in and Fig. 1b, the REE were added in equal amounts and display a flat trend when plotted from La to Lu (i.e. Light to Heavy REE, or large to small Ionic radii). The majority of fluid compositions calculated display either flat to negatively trending plots of REE concentrations, supportive of zircon crystallization and HREE extraction (Fig. 4). Two runs, ZrTP-34 (Fig. 4a) and ZrTP-46 (Fig. 4b), display positively trending REE concentrations indicating possible contamination with zircon. The order of magnitude difference in fluid trace element concentrations between runs largely reflects variation in the weight of extracted quenched solutes, as discussed previously.

5.2.2. Zircon recrystallization experiments:

For our recrystallization experiments, the weights of quenched solutes that could be extracted were insufficient to successfully generate glass beads. This placed a limitation on our ability to directly monitor the fluid composition after completion of the run. In this case, we estimated fluid compositions for our recrystallization experiments were calculated by mass balance using our measured composition of a Mud Tank zircon grain, the composition of doped trace elements, and the average composition of the lower chamber analyses. Mass balance

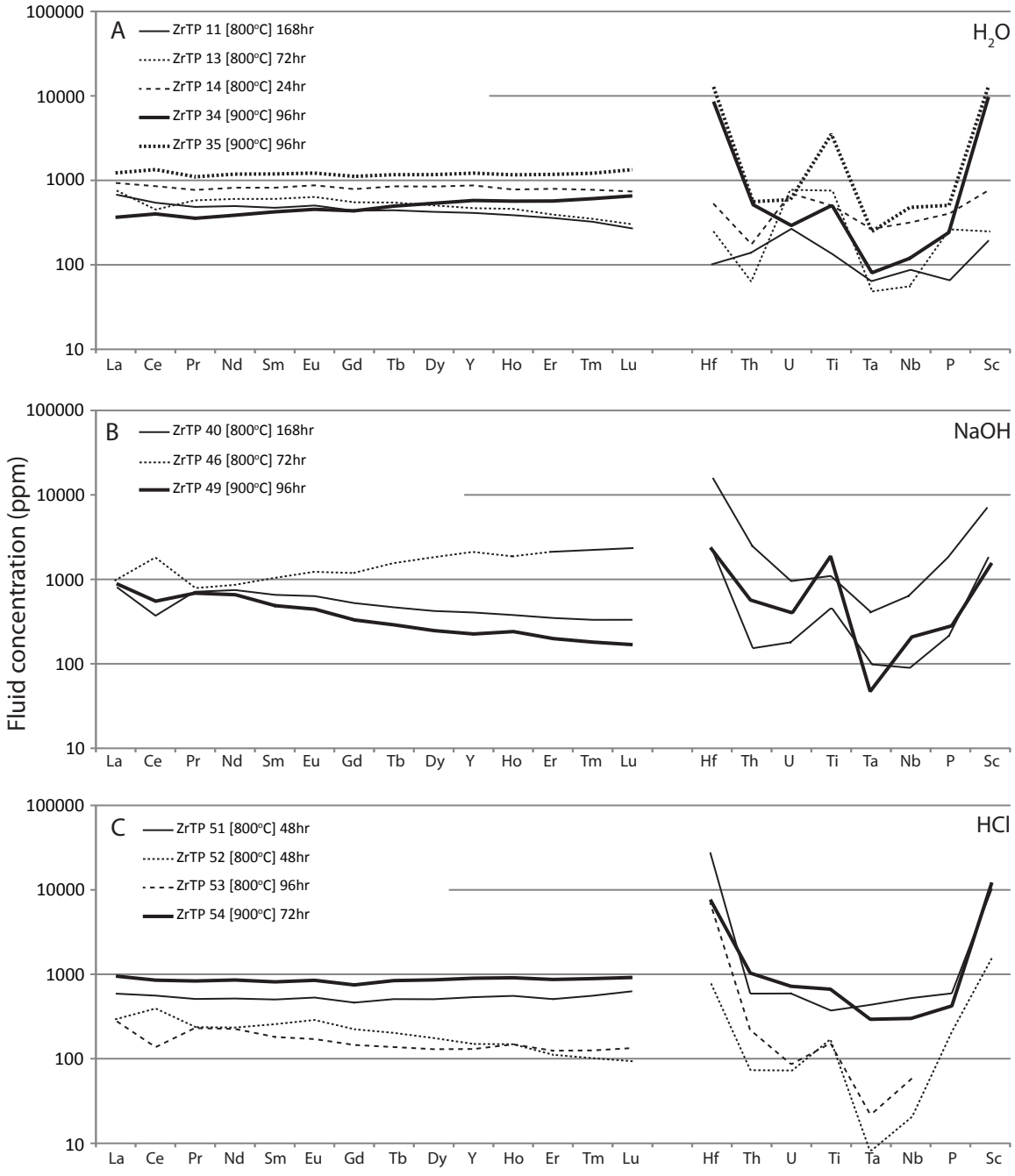

Figure. 4. Plots of calculated final fluid trace element concentration (ppm) for all experimental runs.

Table. 3a. Fluid trace element concentrations (ppm) and 1σ error (1 se) for our zircon synthesis experiments.

	La	Ce	Pr	Nd	Sm	Eu	Gd	Tb	Dy	Y	Ho	Er	Tm	Lu
ZrTP 11	678	543	483	495	472	502	436	440	423	386	410	357	322	268
1 SE	*39*	*29*	*28*	*24*	*25*	*28*	*22*	*24*	*23*	*15*	*22*	*19*	*16*	*13*
ZrTP 13	760	449	579	602	601	633	548	545	504	458	467	392	349	301
1 SE	*28*	*17*	*25*	*25*	*25*	*23*	*23*	*22*	*20*	*21*	*18*	*14*	*14*	*11*
ZrTP 14	928	851	767	815	817	872	787	848	842	777	869	793	770	737
1 SE	*30*	*28*	*25*	*29*	*27*	*28*	*25*	*28*	*26*	*26*	*27*	*24*	*24*	*22*
ZrTP 34	364	399	354	386	424	453	434	495	533	566	576	567	607	654
1 SE	*12*	*13*	*11*	*14*	*16*	*15*	*16*	*16*	*17*	*18*	*18*	*20*	*19*	*21*
ZrTP 35	1225	1338	1100	1185	1189	1215	1111	1165	1166	1159	1217	1174	1213	1337
1 SE	*38*	*41*	*36*	*42*	*40*	*43*	*37*	*37*	*37*	*39*	*39*	*39*	*38*	*45*
ZrTP 40	814	365	711	745	655	632	523	465	422	377	404	348	331	331
1 SE	*26*	*12*	*24*	*30*	*22*	*22*	*18*	*16*	*14*	*14*	*14*	*11*	*11*	*12*
ZrTP 44	1125	976	1014	1039	975	962	862	872	839	828	845	768	754	746
1 SE	*35*	*30*	*32*	*35*	*32*	*31*	*27*	*27*	*26*	*26*	*26*	*24*	*23*	*23*
ZrTP 46	873	1625	707	772	935	1107	1070	1402	1647	1691	1909	1921	2036	2208
1 SE	*35*	*66*	*28*	*36*	*42*	*46*	*47*	*56*	*68*	*71*	*76*	*79*	*82*	*88*
ZrTP 49	891	548	684	657	487	443	330	289	247	240	225	199	180	169
1 SE	*30*	*18*	*23*	*25*	*20*	*16*	*15*	*11*	*10*	*9*	*8*	*8*	*7*	*6*
ZrTP 51	268	130	220	216	174	164	140	132	124	142	125	119	120	128
1 SE	*14*	*6*	*10*	*14*	*13*	*8*	*7*	*9*	*6*	*9*	*9*	*5*	*7*	*6*
ZrTP 52	281	375	227	224	246	275	214	194	168	142	143	107	98	89
1 SE	*11*	*15*	*9*	*13*	*14*	*12*	*13*	*8*	*9*	*6*	*6*	*6*	*4*	*4*
ZrTP 53	565	536	489	494	482	509	443	487	485	532	514	487	534	603
1 SE	*44*	*35*	*30*	*46*	*42*	*39*	*44*	*38*	*33*	*36*	*42*	*40*	*49*	*63*
ZrTP 54	914	815	799	818	779	813	718	807	823	871	860	832	851	879
1 SE	*61*	*64*	*58*	*75*	*70*	*93*	*61*	*91*	*79*	*47*	*108*	*73*	*67*	*76*

Table. 3a. Continued.

	Hf	Th	U	Ti	Ta	Nb	P	Sc	Si	Zr
ZrTP 11	101	139	263	135	63	87	65	197	44886	1668
1 SE	*5*	*9*	*17*	*8*	*3*	*3*	*10*	*11*	*67*	*67*
ZrTP 13	254	60	771	753	48	56	262	248	179613	1838
1 SE	*9*	*2*	*25*	*27*	*2*	*3*	*30*	*10*	*83*	*88*
ZrTP 14	539	169	689	502	265	316	406	774	133794	33648
1 SE	*18*	*5*	*22*	*41*	*8*	*10*	*38*	*24*	*1055*	*1350*
ZrTP 34	8788	521	289	497	79	120	244	9994	153301	88016
1 SE	*294*	*17*	*10*	*26*	*3*	*4*	*61*	*317*	*2736*	*3039*
ZrTP 35	13122	559	589	3327	241	477	507	13357	188165	109565
1 SE	*403*	*18*	*18*	*127*	*8*	*15*	*44*	*429*	*3545*	*4144*
ZrTP 40	2119	152	180	449	99	89	217	1875	85517	17499
1 SE	*66*	*5*	*6*	*17*	*3*	*3*	*18*	*66*	*572*	*628*
ZrTP 44	7147	375	391	1861	93	127	210	2735	137579	27259
1 SE	*226*	*12*	*13*	*53*	*3*	*4*	*41*	*92*	*829*	*931*
ZrTP 46	14983	2298	859	990	361	576	1676	6628	166043	61080
1 SE	*664*	*93*	*34*	*91*	*15*	*24*	*458*	*265*	*22455*	*2537*
ZrTP 49	2506	603	432	2159	54	221	298	1637	237022	8287
1 SE	*92*	*21*	*14*	*102*	*2*	*8*	*120*	*55*	*3879*	*308*
ZrTP 51	7039	221	89	160	23	59		2126	106533	27324
1 SE	*576*	*12*	*3*	*18*	*2*	*4*	*91*	*198*	*254635*	*3110*
ZrTP 52	818	75	75	181	8	21	212	1560	100179	3269
1 SE	*37*	*4*	*4*	*32*	*1*	*2*	*99*	*61*	*1041*	*133*
ZrTP 53	27713	606	608	383	448	537	609	10325	157321	110861
1 SE	*2924*	*53*	*49*	*48*	*38*	*26*	*234*	*443*	*59749*	*5364*
ZrTP 54	7688	1051	739	682	301	308	429	12240	82588	32283
1 SE	*1083*	*83*	*59*	*34*	*28*	*20*	*188*	*827*	*18461*	*1848*

calculations that used the total mass of Mud Tank zircon powder added to the capsule (i.e. assuming complete re-equilibration of all starting material) yielded negative fluid concentrations for some of the more compatible elements (i.e. U, Lu, etc.), suggesting not all the powdered Mud Tank zircon had been involved in recrystallization reactions. To generate useful fluid compositions for partition coefficient calculations, the mass of powdered Mud Tank zircon assumed to have been involved in recrystallization reactions was set at 0.01g. Calculated fluid compositions for our zircon recrystallization experiments are reported in Appendix. H.

5.3. Synthesized zircon composition:

Because zircon grains are smaller than the 30 μm laser beam diameter, most analyses are largely a mix of zircon and unreacted starting material, resulting in highly variable trace element concentrations for individual elements between LA analysis spot locations in a single run. For some experiments we observed a broad positive correlation between concentrations of components compatible in zircon (i.e. Lu or U) and Zr (e.g. Fig. 5). For these runs, analyses that fell along the trend typically contained features expected of zircon and were selected as C_i^{zircon} values for calculation of D_i^{zircon}.

For all experiments that used H_2O, no correlation between compatible component (Lu or U) and Zr could be identified. While a couple of LA analyses display LREE depletion and positive Ce anomalies, typical of zircon, we could not identify a single clear REE pattern that unambiguously belonged to zircon alone (Fig. 6 a-e). A major issue for the experiments on H_2O is that concentrations measured in run products from 800°C and 900°C runs have low precision. Also, the relative difference in concentration for one element between any two analysis spot locations show a poor correlation with the relative difference of a second element of similar

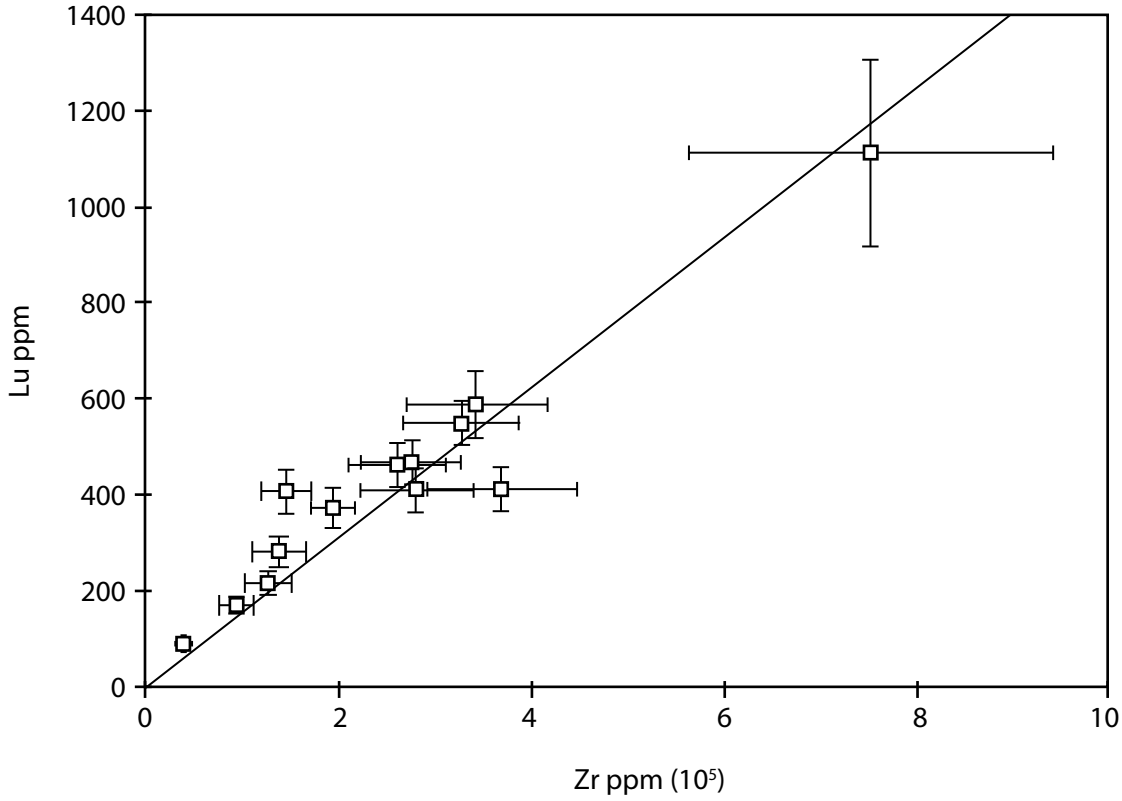

Figure. 5. Plot of Lu concentration vs. Zr concentration for analyses from the lower chamber of run ZrTP-51. Error bars are standard error on each analysis.

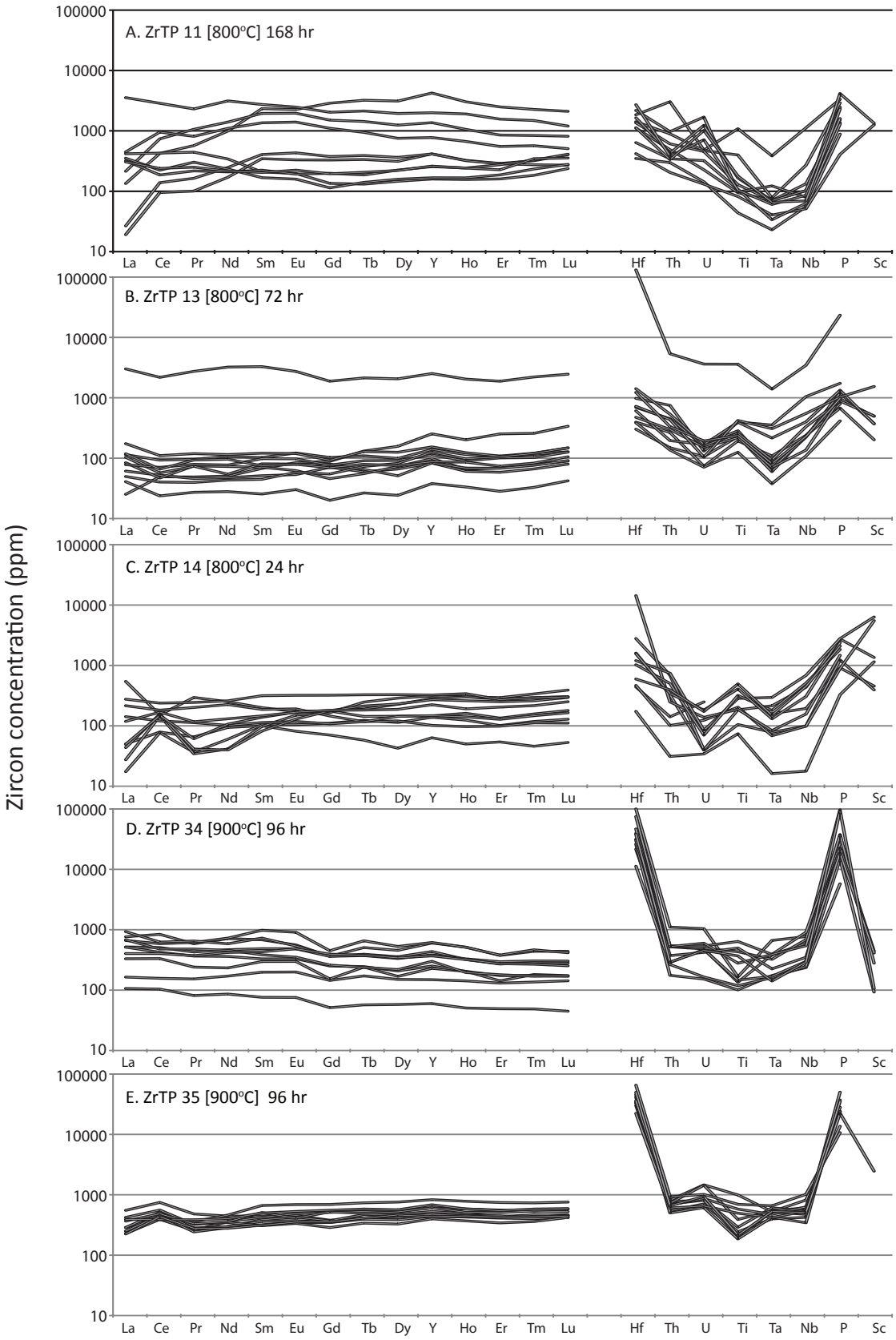

Figure. 6. Plots of lower chamber zircon trace element concentration (ppm) for runs performed using H_2O.

charge and radii, i.e., REE^{+3} trends are not parallel to one another, and Th^{+4}/U^{+4} and Nb^{+5}/Ta^{+5} elemental ratios vary between analysis locations, suggesting equilibrium was not achieved.

In contrast, a number of our NaOH and HCl experiments show coherent partitioning trends consistent with the crystal chemical properties of zircon (Fig. 7 a-e). For NaOH runs ZrTP-40, -47 and -49 and HCl runs -51 and -54, many analyses display prominent positive Ce anomalies (i.e. Ce/Ce*) and positively trending plots of REE concentrations, with Nd/Lu ratios (i.e. LREE/HREE) of 0.10 to 0.25. For the runs performed at 900°C, Ce/Ce* ratios ranged from 1.0 to 2.5 (Fig. 7 c-e), while at 800°C, Ce/Ce* ratios ranged from 3 up to 30 (Fig. 7 a-b). The average composition of lower chamber analyses for runs ZrTP-40, -49, -51, and -54 are reported in Table. 4a. All other lower chamber analyses are reported in Appendix. F.

5.4. Recrystallized zircon composition:

As was the case for zircon synthesis experiments, analysis of material from the lower chambers of our zircon recrystallization experiments involved ablating a 30 µm diameter mass of crystalline material. Unlike zircon synthesis experiments, however, trace element concentrations display a significantly reduced magnitude in diversity between analysis locations within a sample (Fig. 10). This feature extends to accommodate all recrystallization experiments, where trace element concentration profiles for different temperature runs overlap and show a greater consistency to one another (Fig. 10). The average composition of lower chamber analyses for runs ZrMT-02, -03, and -05 are reported in Table. 4b, while all individual lower chamber analyses for these runs are reported in Appendix. G.

The measured concentrations of Zr and Hf, and Zr/Hf ratios in recrystallized zircon are less than those measured in an uncrushed grain of Mud Tank zircon, but identical to our crushed Mud Tank zircon starting material, in which SiO_2 was added to maintain quartz saturation in the

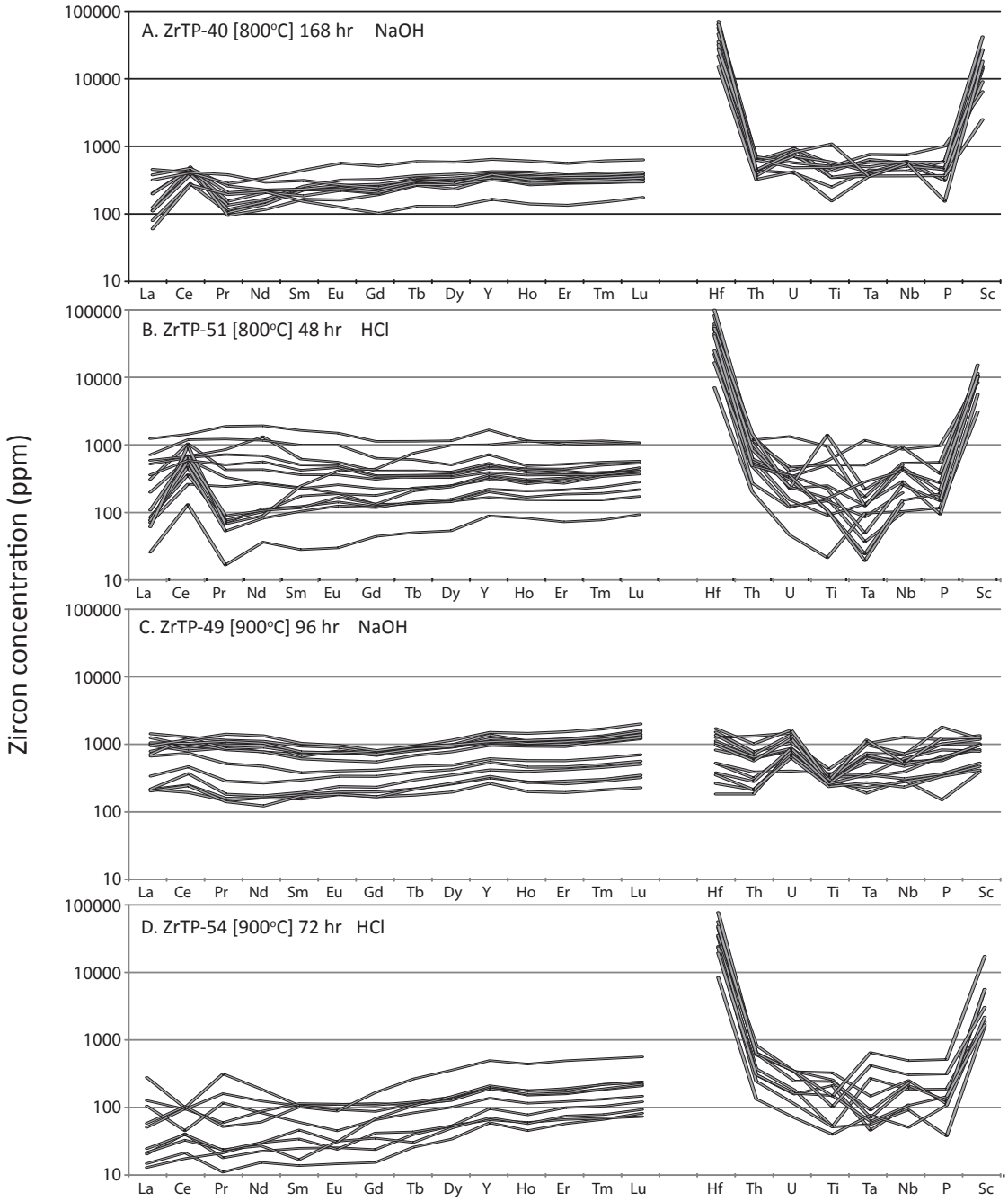

Figure. 7. Plots of lower chamber zircon trace element concentration (ppm) for select runs.

Table. 4a. Lower chamber analyses trace element concentrations (ppm), 1σ error (1 se), and 1σ standard deviation (1 stdev) for our zircon synthesis experiments.

	La	Ce	Pr	Nd	Sm	Eu	Gd	Tb	Dy	Y	Ho	Er	Tm	Lu
ZrTP11	172	478	549	791	1291	1289	1248	1276	1169	1452	1090	905	864	829
1se	*10*	*24*	*28*	*75*	*64*	*46*	*114*	*49*	*111*	*98*	*39*	*44*	*48*	*51*
1 Stdev	*179*	*378*	*417*	*548*	*898*	*878*	*1043*	*1184*	*1160*	*1610*	*1133*	*930*	*826*	*749*
ZrTP13	81	68	69	73	79	88	81	89	90	123	97	99	107	128
1se	*6*	*4*	*7*	*7*	*6*	*7*	*4*	*6*	*8*	*7*	*5*	*10*	*9*	*9*
1 Stdev	*30*	*24*	*28*	*31*	*32*	*35*	*21*	*23*	*15*	*25*	*24*	*25*	*26*	*31*
ZrTP14	42	154	47	65	109	154	178	222	254	295	295	280	304	338
1se	*3*	*8*	*2*	*8*	*8*	*10*	*11*	*12*	*15*	*12*	*11*	*11*	*16*	*15*
1 Stdev	*12*	*6*	*14*	*39*	*30*	*20*	*8*	*30*	*34*	*22*	*24*	*22*	*40*	*54*
ZrTP34	513	451	402	427	464	427	283	330	286	344	283	231	252	243
1se	*481*	*422*	*368*	*422*	*464*	*410*	*256*	*310*	*266*	*324*	*266*	*220*	*238*	*228*
1 Stdev	*264*	*219*	*196*	*218*	*272*	*230*	*131*	*174*	*148*	*182*	*152*	*110*	*134*	*125*
ZrTP35	305	464	322	365	463	481	492	536	553	612	568	542	547	563
1se	*24*	*16*	*19*	*26*	*49*	*32*	*72*	*29*	*26*	*26*	*39*	*44*	*34*	*22*
1 Stdev	*66*	*48*	*55*	*69*	*125*	*122*	*134*	*121*	*119*	*143*	*123*	*117*	*115*	*117*
ZrTP40	178	434	158	182	225	250	248	322	317	374	349	341	353	374
1se	*10*	*29*	*9*	*13*	*19*	*16*	*21*	*21*	*30*	*24*	*26*	*28*	*26*	*22*
1 Stdev	*105*	*76*	*61*	*44*	*32*	*49*	*49*	*38*	*51*	*36*	*51*	*38*	*43*	*42*
ZrTP44	1070	773	993	1016	834	862	789	759	748	788	776	754	756	797
1se	*42*	*32*	*41*	*42*	*58*	*34*	*45*	*25*	*33*	*38*	*34*	*34*	*36*	*35*
1 Stdev	*888*	*298*	*711*	*495*	*294*	*332*	*281*	*320*	*323*	*435*	*378*	*377*	*388*	*468*
ZrTP46	663	852	713	867	958	1110	1051	1139	1135	1251	1196	1132	1168	1245
1se	*38*	*54*	*36*	*96*	*91*	*101*	*147*	*85*	*128*	*111*	*87*	*111*	*101*	*86*
1 Stdev	*388*	*191*	*333*	*512*	*816*	*1019*	*968*	*1017*	*1005*	*1059*	*1018*	*961*	*1014*	*1101*
ZrTP47	550	764	651	763	920	968	1154	1139	1304	1463	1386	1255	1412	1467
1se	*111*	*112*	*75*	*305*	*190*	*189*	*236*	*211*	*318*	*387*	*295*	*308*	*258*	*310*
1 Stdev	*148*	*130*	*216*	*216*	*239*	*253*	*322*	*329*	*365*	*405*	*393*	*375*	*403*	*425*
ZrTP49	699	730	641	616	506	527	496	586	661	840	766	788	860	989
1se	*46*	*54*	*35*	*80*	*57*	*56*	*81*	*50*	*88*	*88*	*64*	*90*	*87*	*78*
1 Stdev	*430*	*384*	*408*	*395*	*282*	*276*	*249*	*295*	*334*	*437*	*413*	*438*	*481*	*569*

Table. 4a. Continued

ZrTP51	85	540	71	100	129	156	137	181	198	282	238	259	296	345
1se	*8*	*54*	*5*	*18*	*21*	*23*	*31*	*21*	*36*	*41*	*27*	*41*	*41*	*37*
1 Stdev	*15*	*149*	*15*	*14*	*32*	*29*	*28*	*48*	*56*	*81*	*62*	*68*	*94*	*113*
ZrTP52	227	339	323	406	443	440	395	326	372	332	336	256	319	305
1se	*75*	*86*	*62*	*278*	*151*	*147*	*129*	*94*	*154*	*138*	*118*	*93*	*96*	*103*
1 Stdev	*133*	*289*	*306*	*414*	*475*	*444*	*364*	*278*	*302*	*241*	*252*	*175*	*209*	*169*
ZrTP53	125	212	174	214	248	242	202	169	211	186	189	134	189	192
1se	*51*	*71*	*42*	*186*	*105*	*105*	*82*	*59*	*111*	*94*	*83*	*58*	*71*	*78*
1 Stdev	*122*	*167*	*125*	*179*	*209*	*217*	*157*	*145*	*155*	*131*	*146*	*94*	*137*	*112*
ZrTP54	30	54	31	41	56	50	71	102	133	192	166	185	206	225
1se	*3*	*6*	*3*	*9*	*11*	*9*	*19*	*14*	*29*	*34*	*22*	*34*	*34*	*29*
1STDEV														

	Hf	Th	U	Ti	Ta	Nb	P	Sc	Si	Zr
ZrTP11	1359	736	635	230	95	198	1316	2039	153320	250067
1se	*109*	*34*	*32*	*39*	*6*	*11*	*8786*	*136*	*5664*	*9231*
1 Stdev	*735*	*808*	*501*	*303*	*102*	*317*	*56*	*1122*		*166473*
ZrTP13	12802	847	470	605	267	664	609	3132	153320	612393
1se	*5769*	*263*	*164*	*207*	*71*	*164*	*10915*	*1045*	*13831*	*210403*
1 Stdev	*39955*	*1579*	*1091*	*1044*	*410*	*1014*	*503*	*6919*		*1385758*
ZrTP14	2421	360	117	257	141	302	2549	1684	153320	185107
1se	*190*	*20*	*7*	*46*	*9*	*17*	*29538*	*109*	*5963*	*36019*
1 Stdev	*4223*	*243*	*74*	*140*	*83*	*221*	*2670*	*841*		*139850*
ZrTP34	41192	468	487	293	306	498	270	36357	153320	576254
1se	*39906*	*441*	*465*	*153*	*289*	*476*	*147*	*30197*	*5240*	*526517*
1 Stdev	*25891*	*264*	*247*	*189*	*164*	*243*	*165*	*31305*		*378135*
ZrTP35	40498	735	987	457	543	627	2595	27842	153320	364811
1se	*4787*	*25*	*60*	*33*	*26*	*27*	*38936*	*1185*	*5268*	*37084*
1 Stdev	*12274*	*135*	*315*	*279*	*88*	*208*		*11878*		*97429*
ZrTP40	43543	521	694	488	498	565	486	17763	153320	313914

Table. 4a. Continued

1se	*3696*	*37*	*39*	*69*	*27*	*24*	*168*	*1317*	*5118*	*16171*
1 Stdev	*19597*	*139*	*203*	*259*	*140*	*105*	*237*	*11607*		*126995*
ZrTP44	24883	680	661	269	644	704	339	18209	153320	307631
1se	*1291*	*26*	*22*	*49*	*29*	*24*	*281*	*874*	*5189*	*18036*
1 Stdev	*7270*	*402*	*385*	*152*	*313*	*327*	*129*	*10527*		*139487*
ZrTP46	54301	1473	912	119	236	213	481	12473	153320	206627
1se	*4614*	*82*	*58*	*26*	*14*	*16*	*713*	*992*	*5208*	*23070*
1 Stdev	*7541*	*573*	*383*	*78*	*65*	*78*	*138*	*8383*		*56965*
ZrTP47	66810	1015	772	162	287	186	272	10566	153320	373448
1se	*32209*	*213*	*140*	*93*	*50*	*35*	*529*	*4107*	*5123*	*1065063*
1 Stdev	*14415*	*419*	*317*	*74*	*147*	*65*	*123*	*5991*		*105000*
ZrTP49	807	543	962	303	539	470	711	835	153320	316603
1se	*84*	*36*	*74*	*71*	*37*	*44*	*954*	*82*	*5127*	*45070*
1 Stdev	*498*	*353*	*376*	*39*	*309*	*166*	*457*	*316*		*42047*
ZrTP51	53341	754	351	299	221	385	326	11147	153320	258862
1se	*8058*	*72*	*43*	*111*	*21*	*52*	*405*	*1664*	*7040*	*54669*
1 Stdev	*29753*	*388*	*338*	*276*	*328*	*284*	*297*	*8850*		*181839*
ZrTP52	57628	355	501	353	258	393	233	3379	153320	635357
1se	*45149*	*110*	*150*	*301*	*68*	*119*	*534*	*1861*	*5308*	*4390293*
1 Stdev	*36354*	*144*	*229*	*229*	*116*	*165*	*222*	*1451*		*329799*
ZrTP53	43291	213	166	322	185	365	161	2359	153320	2556857
1se	*45217*	*80*	*66*	*346*	*60*	*145*	*411*	*1544*	*5775*	
1 Stdev	*23728*	*58*	*88*	*105*	*66*	*160*	*53*	*724*		*1014852*
ZrTP54	37692	489	230	150	225	220	218	5792	153320	154526
1se	*6261*	*48*	*27*	*62*	*24*	*33*	*254*	*907*	*5148*	*36553*
STDEV										

Table. 4b. (b) Lower chamber analyses trace element concentrations (ppm), 1σ error (1 se), and 1σ standard deviation (1 stdev) for our zircon recrystallization experiments.

	La	Ce	Pr	Nd	Sm	Eu	Gd	Tb	Dy	Y	Ho	Er	Tm	Lu
ZrMT 03	102	102	99	112	121	156	152	191	243	350	303	365	471	646
1Se	*4*	*5*	*7*	*11*	*11*	*9*	*16*	*12*	*17*	*19*	*18*	*19*	*26*	*34*
1STDEV	*36*	*30*	*32*	*35*	*27*	*31*	*29*	*35*	*43*	*68*	*51*	*53*	*74*	*105*
ZrMT 02	50	56	54	63	79	97	103	143	188	292	256	314	395	539
1Se	*2*	*2*	*3*	*5*	*6*	*5*	*8*	*7*	*10*	*13*	*12*	*14*	*18*	*23*
1STDEV	*10*	*8*	*7*	*13*	*7*	*10*	*11*	*13*	*20*	*33*	*29*	*34*	*51*	*79*
ZrMT 05	38	46	42	46	64	84	102	142	201	324	280	350	434	586
1SE	*2*	*2*	*2*	*5*	*7*	*4*	*14*	*9*	*12*	*21*	*17*	*22*	*21*	*31*
1STDEV	*10*	*10*	*10*	*10*	*11*	*18*	*16*	*10*	*19*	*11*	*13*	*18*	*23*	*23*

	Hf	Th	U	Ti	Ta	Nb	P	Sc	Si	Zr
ZrMT 03	7418	772	1609	132	133	95	621	1114	149581	303604
1Se	*760*	*31*	*104*	*40*	*6*	*9*	*105*	*79*	*5020*	*31496*
1STDEV	*482*	*117*	*354*	*51*	*39*	*16*	*219*	*138*		*19637*
ZrMT 02	7739	795	712	98	107	56	865	951	149581	325973
1Se	*576*	*28*	*36*	*33*	*4*	*4*	*198*	*51*	*5013*	*24641*
1STDEV	*293*	*285*	*239*		*21*	*18*	*230*	*102*		*5248*
ZrMT 05	7813	617	681	100	96	47	324	784	149581	327301
1SE	*756*	*24*	*32*	*59*	*5*	*2*	*336*	*40*	*5117*	*27514*
1STDEV	*209*	*266*	*71*	*6*	*14*	*13*	*70*	*74*		*11875*

fluid. In this regard, we record no change in Hf concentration or Zr/Hf between original and recrystallized zircon.

All analyses display positively trending REE^{+3} profiles (Fig. 10), typical of zircon. HREE and MREE show a limited range in concentration and gradient, with Gd/Lu ratios from 0.35 to 0.14, while LREE show twice the magnitude of diversity, with decreasing LREE to MREE gradients as concentration increases. With decreasing LREE concentrations, Ce*/Ce ratios increase (Fig. 10), suggesting the increase in concentration and flattening of profile gradient represent a mixed analysis with inter-grain quenched solute (i.e. fluid). Th and U contents vary between runs and yield Th^{+4}/U^{+4} ratios between 1.4 to 0.4, with an average of 0.82 and standard deviation of 0.52. Two analyses from the 900°C run record higher Th/U ratios of 1.9 and 2.3. Nb^{+5}/Ta^{+5} ratios for the 900°C and 1000°C runs vary from 0.7 to 1.2, and 0.9 to 0.6 for the 800°C run.

6. D values:

Zircon/fluid partition coefficients were calculated assuming a Henry's Law relationship (Eq. vii); i.e. for trace element i at equilibrium, the partition coefficient ($D_i^{zircon/fluid}$) will equal the concentration in the zircon (C_i^{zircon}) over that of the fluid (C_i^{fluid}):

Eq. vii. $$\boldsymbol{D_i^{zircon/fluid} = C_i^{zircon}/C_i^{fluid}}.$$

Uncertainties are estimated by propagating errors in analysis concentrations (Eq. viii: e.g., Skoog et al. 1994). The 1σ error on $D_i^{zircon/fluid}$ is calculated using Eq. viii.

Eq. viii. $$\boldsymbol{SE\ D_i^{zircon/fluid} = \sigma\ C_i^{zircon}/C_i^{zircon} + \sigma\ C_i^{fluid}/C_i^{fluid} \times D_i^{zircon/fluid}}$$

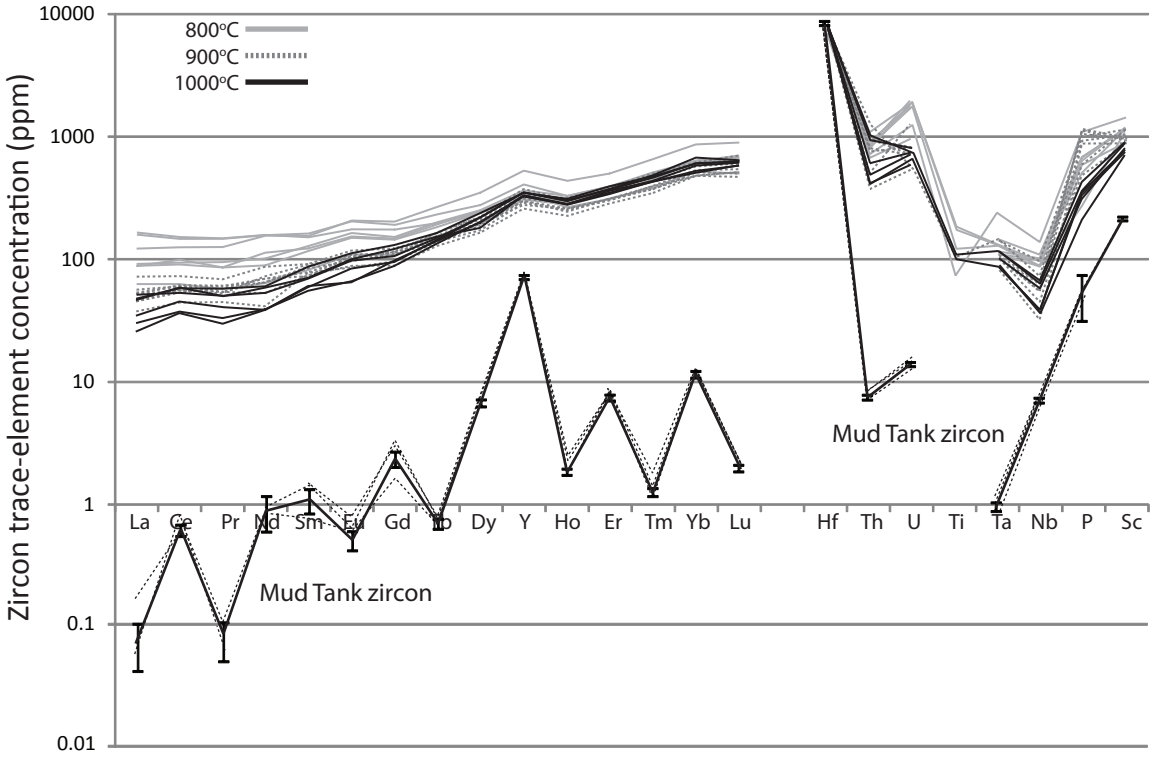

Figure. 8. Plot of lower chamber zircon trace element concentration (ppm) for recrystallization experiments.

Weighted mean partition coefficients ($D_i^{Zircon/fluid}$) are calculated for our zircon synthesis experiments using Eq. ix and reported in Table. 5, with their weighted mean standard deviation, calculated using Eq. x.

Eq. ix. $$\boldsymbol{D_\iota} = \frac{\sum_{i=1}^{n} \boldsymbol{w_i} \boldsymbol{D_i^{zircon/fluid}}}{\sum_{i=1}^{n} \boldsymbol{w_i}}$$

Where $$\boldsymbol{w_i} = \frac{\mathbf{1}}{\boldsymbol{SE}^2}$$

Eq. x. $$\boldsymbol{\sigma} = \sqrt{\frac{\sum_{i=1}^{n} \boldsymbol{w_i}}{\boldsymbol{N}} \frac{\sum_{i=1}^{n} \boldsymbol{w_i} \left(\boldsymbol{D_i} - \boldsymbol{D_\iota} \right)^2}{\boldsymbol{N-1}}}$$

6.1. Zircon synthesis D values:

Weighted mean $D_{REE}^{Zircon/fluid}$ for experiments ZrTP-40, -47, -49, -51, and -54 (as discussed above), display near-parallel trends between run REE concentrations (Fig. 9), with $D^{Zircon/fluid}$ (Gd/Lu) ratios that range between 0.24 to 0.40. The two 800°C runs, ZrTP-40 (NaOH) and ZrTP-51 (HCl), overlap with near equal D values (i.e. $D_{La}^{Zircon/fluid}$ = 0.137 and 0.147, and $D_{Lu}^{Zircon/fluid}$ = 1.151 and 1.127, for ZrTP-40 and-51, respectively). Our two 900°C runs, ZrTP-49 (NaOH) and ZrTP-54 (HCl), display over an order of magnitude variation in $D_{REE}^{Zircon/fluid}$ values between runs (Fig. 7c-e); features that are heavily influenced by the weights of quenched solutes successfully extracted and final fluid weights, and to a much smaller degree, their temperature. When $D^{Zircon/fluid}$ values spread over a wide range for an individual run the maximum $D^{Zircon/fluid}$ values are most likely our best estimates. This is due to most material in the lower chamber being either quartz or unreacted starting material. Since neither of these components contains the

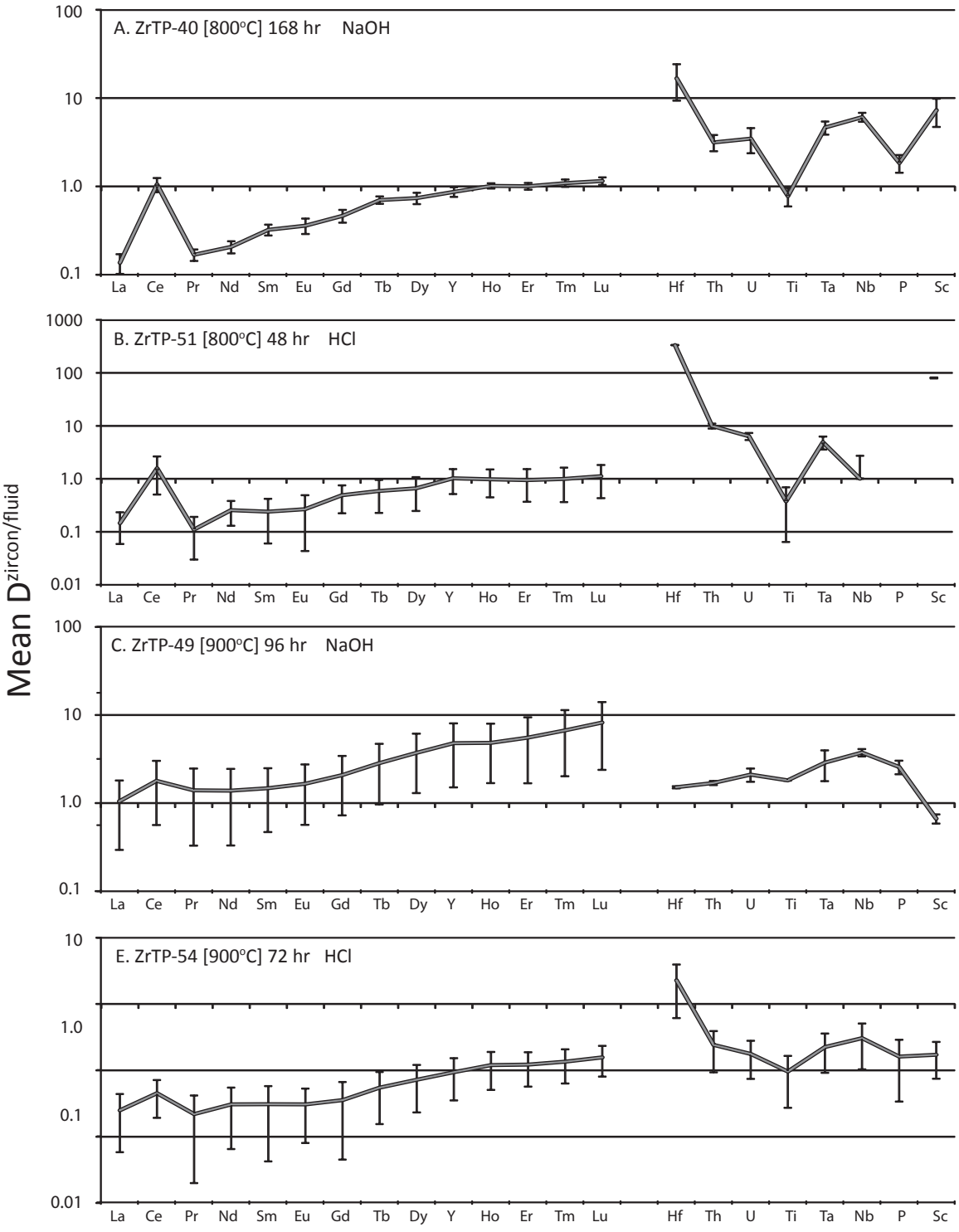

Figure. 9. Plots of calculated weighted mean $D^{zircon/fluid}$ partition coefficients for select runs. Error bars are standard deviation.

Table. 5. Weighted mean $D_i^{zircon/fluid}$ values for our synthesis experiments and mean $D_i^{zircon/fluid}$ values for our recrystallization experiments, and their 1σ standard deviation (stdev).

	La	Ce	Pr	Nd	Sm	Eu	Gd	Tb	Dy	Y	Ho	Er	Tm	Lu
ZrTP40	0.150	1.110	0.185	0.226	0.334	0.372	0.452	0.678	0.724	0.977	0.838	0.963	1.042	1.112
stdev	*0.059*	*0.203*	*0.053*	*0.048*	*0.043*	*0.067*	*0.067*	*0.066*	*0.095*	*0.077*	*0.103*	*0.091*	*0.109*	*0.107*
ZrTP49	0.330	0.624	0.307	0.320	0.506	0.628	0.809	1.051	1.432	1.880	1.612	1.799	2.151	2.525
stdev	*0.230*	*0.425*	*0.247*	*0.258*	*0.326*	*0.381*	*0.491*	*0.655*	*0.869*	*1.122*	*1.076*	*1.248*	*1.494*	*1.803*
ZrTP51	0.308	3.652	0.297	0.450	0.681	0.899	0.925	1.234	1.396	1.751	1.708	1.943	2.072	2.245
stdev	*0.036*	*0.802*	*0.053*	*0.052*	*0.096*	*0.122*	*0.117*	*0.239*	*0.296*	*0.378*	*0.345*	*0.389*	*0.524*	*0.583*
ZrTP54	0.020	0.032	0.022	0.029	0.028	0.028	0.034	0.045	0.061	0.091	0.075	0.096	0.102	0.114
stdev	*0.009*	*0.017*	*0.011*	*0.014*	*0.019*	*0.015*	*0.023*	*0.026*	*0.034*	*0.048*	*0.041*	*0.049*	*0.053*	*0.057*
ZrMT-02	0.063	0.071	0.069	0.080	0.101	0.125	0.134	0.188	0.252	0.397	0.352	0.441	0.577	0.840
stdev	*0.013*	*0.010*	*0.009*	*0.017*	*0.009*	*0.014*	*0.014*	*0.017*	*0.029*	*0.051*	*0.045*	*0.055*	*0.088*	*0.155*
ZrMT-03	0.144	0.143	0.139	0.157	0.172	0.225	0.217	0.279	0.365	0.543	0.470	0.582	0.801	1.228
STDEV	*0.054*	*0.044*	*0.046*	*0.051*	*0.041*	*0.048*	*0.044*	*0.057*	*0.074*	*0.131*	*0.094*	*0.105*	*0.165*	*0.291*
ZrMT-05	0.053	0.064	0.058	0.064	0.090	0.119	0.145	0.205	0.297	0.489	0.425	0.546	0.700	1.008
stdev	*0.014*	*0.014*	*0.015*	*0.014*	*0.016*	*0.027*	*0.023*	*0.015*	*0.031*	*0.019*	*0.021*	*0.032*	*0.043*	*0.050*

	Hf	Th	U	Ti	Ta	Nb	P	Sc	Si	Zr
ZrTP40	12.20	3.03	3.20	0.64	4.54	5.87	1.63	2.40	13.18	1.79
stdev	*13.05*	*2.88*	*3.08*	*0.66*	*1.95*	*5.57*	*1.68*	*3.27*	*13.38*	*1.67*
ZrTP49	0.14	0.48	1.63	0.14	5.88	1.67	1.04	0.37	36.90	0.65
stdev	*0.11*	*0.45*	*1.60*	*0.09*	*2.53*	*1.61*	*1.22*	*0.37*	*35.58*	*0.59*
ZrTP51	2.23	1.74	1.04	0.24	1.40	2.55	-	2.73	3.04	1.44
stdev	*2.98*	*1.92*	*1.32*	*0.36*	*1.46*	*2.90*	-	*3.00*	*3.90*	*1.35*
ZrTP54	2.28	0.24	0.18	0.10	0.23	0.31	0.16	0.17	2.48	1.86
stdev	*2.66*	*0.20*	*0.12*	*0.08*	*0.31*	*0.27*	*0.18*	*0.17*	*2.77*	*1.73*
ZrMT-02		0.59	0.52	-	0.29	0.15	0.35	1.65	1.36	3.14
stdev		*0.240*	*0.209*		*0.061*	*0.049*	*0.177*	*0.266*		*0.098*
ZrMT-03		0.62	1.71	-	0.40	0.28	0.53	2.65	1.60	3.63
Stdev		*0.117*	*0.509*		*0.143*	*0.050*	*0.246*	*0.639*		*0.501*
ZrMT-05		0.48	0.53	-	0.28	0.13	0.13	1.35	1.47	3.31
stdev		*0.233*	*0.062*		*0.043*	*0.039*	*0.034*	*0.170*		*0.217*

trace elements we are interested in measuring, they act as dilutants when incorporated in mixed lower chamber analyses, decreasing Ci^{zircon} and therefore $D_i^{zircon/fluid}$ of all trace elements.

As noted previously, Ce/Ce* anomalies measured in the zircon analyses for our 800°C runs are considerably more prominent than those of our 900°C runs. These features are carried forward in our D values, where our 800°C runs display prominent $D^{Zircon/fluid}$(Ce/Ce*) anomalies (i.e. ZrTP-40 = 7 and ZrTP-51 = 12), while those for our 900°C runs are smaller and range between 1.5 to 1.9. Weighted mean $D_{HFSE}^{Zircon/fluid}$, however, contains no clear patterns between runs (Fig. 9) and have large standard deviations. $D^{Zircon/fluid}$(Zr/Hf), $D^{Zircon/fluid}$(Th/U), and $D^{Zircon/fluid}$(Nb/Ta) ratios vary significantly between runs, with no clear correlation.

6.2. Zircon recrystallization D values:

Because the lower chamber analyses of our recrystallization experiments do not display the same magnitude of diversity as our zircon synthesis experiments, it was unnecessary to calculate weighted mean partition coefficients, and we present in Table. 5. the results of mean calculations. Similar to our zircon synthesis experiments, partition coefficients are low, rarely exceeding ~10 for elements expected to be compatible in zircon (Fig. 10).

Partition coefficients for the trivalent elements (REE, Y, and Sc) increase with decreasing element ionic radii (Fig. 10). The higher $D^{Zircon/fluid}$ values for the LREE in our 800°C run most likely result from mixed analyses, which would affect these low concentration elements most. This is in part supported by small positive $D^{Zircon/fluid}$ (Ce/Ce*) anomalies (maximum = 1.32) being present only when LREE concentrations in the analyzed zircon are low, and the flattening of LREE profile gradients recorded in some 800°C analyses (Fig. 10).

$D^{Zircon/fluid}$ values for trivalent LREE display a board positive correlation with pentavalent elements (P, Nb, and Ta), suggesting potential incorporation via coupled substitution

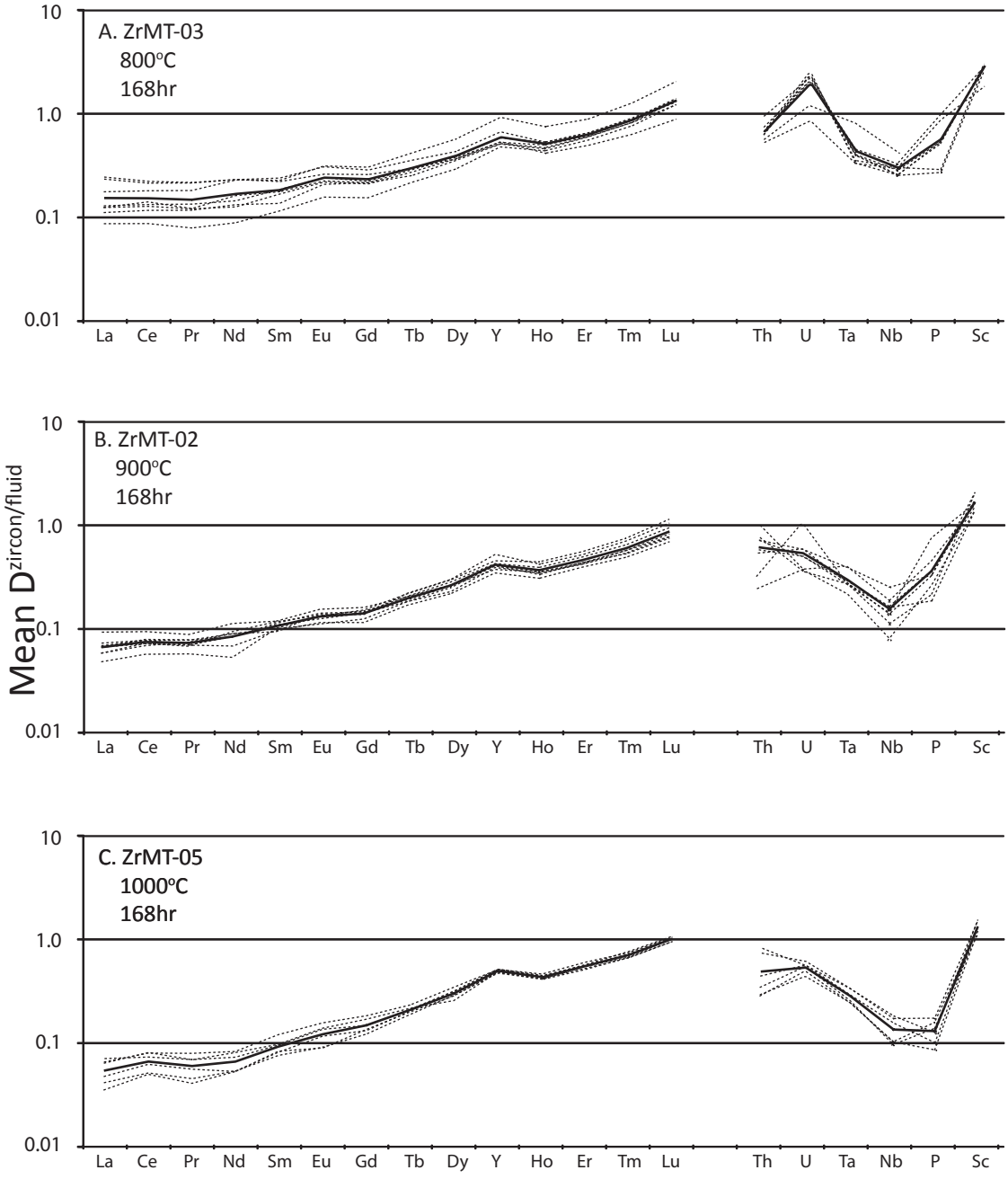

Figure. 10. Plots of calculated weighted mean $D^{zircon/fluid}$ partition coefficients for zircon recrystallization experiments. Dashed lines represent D values calculated using a single analysis from the lower chamber, black lines represent the average for the individual analyses.

mechanisms (Eq. i). The incorporation of trivalent elements, however, far exceeds the pentavalent elements, suggesting their coupled substitution mechanism to be limited. For trivalent MREE, HREE, Y and Sc, which show no clear correlation with pentavalent elements, charge compensation involving a trivalent element and H^{+} for either Zr^{+4} or Si^{+4} may be important under these hydrothermal conditions (i.e. Trail et al., 2011).

$D^{Zircon/fluid}$ values for Th^{+4} and U^{+4} are comparable to trivalent MREE and HREE (Fig. 10), with an average of 0.5 to 0.6 for both elements at 900°C and 1000°C, increasing to $D_{Th}^{Zircon/fluid}$ = 1.0 and $D_{U}^{Zircon/fluid}$ = 2.2 for our 800°C run. $D^{Zircon/fluid}$ (Th/U) ratios vary slightly from 0.28 to 2.71, with an average of ~0.87, suggesting minimal fractionation.

7. Discussion:

7.1. Constraints on experimental reactions:

It is expected that upon attainment of experimental run conditions the fluid becomes supercritical, saturating all compartments of the capsule. Under these conditions, the fluid begins to dissolve the dried trace element components and starting material. Experimental hydrothermal solubility measurements using crystalline Zr-rich compounds are limited in number, especially at conditions relevant for high-grade metamorphism, but have shown zircon dissolution to progress incongruently, forming aqueous species of Zr and Si (Eq. xi), followed by precipitation of baddeleyite (Eq. xii) (e.g. Tole 1985; Ayers et al., 2012).

Eq. xi. $$ZrSiO_{4\,(xt)} + 4H_2O = Zr(OH)_4 + H_4SiO_4$$

Eq. xii. $$Zr(OH)_4 = ZrO_{2(xt)} + 2H_2O$$

As shown in Fig. 11, under quartz saturated conditions, baddeleyite is no longer an equilibrium phase. For our zircon synthesis experiments, by maintaining quartz saturated conditions, the system favors baddeleyite dissolution and zircon precipitation (Eq. xi and v). As long as unreacted starting material remained in contact with fluid, zircon growth is expected to occur at a steady state, with baddeleyite dissolution being the rate-limiting step due to its exceptionally low solubility.

In regard to our zircon recrystallization experiments, in the presence of quartz-saturated fluid, zircon is an equilibrium phase and congruent dissolution occurs until the fluid is saturated in zircon (Fig. 11). This means, unlike our zircon synthesis experiments, zircon recrystallization experiments require a different reaction pathway to attain re-equillibrium, one that results in congruent dissolution and subsequent re-precipitation (e.g. Tromans, 2006). Using observations from natural samples, zircon recrystallization during hydrothermal infiltration is proposed to occur via two thermodynamically independent diffusion-reaction mechanisms. Firstly, the inward diffusion of hydrous components facilitates recovery of structurally damaged zircon in the solid state, and secondly, a coupled interface dissolution-reprecipitation mechanism, in which an inwardly diffusing hydrous component catalyzes congruent zircon dissolution, leading to fluid super-saturation and epitaxial precipitation of new re-equilibrated zircon as the reaction front continues to migrate inward (e.g. Geisler et al., 2007).

Mud Tank zircon was chosen as the starting material due to its gem quality purity, i.e. low trace-element content, lack of inclusions, and un-damaged (or insignificantly damaged) crystalline lattice. Studies of these hydrothermal zircon recrystallization processes suggest

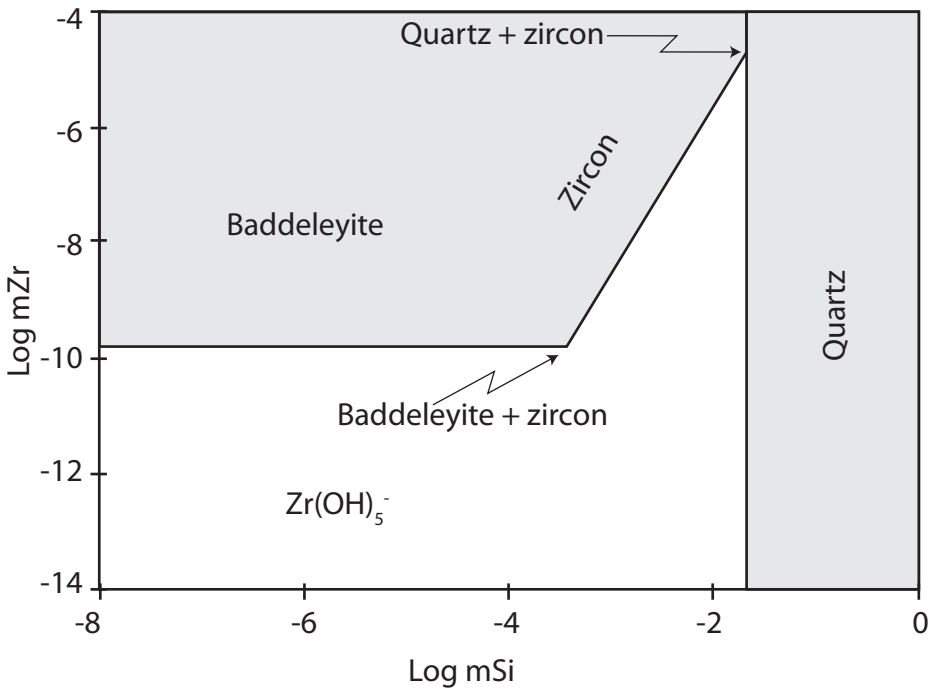

Figure. 11. A solubility diagram for the system ZrO_2-SiO_2-H_2O at 200^0C and 1m NaOH. Reproduced from Ayers et al., (2012).

zircon-fluid reactions are driven by expulsion of non-ideal and thermodynamically unstable solid-solution components (i.e. thorite and coffinite) (e.g. Geisler et al., 2007; Ferris et al., 2010), and recovery of structural damage and metamictization (radiation damage) (e.g. Geisler et al., 2007). For Mud Tank zircon, which lacks these features, the difference in Gibbs free energy between the original Mud Tank zircon and zircon in equilibrium with the fluid phase is expected to be small. However, crystals that are roughly a micron or smaller in size have high surface free energies, which cause them to have higher solubilities than larger grains. Therefore, we used finely ground Mud Tank zircon powder to promote interface dissolution-repecipitation and zircon re-equilibration.

Using Fig. 3b.iii and 3b.iv, zircon recrystallization experiments appear to contain hydrothermally altered coarse Mud Tank zircon fragments, surrounded by a homogeneous grey re-equilibrated zircon matrix (Fig. 3b. vi). The lack of observable individual idiomorphic zircon grains indicates recrystallization did not involve significant crystal growth, but rather, an in-situ coupled interface dissolution-reprecipitation mechanism as described above. Polycrystalline aggregates of recrystallized zircon have been observed in natural samples (e.g. Tomaschek et al., 2003; Corfu et al., 2003; Rubatto et al., 2008), suggesting that progress toward textural equilibrium lags behind the attainment of chemical equilibrium (Putnis et al., 2005: Soman et al., 2010).

For our 800°C H_2O fluid runs, baddeleyite and zircon solubilities and zircon growth rates are expected to be at their lowest. In hydrothermal systems, the solubility of zircon and baddeleyite are largely insensitive to changes in physical environment (i.e. pressure and temperature), but show a strong dependence on fluid pH (e.g. Tole 1985; Ayers et al., 2012). This is because Zr-hydroxyl complexes, i.e. $Zr(OH)_4$, display an amphoteric behavior, being able to donate or accept a hydrogen cation (i.e. proton). With the formation of Zr-hydroxide

complexes in the fluid other than $Zr(OH)_4^0$ (i.e. $Zr(OH)^{+3}$, $Zr(OH)_2^{+2}$, $Zr(OH)_3^+$, and $Zr(OH)_5^-$), the solubility of baddeleyite and zircon in our starting material increases. By using 1M HCl and NaOH fluids, the rates of baddeleyite dissolution and zircon growth are expected to be significantly enhanced, favoring attainment of equilibrium. Continued growth of insoluble Zr-bearing minerals (i.e. zircon or baddeleyite) is generally controlled through surface or interface reactions that have large activation energies. This makes their rate of growth greatest at high temperatures (Watson and Harrison 1983; Carlson 1989; Klemme and Meyer 2003).

An issue, however, with enhancing zircon growth kinetics is that by raising the rate of zircon growth we also increase the rate of consumption of trace elements in the fluid. If the rate of trace element consumption exceeds the rate of diffusion to the zircon interface, a region of trace element depletion, or diffusive boundary, will develop around the zircon and lead to disequilibrium with the bulk system (Luo and Ayers, 2009). These circumstances can be described in terms of a Peclet number (Pe) >1; i.e. the rate of advection/rate of diffusion, which in this case represents the ratio of zircon growth time scale (linear growth rate times the width of the diffusive boundary) and the diffusive time scale (element diffusivity in the fluid). When the Peclet number is high, the zircon surface is in equilibrium with a depleted boundary layer but not the bulk fluid.

7.2. Assessment of equilibrium.

7.2.1. Zircon synthesis experiments.

For the 800°C H_2O synthesis experiments (ZrTP-11, -13, and -14), run durations were staged at 24, 72, and 168 hours (i.e. one day to two weeks). The intent was to determine the time required to reach chemical equilibrium, which should be greatest at the lowest

experimental temperatures. However, despite our best attempts, establishing the attainment of equilibrium under these conditions using lower chamber trace element analyses proved impossible. The origin of trace element heterogeneity for these H_2O zircon synthesis runs likely relates to the low solubility of ZrO_2 (i.e. baddeleyite) in the starting material, and the low diffusivity of Zr^{+4} in hydrothermal fluids (e.g. Ayers et al., 2012). A significant factor controlling interface reaction rates and zircon growth is the rate at which reactants (Zr^{+4}) can diffuse from their source to a site of nucleation and growth. When diffusivity is low, growth is suppressed through the development of chemically depleted regions surrounding the zircon grain, while nucleation is enhanced. This leads to a zircon grain population with a small (Fig. 3a.v) and spatially uniform radii (e.g. Carlson 1989), as shown in Fig. 3a.iv.

For the majority of our synthesis experiments, the small zircon grain sizes and difficulty in their identification supports this situation of suppressed zircon growth and a limited extent of reaction progression. Under these conditions, the fluid phase retains a high concentration of doped trace elements, and following completion of the run, quenched solutes in the inter-grain regions of the lower chamber will be particularly trace element rich, making LA analyses of the lower chamber particularly susceptible to solute contamination. This scenario is supported by the variance in element concentration being greatest (lowest precision) for elements that are typically incompatible in zircon (i.e. LREE), and thus strongly enriched in the quenched solutes. In contrast, elements that are compatible in zircon (i.e. HREE, Hf, U and Th) will have a higher concentration in the crystalline zircon and lower in the quenched solutes, reducing the effect of solute contamination. Like Zr though, the high valence of dissolved Hf, Nb, Ta, U, and Th (i.e. HFSE) ions results in low chemical diffusivities, and it is reasonable to expect disequilibrium partitioning for these highly charged HFSE. At the higher temperatures diffusivities should be higher and the rate of zircon growth greater, which should all promote the complete reaction of

starting material and the attainment of equilibrium. However, for our 900°C H_2O runs, we observed a similar degree of variability in concentrations and element ratios to runs at 800°C; supporting the insignificance of temperature relative to pH for baddeleyite dissolution and zircon reaction, as described above.

Along with contamination from quenched solutes, analyses are also susceptible to mixing involving clumps or clusters of 10 to 60 μm diameter Zr-rich material, which are found throughout the lower chamber (Fig. 3a.vi). We interpret these to represent inner core-like domains of unreacted starting material, surrounded by thin (i.e. <5 μm) zircon overgrowths. The generation of these features indicates that diffusivity of Zr^{+4}, as hydrothermal or silica complexes, is a spatially limited process, where ZrO_2 dissolution and zircon nucleation occur practically in-situ upon fluid infiltration. Once a corona of zircon has formed around a clump of starting material it is no longer in contact with the fluid, and progressive zircon crystallization can only occur with inter-granular or inter-grain diffusion of fluid and Si^{+4} across the boundary of the zircon corona, which we do not expect.

These features, however, do not necessarily indicate localized equilibrium (i.e. on the zircon grain scale) was not attained, although it appears unlikely for all elements, only that it is difficult to confirm. If we assume equilibrium to have been attained, trace-elements should be either retained in the fluid (i.e. Quenched solutes) or incorporated into zircon grains (i.e. following Henry's law). Under these circumstances, analyses from the lower chamber should display smooth linear trends of isovalent REE^{+3} concentrations (i.e. M-$HREE^{+3}$) that represent a simple mixture of these two components. The highly variable REE^{+3} patterns observed in a significant number of runs (e.g. Figs. 5 and 6), however, does not support a simple mixing relationship. These complex trends suggest either that the distribution of trace elements during the run was heterogeneous (i.e. not at equilibrium), or that other insoluble phases co-

precipitated and contributed in variable amounts to mixed analyses. Because Sc^{+3} and Hf^{+4} were added as oxide powders to the starting material, possible candidates will likely involve these elements, and we did indeed observe rare micron to sub-micron sized grains of Hf and Sc rich material.

For runs that used HCl and NaOH as their fluid phase, we observe evidence of potential attainment of equilibrium during zircon growth. A number of positively trending plots of $D_{REE}^{zircon/fluid}$ values, with positive Ce anomalies (Fig. 7 and 8), are typical of zircon grown under these oxidizing conditions. Despite this, however, measured $D^{Zircon/fluid}$ values for the HFSE are highly variable (Fig. 9), making it unclear what factors are important for identifying attainment of equilibrium during our synthesis runs.

7.2.2. Zircon recrystallization experiments.

In contrast to our zircon-H_2O synthesis experiments, the overlapping zircon REE concentration (Fig. 8) and $D_{REE}^{Zircon/fluid}$ profiles (Fig. 10) calculated for our zircon recrystallization experiments favor partitioning equilibrium for these elements to have been attained. Without the need for fluid diffusion or advection of zircon structural components toward an interface of a growing zircon grain, the competition between rates of trace-element incorporation and fluid diffusion/advection during recrystallization are minimized, and the generation of chemically depleted regions is not expected to be important. In this regard, in-situ recrystallization of zircon will be kinetically favored relative to baddeleyite dissolution and growth of centralized zircon grains, leading to a greater extent of reaction progression, attainment of equilibrium, and a lower probability of contamination from interstitial quenched solutes.

The equal concentrations of both Zr and Hf measured in the original and recrystallized Mud Tank zircon is consistent with re-equilibration involving in-situ recrystallization and

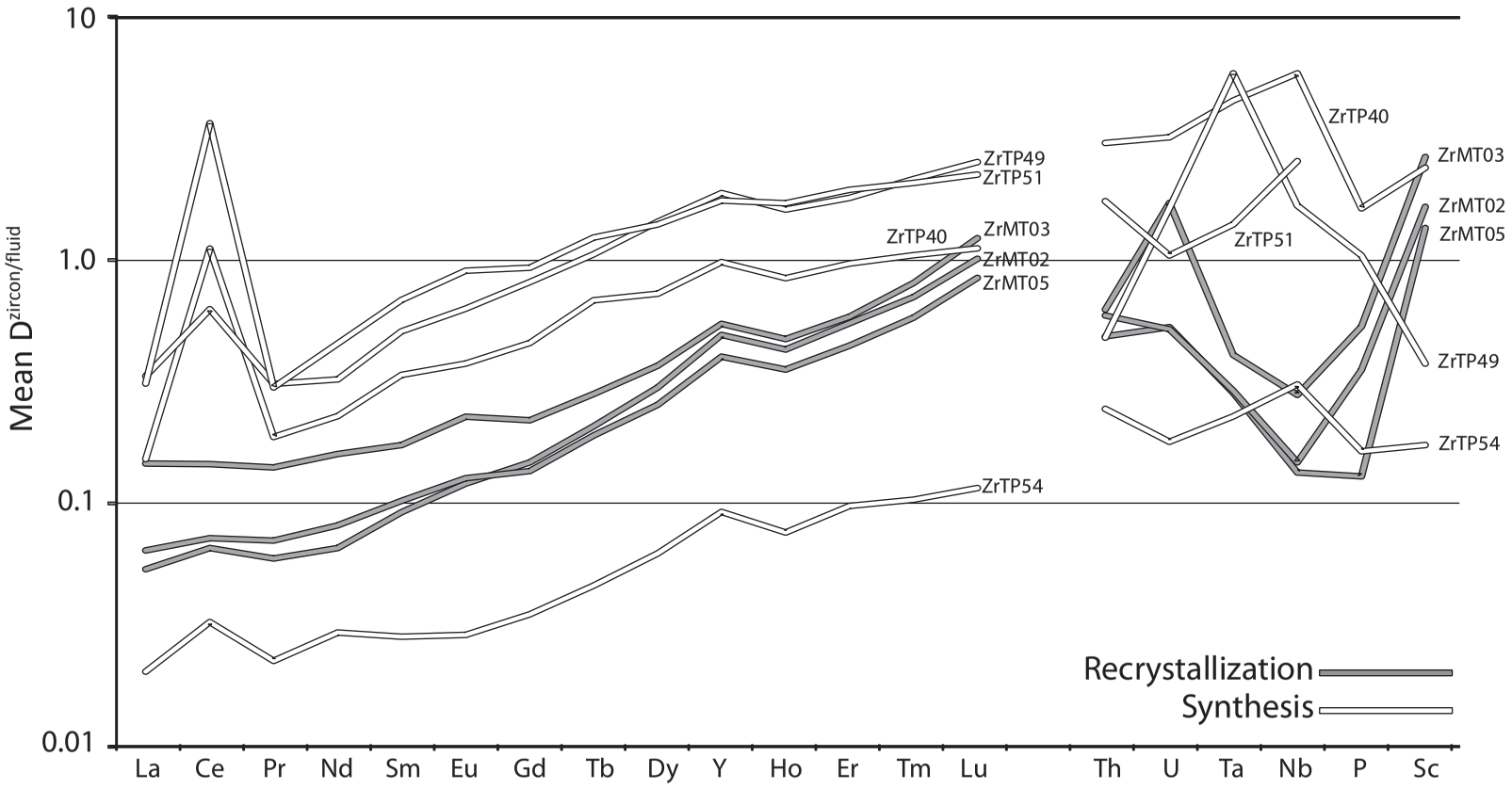

Figure. 12. Plot of calculated weighted mean $D^{zircon/fluid}$ partition coefficients for both zircon synthesis and recrystallization experiments.

retention of the ideal solid-solution end member Hafnon ($HfSiO_4$). The low $D_{Th}^{Zircon/fluid}$ and $D_U^{Zircon/fluid}$ values, however, indicate the thorite ($ThSiO_4$) and coffinite ($USiO_4$) solid-solution end members are not particularly stable during recrystallization, consistent with natural and theoretical observations (e.g. Geisler et al., 2007; Ferris et al., 2010). The lack of significant Th/U fractionation (i.e. $D^{zircon/fluid}$(Th/U) >~0.4) suggests the generation of Th/U ratios 10^{-2} to 10^{-3} in zircon grains from metamorphic and hydrothermally altered rocks relates to either exsolution or extraction of a Th-rich component (e.g. Thorite, monazite, alanite), and preservation of U components in zircon during recrystallization.

7.3. Comparison of $D^{Zircon/fluid}$ values between synthesis and recrystallization experiments.

Despite the challenges associated with evaluation of analyses collected from the lower chambers of our zircon synthesis experiments, calculated $D_{REE}^{zircon/fluid}$ values for both our zircon synthesis and recrystallization experiments show a similar magnitude in the difference between $D_{LREE}^{Zircon/fluid}$ and $D_{HREE}^{Zircon/fluid}$ (Fig. 12). This feature supports both zircon synthesis and recrystallization experiments to be complimentary approaches to evaluate trace-element partitioning in zircon. For the +4 and +5 trace elements, there exists no clear relationship between zircon synthesis and recrystallization experiments, highlighting the difficulty in attaining equilibrium partitioning and collection of clean analyses in our zircon synthesis experiments.

8. Conclusions

This study presents the first zircon-hydrothermal fluid partition coefficients measured. The challenge to synthesis zircon in hydrothermal fluids at high pressures and temperatures by

itself has been a significant technical challenge, but allows for exploration of other research avenues to investigate the geochemical and thermodynamic behavior of zircon in hydrothermal systems appropriate to high-grade metamorphic systems.

The degree to which our hydrothermal zircon grains incorporate the REE's appears to be considerably lower than for zircon grains synthesized from a melt (e.g. Rubatto and Hermann 2007; Luo and Ayers 2009). In their 1.5 GPa Zircon/melt experiments, Luo and Ayers (2009) used a peralkaline starting-material doped with 500-300 ppm HREE (i.e. compatible elements: Ho, Yb and Lu), and measured ~5000 ppm of these elements in their experimentally grown zircon grains. Despite doping our fluids with up to three times the concentration of HREE used by Luo and Ayers (2009), i.e. 1000-1500 ppm, our zircon analyses typically contained <500-1000 ppm. While this feature is not inconsistent with the observations of low REE concentrations for zircon grains proposed to have grown naturally from a hydrothermal fluid, sampling of unreacted starting material and quartz by our 20-30 μm diameter laser spots may have diluted the trace elements contained in zircon and biased our measured $D^{Zircon/fluid}$ toward low values.

Although it was particularly challenging to evaluate the attainment of equilibrium, measured $D^{Zircon/fluid}$ values for +3 ions from a number of runs have the characteristics expected for zircon, including positively trending $D_{REE}^{Zircon/fluid}$ values and prominent Ce anomalies. Inconsistent $D^{Zircon/fluid}$ values for the +5 cations P, Ta, and Nb suggest that they did not achieve partitioning equilibrium under the conditions of our experiments, owing to their limited diffusivity or complex behavior in hydrothermal fluids. This feature limits our ability to explore substitution mechanisms for trivalent cations (i.e. REE) and may be an important limiting factor for attaining equilibrium in our experiments.

9. References

Ayers, J.C., Brenan, J.B., Watson, E.B., Wark, D.A., Minarik, W.G., 1992. A new capsule technique for hydrothermal experiments using the piston-cylinder apparatus. American Mineralogist 77, 1080-1086.

Ayers, J.C., Dittmer, S.K., Layne, G.D., 1997. Partitioning of elements between peridotite and H2O at 2.0-3.0 GPa and 900-1100°C, and application to models of subduction zone processes. Earth And Planetary Science Letters 150, 381-398.

Ayers J.C., Zhang L., Luo Y., Peters T., 2012. Zircon and Baddeleyite Solubility in Alkaline Aqueous Fluids at Upper Crustal Conditions. Submitted

Ayers, J.C., Watson, E.B., 1991. Solubility Of Apatite, Monazite, Zircon, And Rutile In Supercritical Aqueous Fluids With Implications For Subduction Zone Geochemistry. Philosophical Transactions Of The Royal Society Of London Series A-Mathematical Physical And Engineering Sciences 335, 365-375.

Becker, H., Jochum, K.P., Carlson, R.W., 1999. Constraints from high-pressure veins in eclogites on the composition of hydrous fluids in subduction zones. Chemical Geology 160, 291-308.

Carlson, W.D., 1989. The significance of intergranular diffusion to the mechanisms and kinetics of porphyroblast crystallization. Contributions To Mineralogy And Petrology 103, 1-24.

Cherniak, D.J., 2010. Diffusion in Accessory Minerals Zircon, Titanite, Apatite, Monazite and Xenotime, in: Zhang, Y.X.C.D.J. (Ed.), Diffusion in Minerals and Melts, pp. 827-869.

Cherniak, D.J., Watson, E.B., 2003. Diffusion in zircon, in: Hanchar, J.M.H.P.W.O. (Ed.), Zircon, pp. 113-143.

Claiborne, L.L., Miller, C.F., Flanagan, D.M., Clynne, M.A., Wooden, J.L., 2010. Zircon reveals protracted magma storage and recycling beneath Mount St. Helens. Geology 38, 1011-1014.

Ferriss, E.D.A., Ewing, R.C., Becker, U., 2010. Simulation of thermodynamic mixing properties of actinide-containing zircon solid solutions. American Mineralogist 95, 229-241.

Freda, C., Baker, D.R., Ottolini, L., 2001. Reduction of water loss from gold-palladium capsules during piston-cylinder experiments by use of pyrophyllite powder. American Mineralogist 86, 234-237.

Geisler, T., Schaltegger, U., Tomaschek, F., 2007. Re-equilibration of zircon in aqueous fluids and melts. Elements 3, 43-50.

Glodny, J., Kuhn, A., Austrheim, H., 2008. Geochronology of fluid-induced eclogite and amphibolite facies metamorphic reactions in a subduction-collision system, Bergen Arcs, Norway. Contributions To Mineralogy And Petrology 156, 27-48.

Hanchar, J.M., Finch, R.J., Hoskin, P.W.O., Watson, E.B., Cherniak, D.J., Mariano, A.N., 2001. Rare earth elements in synthetic zircon: Part 1. Synthesis, and rare earth element and phosphorus doping. American Mineralogist 86, 667-680.

Hawkesworth, C., Cawood, P., Kemp, T., Storey, C., Dhuime, B., 2009. A Matter of Preservation. Science 323, 49-50.

Hoskin, P.W.O., Schaltegger, U., 2003. The composition of zircon and igneous and metamorphic petrogenesis, in: Hanchar, J.M.H.P.W.O. (Ed.), Zircon, pp. 27-62.

Jiang, S.-Y., Wang, R.-C., Xu, X.-S., Zhao, K.-D., 2005. Mobility of high field strength elements (HFSE) in magmatic-, metamorphic-, and submarine-hydrothermal systems. Physics and Chemistry of the Earth, Parts A/B/C 30, 1020-1029.

Klemme, S., Meyer, H.-P., 2003. Trace element partitioning between baddeleyite and carbonatite melt at high pressures and high temperatures. Chemical Geology 199, 233-242.

Kosler, J., Tubrett, M.N., Sylvester, P.J., 2001. Application of Laser Ablation ICP-MS to U-Th-Pb Dating of Monazite. Geostandards Newsletter 25, 375-386.

Liermann, H.-P., Isachsen, C., Altenberger, U., Oberhansli, R., 2002. Behavior of zircon during high-pressure, low-temperature metamorphism: Case study from the Internal Unit of the Sesia Zone (Western Italian Alps). Eur J Mineral 14, 61-71.

Luo, Y., Ayers, J.C., 2009. Experimental measurements of zircon/melt trace-element partition coefficients. Geochimica Et Cosmochimica Acta 73, 3656-3679.

Miller, C.F., McDowell, S.M., Mapes, R.W., 2003. Hot and cold granites? Implications of zircon saturation temperatures and preservation of inheritance. Geology 31, 529-532.

Miller, J.S., Matzel, J.E.P., Miller, C.F., Burgess, S.D., Miller, R.B., 2007a. Zircon growth and recycling during the assembly of large, composite arc plutons. Journal Of Volcanology And Geothermal Research 167, 282-299.

Newton, R.C., Manning, C.E., Hanchar, J.M., Colasanti, C.V., 2010. Free energy of formation of zircon based on solubility measurements at high temperature and pressure. American Mineralogist 95, 52-58.

Rubatto, D., Hermann, J., 2003. Zircon formation during fluid circulation in eclogites (Monviso, Western Alps): Implications for Zr and Hf budget in subduction zones. Geochimica Et Cosmochimica Acta 67, 2173-2187.

Rubatto, D., Hermann, J., 2007a. Zircon behaviour in deeply subducted rocks. Elements 3, 31-35.

Schmidt, C., Rickers, K., Wirth, R., Nasdala, L., Hanchar, J.M., 2006. Low-temperature Zr mobility: An in situ synchrotron-radiation XRF study of the effect of radiation damage in zircon on the element release in H2O+HCl +/- SiO2 fluids. American Mineralogist 91, 1211-1215.

Skoog, D.A., D.M. West, F.J. Holler, 1994, Analytical chemistry (6th ed)Harcourt Brace College Publishers, Orlando, Florida.

Spandler, C., Hermann, J., Arculus, R., Mavrogenes, J., 2003. Redistribution of trace elements during prograde metamorphism from lawsonite blueschist to eclogite facies; implications for deep subduction-zone processes. Contributions to Mineralogy and Petrology 146, 205-222.

Spandler, C., Pettke, T., Rubatto, D., 2011. Internal and External Fluid Sources for Eclogite-facies Veins in the Monviso Meta-ophiolite, Western Alps: Implications for Fluid Flow in Subduction Zones. Journal Of Petrology 52, 1207-1236.

Speer, J.A., 1980. Zircon. Reviews in Mineralogy and Geochemistry 5, 67-112.

Tole, M.P., 1985. The Kinetics Of Dissolution Of Zircon (Zrsio4). Geochimica Et Cosmochimica Acta 49, 453-458.

Watson, E.B., Cherniak, D.J., Hanchar, J.M., Harrison, T.M., Wark, D.A., 1997. The incorporation of Pb into zircon. Chemical Geology 141, 19-31.

Watson, E.B., Harrison, T.M., 1983. Zircon Saturation Revisited - Temperature And Composition Effects In A Variety Of Crustal Magma Types. Earth And Planetary Science Letters 64, 295-304.

Zeh, A., Gerdes, A., Will, T.M., Frimmel, H.E., 2010. Hafnium isotope homogenization during metamorphic zircon growth in amphibolite-facies rocks: Examples from the Shackleton Range (Antarctica). Geochimica Et Cosmochimica Acta 74, 4740.

Zhang, Z.-M., Shen, K., Sun, W.-D., Liu, Y.-S., Liou, J.G., Shi, C., Wang, J.-L., 2008. Fluids in deeply subducted continental crust: Petrology, mineral chemistry and fluid inclusion of UHP metamorphic veins from the Sulu orogen, eastern China. Geochimica Et Cosmochimica Acta 72, 3200-3228.

Zheng, Y.F., Gao, T.S., Wu, Y.B., Gong, B., Liu, X.M., 2007. Fluid flow during exhumation of deeply subducted continental crust: zircon U-Pb age and O-isotope studies of a quartz vein within ultrahigh-pressure eclogite. J. Metamorph. Geol. 25, 267-283.

CHAPTER V

CONCLUSIONS

Zircon ($ZrSiO_4$) grains extracted from high grade metamorphic and hydrothermally altered continental crust have the potential to record multiple events associated with a protracted history of crustal growth and evolution. When combined with other petrologic, geochemical, and geochronological information, detailed geodynamic models can be developed to unravel and understand the timing and nature of complex processes associated with mountain building in a particular region. For the Dabie Mountains in Central-East China, zircon grains extracted from eclogites in the Huwan Shear Zone, and a Tonalite Gneiss in the Northern Dabie Complex, provide evidence for a protracted and sequential period of continental accretion, collision, and mountain belt construction during the amalgamation and suturing of the South and North China Blocks.

During these events, zircon grains hosted in their respective crustal lithologies responded to metamorphism by reacting with either locally produced or externally intruded hydrothermal fluids, which facilitate recrystallization and alteration, leading to generation of new textures, trace element characteristics, and geochronological information. Of particular note is the loss of radiogenic Pb, which effectively restarts the zircon geochronometer, and a reduction in the concentration of incompatible Light Rare Earth Elements (i.e. La, Pr, Nd, Sm), relative to their Heavy Rare Earth Elements (i.e. Ho, Er, Yb, Lu), and thorium (Th) relative to uranium (U). The loss of these components provides convincing evidence that the non-ideal thorite ($ThSiO_4$) solid solution end member in zircon ($ZrSiO_4$) is no longer thermodynamically stable under high grade metamorphic and hydrothermal conditions. This leads to rejection of

the thorite end member by zircon in an attempt to re-equilibrate under its new conditions. This attainment of equilibrium during metamorphism occurs through the diffusion-reaction recrystallization mechanism of coupled interface dissolution-reprecipitation, in which an inwardly diffusing hydrous component catalyzes dissolution and un-mixing of the thorite and zircon end members, followed by fluid super-saturation and epitaxial precipitation of new re-equilibrated zircon with migration of the reaction front. In most cases, zircon recrystallization and alteration did not lead to changes in their original Hf isotopic composition, suggesting recrystallization is an in-situ processes and the ideal solid solution end member hafnon ($HfSiO_4$), is thermodynamically preserved. Due to this feature, evidence of new zircon growth during metamorphism can be recognized by the addition of a zircon rim whose Hf isotope composition is different to that of its respective core.

This conclusion is supported by the zircon/fluid element partitioning study, where the equal concentrations of both Zr and Hf measured in both the original and recrystallized Mud Tank zircon is consistent with re-equilibration involving in-situ recrystallization and preservation of the ideal solid-solution end member Hafnon ($HfSiO_4$). The low $D_{Th}^{Zircon/fluid}$ and $D_{U}^{Zircon/fluid}$ values, indicate thorite and coffinite ($USiO_4$) solid-solution end members are not particularly stable during recrystallization of zircon, and the lack of significant Th/U fractionation (i.e. $D^{zircon/fluid}(Th/U) >\sim 0.4$) for either zircon synthesis or recrystallization experiments suggests the generation of Th/U ratios 10^{-2} to 10^{-3} in zircon grains from metamorphic and hydrothermally altered rocks, likely relates to exsolution or extraction of a Th-rich component with preservation of U components in zircon during metamorphism.

APPENDIX A

ANALYSES OF USGS ROCK STANDARDS BCR-2, BHVO-1 AND AGV-1.

	Measured AGV-1	Measured AGV-1	Measured AGV-1	AGV-1	Measured BCR-2	Measured BCR-2	Ref BCR-2	Measured BHVO-1	Ref BHVO-1	Measured BHVO-2	Measured BHVO-2	Ref BHVO-2	Measured G-2	Ref G-2
Li	10.8	10.7	10.8	10.7	9.5	10.0	9.0	4.8	4.6	4.8	4.6	4.8	32.7	34.0
Be	2.2	2.1	2.1	2.1	2.1	2.3	1.6	0.9	1.1	1.0	1.0	1.1	2.5	2.5
Sc	12.6	12.6	12.3	12.2	32.7	33.4	33.0	14.1	31.8	31.6	30.6	32.0	3.7	3.5
V	121	120	118	121	416	422	416	314	317	320	311	317	34	36
Cr	9.9	11.3	11.5	10.1	20.2	15.9	18.0	277.6	289.0	282.8	274.9	280.0	13.5	8.7
Cr	9.5	11.0	11.2	10.1	20.1	16.2	18.0	279.7	289.0	282.6	276.0	280.0	12.7	8.7
Co	15.7	15.7	15.0	15.3	36.8	37.7	37.0	44.4	45.0	44.9	43.6	45.0	4.4	4.6
Ni	15.2	16.3	16.5	16.0	15.9	12.2	13.0	119.9	121.0	118.6	118.0	119.0	4.5	5.0
Cu	57.6	57.7	56.1	58.0	22.2	22.2	19.0	132.5	136.0	127.6	124.7	127.0	9.4	11.0
Zn	88.7	87.4	86.6	88.0	129.3	129.6	127.0	102.3	105.0	103.2	102.1	103.0	82.2	86.0
Ga	20.7	20.2	20.4	20.0	21.9	22.4	23.0	21.1	21.0	21.5	20.7	21.7	23.6	23.0
Ge	1.21	1.19	1.17	1.25	1.68	1.67	0.00	1.67	1.64	1.68	1.66	1.60	1.09	1.14
Rb	68.4	67.7	66.3	66.6	47.3	47.0	48.0	9.5	11.0	10.2	9.6	9.8	167.1	170.0
Sr	668	659	650	660	338	337	346	389	403	394	386	389	475	478
Y	20.2	19.9	19.5	20.0	36.4	36.8	37.0	24.9	27.6	26.7	26.1	26.0	10.4	11.0
Zr	231	228	225	227	184	184	188	166	179	171	165	172	342	309
Nb	14.6	14.6	14.3	14.6	12.5	12.6	13.2	18.4	18.6	18.6	18.1	18.1	12.7	12.0
Cs	1.26	1.25	1.22	1.28	1.12	1.12	1.10	0.13	0.10	0.13	0.13	0.10	1.31	1.34
Ba	1220	1199	1196	1200	670	663	683	130	139	131	128	130	1857	1880
La	38.8	38.2	37.8	38.2	25.1	24.7	25.0	14.6	15.8	15.3	14.8	15.0	87.9	89.0
Ce	69.4	68.8	67.6	67.6	52.5	51.7	53.0	36.2	39.0	37.1	36.2	38.0	160.6	160.0
Pr	8.1	7.9	7.9	7.8	6.5	6.5	6.8	5.0	5.7	5.1	4.9	5.3	15.6	18.0
Nd	32.1	32.1	31.5	31.7	29.1	28.6	28.0	24.3	25.2	24.7	24.2	25.0	53.2	55.0
Sm	5.88	5.80	5.71	5.72	6.59	6.52	6.70	5.90	6.20	6.07	5.91	6.20	7.23	7.20
Eu	1.67	1.64	1.62	1.58	1.94	1.94	2.00	1.95	2.06	2.00	1.95	2.07	1.43	1.40
Gd	5.0	4.9	4.9	4.7	6.6	6.6	6.8	5.9	6.4	6.1	5.9	6.3	4.8	4.3

Tb	0.682	0.677	0.662	0.708	1.072	1.071	1.070	0.925	0.960	0.947	0.926	0.900	0.504	0.480
Dy	3.67	3.65	3.57	3.55	6.35	6.36	6.41	5.13	5.20	5.29	5.15	5.31	2.29	2.40
Ho	0.709	0.702	0.690	0.685	1.335	1.334	1.330	0.983	0.990	1.017	0.984	1.040	0.377	0.400
Er	1.87	1.85	1.80	1.82	3.60	3.60	3.66	2.43	2.40	2.51	2.41	2.54	0.94	0.92
Tm	0.27	0.27	0.26	0.28	0.54	0.54	0.54	0.33	0.33	0.34	0.33	0.33	0.13	0.18
Yb	1.71	1.68	1.66	1.63	3.43	3.42	3.50	1.97	2.02	2.02	1.94	2.00	0.74	0.80
Lu	0.255	0.249	0.240	0.244	0.509	0.503	0.510	0.271	0.291	0.280	0.269	0.280	0.104	0.110
Hf	5.1	5.0	4.9	5.1	4.7	4.7	4.8	4.2	4.4	4.3	4.2	4.1	7.9	7.9
Ta	0.9	0.9	0.9	0.9	0.8	0.8	0.8	1.2	1.2	1.2	1.1	1.1	0.8	0.9
Pb	36.9	37.5	35.6	36.0	10.7	10.8	11.0	2.0	2.6	1.6	1.7	2.6	32.1	30.0
Th	6.6	6.7	6.4	6.5	6.2	6.1	6.2	0.9	1.1	1.2	1.2	1.2	24.8	25.0
U	1.94	1.91	1.87	1.92	1.68	1.66	1.69	0.42	0.42	0.41	0.40	0.42	1.79	2.07

APPENDIX B

1σ ERROR VALUES FOR ZIRCON TRACE ELEMENT ANALYSES.

Sujiahe	La (1σ)	Ce	Pr	Nd	Sm	Eu	Gd	Tb	Dy	Ho	Er	Tm	Yb	Lu	Th	U
SJH1-01.1	<0.00	0.019	0.0013	0.016	0.024	0.012	0.096	0.024	0.19	0.044	0.13	0.023	0.16	0.028	0.17	8.28
SJH1-01.2	0.0009	0.56	0.0042	0.041	0.072	0.022	0.29	0.097	1.19	0.47	2.21	0.55	6.16	1.31	3.61	5.23
SJH1-02.1	0.00097	0.02	0.0013	0.015	0.026	0.011	0.086	0.023	0.19	0.055	0.2	0.047	0.49	0.11	0.13	6.97
SJH1-02.2	0.0018	0.37	0.0043	0.055	0.098	0.024	0.44	0.14	1.72	0.68	3.12	0.74	7.93	1.69	4.44	7.3
SJH1-03.1	<0.00	0.015	0.0011	0.0043	0.02	0.012	0.085	0.037	0.5	0.22	1.08	0.29	3.42	0.8	0.05	14.7
SJH1-03.2	0.0019	0.018	0.0011	0.011	0.017	0.0085	0.077	0.028	0.38	0.18	0.93	0.26	3.23	0.81	0.07	16.06
SJH1-04.1	0.0038	0.41	0.014	0.17	0.24	0.052	1	0.31	3.43	1.26	5.2	1.14	11.06	2.17	3.75	5.61
SJH1-04.2	<0.00	0.024	0.00079	0.0082	0.024	0.013	0.12	0.039	0.43	0.16	0.69	0.17	1.85	0.4	0.08	14.66
SJH1-05.1	0.0053	0.17	0.0042	0.028	0.038	0.014	0.12	0.037	0.41	0.17	0.8	0.21	2.61	0.65	2.48	13.54
SJH1-05.2	0.0012	0.021	0.0021	0.021	0.036	0.016	0.11	0.027	0.2	0.048	0.13	0.024	0.21	0.04	0.21	5.36
SJH1-06.1	0.0051	0.42	0.014	0.17	0.22	0.046	0.84	0.24	2.62	0.92	3.64	0.77	7.27	1.43	6.2	7.21
SJH1-06.2	<0.00	0.021	0.0009	0.012	0.025	0.015	0.11	0.024	0.16	0.033	0.085	0.013	0.099	0.015	0.2	6.36
SJH1-07.1	0.0024	0.26	0.011	0.18	0.41	0.037	2.47	0.77	7.72	2.35	8.01	1.53	13.3	2.34	53.55	129.33
SJH1-07.2	0.0048	0.023	0.0046	0.03	0.028	0.0094	0.077	0.021	0.17	0.047	0.14	0.027	0.23	0.04	0.13	8.05
SJH1-09.1	0.0092	1.7	0.029	0.38	0.44	0.062	1.54	0.4	3.77	1.21	4.53	0.95	8.98	1.71	45.83	48.64
SJH1-09.2	<0.00	0.013	0.0015	0.013	0.031	0.013	0.11	0.038	0.47	0.18	0.8	0.18	1.92	0.4	0.082	19.95
SJH1-10.1	<0.00	0.098	0.00048	0.0087	0.012	0.0072	0.041	0.014	0.17	0.083	0.46	0.14	1.88	0.54	0.73	8.97
SJH1-10.2	0.0012	0.016	0.0008	0.012	0.019	0.0081	0.066	0.016	0.11	0.024	0.066	0.012	0.11	0.019	0.1	8.79
SJH1-12.1	0.0075	1.57	0.04	0.53	0.7	0.11	2.65	0.77	8.43	3.06	12.74	2.77	27.21	5.4	29.12	25.43
SJH1-12.2	0.012	0.025	0.0054	0.036	0.026	0.011	0.084	0.032	0.4	0.15	0.6	0.13	1.33	0.28	0.05	1.95

Xiongdian	La (1σ)	Ce	Pr	Nd	Sm	Eu	Gd	Tb	Dy	Ho	Er	Tm	Yb	Lu	Th	U
HXD98-7-01.1	<0.00	0.0016	0.00046	0.005	0.0048	0.0023	0.015	0.006	0.065	0.032	0.19	0.053	0.61	0.15	0.0016	0.075
HXD98-7-01.2	0.001	0.0064	<0.00	0.0037	0.0093	0.004	0.026	0.0084	0.1	0.05	0.29	0.083	1	0.27	0.0098	0.84
HXD98-7-02	<0.00	0.044	0.0024	0.024	0.045	0.032	0.21	0.086	1.18	0.57	2.93	0.67	6.32	1.07	0.042	0.059
HXD98-7-03	<0.00	0.0017	0.00062	0.0033	0.012	0.0056	0.038	0.015	0.17	0.061	0.2	0.033	0.22	0.035	0.00064	0.025
HXD98-7-04	0.0028	0.28	0.0036	0.044	0.078	0.031	0.21	0.068	0.78	0.35	1.77	0.45	5.12	1.18	0.87	5.19
HXD98-7-05	0.00083	0.12	0.0021	0.024	0.053	0.025	0.26	0.11	1.58	0.77	4.05	0.99	10.65	2.47	0.37	2.31
HXD98-8-01.1	0.0021	0.04	0.0017	0.02	0.041	0.02	0.14	0.051	0.67	0.31	1.65	0.42	4.71	1.09	0.1	6.7
HXD98-8-01.2	<0.00	0.044	0.00097	0.02	0.047	0.024	0.16	0.06	0.75	0.34	1.79	0.45	5.05	1.18	0.1	6.79
HXD98-8-02.1	0.072	7.06	0.17	1.74	1.34	0.61	3.22	0.69	5.42	1.49	4.73	0.77	6.26	1.11	24.27	15.24
HXD98-8-02.2	0.002	0.078	0.0011	0.013	0.014	0.0055	0.036	0.0086	0.081	0.032	0.16	0.043	0.52	0.14	0.19	12.21
HXD98-8-03.1	0.17	12.05	0.31	2.57	1.66	0.71	3.27	0.67	4.94	1.36	4.62	0.86	8.22	1.74	28.55	14.64
HXD98-8-03.2	<0.00	0.046	0.0016	0.012	0.016	0.008	0.048	0.014	0.15	0.068	0.38	0.11	1.24	0.3	0.042	2.33
HXD98-8-04.1	<0.00	0.0076	0.00057	0.0086	0.011	0.0055	0.041	0.015	0.2	0.1	0.55	0.15	1.61	0.37	0.012	4.26
HXD98-8-05.1	<0.00	0.042	0.0013	0.017	0.037	0.018	0.15	0.06	0.86	0.43	2.37	0.61	6.94	1.64	0.13	8.29
HXD98-8-06.1	<0.00	0.0062	0.00089	0.0094	0.016	0.0097	0.077	0.039	0.65	0.36	2.07	0.53	5.85	1.32	0.014	2.38
HXD-20-01.1	<0.00	0.25	0.0028	0.026	0.052	0.022	0.22	0.098	1.33	0.64	3.26	0.82	9.14	2.24	0.37	1.27
HXD-20-01.2	0.0023	0.27	0.0017	0.023	0.05	0.022	0.26	0.12	1.57	0.77	3.91	1	10.92	2.69	1.56	4.64
HXD-20-02.1	<0.00	0.13	0.0013	0.015	0.026	0.015	0.11	0.047	0.66	0.33	1.72	0.47	5.56	1.5	0.84	2.15
HXD-20-02.2	<0.00	0.21	0.0028	0.033	0.079	0.028	0.2	0.075	0.92	0.45	2.19	0.59	6.66	1.7	1.15	3.19
HXD-20-03.1	<0.00	0.0013	<0.00	<0.00	<0.00	0.0021	0.01	0.0031	0.03	0.014	0.054	0.012	0.074	0.014	0.0012	0.0046
HXD-20-03.2	<0.00	0.069	<0.00	0.014	0.051	0.019	0.19	0.074	1.03	0.5	2.33	0.55	5.35	1.29	0.2	0.39
HXD-20-04	0.0016	0.52	0.0029	0.029	0.03	0.013	0.066	0.018	0.16	0.059	0.27	0.066	0.73	0.18	23.4	48.55
HXD-20-05	<0.00	0.015	0.0011	0.0082	0.017	0.0064	0.043	0.015	0.18	0.1	0.53	0.14	1.62	0.42	0.044	0.9
HXD-20-06	0.0015	0.13	0.0018	0.022	0.049	0.021	0.23	0.1	1.34	0.66	3.24	0.8	8.61	2.13	0.4	2.41
HXD-20-06a	<0.00	0.064	0.00099	0.013	0.013	0.017	0.02	0.0039	0.025	0.0071	0.023	0.0064	0.047	0.0092	0.17	2.64
HXD-20-07.1	0.0012	0.12	0.0019	0.02	0.036	0.021	0.1	0.039	0.44	0.19	0.81	0.16	1.61	0.38	3.47	18.53
HXD-20-07.2	<0.00	0.13	0.0011	0.014	0.021	0.013	0.069	0.023	0.25	0.1	0.45	0.1	1.11	0.28	2.33	20.63

HXD-20-08	0.0016	0.1	0.00079	0.01	0.026	0.012	0.12	0.053	0.77	0.4	2.05	0.51	5.42	1.26	0.95	30.44
HXD-20-09	<0.00	0.74	0.0035	0.039	0.091	0.035	0.51	0.23	3.14	1.47	7.1	1.76	18.25	4.13	3.54	8.31
HXD-20-10.1	<0.00	0.2	0.0025	0.026	0.05	0.022	0.21	0.09	1.19	0.57	2.78	0.69	7.32	1.78	0.65	2.86
HXD-20-10.2	<0.00	0.084	0.0013	0.013	0.032	0.014	0.11	0.043	0.55	0.25	1.23	0.3	3.12	0.73	0.22	2.29
HXD-20-11.1	0.0014	0.1	0.0012	0.023	0.042	0.021	0.29	0.16	2.54	1.3	6.2	1.41	13.61	2.93	0.16	1.14
HXD-20-11.2	0.0039	0.028	0.0017	0.0061	0.0085	0.0071	0.031	0.011	0.12	0.052	0.24	0.058	0.59	0.14	0.094	1.42
HXD-20-12.1	<0.00	0.24	0.003	0.028	0.066	0.024	0.3	0.12	1.62	0.79	3.96	0.99	10.65	2.56	0.037	0.12
HXD-20-12.2	<0.00	0.14	0.0027	0.025	0.059	0.022	0.17	0.065	0.83	0.41	2.08	0.53	5.76	1.48	0.092	0.26
HXD-20-13	<0.00	0.17	0.0016	0.019	0.043	0.02	0.21	0.083	1.15	0.57	2.94	0.76	8.48	2.14	0.78	5.92
HXD-20-14	<0.00	0.13	0.0018	0.016	0.023	0.013	0.11	0.044	0.63	0.33	1.75	0.49	5.88	1.62	1.75	5.41
HXD-20-16.1	<0.00	0.097	0.0029	0.018	0.034	0.017	0.11	0.043	0.53	0.25	1.27	0.33	3.63	0.91	0.26	2.21
HXD-20-16.2	0.0016	0.00084	0.00056	0.0074	0.0068	0.00086	0.012	0.0044	0.07	0.037	0.15	0.029	0.23	0.04	0.00025	0.012
HXD-20-17	<0.00	0.058	0.003	0.028	0.049	0.018	0.13	0.041	0.34	0.11	0.42	0.095	0.92	0.21	0.83	37.08
HXD-20-18	0.0041	0.049	0.0024	0.013	0.017	0.0094	0.048	0.021	0.22	0.11	0.51	0.14	1.56	0.41	0.17	0.65
HXD-20-19.1	<0.00	0.27	0.0027	0.028	0.052	0.022	0.19	0.081	1.09	0.54	2.87	0.77	8.81	2.3	1.13	3.14
HXD-20-19.2	0.0036	0.32	0.0029	0.036	0.057	0.026	0.31	0.14	1.99	0.96	4.87	1.26	14	3.46	0.97	2.18
HXD-20-20.1	<0.00	0.23	0.0022	0.026	0.069	0.033	0.43	0.19	2.68	1.3	6.53	1.6	16.87	3.91	2.2	8.8
HXD-20-20.2	0.0041	0.13	0.0053	0.04	0.069	0.027	0.22	0.07	0.72	0.27	1.12	0.24	2.25	0.51	2.82	18.59
HXD-20-21.1	<0.00	0.19	0.0026	0.023	0.046	0.02	0.17	0.07	0.96	0.47	2.39	0.64	7.49	1.99	0.72	2.41
HXD-20-21.2	<0.00	0.19	0.0017	0.02	0.032	0.014	0.18	0.073	1.01	0.51	2.58	0.68	7.64	1.93	0.43	1.26

APPENDIX C

1σ ERROR VALUES FOR ZIRCON TRACE ELEMENT ANALYSES.

	La (1σ)	Ce	Pr	Nd	Sm	Eu	Gd	Tb	Dy	Ho	Er	Tm	Yb	Lu	Th	U
CTF1 01.1	0.0037	1.01	0.004	0.047	0.072	0.032	0.19	0.049	0.4	0.12	0.46	0.093	0.89	0.19	1.2	28
CTF1 01.2	0.0052	0.03	0.002	0.013	0.023	0.0083	0.048	0.011	0.089	0.026	0.097	0.021	0.18	0.038	0.1	16
CTF1 02.1	0.0017	0.63	0.0021	0.025	0.034	0.016	0.093	0.026	0.24	0.076	0.29	0.059	0.59	0.13	0.6	18
CTF1 03.1		0.54	0.0043	0.064	0.092	0.045	0.26	0.078	0.7	0.22	0.87	0.18	1.71	0.36	0.8	15
CTF1 03.2	0.2	1.16	0.1	0.66	0.2	0.064	0.32	0.071	0.54	0.14	0.45	0.082	0.72	0.13	6.3	40
CTF1 04.1	0.0035	0.84	0.0099	0.13	0.29	0.14	1.06	0.31	2.5	0.71	2.31	0.39	3.12	0.55	16.9	136
CTF1 05.1	0.0018	1.41	0.006	0.076	0.1	0.055	0.3	0.082	0.69	0.21	0.81	0.16	1.52	0.33	1.9	34
CTF1 06.1	0.0076	0.62	0.0072	0.062	0.084	0.04	0.23	0.068	0.62	0.2	0.76	0.15	1.45	0.3	0.8	22
CTF1 06.2	0.0081	0.58	0.007	0.082	0.1	0.052	0.31	0.094	0.85	0.27	1.08	0.22	2.04	0.41	0.9	20
CTF1 07.1	0.19	1.44	0.11	0.98	0.39	0.11	0.3	0.051	0.3	0.079	0.27	0.054	0.49	0.1	21.5	44
CTF1 07.2	0.42	3.97	0.3	2.86	0.99	0.27	0.76	0.12	0.65	0.15	0.42	0.073	0.64	0.13	60.8	115
CTF1 08.1	0.0041	0.33	0.0052	0.047	0.062	0.026	0.14	0.033	0.26	0.078	0.28	0.053	0.46	0.098	3.9	34
CTF1 09.1	0.005	0.36	0.0033	0.024	0.039	0.017	0.09	0.026	0.21	0.071	0.29	0.061	0.57	0.12	0.5	9
CTF1 10.1	0.013	0.35	0.0088	0.084	0.11	0.063	0.48	0.16	1.33	0.39	1.33	0.23	1.86	0.34	4.3	84
CTF1 11.1	0.025	1.27	0.023	0.3	0.38	0.18	1.38	0.45	4.39	1.55	6.7	1.62	17.94	4.29	90.3	449
CTF1 12.1	0.077	0.62	0.021	0.13	0.092	0.045	0.26	0.091	0.91	0.35	1.6	0.37	3.97	0.88	42.9	319
CTF1 13.1	0.035	5.21	0.12	1.77	1.57	0.65	2.82	0.55	3.35	0.72	2.02	0.34	2.81	0.55	49.2	185
CTF1 13.2		0.027	0.0011	0.009	0.02	0.0084	0.052	0.012	0.098	0.03	0.11	0.023	0.2	0.042	0.1	17
CTF1 14.1	0.0032	0.96	0.0073	0.1	0.13	0.059	0.37	0.097	0.85	0.26	0.97	0.2	1.85	0.38	0.9	19
CTF1 15.1	0.0041	0.12	0.0024	0.013	0.021	0.0072	0.044	0.0099	0.076	0.025	0.095	0.022	0.19	0.046	1	11
CTF1 15.2	0.065	0.15	0.012	0.068	0.044	0.02	0.08	0.016	0.13	0.039	0.15	0.034	0.29	0.061	1.1	12
CTF1 16.1	0.0021	0.29	0.004	0.053	0.073	0.028	0.14	0.033	0.28	0.077	0.26	0.051	0.46	0.095	3.4	31
CTF1 16.2	0.015	0.18	0.0066	0.052	0.055	0.024	0.12	0.029	0.24	0.071	0.31	0.075	0.84	0.2	2.5	39
CTF1 17.1	0.017	4.27	0.038	0.55	0.6	0.26	1.2	0.24	1.5	0.33	0.94	0.15	1.22	0.24	54.1	151
CTF1 17.2	0.018	0.035	0.006	0.042	0.034	0.013	0.062	0.015	0.12	0.036	0.13	0.028	0.23	0.047	0.1	20
CTF1 18.1	0.0017	1.2	0.0029	0.036	0.053	0.026	0.14	0.041	0.36	0.11	0.41	0.086	0.81	0.17	1.3	44
CTF1 19.1		0.27	0.0026	0.028	0.045	0.023	0.13	0.039	0.33	0.099	0.34	0.067	0.59	0.11	4.1	34

APPENDIX D

ZIRCON EXPERIMENT STARTING MATERIAL COMPOSITION (ppm) AND 1σ ERROR (1 se) VALUES.

Mud Tank zircon Grain composition

Analysis #	La (ppm)	Ce	Pr	Nd	Sm	Eu	Gd	Tb	Dy	Y	Ho	Er	Tm	Lu
1	-	0.48	0.08	0.89	1.12	0.32	1.33	0.69	6.29	64.9	1.68	5.99	1.18	1.51
2	-	0.66	0.09	0.77	0.70	0.54	1.51	0.61	6.52	68.8	1.93	7.51	1.57	1.97
3	0.06	0.69	0.06	-	1.34	0.71	2.75	0.69	6.82	73.4	2.14	7.66	0.94	2.02
4	0.16	0.52	-	0.86	1.29	0.56	3.06	0.66	5.67	71.8	1.53	7.89	1.19	2.01
5		0.59	-	-	0.72	0.29	2.61	0.68	7.01	68.6	1.55	6.72	1.14	1.94

	Hf (ppm)	Th	U	Ti	Ta	Nb	Sc	P	Si	Zr
1	8935	6.2	12.7	-	0.92	6.46	201	-	149581	411435
2	8686	7.3	13.1	-	0.84	6.99	213	51	149581	415118
3	8475	8.6	16.4	-	1.10	7.14	215	-	149581	414067
4	8409	8.7	15.3	-	0.95	6.93	213	-	149581	415318
5	9151	6.9	12.5	-	0.77	6.52	205	-	149581	419091

	La (1 se)	Ce	Pr	Nd	Sm	Eu	Gd	Tb	Dy	Y	Ho	Er	Tm	Lu
1	0.03	0.06	0.03	0.25	0.21	0.08	0.26	0.06	0.41	2.36	0.10	0.35	0.09	0.10
2	0.03	0.07	0.02	0.32	0.24	0.09	0.26	0.06	0.43	2.52	0.12	0.42	0.10	0.12
3	0.03	0.07	0.03	0.24	0.26	0.09	0.35	0.07	0.43	2.70	0.12	0.42	0.08	0.12
4	0.04	0.06	0.03	0.25	0.25	0.09	0.39	0.06	0.38	2.68	0.10	0.44	0.09	0.13
5	0.03	0.07	0.03	0.29	0.21	0.09	0.35	0.07	0.44	2.60	0.10	0.39	0.08	0.12

	Hf (1 se)	Th	U	Ti	Ta	Nb	Sc	P	Si	Zr
1	341	0.30	0.51	-	0.07	0.28	7.2	19	4798	17321
2	336	0.35	0.53	-	0.07	0.30	7.6	25	4800	17750
3	332	0.40	0.64	-	0.08	0.30	7.8	22	4797	18028
4	335	0.41	0.61	-	0.08	0.30	7.8	20	4799	18463
5	371	0.34	0.52	-	0.07	0.29	7.6	19	4799	19061

Crushed Mud Tank zircon composition

Analysis #	La (ppm)	Ce	Pr	Nd	Sm	Eu	Gd	Tb	Dy	Y	Ho	Er	Tm	Lu
1	-	0.98	0.22	-	-	-		0.62	5.47	49.5	0.80	5.17	1.13	1.21
2	0.30	0.91	0.20	-	1.93	-	3.84	0.50	4.21	46.9	1.25	4.22	1.02	0.62
3	0.31	1.29	-	-	1.20	-	2.87	0.81	5.78	49.1	1.73	3.62	0.92	0.85
4	-	0.81	0.24	3.04	-	-	2.54	0.83	5.04	47.8	1.24	4.60	0.59	1.22
5	0.61	0.59	-	-	-	-	3.23	0.45	3.37	45.9	0.78	2.02	0.49	0.92
6	0.85	0.98	0.33	-	1.85	0.94	-	0.74	4.66	45.7	0.76	5.93	0.90	0.98
7	-	0.91	-	-	2.78	-	-	0.58	2.94	42.1	1.49	3.20	0.70	0.57
8	0.35	1.35	0.28	2.38	-	0.96	1.98	0.52	6.44	49.3	0.87	5.71	0.33	0.90
9	0.40	0.64	-	-	-	0.75	2.31	0.65	6.58	45.6	1.59	2.63	0.93	0.89
10	0.69	0.95	0.21	3.81	-	0.53	2.30	0.30	6.01	43.1	1.12	2.97	-	1.31

Analysis #	Hf (ppm)	Th	U	Ti	Ta	Nb	Sc	P	Si	Zr
1	6859	4.1	10.0	-	0.65	5.49	163	185	149581	305015
2	7500	6.0	9.3	-	0.83	6.09	195	293	149581	325046
3	6786	4.7	9.3	-	0.82	4.63	166	-	149581	287817
4	6848	4.8	11.8	-	0.45	4.69	159	120	149581	293440
5	6549	3.7	9.4	-	0.54	5.30	162	172	149581	287447
6	6650	4.7	9.1	-	0.74	4.39	166	240	149581	281824
7	5822	4.2	9.8	-	0.49	4.69	145	180	149581	252825
8	6252	3.1	9.6	-	0.59	4.25	144	-	149581	279356
9	6208	4.7	9.9	-	0.47	3.80	145	216	149581	257912
10	6623	5.0	8.5	-	0.71	4.97	171	-	149581	274514

Analysis #	La (1 se)	Ce	Pr	Nd	Sm	Eu	Gd	Tb	Dy	Y	Ho	Er	Tm	Lu
1	0.12	0.16	0.10	0.68	0.57	0.22	0.71	0.13	0.69	3.79	0.17	0.62	0.16	0.17
2	0.12	0.21	0.12	0.28	1.05	0.23	1.41	0.17	0.89	3.86	0.24	0.75	0.21	0.19
3	0.11	0.17	0.07	0.64	0.59	0.16	0.77	0.13	0.66	3.91	0.20	0.51	0.14	0.12
4	0.09	0.15	0.07	0.69	0.43	0.18	0.76	0.13	0.65	3.90	0.17	0.54	0.13	0.16
5	0.10	0.13	0.09	0.80	0.42	0.20	0.94	0.11	0.57	3.83	0.15	0.46	0.13	0.17

6	0.15	0.16	0.08	0.58	0.68	0.19	0.62	0.12	0.64	3.91	0.14	0.66	0.14	0.15
7	0.11	0.23	0.07	0.75	1.04	0.26	0.88	0.17	0.72	3.84	0.26	0.63	0.18	0.16
8	0.09	0.16	0.07	0.76	0.43	0.22	0.74	0.11	0.74	4.40	0.15	0.66	0.11	0.13
9	0.15	0.17	0.12	0.91	0.80	0.28	1.10	0.17	0.92	4.23	0.24	0.57	0.17	0.19
10	0.23	0.25	0.12	1.43	0.76	0.33	1.19	0.16	1.22	4.29	0.29	0.82	0.16	0.28

Analysis #	Hf (1 se)	Th	U	Ti	Ta	Nb	Sc	P	Si	Zr
1	786	0.32	0.66	-	0.15	0.41	9.8	316	4988	30301
2	885	0.56	0.80	-	0.21	0.62	12.5	537	5273	33214
3	818	0.31	0.62	-	0.13	0.36	10.3	44	4942	30048
4	847	0.32	0.77	-	0.12	0.37	10.1	258	4936	31413
5	831	0.28	0.64	-	0.14	0.41	10.5	397	4954	31556
6	865	0.32	0.63	-	0.13	0.35	11.0	598	4939	31712
7	779	0.45	0.85	-	0.16	0.53	10.4	488	5233	29233
8	855	0.25	0.68	-	0.12	0.36	10.0	167	4924	33009
9	871	0.40	0.79	-	0.17	0.42	10.5	697	5114	31264
10	954	0.59	0.89	-	0.21	0.63	13.3	513	5453	34164

Composition of trace elements added to the fluid phase from standard solutions. Hf and Sc are added as oxide powders.

Analysis #	La (ppm)	Ce	Pr	Nd	Sm	Eu	Gd	Tb	Dy	Y	Ho	Er	Tm	Lu
1	936	824	794	869	808	860	905	809	799	855	824	801	770	815
2	1017	932	884	899	994	961	874	903	901	999	932	877	872	918
3	927	884	844	892	898	938	888	885	867	968	896	874	876	902
4	930	925	842	946	910	951	845	893	846	964	878	882	845	893

Analysis #	Hf (ppm)	Th	U	Ti	Ta	Nb	Sc
1	91670	1821	1760	579	430	512	16960
2	99656	1985	1821	719	491	581	18585
3	99053	1887	1810	724	472	562	17465
4	101194	1894	1848	585	476	543	17737

Analysis #	La (1 se)	Ce	Pr	Nd	Sm	Eu	Gd	Tb	Dy	Y	Ho	Er	Tm	Lu
1	23	27	22	36	31	28	40	23	26	25	23	26	22	25
2	24	31	23	35	35	31	37	24	27	28	26	27	24	28
3	22	30	23	35	32	31	39	24	26	28	25	27	24	28
4	22	32	23	37	33	32	38	25	26	28	25	27	24	28

Analysis #	Hf (1 se)	Th	U	Ti	Ta	Nb	Sc
1	2807	59	48	160	12	14	458
2	3072	64	49	140	13	14	498
3	3124	62	49	139	12	14	474
4	3261	64	51	131	12	13	488

APPENDIX E

ZIRCON SYNTHESIS EXPERIMENT GLASS COMPOSITION (ppm) AND 1σ ERROR (1 se) VALUES.

Analysis #	La (ppm)	Ce	Pr	Nd	Sm	Eu	Gd	Tb	Dy	Y	Ho	Er	Tm	Lu
ZrTP11.05	1690	1344	1213	1252	1192	1244	1095	1107	1064	978	1038	898	803	664
ZrTP11.06	1748	1421	1244	1250	1199	1298	1107	1142	1091	1000	1066	917	826	691
ZrTP11.07	1839	1468	1318	1354	1293	1356	1178	1180	1140	1034	1095	963	874	722
ZrTP11.08	1825	1454	1286	1326	1263	1344	1167	1172	1130	1026	1105	956	863	719
ZrTP11.09	1782	1430	1264	1304	1238	1338	1161	1169	1113	1013	1069	943	849	715
ZrTP13.24	505	295	381	402	399	418	355	357	328	303	304	251	227	192
ZrTP13.25	495	294	373	390	392	412	353	353	324	298	304	251	224	194
ZrTP13.26	500	294	377	381	386	408	359	355	329	298	303	259	227	197
ZrTP13.27	501	294	390	401	401	423	369	364	340	304	312	264	233	200
ZrTP13.28	472	282	360	381	378	398	343	343	317	284	297	249	224	194
ZrTP14.05	797	724	657	698	709	745	663	729	720	676	737	674	654	618
ZrTP14.06	810	748	670	719	717	763	699	742	735	679	761	701	675	645
ZrTP14.07	815	751	675	719	716	768	685	737	733	682	753	690	671	645
ZrTP14.08	810	741	666	707	711	758	694	740	745	674	762	691	675	648
ZrTP14.09	824	753	682	718	716	775	697	755	746	685	782	705	689	663
ZrTP34.05	303	323	293	322	344	368	369	423	454	488	495	491	519	582
ZrTP34.06	298	329	290	315	347	379	376	422	469	489	493	499	527	590
ZrTP34.07	273	300	264	283	314	320	305	339	372	393	409	383	433	426
ZrTP34.08	273	301	271	296	327	368	341	394	416	459	456	460	483	536
ZrTP34.09	240	266	233	256	282	291	262	309	320	331	344	331	352	361
ZrTP35.05	753	856	685	731	720	758	697	718	729	712	753	731	755	822
ZrTP35.06	775	838	690	754	739	751	701	732	734	739	773	740	762	847
ZrTP35.07	755	820	675	719	738	750	686	725	720	716	745	727	747	832
ZrTP35.08	761	831	683	739	757	759	683	723	724	712	755	732	746	822
ZrTP35.09	760	810	684	736	739	754	684	719	712	721	754	715	756	831

ZrTP40.05	1098	498	960	1010	889	863	713	630	567	512	543	480	450	449
ZrTP40.06	1139	504	991	1036	898	887	725	649	588	522	568	484	460	463
ZrTP40.07	1106	505	965	1025	892	852	711	635	574	506	550	479	454	446
ZrTP40.08	1105	496	970	1016	891	856	707	633	587	516	545	465	446	448
ZrTP40.09	1110	493	968	1003	903	861	714	632	567	518	551	470	453	453
ZrTP44.05	1141	982	1019	1042	985	1010	879	882	866	841	858	789	776	763
ZrTP44.06	1135	982	1017	1035	982	990	846	877	836	811	837	771	749	733
ZrTP44.07	1159	992	1038	1043	986	927	882	878	832	857	869	786	780	776
ZrTP44.08	1114	991	1025	1078	973	969	881	885	849	833	853	757	748	744
ZrTP44.09	1173	1015	1056	1083	1031	996	892	912	883	867	881	800	778	775
ZrTP46.01	909	1742	745	781	978	1136	1079	1463	1639	1787	1980	2014	2107	2290
ZrTP46.02	925	1702	759	858	959	1145	1123	1455	1727	1802	1991	2041	2113	2264
ZrTP46.03	970	1757	771	856	1032	1255	1225	1571	1889	1870	2142	2159	2266	2477
ZrTP46.04	936	1792	770	835	1041	1232	1171	1536	1785	1827	2062	2045	2225	2443
ZrTP46.05	979	1792	777	841	1043	1218	1185	1556	1862	1853	2145	2127	2297	2460
ZrTP47.01	961	760	858	889	1008	976	816	782	692	637	641	524	481	427
ZrTP47.02	972	750	866	912	978	974	805	788	704	667	662	559	497	430
ZrTP47.03	982	749	855	899	958	931	834	771	682	663	655	533	484	419
ZrTP47.04	1029	807	921	959	1031	1029	902	836	752	704	682	586	525	456
ZrTP47.05	964	750	861	933	960	970	834	774	724	655	654	544	494	430
ZrTP49.01	775	475	606	586	423	400	293	247	226	212	204	166	157	143
ZrTP49.02	834	510	585	590	430	386	306	267	215	218	197	191	166	161
ZrTP49.03	784	478	609	580	425	384	282	248	222	210	189	171	151	146
ZrTP49.04	793	490	612	572	442	399	292	263	219	214	206	185	164	151
ZrTP49.05	776	483	628	595	445	400	294	261	217	213	206	170	162	148
ZrTP51.01	420	206	349	318	265	259	201	210	200	219	194	194	189	193
ZrTP51.02	416	202	339	327	280	246	226	206	184	225	194	179	188	199
ZrTP51.03	415	203	343	354	269	253	215	199	204	221	194	184	183	197

ZrTP51.04	419	203	342	337	276	264	235	206	204	221	199	184	189	206
ZrTP51.05	414	200	338	341	260	252	207	202	173	215	188	184	186	202
ZrTP52.01	344	583	326	369	301	420	362	233	212	193	183	141	137	107
ZrTP52.02	544	624	426	318	530	499	369	389	356	270	285	209	164	186
ZrTP52.03	414	597	287	330	269	378	285	237	195	174	185	149	133	106
ZrTP52.04	520	609	440	414	503	508	404	399	350	302	298	212	214	202
ZrTP52.05	470	649	375	400	405	444	327	322	263	223	221	161	149	130
ZrTP53.01	509	474	421	405	432	452	402	427	430	461	460	435	476	530
ZrTP53.02	484	469	439	428	408	431	403	418	428	476	438	428	450	509
ZrTP53.03	498	481	432	463	434	459	379	441	443	467	467	441	476	537
ZrTP53.04	489	462	424	438	422	451	397	429	408	483	446	424	467	524
ZrTP53.05	489	454	420	423	406	428	351	414	407	439	433	399	465	532
ZrTP54.01	2298	2073	2101	2060	2057	2105	1822	2061	2128	2266	2169	2053	2166	2248
ZrTP54.02	2420	2181	2106	2187	2074	2126	1904	2156	2210	2317	2285	2230	2233	2323
ZrTP54.03	2314	2064	2044	2082	1954	2053	1816	2021	2009	2196	2166	2105	2157	2190
ZrTP54.04	2285	2029	1946	2016	1916	2031	1758	2002	2024	2141	2123	2087	2103	2182
ZrTP54.05	2370	2081	2026	2118	1965	2084	1885	2077	2160	2224	2253	2168	2233	2302

Analysis #	Hf (ppm)	Th	U	Ti	Ta	Nb	P	Sc	Si	Zr
ZrTP11.05	249	347	650	337	159	223	42	490	116860	4217
ZrTP11.06	261	359	676	347	163	223	181	510	116860	4296
ZrTP11.07	269	379	727	363	170	236	180	523	116860	4524
ZrTP11.08	272	373	711	360	171	229	206	528	116860	4419
ZrTP11.09	268	363	690	357	168	226	231	527	116860	4363
ZrTP13.24	160	37	497	488	31	37	<30	164	116860	1220
ZrTP13.25	162	38	498	496	30	37	132	161	116860	1213
ZrTP13.26	165	40	497	479	31	35	150	162	116860	1176
ZrTP13.27	170	40	517	510	33	37	227	163	116860	1220
ZrTP13.28	168	39	496	474	31	35	170	156	116860	1143
ZrTP14.05	457	141	567	425	226	276	348	667	116860	28976
ZrTP14.06	470	147	599	430	230	274	347	678	116860	29246
ZrTP14.07	470	149	612	443	230	277	305	668	116860	29558
ZrTP14.08	472	151	606	443	234	274	377	676	116860	29292
ZrTP14.09	483	152	626	446	236	279	389	690	116860	29815
ZrTP34.05	7766	459	232	408	65	97	249	8349	116860	73909
ZrTP34.06	7716	452	232	404	66	96	422	8432	116860	74608
ZrTP34.07	5937	366	211	380	58	90	103	6905	116860	59720
ZrTP34.08	7167	409	219	352	60	92	51	7842	116860	70688
ZrTP34.09	4913	298	207	352	52	81	104	6571	116860	56494
ZrTP35.05	8181	350	370	2099	149	295	316	8271	116860	66679
ZrTP35.06	8299	350	366	2076	150	304	297	8277	116860	69162
ZrTP35.07	8150	346	371	2062	150	291	316	8321	116860	67684
ZrTP35.08	8026	342	367	2041	149	296	353	8347	116860	68603
ZrTP35.09	8095	350	355	2053	150	296	288	8262	116860	68089
ZrTP40.05	2888	205	243	606	132	122	304	2533	116860	24029
ZrTP40.06	2962	212	255	623	139	122	290	2632	116860	24194

ZrTP40.07	2854	204	244	612	134	122	276	2525	116860	23595
ZrTP40.08	2878	207	242	613	133	121	328	2532	116860	23894
ZrTP40.09	2894	208	243	615	135	122	284	2587	116860	23844
ZrTP44.05	7329	390	396	1574	98	132	276	2783	116860	27590
ZrTP44.06	7104	375	396	1562	93	124	261	2711	116860	27005
ZrTP44.07	7236	380	395	1566	91	130	113	2786	116860	28292
ZrTP44.08	7215	368	390	1549	91	119	215	2806	116860	27319
ZrTP44.09	7447	396	412	1640	98	140	197	2820	116860	28375
ZrTP46.01	15651	2359	900	1086	382	610	1768	7043	179029	65015
ZrTP46.02	15434	2471	912	997	360	578	1942	6703	179029	61849
ZrTP46.03	16494	2526	958	1137	399	619	<1141	7441	181366	67657
ZrTP46.04	16833	2594	930	853	380	617	2614	7223	179029	66960
ZrTP46.05	16576	2472	944	1280	432	687	902	7415	179029	68675
ZrTP47.01	655	452	490	1012	229	674	<388	613	212685	9576
ZrTP47.02	707	471	524	1113	271	772	<418	666	212685	9601
ZrTP47.03	679	460	500	841	204	650	<371	633	212685	9252
ZrTP47.04	772	484	525	1160	265	760	<400	676	212685	10167
ZrTP47.05	726	457	514	1264	264	780	<431	656	212685	9718
ZrTP49.01	2114	521	370	1954	46	193	<224	1447	210815	7280
ZrTP49.02	2276	534	415	1847	43	197	<230	1503	210815	7551
ZrTP49.03	2209	527	382	1821	47	196	<201	1429	210815	7248
ZrTP49.04	2289	557	385	1995	51	196	265	1451	210815	7345
ZrTP49.05	2255	543	370	1986	50	201	<225	1447	210815	7430
ZrTP51.01	10998	349	138	244	34	95	<345	3283	165474	42523
ZrTP51.02	10935	341	138	240	36	91	<328	3287	165474	42138
ZrTP51.03	10759	346	136	268	35	92	<269	3285	165474	41739

ZrTP51.04	11089	348	144	226	37	91	<281	3308	165474	43246
ZrTP51.05	10885	334	136	263	35	91	<245.	3346	165474	42558
ZrTP52.01	950	88	121	367	9	30	104	2283	163604	4614
ZrTP52.02	1495	168	113	202	13	28	509	2940	163604	6111
ZrTP52.03	1076	95	134	305	12	31	<64	2057	163604	4267
ZrTP52.04	1815	141	124	234	19	49	635	2952	163604	6607
ZrTP52.05	1343	120	116	368	16	32	135	2507	163604	5098
ZrTP53.01	24941	551	551	294	406	482	606	9328	137427	99060
ZrTP53.02	23573	517	511	346	379	464	452	8793	137427	96507
ZrTP53.03	24711	541	552	357	392	466	<351	9213	137427	97283
ZrTP53.04	24046	520	503	360	381	470	478	9134	137427	97269
ZrTP53.05	23771	516	540	314	398	463	594	8631	137427	94092
ZrTP54.01	19716	2652	1896	1706	765	787	<662	31673	211283	83050
ZrTP54.02	20293	2747	1935	1811	782	798	1494	32098	211283	84882
ZrTP54.03	19377	2612	1884	1763	762	786	<725	31088	211283	82931
ZrTP54.04	19138	2694	1834	1711	757	768	700	30210	211283	80036
ZrTP54.05	19818	2733	1911	1737	779	802	<593	31502	211283	82045

Analysis #	La (1se)	Ce	Pr	Nd	Sm	Eu	Gd	Tb	Dy	Y	Ho	Er	Tm	Lu
ZrTP11.05	98	72	72	62	64	71	56	62	57	39	57	47	41	34
ZrTP11.06	106	80	77	65	68	77	59	67	61	41	61	51	44	37
ZrTP11.07	118	87	86	74	77	85	65	72	68	44	66	56	49	40
ZrTP11.08	124	91	89	76	79	89	68	76	71	45	70	58	51	42
ZrTP11.09	128	95	93	78	82	94	71	80	73	46	72	61	53	44
ZrTP13.24	18	11	15	16	16	14	14	13	12	13	11	8	8	7
ZrTP13.25	18	11	15	15	16	14	14	14	12	13	11	9	9	7
ZrTP13.26	18	11	16	16	16	14	15	14	13	14	12	9	9	7
ZrTP13.27	19	11	17	17	17	15	16	15	14	15	12	9	10	8
ZrTP13.28	18	11	17	17	17	15	16	15	13	14	12	9	9	8
ZrTP14.05	25	23	21	24	23	23	21	24	22	22	23	21	20	19
ZrTP14.06	26	24	22	25	23	24	22	24	22	22	24	21	21	20
ZrTP14.07	26	24	22	26	23	24	22	24	22	23	24	21	21	20
ZrTP14.08	26	24	22	26	24	24	22	25	22	23	24	21	21	20
ZrTP14.09	27	25	23	27	24	25	22	26	23	23	25	22	22	20
ZrTP34.05	9	10	9	11	12	12	13	13	14	15	15	16	16	18
ZrTP34.06	9	10	9	11	12	12	13	13	15	15	16	17	16	18
ZrTP34.07	9	9	8	10	11	10	11	11	12	12	13	13	13	13
ZrTP34.08	9	10	9	11	12	12	13	13	13	14	15	16	15	17
ZrTP34.09	8	9	7	10	11	10	10	10	10	10	11	12	11	11
ZrTP35.05	23	26	22	25	24	26	23	22	23	23	24	24	23	27
ZrTP35.06	24	25	22	26	24	26	23	23	23	24	24	24	23	28
ZrTP35.07	24	25	22	25	25	26	23	23	22	24	24	24	23	28
ZrTP35.08	24	25	22	27	26	27	23	23	23	24	24	25	23	28
ZrTP35.09	24	25	23	27	26	28	23	23	22	24	24	24	24	28
ZrTP40.05	35	17	32	40	29	29	24	21	18	18	18	15	14	15

ZrTP40.06	36	17	33	42	30	30	24	22	19	19	19	16	15	16
ZrTP40.07	36	17	33	42	30	29	24	22	19	19	18	16	14	15
ZrTP40.08	36	17	33	43	30	30	24	22	19	20	18	15	14	16
ZrTP40.09	36	18	33	44	31	30	25	22	19	20	19	16	15	16
ZrTP44.05	41	36	39	40	38	38	38	35	35	36	33	31	30	29
ZrTP44.06	41	36	39	39	38	37	37	35	34	35	32	31	29	27
ZrTP44.07	42	36	40	40	39	35	39	35	34	37	34	32	30	29
ZrTP44.08	41	36	39	42	38	37	39	36	35	36	33	30	29	28
ZrTP44.09	43	37	40	41	40	37	39	36	36	37	34	32	30	29
ZrTP46.01	35	68	28	34	41	45	45	55	65	71	75	78	81	87
ZrTP46.02	38	71	31	41	44	48	51	59	73	77	81	85	87	93
ZrTP46.03	41	75	32	43	49	54	57	66	82	82	89	93	96	104
ZrTP46.04	39	76	32	40	48	53	54	63	77	79	85	87	93	102
ZrTP46.05	36	68	29	36	43	47	49	57	72	73	79	81	87	92
ZrTP47.01	33	26	28	34	37	33	32	26	26	22	21	19	16	15
ZrTP47.02	33	25	29	34	35	32	31	26	26	23	22	20	17	15
ZrTP47.03	33	25	28	33	34	30	31	26	25	22	21	19	16	14
ZrTP47.04	35	27	30	35	37	34	34	28	27	24	22	21	17	15
ZrTP47.05	33	25	28	34	34	32	31	26	26	22	21	20	16	15
ZrTP49.01	25	15	20	20	16	14	11	9	8	7	7	6	5	5
ZrTP49.02	32	20	23	33	25	17	20	12	13	10	9	11	8	8
ZrTP49.03	25	15	20	20	16	13	11	9	8	7	7	6	5	5
ZrTP49.04	26	16	20	20	16	13	11	9	8	7	7	6	6	5
ZrTP49.05	25	15	20	21	16	14	11	9	8	7	7	6	6	5
ZrTP51.01	20	9	15	19	18	12	10	13	9	12	13	7	10	8
ZrTP51.02	20	9	15	20	20	12	11	13	9	13	14	7	11	9
ZrTP51.03	21	10	16	23	20	12	10	13	9	14	14	7	11	9
ZrTP51.04	22	10	16	23	22	14	12	15	10	14	16	7	12	10

ZrTP51.05	23	10	17	24	21	13	10	15	9	15	15	7	12	10
ZrTP52.01	13	21	12	20	16	16	19	9	11	8	7	8	6	5
ZrTP52.02	30	34	24	34	43	31	34	22	29	17	17	18	11	12
ZrTP52.03	15	21	10	18	15	15	15	9	10	7	7	8	5	5
ZrTP52.04	20	23	17	20	22	20	19	15	15	12	12	9	8	8
ZrTP52.05	16	22	13	18	18	16	15	11	12	8	8	7	6	5
ZrTP53.01	35	27	23	33	33	30	35	29	26	27	33	31	38	47
ZrTP53.02	35	29	25	37	33	31	37	30	27	30	33	32	39	49
ZrTP53.03	39	31	26	42	38	35	38	34	29	31	38	36	44	55
ZrTP53.04	40	32	27	43	39	36	42	35	29	34	38	36	46	58
ZrTP53.05	44	34	29	47	42	38	42	37	32	34	41	38	50	64
ZrTP54.01	130	136	129	156	154	197	130	189	168	107	221	149	143	160
ZrTP54.02	149	156	140	182	171	221	149	219	192	117	259	178	162	182
ZrTP54.03	154	161	148	191	176	236	155	227	192	119	272	185	170	188
ZrTP54.04	163	171	151	201	187	255	163	246	211	122	293	199	180	203
ZrTP54.05	182	189	169	229	207	284	188	278	244	135	339	225	207	232

Analysis #	Hf (1se)	Th	U	Ti	Ta	Nb	P	Sc	Si	Zr
ZrTP11.05	13	22	42	19	8	9	13	28	3703	177
ZrTP11.06	14	24	46	20	8	9	22	30	3703	187
ZrTP11.07	16	27	52	22	9	10	23	33	3702	204
ZrTP11.08	17	28	54	23	9	10	28	35	3703	207
ZrTP11.09	17	29	56	25	10	10	33	37	3702	214
ZrTP13.24	5	1.2	16	17	1.0	1.6	11	6	3703	54
ZrTP13.25	6	1.2	16	17	1.0	1.7	15	6	3703	55
ZrTP13.26	6	1.3	16	17	1.0	1.7	15	7	3702	56
ZrTP13.27	6	1.3	17	18	1.1	1.8	22	7	3703	60
ZrTP13.28	6	1.3	16	17	1.1	1.8	18	7	3702	59
ZrTP14.05	15	4	18	32	7	9	31	21	3711	1113
ZrTP14.06	16	4	19	34	7	9	29	21	3706	1152
ZrTP14.07	16	5	19	37	7	9	27	21	3708	1201
ZrTP14.08	16	5	19	40	7	9	32	21	3706	1231
ZrTP14.09	17	5	20	42	7	9	34	22	3706	1300
ZrTP34.05	252	14	7	14	2.1	3.0	22	259	3711	2486
ZrTP34.06	254	14	8	16	2.2	3.0	36	263	3733	2549
ZrTP34.07	197	12	7	14	1.9	2.8	12	216	3718	2068
ZrTP34.08	247	14	7	28	2.1	2.9	98	254	3918	2545
ZrTP34.09	168	10	7	14	1.8	2.5	10	208	3720	2029
ZrTP35.05	249	11	11	75	5	9	23	260	3709	2384
ZrTP35.06	253	11	11	76	5	10	23	262	3704	2524
ZrTP35.07	249	11	12	77	5	9	25	265	3705	2532
ZrTP35.08	247	11	12	80	5	10	31	270	3734	2645
ZrTP35.09	249	11	11	81	5	10	25	268	3704	2696
ZrTP40.05	89	7	8	21	5	4	23	88	3708	832
ZrTP40.06	91	7	8	22	5	4	22	93	3706	848

ZrTP40.07	88	7	8	22	5	4	22	90	3707	839
ZrTP40.08	89	7	8	22	5	4	25	92	3704	863
ZrTP40.09	90	7	8	23	5	4	23	96	3709	877
ZrTP44.05	286	14	13	51	4	5	34	99	3743	1151
ZrTP44.06	277	13	13	51	4	5	25	96	3725	1125
ZrTP44.07	285	13	13	55	4	5	31	100	3794	1186
ZrTP44.08	283	13	13	53	4	5	32	100	3779	1144
ZrTP44.09	291	14	14	53	4	5	26	100	3731	1183
ZrTP46.01	667	91	34	89	15	24	458	269	7885	2586
ZrTP46.02	696	102	37	99	16	25	539	275	8712	2623
ZrTP46.03	761	107	40	111	18	27	511	313	9151	2941
ZrTP46.04	770	109	39	105	17	27	618	301	8925	2886
ZrTP46.05	694	93	35	89	17	26	352	277	7640	2680
ZrTP47.01	27	16	17	67	8	23	167	23	7536	370
ZrTP47.02	28	16	18	69	9	26	174	24	7515	370
ZrTP47.03	26	16	17	54	7	21	151	23	7362	353
ZrTP47.04	30	16	18	67	9	25	159	24	7442	389
ZrTP47.05	28	16	18	74	9	26	171	24	7474	373
ZrTP49.01	74	17	12	81	1.8	6	89	47	6940	262
ZrTP49.02	99	21	17	135	2.9	9	185	59	8437	315
ZrTP49.03	77	17	12	76	1.8	7	85	46	6923	261
ZrTP49.04	80	18	12	81	1.9	7	88	47	6902	264
ZrTP49.05	79	18	12	82	1.9	7	87	47	6922	267
ZrTP51.01	793	18	5	31	2.6	5	131	265	5845	4167
ZrTP51.02	841	18	5	30	2.9	5	127	285	5829	4453
ZrTP51.03	879	19	5	27	2.9	6	104	305	5686	4737
ZrTP51.04	963	20	5	27	3.3	6	200	329	5743	5263
ZrTP51.05	1001	20	5	27	3.3	6	144	354	5661	5532

ZrTP52.01	40	4	5	44	1.0	2.2	79	80	6161	169
ZrTP52.02	96	12	9	91	2.4	4.2	367	154	10366	339
ZrTP52.03	43	4	6	38	1.1	2.1	67	71	6074	154
ZrTP52.04	71	6	5	54	1.3	2.7	225	110	7047	248
ZrTP52.05	49	5	5	37	1.1	1.9	69	84	5869	175
ZrTP53.01	2259	42	39	36	30	22	210	374	5105	4403
ZrTP53.02	2302	42	38	37	30	21	179	361	5044	4439
ZrTP53.03	2599	47	44	40	33	22	147	390	5076	4664
ZrTP53.04	2713	48	43	40	34	23	200	396	4989	4830
ZrTP53.05	2897	52	50	55	39	26	283	412	5865	5095
ZrTP54.01	2255	175	126	84	59	43	332	1821	7833	4123
ZrTP54.02	2585	198	142	90	67	47	804	2003	7922	4527
ZrTP54.03	2729	206	151	90	71	50	371	2102	8034	4752
ZrTP54.04	2954	230	159	84	77	52	498	2195	7877	4886
ZrTP54.05	3333	252	179	85	86	59	405	2457	7838	5346

APPENDIX F

ZIRCON SYNTHESIS EXPERIMENT LOWER CHAMBER ANALYSES (ppm) AND

1σ ERROR (1 se) VALUES.

Analysis #	La (ppm)	Ce	Pr	Nd	Sm	Eu	Gd	Tb	Dy	Y	Ho	Er	Tm	Lu
ZrTP11.05	1690	1344	1213	1252	1192	1244	1095	1107	1064	978	1038	898	803	664
ZrTP11.06	1748	1421	1244	1250	1199	1298	1107	1142	1091	1000	1066	917	826	691
ZrTP11.07	1839	1468	1318	1354	1293	1356	1178	1180	1140	1034	1095	963	874	722
ZrTP11.08	1825	1454	1286	1326	1263	1344	1167	1172	1130	1026	1105	956	863	719
ZrTP11.09	1782	1430	1264	1304	1238	1338	1161	1169	1113	1013	1069	943	849	715
ZrTP13.24	505	295	381	402	399	418	355	357	328	303	304	251	227	192
ZrTP13.25	495	294	373	390	392	412	353	353	324	298	304	251	224	194
ZrTP13.26	500	294	377	381	386	408	359	355	329	298	303	259	227	197
ZrTP13.27	501	294	390	401	401	423	369	364	340	304	312	264	233	200
ZrTP13.28	472	282	360	381	378	398	343	343	317	284	297	249	224	194
ZrTP14.05	797	724	657	698	709	745	663	729	720	676	737	674	654	618
ZrTP14.06	810	748	670	719	717	763	699	742	735	679	761	701	675	645
ZrTP14.07	815	751	675	719	716	768	685	737	733	682	753	690	671	645
ZrTP14.08	810	741	666	707	711	758	694	740	745	674	762	691	675	648
ZrTP14.09	824	753	682	718	716	775	697	755	746	685	782	705	689	663
ZrTP34.05	303	323	293	322	344	368	369	423	454	488	495	491	519	582
ZrTP34.06	298	329	290	315	347	379	376	422	469	489	493	499	527	590
ZrTP34.07	273	300	264	283	314	320	305	339	372	393	409	383	433	426
ZrTP34.08	273	301	271	296	327	368	341	394	416	459	456	460	483	536
ZrTP34.09	240	266	233	256	282	291	262	309	320	331	344	331	352	361
ZrTP35.05	753	856	685	731	720	758	697	718	729	712	753	731	755	822
ZrTP35.06	775	838	690	754	739	751	701	732	734	739	773	740	762	847
ZrTP35.07	755	820	675	719	738	750	686	725	720	716	745	727	747	832
ZrTP35.08	761	831	683	739	757	759	683	723	724	712	755	732	746	822
ZrTP35.09	760	810	684	736	739	754	684	719	712	721	754	715	756	831
ZrTP40.05	1098	498	960	1010	889	863	713	630	567	512	543	480	450	449
ZrTP40.06	1139	504	991	1036	898	887	725	649	588	522	568	484	460	463

ZrTP40.07	1106	505	965	1025	892	852	711	635	574	506	550	479	454	446
ZrTP40.08	1105	496	970	1016	891	856	707	633	587	516	545	465	446	448
ZrTP40.09	1110	493	968	1003	903	861	714	632	567	518	551	470	453	453
ZrTP44.05	1141	982	1019	1042	985	1010	879	882	866	841	858	789	776	763
ZrTP44.06	1135	982	1017	1035	982	990	846	877	836	811	837	771	749	733
ZrTP44.07	1159	992	1038	1043	986	927	882	878	832	857	869	786	780	776
ZrTP44.08	1114	991	1025	1078	973	969	881	885	849	833	853	757	748	744
ZrTP44.09	1173	1015	1056	1083	1031	996	892	912	883	867	881	800	778	775
ZrTP46.01	909	1742	745	781	978	1136	1079	1463	1639	1787	1980	2014	2107	2290
ZrTP46.02	925	1702	759	858	959	1145	1123	1455	1727	1802	1991	2041	2113	2264
ZrTP46.03	970	1757	771	856	1032	1255	1225	1571	1889	1870	2142	2159	2266	2477
ZrTP46.04	936	1792	770	835	1041	1232	1171	1536	1785	1827	2062	2045	2225	2443
ZrTP46.05	979	1792	777	841	1043	1218	1185	1556	1862	1853	2145	2127	2297	2460
ZrTP47.01	961	760	858	889	1008	976	816	782	692	637	641	524	481	427
ZrTP47.02	972	750	866	912	978	974	805	788	704	667	662	559	497	430
ZrTP47.03	982	749	855	899	958	931	834	771	682	663	655	533	484	419
ZrTP47.04	1029	807	921	959	1031	1029	902	836	752	704	682	586	525	456
ZrTP47.05	964	750	861	933	960	970	834	774	724	655	654	544	494	430
ZrTP49.01	775	475	606	586	423	400	293	247	226	212	204	166	157	143
ZrTP49.02	834	510	585	590	430	386	306	267	215	218	197	191	166	161
ZrTP49.03	784	478	609	580	425	384	282	248	222	210	189	171	151	146
ZrTP49.04	793	490	612	572	442	399	292	263	219	214	206	185	164	151
ZrTP49.05	776	483	628	595	445	400	294	261	217	213	206	170	162	148
ZrTP51.01	420	206	349	318	265	259	201	210	200	219	194	194	189	193
ZrTP51.02	416	202	339	327	280	246	226	206	184	225	194	179	188	199
ZrTP51.03	415	203	343	354	269	253	215	199	204	221	194	184	183	197
ZrTP51.04	419	203	342	337	276	264	235	206	204	221	199	184	189	206
ZrTP51.05	414	200	338	341	260	252	207	202	173	215	188	184	186	202

ZrTP52.01	344	583	326	369	301	420	362	233	212	193	183	141	137	107
ZrTP52.02	544	624	426	318	530	499	369	389	356	270	285	209	164	186
ZrTP52.03	414	597	287	330	269	378	285	237	195	174	185	149	133	106
ZrTP52.04	520	609	440	414	503	508	404	399	350	302	298	212	214	202
ZrTP52.05	470	649	375	400	405	444	327	322	263	223	221	161	149	130
ZrTP53.01	509	474	421	405	432	452	402	427	430	461	460	435	476	530
ZrTP53.02	484	469	439	428	408	431	403	418	428	476	438	428	450	509
ZrTP53.03	498	481	432	463	434	459	379	441	443	467	467	441	476	537
ZrTP53.04	489	462	424	438	422	451	397	429	408	483	446	424	467	524
ZrTP53.05	489	454	420	423	406	428	351	414	407	439	433	399	465	532
ZrTP54.01	2298	2073	2101	2060	2057	2105	1822	2061	2128	2266	2169	2053	2166	2248
ZrTP54.02	2420	2181	2106	2187	2074	2126	1904	2156	2210	2317	2285	2230	2233	2323
ZrTP54.03	2314	2064	2044	2082	1954	2053	1816	2021	2009	2196	2166	2105	2157	2190
ZrTP54.04	2285	2029	1946	2016	1916	2031	1758	2002	2024	2141	2123	2087	2103	2182
ZrTP54.05	2370	2081	2026	2118	1965	2084	1885	2077	2160	2224	2253	2168	2233	2302

Analysis #	Hf (ppm)	Th	U	Ti	Nb	Ta	P	Sc	Si	Zr
ZrTP11.05	249	347	650	337	223	159	42	490	116860	4217
ZrTP11.06	261	359	676	347	223	163	181	510	116860	4296
ZrTP11.07	269	379	727	363	236	170	180	523	116860	4524
ZrTP11.08	272	373	711	360	229	171	206	528	116860	4419
ZrTP11.09	268	363	690	357	226	168	231	527	116860	4363
ZrTP13.24	160	37	497	488	37	31	<30	164	116860	1220
ZrTP13.25	162	38	498	496	37	30	132	161	116860	1213
ZrTP13.26	165	40	497	479	35	31	150	162	116860	1176
ZrTP13.27	170	40	517	510	37	33	227	163	116860	1220
ZrTP13.28	168	39	496	474	35	31	170	156	116860	1143
ZrTP14.05	457	141	567	425	276	226	348	667	116860	28976
ZrTP14.06	470	147	599	430	274	230	347	678	116860	29246
ZrTP14.07	470	149	612	443	277	230	305	668	116860	29558
ZrTP14.08	472	151	606	443	274	234	377	676	116860	29292
ZrTP14.09	483	152	626	446	279	236	389	690	116860	29815
ZrTP34.05	7766	459	232	408	97	65	249	8349	116860	73909
ZrTP34.06	7716	452	232	404	96	66	422	8432	116860	74608
ZrTP34.07	5937	366	211	380	90	58	103	6905	116860	59720
ZrTP34.08	7167	409	219	352	92	60	51	7842	116860	70688
ZrTP34.09	4913	298	207	352	81	52	104	6571	116860	56494
ZrTP35.05	8181	350	370	2099	295	149	316	8271	116860	66679
ZrTP35.06	8299	350	366	2076	304	150	297	8277	116860	69162
ZrTP35.07	8150	346	371	2062	291	150	316	8321	116860	67684
ZrTP35.08	8026	342	367	2041	296	149	353	8347	116860	68603
ZrTP35.09	8095	350	355	2053	296	150	288	8262	116860	68089
ZrTP40.05	2888	205	243	606	122	132	304	2533	116860	24029
ZrTP40.06	2962	212	255	623	122	139	290	2632	116860	24194

ZrTP40.07	2854	204	244	612	122	134	276	2525	116860	23595
ZrTP40.08	2878	207	242	613	121	133	328	2532	116860	23894
ZrTP40.09	2894	208	243	615	122	135	284	2587	116860	23844
ZrTP44.05	7329	390	396	1574	132	98	276	2783	116860	27590
ZrTP44.06	7104	375	396	1562	124	93	261	2711	116860	27005
ZrTP44.07	7236	380	395	1566	130	91	113	2786	116860	28292
ZrTP44.08	7215	368	390	1549	119	91	215	2806	116860	27319
ZrTP44.09	7447	396	412	1640	140	98	197	2820	116860	28375
ZrTP46.01	15651	2359	900	1086	610	382	1768	7043	179029	65015
ZrTP46.02	15434	2471	912	997	578	360	1942	6703	179029	61849
ZrTP46.03	16494	2526	958	1137	619	399	<1141	7441	181366	67657
ZrTP46.04	16833	2594	930	853	617	380	2614	7223	179029	66960
ZrTP46.05	16576	2472	944	1280	687	432	902	7415	179029	68675
ZrTP47.01	655	452	490	1012	674	229	<388	613	212685	9576
ZrTP47.02	707	471	524	1113	772	271	<418	666	212685	9601
ZrTP47.03	679	460	500	841	650	204	<371	633	212685	9252
ZrTP47.04	772	484	525	1160	760	265	<400	676	212685	10167
ZrTP47.05	726	457	514	1264	780	264	<431	656	212685	9718
ZrTP49.01	2114	521	370	1954	193	46	<224	1447	210815	7280
ZrTP49.02	2276	534	415	1847	197	43	<230	1503	210815	7551
ZrTP49.03	2209	527	382	1821	196	47	<201	1429	210815	7248
ZrTP49.04	2289	557	385	1995	196	51	265	1451	210815	7345
ZrTP49.05	2255	543	370	1986	201	50	<225	1447	210815	7430
ZrTP51.01	10998	349	138	244	95	34	<345	3283	165474	42523
ZrTP51.02	10935	341	138	240	91	36	<328	3287	165474	42138
ZrTP51.03	10759	346	136	268	92	35	<269	3285	165474	41739
ZrTP51.04	11089	348	144	226	91	37	<281	3308	165474	43246
ZrTP51.05	10885	334	136	263	91	35	<245.	3346	165474	42558

ZrTP52.01	950	88	121	367	30	9	104	2283	163604	4614
ZrTP52.02	1495	168	113	202	28	13	509	2940	163604	6111
ZrTP52.03	1076	95	134	305	31	12	<64	2057	163604	4267
ZrTP52.04	1815	141	124	234	49	19	635	2952	163604	6607
ZrTP52.05	1343	120	116	368	32	16	135	2507	163604	5098
ZrTP53.01	24941	551	551	294	482	406	606	9328	137427	99060
ZrTP53.02	23573	517	511	346	464	379	452	8793	137427	96507
ZrTP53.03	24711	541	552	357	466	392	<351	9213	137427	97283
ZrTP53.04	24046	520	503	360	470	381	478	9134	137427	97269
ZrTP53.05	23771	516	540	314	463	398	594	8631	137427	94092
ZrTP54.01	19716	2652	1896	1706	787	765	<662	31673	211283	83050
ZrTP54.02	20293	2747	1935	1811	798	782	1494	32098	211283	84882
ZrTP54.03	19377	2612	1884	1763	786	762	<725	31088	211283	82931
ZrTP54.04	19138	2694	1834	1711	768	757	700	30210	211283	80036
ZrTP54.05	19818	2733	1911	1737	802	779	<593	31502	211283	82045

Analysis #	La (1se)	Ce	Pr	Nd	Sm	Eu	Gd	Tb	Dy	Y	Ho	Er	Tm	Lu
ZrTP11.05	97.9	72.5	71.6	62.3	64.2	70.9	55.6	61.6	57.3	39.1	56.7	47.4	41.0	33.8
ZrTP11.06	106.2	80.1	77.1	64.8	67.5	77.5	58.7	66.6	61.5	41.1	61.0	50.6	44.0	36.7
ZrTP11.07	117.7	87.1	86.1	73.5	76.6	85.3	65.5	72.4	67.5	43.9	65.9	55.8	48.8	40.2
ZrTP11.08	123.5	91.0	88.8	75.6	78.8	89.2	68.2	75.9	70.5	45.2	70.1	58.4	50.8	42.1
ZrTP11.09	127.8	94.7	92.5	78.3	81.6	94.1	71.5	80.1	73.4	46.4	71.7	60.8	52.7	44.2
ZrTP13.24	17.8	10.7	15.2	15.5	15.7	14.3	14.1	13.4	12.1	13.0	11.2	8.4	8.5	6.9
ZrTP13.25	17.7	10.9	15.3	15.5	15.8	14.3	14.4	13.6	12.2	13.2	11.5	8.5	8.6	7.1
ZrTP13.26	18.3	11.1	16.0	15.6	16.1	14.5	15.2	14.1	12.7	13.7	11.7	8.9	9.0	7.4
ZrTP13.27	18.8	11.5	17.2	17.0	17.3	15.3	16.2	15.0	13.5	14.6	12.5	9.3	9.5	7.7
ZrTP13.28	18.2	11.3	16.5	16.8	17.0	14.8	15.6	14.6	13.0	14.2	12.3	8.9	9.5	7.7
ZrTP14.05	25.1	23.2	21.2	24.3	22.9	23.3	20.8	23.6	21.8	21.9	22.9	20.5	20.5	18.8
ZrTP14.06	25.7	24.1	21.8	25.3	23.3	24.0	22.0	24.3	22.2	22.2	23.7	21.3	21.2	19.6
ZrTP14.07	26.0	24.4	22.2	25.8	23.5	24.3	21.7	24.4	22.1	22.5	23.6	21.0	21.2	19.6
ZrTP14.08	26.1	24.4	22.1	26.0	23.6	24.2	22.1	24.8	22.5	22.6	24.0	21.1	21.5	19.7
ZrTP14.09	26.8	25.1	23.0	27.0	24.0	24.9	22.3	25.7	22.5	23.3	24.8	21.5	22.1	20.2
ZrTP34.05	9.4	10.1	8.9	11.2	12.0	11.7	12.6	13.1	14.0	14.8	15.4	16.3	15.8	18.1
ZrTP34.06	9.4	10.4	8.9	11.4	12.4	12.2	13.2	13.2	14.7	14.9	15.5	16.9	16.1	18.5
ZrTP34.07	8.6	9.5	8.1	10.3	11.4	10.4	10.8	10.7	11.7	12.0	12.9	13.1	13.2	13.4
ZrTP34.08	8.9	9.8	8.5	11.2	12.5	12.3	12.7	12.8	13.4	14.4	14.9	16.4	15.2	17.4
ZrTP34.09	7.7	8.5	7.2	9.8	10.7	9.6	9.7	9.8	10.2	10.1	11.0	11.8	10.8	11.5
ZrTP35.05	23.3	25.9	21.8	24.9	23.6	25.8	22.6	22.4	22.6	23.0	23.6	23.6	23.2	26.6
ZrTP35.06	24.0	25.4	22.1	26.0	24.5	26.0	22.8	22.9	22.8	24.0	24.3	24.1	23.4	27.7
ZrTP35.07	23.5	24.9	21.9	25.2	24.7	26.4	22.6	22.8	22.5	23.6	23.6	23.9	23.0	27.5
ZrTP35.08	24.0	25.4	22.5	26.8	26.1	27.4	23.2	23.0	23.0	23.9	24.3	24.6	23.2	27.7
ZrTP35.09	24.0	24.7	22.7	26.9	25.6	27.7	23.1	22.9	22.5	24.4	24.3	24.2	23.5	28.3
ZrTP40.05	34.8	16.8	31.7	39.7	29.4	29.0	23.5	21.1	18.4	18.4	17.8	15.4	14.2	15.2

ZrTP40.06	36.3	17.2	33.0	41.6	30.0	30.1	24.1	21.9	19.2	19.1	18.8	15.7	14.6	15.8
ZrTP40.07	35.5	17.4	32.5	42.2	30.1	29.2	23.9	21.7	18.9	18.8	18.4	15.6	14.5	15.5
ZrTP40.08	35.7	17.3	33.1	42.9	30.4	29.8	24.0	21.9	19.4	19.6	18.4	15.3	14.3	15.8
ZrTP40.09	36.2	17.5	33.5	43.7	31.3	30.5	24.6	22.2	19.0	20.1	18.9	15.6	14.7	16.2
ZrTP44.05	41.5	35.8	38.8	39.7	38.4	37.9	38.3	35.3	35.0	35.9	32.9	31.3	29.6	28.6
ZrTP44.06	41.2	35.7	38.6	39.3	38.1	37.1	36.8	35.0	33.8	34.6	32.0	30.5	28.5	27.4
ZrTP44.07	42.4	36.4	39.8	40.5	39.0	35.2	39.0	35.4	34.1	36.8	33.6	31.6	30.0	29.4
ZrTP44.08	40.7	36.3	39.2	41.6	38.4	36.6	38.8	35.6	34.7	35.7	32.9	30.3	28.7	28.1
ZrTP44.09	42.6	37.0	40.1	41.1	40.1	37.3	38.8	36.4	35.7	37.0	33.7	31.7	29.7	29.0
ZrTP46.01	34.6	67.8	28.3	34.3	41.5	44.6	45.4	55.1	64.6	71.3	74.5	78.4	81.2	87.4
ZrTP46.02	37.9	71.0	31.0	40.5	44.2	48.3	50.8	59.0	73.1	76.8	80.6	85.4	87.3	92.7
ZrTP46.03	40.9	75.2	32.5	42.5	48.9	54.4	57.1	65.5	82.3	81.8	89.1	92.9	96.1	104.2
ZrTP46.04	39.0	76.0	32.1	40.4	48.4	52.9	54.1	63.4	77.0	79.1	85.0	87.1	93.5	101.8
ZrTP46.05	36.4	68.4	28.9	35.9	43.3	46.9	48.8	57.4	71.7	72.5	79.0	81.1	86.7	92.0
ZrTP47.01	32.9	25.6	28.5	33.8	37.0	32.6	31.7	26.4	25.9	22.0	21.2	19.3	16.2	14.7
ZrTP47.02	33.1	25.1	28.6	33.8	35.4	32.3	30.9	26.4	26.0	22.8	21.7	20.3	16.6	14.7
ZrTP47.03	33.0	24.8	27.9	32.7	34.1	30.5	31.3	25.6	24.8	22.4	21.2	19.0	15.9	14.1
ZrTP47.04	34.7	26.8	30.2	34.8	36.6	33.8	33.7	27.8	27.3	23.9	22.2	20.9	17.3	15.4
ZrTP47.05	32.6	25.0	28.3	34.1	34.4	32.0	31.5	25.9	26.4	22.3	21.3	19.5	16.4	14.6
ZrTP49.01	25.2	15.2	19.7	20.3	15.7	13.6	11.3	8.6	8.1	7.1	7.0	5.8	5.4	4.9
ZrTP49.02	31.9	20.0	22.6	32.5	25.1	17.5	20.1	11.7	13.4	10.1	9.0	11.1	7.7	7.6
ZrTP49.03	25.5	15.3	19.8	20.1	15.7	13.1	10.9	8.7	8.0	7.1	6.5	6.0	5.2	4.9
ZrTP49.04	25.7	15.7	19.8	19.7	16.2	13.5	11.1	9.1	7.8	7.1	7.0	6.4	5.6	5.1
ZrTP49.05	25.2	15.5	20.4	20.5	16.4	13.6	11.2	9.1	7.8	7.1	7.1	6.0	5.5	5.0
ZrTP51.01	19.6	9.0	14.9	19.1	17.9	11.9	9.5	12.7	9.1	12.2	12.8	7.4	10.2	8.3
ZrTP51.02	20.3	9.2	15.0	20.4	19.8	11.8	10.7	13.2	8.6	13.2	13.6	6.9	10.6	8.9
ZrTP51.03	21.0	9.5	15.6	22.9	20.0	12.4	10.3	13.3	9.4	13.6	14.3	7.0	10.8	9.0
ZrTP51.04	22.2	9.9	16.2	23.1	21.6	13.6	11.5	14.7	9.8	14.4	15.6	7.2	11.7	9.8

ZrTP51.05	22.9	10.1	16.5	24.3	21.3	13.4	10.5	15.1	8.5	14.7	15.5	7.1	12.0	9.9
ZrTP52.01	12.7	20.8	11.9	20.0	16.4	16.5	18.7	9.0	11.3	8.0	7.4	7.7	5.7	4.8
ZrTP52.02	30.1	34.2	23.8	33.6	43.4	30.9	34.3	22.4	28.9	17.4	17.4	18.0	11.0	12.4
ZrTP52.03	14.8	20.9	10.5	17.8	14.7	14.7	15.2	9.0	10.3	7.2	7.3	7.7	5.4	4.6
ZrTP52.04	19.6	22.9	16.6	19.6	22.5	19.8	18.6	15.2	15.3	11.9	11.5	9.5	8.4	8.0
ZrTP52.05	16.1	21.9	12.9	18.5	17.9	16.0	15.2	11.3	11.6	8.3	8.0	7.3	5.6	5.1
ZrTP53.01	34.7	27.4	22.8	32.6	32.8	30.3	34.9	29.1	25.5	27.2	32.5	30.9	38.0	47.2
ZrTP53.02	35.2	28.7	25.0	36.7	33.1	30.8	37.4	30.3	26.7	29.7	33.1	32.4	38.6	48.8
ZrTP53.03	38.7	31.2	26.0	42.5	37.7	35.0	37.9	34.2	29.3	30.9	37.7	35.7	43.8	55.5
ZrTP53.04	40.3	31.6	26.9	42.8	39.0	36.4	42.2	35.4	28.5	33.8	38.4	36.4	45.9	58.0
ZrTP53.05	43.9	34.0	29.2	46.7	42.4	38.1	42.0	37.3	32.3	33.7	40.6	37.9	49.6	63.9
ZrTP54.01	130.0	135.8	128.5	155.7	154.1	197.4	130.4	188.7	167.7	107.4	221.2	148.8	142.9	160.3
ZrTP54.02	148.5	156.2	140.2	182.3	170.7	221.3	149.3	219.3	192.4	117.2	259.5	178.1	161.6	182.1
ZrTP54.03	153.7	161.0	147.7	190.5	175.7	235.6	155.4	227.0	192.1	118.5	272.0	184.6	170.5	188.0
ZrTP54.04	163.1	171.0	151.4	201.0	186.7	254.9	162.9	246.4	210.9	122.2	292.6	199.2	180.2	203.4
ZrTP54.05	181.6	189.0	169.3	229.2	206.8	284.5	188.4	278.4	244.2	134.6	338.6	224.7	206.9	232.3

Analysis #	Hf (1se)	Th	U	Ti	Nb	Ta	P	Sc	Si	Zr
ZrTP11.05	13	22	42	19	8.8	7.7	13	28	3703	177
ZrTP11.06	14	24	46	20	9.0	8.2	22	30	3703	187
ZrTP11.07	16	27	52	22	9.8	8.9	23	33	3702	204
ZrTP11.08	17	28	54	23	9.9	9.4	28	35	3703	207
ZrTP11.09	17	29	56	25	10.1	9.7	33	37	3702	214
ZrTP13.24	5.4	1.2	16	17	1.6	1.0	11	6	3703	54
ZrTP13.25	5.5	1.2	16	17	1.7	1.0	15	6	3703	55
ZrTP13.26	5.7	1.3	16	17	1.7	1.0	15	7	3702	56
ZrTP13.27	6.0	1.3	17	18	1.8	1.1	22	7	3703	60
ZrTP13.28	6.0	1.3	16	17	1.8	1.1	18	7	3702	59
ZrTP14.05	15	4.3	18	32	8.9	6.8	31	21	3711	1113
ZrTP14.06	16	4.5	19	34	8.9	7.0	29	21	3706	1152
ZrTP14.07	16	4.5	19	37	9.1	7.0	27	21	3708	1201
ZrTP14.08	16	4.6	19	40	9.1	7.1	32	21	3706	1231
ZrTP14.09	17	4.6	20	42	9.4	7.1	34	22	3706	1300
ZrTP34.05	252	14	7.5	14	3.0	2.1	22	259	3711	2486
ZrTP34.06	254	14	7.6	16	3.0	2.2	36	263	3733	2549
ZrTP34.07	197	12	7.0	14	2.8	1.9	12	216	3718	2068
ZrTP34.08	247	14	7.5	28	2.9	2.1	98	254	3918	2545
ZrTP34.09	168	10	7.0	14	2.5	1.8	10	208	3720	2029
ZrTP35.05	249	11	11	75	9.3	4.7	23	260	3709	2384
ZrTP35.06	253	11	11	76	10	4.7	23	262	3704	2524
ZrTP35.07	249	11	12	77	9.3	4.7	25	265	3705	2532
ZrTP35.08	247	11	12	80	10	4.8	31	270	3734	2645
ZrTP35.09	249	11	11	81	10	4.8	25	268	3704	2696

ZrTP40.05	89	6.6	7.5	21	4.2	4.5	23	88	3708	832
ZrTP40.06	91	6.9	7.9	22	4.3	4.8	22	93	3706	848
ZrTP40.07	88	6.7	7.6	22	4.3	4.7	22	90	3707	839
ZrTP40.08	89	6.8	7.6	22	4.4	4.7	25	92	3704	863
ZrTP40.09	90	6.9	7.6	23	4.5	4.9	23	96	3709	877
ZrTP44.05	286	14	13	51	4.9	3.8	34	99	3743	1151
ZrTP44.06	277	13	13	51	4.6	3.6	25	96	3725	1125
ZrTP44.07	285	13	13	55	5.0	3.6	31	100	3794	1186
ZrTP44.08	283	13	13	53	4.5	3.6	32	100	3779	1144
ZrTP44.09	291	14	14	53	5.2	3.8	26	100	3731	1183
ZrTP46.01	667	91	34	89	24	15	458	269	7885	2586
ZrTP46.02	696	102	37	99	25	16	539	275	8712	2623
ZrTP46.03	761	107	40	111	27	18	511	313	9151	2941
ZrTP46.04	770	109	39	105	27	17	618	301	8925	2886
ZrTP46.05	694	93	35	89	26	17	352	277	7640	2680
ZrTP47.01	27	16	17	67	23	8.0	167	23	7536	370
ZrTP47.02	28	16	18	69	26	9.3	174	24	7515	370
ZrTP47.03	26	16	17	54	21	7.0	151	23	7362	353
ZrTP47.04	30	16	18	67	25	9.0	159	24	7442	389
ZrTP47.05	28	16	18	74	26	9.0	171	24	7474	373
ZrTP49.01	74	17	12	81	6.5	1.8	89	47	6940	262
ZrTP49.02	99	21	17	135	9.3	2.9	185	59	8437	315
ZrTP49.03	77	17	12	76	6.6	1.8	85	46	6923	261
ZrTP49.04	80	18	12	81	6.5	1.9	88	47	6902	264
ZrTP49.05	79	18	12	82	6.7	1.9	87	47	6922	267
ZrTP51.01	793	18	4.8	31	5.3	2.6	131	265	5845	4167
ZrTP51.02	841	18	4.8	30	5.3	2.9	127	285	5829	4453
ZrTP51.03	879	19	4.6	27	5.6	2.9	104	305	5686	4737

ZrTP51.04	963	20	4.9	27	5.9	3.3	200	329	5743	5263
ZrTP51.05	1001	20	4.6	27	6.2	3.3	144	354	5661	5532
ZrTP52.01	40	4.1	5.4	44	2.2	1.0	79	80	6161	169
ZrTP52.02	96	12	8.8	91	4.2	2.4	367	154	10366	339
ZrTP52.03	43	4.3	5.7	38	2.1	1.1	67	71	6074	154
ZrTP52.04	71	5.8	5.2	54	2.7	1.3	225	110	7047	248
ZrTP52.05	49	4.8	4.7	37	1.9	1.1	69	84	5869	175
ZrTP53.01	2259	42	39	36	22	30	210	374	5105	4403
ZrTP53.02	2302	42	38	37	21	30	179	361	5044	4439
ZrTP53.03	2599	47	44	40	22	33	147	390	5076	4664
ZrTP53.04	2713	48	43	40	23	34	200	396	4989	4830
ZrTP53.05	2897	52	50	55	26	39	283	412	5865	5095
ZrTP54.01	2255	175	126	84	43	59	332	1821	7833	4123
ZrTP54.02	2585	198	142	90	47	67	804	2003	7922	4527
ZrTP54.03	2729	206	151	90	50	71	371	2102	8034	4752
ZrTP54.04	2954	230	159	84	52	77	498	2195	7877	4886
ZrTP54.05	3333	252	179	85	59	86	405	2457	7838	5346

APPENDIX G

ZIRCON RECRYSTALLIZATION EXPERIMENT LOWER CHAMBER ANALYSES (ppm)

AND 1σ ERROR (1 se) VALUES.

Experiment ZrMT-02

Analysis #	La (ppm)	Ce	Pr	Nd	Sm	Eu	Gd	Tb	Dy	Y	Ho	Er	Tm	Lu
1	43	51	55	67	70	102	101	159	213	357	289	350	454	628
2	36	42	43	40	74	82	92	133	180	286	234	301	355	479
3	50	53	52	51	71	85	85	123	158	247	217	274	332	449
4	54	58	52	63	81	92	105	134	166	276	241	290	361	492
5	69	70	66	83	88	113	118	148	190	286	247	298	378	494
6	50	59	58	62	84	104	107	149	202	299	271	334	422	580
7	43	54	51	70	87	99	109	138	187	266	246	292	380	519
8	51	57	58	67	75	98	111	157	211	316	303	371	478	671
9	285	254	231	238	245	233	257	271	304	427	336	379	445	537
10	284	271	245	236	262	229	231	278	298	404	321	357	420	505

Analysis #	Hf (ppm)	P	Sc	Th	U	Ti	Ta	Nb	Si	Zr
1	7871	956	1101	927	780		137	91	149581	325672
2	7707	1076	888	922	675		104	60	149581	332319
3	7471	470	839	980	504		98	59	149581	321528
4	7587	1004	921	1224	526	98	139	67	149581	321524
5	7583	1106	935	770	682		97	52	149581	327195
6	7863	888	988	723	782		100	51	149581	325524
7	7477	842	843	352	516		79	29	149581	319630
8	8354	577	1091	458	1232		98	41	149581	334395
9	*7658*	*536*	*896*	*521*	*702*		*85*	*38*	*149581*	*325428*
10	*7290*	*460*	*834*	*471*	*738*		*81*	*36*	*149581*	*307144*

Analysis #	La (1 se)	Ce	Pr	Nd	Sm	Eu	Gd	Tb	Dy	Y	Ho	Er	Tm	Lu
1	1.7	2.2	2.8	5.2	5.0	4.7	7.7	7.6	11.1	15.1	13.5	14.9	19.4	26.0
2	1.5	1.8	2.2	3.5	5.3	3.9	7.1	6.5	9.6	12.3	11.0	12.9	15.4	20.0
3	2.0	2.3	2.7	4.3	5.3	4.1	6.9	6.1	8.7	10.8	10.4	12.0	14.6	19.0
4	2.1	2.5	2.7	5.1	5.8	4.4	8.2	6.6	9.0	12.0	11.5	12.6	15.9	20.9
5	2.7	3.0	3.5	6.6	6.4	5.3	9.4	7.5	10.4	12.6	12.0	13.2	16.8	21.2

6	2.0	2.5	3.1	5.1	6.2	5.0	8.6	7.5	11.1	13.2	13.2	14.8	18.9	25.0
7	1.8	2.4	2.8	5.8	6.5	4.8	9.0	7.1	10.5	11.9	12.2	13.1	17.2	22.7
8	2.1	2.6	3.3	5.8	6.0	4.9	9.7	8.5	12.3	14.7	15.7	17.2	22.5	30.4
9	10.8	10.7	12.4	18.4	17.6	11.1	21.0	14.1	17.1	19.4	16.9	17.1	20.4	23.8
10	10.8	11.5	13.4	18.6	19.2	11.0	19.3	14.7	17.0	18.6	16.4	16.4	19.6	22.7

Analysis #	Hf (1 se)	P	Sc	Th	U	Ti	Ta	Nb	Si	Zr
1	551	245	57	33	37	28	5.2	6.2	4972	23195
2	546	256	46	33	32	30	4.0	4.2	4999	23946
3	538	162	44	35	24	38	3.8	4.2	5078	23513
4	553	220	49	44	26	36	5.3	4.8	5008	23833
5	563	235	51	28	34	39	3.8	3.8	5058	24687
6	594	182	54	26	39	31	3.9	3.8	4992	24983
7	576	165	47	13	26	31	3.2	2.3	4992	25018
8	688	122	64	17	66	33	3.9	3.3	5005	27955
9	603	127	51	19	36	35	3.4	3.0	5025	26025
10	587	112	48	17	39	33	3.3	2.9	5021	25105

Experiment ZrMT-03

Analysis #	La (ppm)	Ce	Pr	Nd	Sm	Eu	Gd	Tb	Dy	Y	Ho	Er	Tm	Lu
1	159	145	142	151	145	168	167	189	229	324	255	298	366	479
2	117	120	120	149	148	198	194	256	335	503	418	480	626	858
3	152	140	141	151	155	195	183	223	265	388	315	375	489	656
4	60	60	55	61	79	105	104	143	188	294	267	329	426	610
5	84	87	82	85	112	143	138	176	230	313	284	351	453	653
6	84	95	82	108	117	147	141	184	237	321	298	357	475	635
7	87	90	91	97	123	157	145	192	241	348	315	377	480	672
8	76	79	80	90	92	137	141	164	222	311	277	350	452	610
9	507	464	476	445	433	443	413	448	493	743	528	550	676	811
10	362	351	367	324	338	334	332	362	393	637	449	486	607	761

Analysis #	Hf (ppm)	P	Sc	Th	U	Ti	Ta	Nb	Si	Zr
1	6536	571	862	632	923		105	95	149581	272291
2	7893	1052	1371	670	1195	66	225	129	149581	279141
3	6874	660	1115	839	1712		140	103	149581	298248
4	7404	493	1118	1014	1785		111	97	149581	317472
5	7559	656	1116	774	1696	117	124	82	149581	301633
6	7456	657	1112	731	1836	178	126	91	149581	317227
7	7783	616	1152	737	1820	168	125	83	149581	315259
8	7834	266	1062	778	1907		106	83	149581	327560
9	7697	895	1339	1660	1774		312	132	149581	309902
10	7190	832	1263	1496	1844		246	120	149581	301847

Analysis #	La (1 se)	Ce	Pr	Nd	Sm	Eu	Gd	Tb	Dy	Y	Ho	Er	Tm	Lu
1	6.4	6.7	8.7	13.5	12.1	8.9	16.0	11.1	14.5	16.3	14.4	14.8	18.6	23.4
2	4.9	5.7	7.6	13.9	12.8	10.7	19.2	15.4	21.7	25.7	24.1	24.2	32.4	42.7
3	6.3	6.6	9.0	14.1	13.6	10.7	18.5	13.6	17.5	20.2	18.5	19.2	25.7	33.1
4	2.6	3.0	3.6	6.3	7.3	6.0	11.0	9.0	12.9	15.7	16.0	17.3	22.9	31.4
5	3.7	4.3	5.5	8.8	10.5	8.2	14.9	11.3	16.1	17.0	17.4	18.8	24.8	34.3

6	3.8	4.9	5.7	11.3	11.3	8.6	15.7	12.1	17.0	17.8	18.7	19.5	26.6	34.1
7	3.9	4.6	6.3	10.2	11.9	9.3	16.3	12.8	17.4	19.6	20.0	20.7	27.2	36.5
8	3.4	4.1	5.7	9.6	9.2	8.2	16.3	11.2	16.3	17.8	18.0	19.5	26.0	33.7
9	19.9	20.5	27.9	37.3	33.9	22.4	37.4	25.3	29.8	36.0	28.7	26.3	33.2	38.4
10	14.3	15.7	21.9	27.9	27.1	17.1	30.9	20.8	24.3	31.4	24.9	23.6	30.3	36.5

Analysis #	Hf (1 se)	P	Sc	Th	U	Ti	Ta	Nb	Si	Zr
1	609	100	56	24	55	32	4.4	8.4	4952	25707
2	755	162	91	26	73	33	9.4	11.7	5019	27052
3	675	109	76	33	106	31	5.9	9.6	4979	29633
4	746	88	78	41	113	31	4.8	9.3	5009	32366
5	782	108	80	31	110	44	5.4	8.1	5045	31552
6	792	114	81	30	122	61	5.7	9.2	5134	34061
7	847	99	86	31	124	55	5.6	8.6	5027	34674
8	874	62	81	33	132	36	4.8	8.7	4993	36924
9	682	148	83	63	101	30	12.5	11.1	4995	27843
10	653	134	80	57	107	29	10.0	10.4	4964	27793

Experiment ZrMT-05

Analysis #	La (ppm)	Ce	Pr	Nd	Sm	Eu	Gd	Tb	Dy	Y	Ho	Er	Tm	Lu
1	49	51	48	51	67	93	102	143	211	334	290	355	442	597
2	33	43	39	37	57	80	91	138	210	335	284	360	464	613
3	46	56	55	58	84	108	125	158	229	333	297	378	454	604
4	29	36	32	37	53	63	85	129	194	310	269	347	417	587
5	25	35	28	37	58	62	93	136	192	315	271	335	411	558
6	45	56	48	56	68	96	116	147	173	317	267	327	413	559
7	74	84	80	82	93	113	118	154	189	307	263	310	368	495
8	53	62	64	61	80	129	112	160	219	355	321	402	508	760
9	90	101	93	103	93	143	140	161	343	347	281	352	426	564

Analysis #	Hf (ppm)	P	Sc	Th	U	Ti	Ta	Nb	Si	Zr
1	7934	353	863	901	771		113	59	149581	335278
2	7875	417	878	991	711	104	112	63	149581	337426
3	7836	341	756	393	568		84	35	149581	324180
4	7699	303	784	576	713		98	54	149581	316458
5	8069	325	728	383	632	96	83	36	149581	339426
6	7466	205	694	458	689		87	33	149581	311035
7	7100	311	660	375	539		70	37	149581	303460
8	8996	376	881	398	1069		93	37	149581	318563
9	7429	327	790	634	743	82	84	54	149581	315141

Analysis #	La (1 se)	Ce	Pr	Nd	Sm	Eu	Gd	Tb	Dy	Y	Ho	Er	Tm	Lu
1	2.5	2.2	2.4	4.8	6.9	3.7	12.8	8.1	11.5	20.1	16.2	20.7	20.3	29.4
2	1.9	2.1	2.1	4.1	6.3	3.5	11.9	8.0	11.9	20.6	16.3	21.5	21.7	30.8
3	2.4	2.5	2.8	5.7	9.0	4.3	16.5	9.2	12.8	20.8	17.3	22.7	21.4	30.7
4	1.6	1.7	1.7	4.0	6.1	2.7	11.7	7.8	11.1	19.9	16.1	21.5	20.2	30.6
5	1.5	1.7	1.6	4.2	7.0	2.7	13.6	8.5	11.5	21.2	16.9	21.6	20.6	30.2
6	2.8	3.0	2.9	7.1	9.0	4.6	18.3	9.8	11.6	22.6	17.7	22.7	22.0	32.2
7	4.0	3.8	4.2	8.4	10.7	4.6	16.6	9.5	11.2	20.2	16.1	19.7	18.1	26.4

8	2.9	2.8	3.3	6.1	8.9	5.2	15.1	9.5	12.5	22.5	18.9	24.6	24.3	39.2
9	4.7	4.4	4.7	9.8	9.9	5.7	18.2	9.4	19.0	21.5	16.2	21.1	20.1	28.5

Analysis #	Hf (1 se)	P	Sc	Th	U	Ti	Ta	Nb	Si	Zr
1	714	297	41	33	34	31	5.5	2.7	4996	26272
2	719	366	43	37	32	55	5.7	3.0	5148	26798
3	735	331	37	15	26	42	4.2	1.7	5028	26430
4	749	328	39	22	33	39	5.1	2.6	4981	26735
5	819	396	38	15	31	63	4.5	1.8	5036	29935
6	799	296	39	19	36	122	5.1	2.0	5515	28917
7	706	357	34	15	26	53	3.7	1.9	5059	26198
8	859	384	44	15	50	36	4.8	1.8	5049	26435
9	686	302	39	24	34	50	4.3	2.6	5093	25332

APPENDIX H

CALCULATED ZIRCON RECRYSTALLIZATION EXPERIMENT FINAL FLUID COMPOSITION (ppm).

Experiment ZrMT-02

Analysis #	La (ppm)	Ce	Pr	Nd	Sm	Eu	Gd	Tb	Dy	Y	Ho	Er	Tm	Lu
1	697	701	702	700	702	694	695	687	675	659	665	652	628	590
2	711	710	710	700	701	684	686	664	639	599	610	591	541	463
3	699	703	703	700	698	685	689	676	663	637	645	626	586	531
4	730	730	732	730	724	715	716	702	689	669	661	641	607	546
5	722	721	722	722	713	702	704	691	675	663	655	634	598	532
6	722	718	722	714	711	701	703	688	672	660	650	632	591	538
7	721	720	720	718	709	698	702	686	671	651	645	626	589	525
8	725	723	723	720	719	704	703	695	677	663	658	635	599	546
9	654	667	663	672	676	673	681	671	658	585	648	642	605	565
10	696	699	695	707	703	705	705	696	687	616	671	660	625	580

Analysis #	Hf (ppm)	Th	U	Ti	Ta	Nb	P	Sc	Si	Zr
1	378	1296	1200	376	341	346	198	514	93276	94816
2	-77	1283	1109	354	301	335	37	343	93276	92522
3	264	1226	936	376	330	344	168	429	93276	86121
4	87	1168	911	376	339	346	224	428	93276	79680
5	35	1248	941	337	335	351	170	428	93276	84987
6	69	1263	894	317	334	348	169	430	93276	79762
7	-40	1260	900	320	335	350	183	417	93276	80422
8	-57	1247	870	376	341	350	300	446	93276	76301
9	-1845	1126	1092	403	311	364	155	411	69529	-2911
10	-1697	1173	1072	403	331	368	173	433	69529	-558

Experiment ZrMT-03

Analysis #	La (ppm)	Ce	Pr	Nd	Sm	Eu	Gd	Tb	Dy	Y	Ho	Er	Tm	Lu
1	789	787	786	783	782	772	773	756	742	717	718	702	670	619
2	792	790	790	791	781	778	776	763	751	737	734	716	699	663
3	788	787	787	787	782	777	778	766	758	748	739	724	706	671
4	786	785	787	784	779	775	772	763	755	740	732	719	697	659
5	782	782	783	778	777	769	768	759	748	737	730	717	692	658
6	788	785	785	784	778	772	771	759	745	733	724	706	679	633
7	789	787	787	782	777	773	771	762	749	743	731	719	691	651
8	787	785	785	783	780	774	770	756	742	728	714	696	663	607
9	655	659	668	671	662	673	672	657	650	615	642	630	609	581

Analysis #	Hf (ppm)	Th	U	Ti	Ta	Nb	P	Sc	Si	Zr
1	447	1342	1386	403	363	378	137	537	109674	103866
2	495	1343	1417	403	372	387	102	599	109674	101924
3	564	1326	1467	403	374	387	279	613	109674	105076
4	530	1255	1460	374	362	385	123	589	109674	105077
5	532	1387	1415	403	375	389	93	585	109674	103421
6	450	1401	1386	403	374	390	157	570	109674	103909
7	562	1509	1463	403	380	396	170	612	109674	105630
8	306	1479	1254	403	374	392	248	540	109674	101318
9	-2066	1348	1258	376	349	364	282	470	55741	-21002

Experiment ZrMT-05

Analysis #	La (ppm)	Ce	Pr	Nd	Sm	Eu	Gd	Tb	Dy	Y	Ho	Er	Tm	Lu
1	715	715	715	715	711	704	702	692	676	661	656	641	617	579
2	719	717	717	718	713	707	705	693	677	661	657	639	612	575
3	716	713	713	713	707	701	696	688	672	661	654	635	615	578
4	720	718	719	718	714	712	707	695	681	667	661	643	624	582
5	721	719	720	718	713	712	704	694	681	666	660	646	625	589
6	716	713	715	713	711	703	699	691	686	665	661	648	625	589
7	705	702	704	701	704	692	692	687	642	641	657	640	621	587
8	714	712	711	712	707	695	699	687	673	639	647	627	601	538
9	709	706	707	707	704	699	698	689	680	651	662	650	636	604

Analysis #	Hf (ppm)	Th	U	Ti	Ta	Nb	P	Sc	Si	Zr
1	516	1238	1272	365	337	352	290	563	101830	97004
2	531	1215	1287	339	337	351	274	560	101830	96470
3	541	1364	1322	365	344	358	293	590	101830	99764
4	575	1319	1286	365	341	353	302	583	101830	101684
5	483	1366	1306	341	344	358	297	597	101830	95973
6	633	1348	1292	365	344	358	326	605	101830	103033
7	-1483	1302	1275	344	344	352	321	531	65436	1037
8	-1872	1361	1194	365	342	356	306	508	65436	186
9	-1401	1367	1326	365	348	356	326	563	65436	3942

APPENDIX I

ZIRCON SYNTHESIS EXPERIMENT GLASS Si and Zr OXIDE COMPOSITION (wt.%).

		Measured			Normalized			Calculated		
Sample	Analysis #	SiO_2 wt%	ZrO_2 wt%	Total %	SiO_2 wt%	ZrO_2 wt%	Total %	Si wt %	Zr wt%	Total %
ZrTP11	1 / 1 .	25.4	0.8	26.2	97.1	2.9	100	45.4	2.2	47.5
ZrTP11	1 / 2 .	24.8	0.8	25.6	97.0	3.0	100	45.3	2.2	47.6
ZrTP11	1 / 3 .	24.7	0.8	25.4	97.0	3.0	100	45.3	2.3	47.6
ZrTP11	1 / 4 .	24.0	0.7	24.7	97.2	2.8	100	45.4	2.1	47.5
ZrTP11	1 / 5 .	23.0	0.7	23.7	97.1	2.9	100	45.4	2.1	47.5
ZrTP11	1 / 6 .	23.1	0.6	23.7	97.3	2.7	100	45.5	2.0	47.5
ZrTP11	1 / 7 .	23.1	0.7	23.8	97.2	2.8	100	45.4	2.1	47.5
ZrTP11	1 / 8 .	24.2	0.7	24.9	97.3	2.7	100	45.5	2.0	47.5
ZrTP11	1 / 9 .	23.2	0.6	23.8	97.3	2.7	100	45.5	2.0	47.5
ZrTP11	1 / 10 .	24.0	0.7	24.7	97.1	2.9	100	45.4	2.2	47.5
Average		23.9	0.7	24.6	97.1	2.9	100	45.4	2.1	47.5
ZrTP13	3 / 1 .	11.9	0.1	11.9	99.5	0.5	100	46.5	0.4	46.9
ZrTP13	3 / 2 .	11.9	0.0	12.0	99.6	0.4	100	46.6	0.3	46.8
ZrTP13	3 / 3 .	12.2	0.1	12.3	99.1	0.9	100	46.3	0.7	47.0
ZrTP13	3 / 4 .	12.3	0.1	12.4	99.3	0.7	100	46.4	0.6	46.9
ZrTP13	3 / 5 .	12.2	0.1	12.3	99.2	0.8	100	46.4	0.6	47.0
ZrTP13	3 / 6 .	12.0	0.1	12.1	99.1	0.9	100	46.3	0.7	47.0
ZrTP13	3 / 7 .	12.1	0.1	12.1	99.4	0.6	100	46.4	0.5	46.9
ZrTP13	3 / 8 .	12.3	0.1	12.4	99.2	0.8	100	46.4	0.6	47.0
ZrTP13	3 / 9 .	12.4	0.1	12.5	99.3	0.7	100	46.4	0.6	46.9
ZrTP13	3 / 10 .	12.2	0.1	12.3	99.4	0.6	100	46.4	0.5	46.9
Average		12.1	0.1	12.2	99.3	0.7	100	46.4	0.5	46.9
ZrTP14	4 / 1 .	13.8	3.2	17.0	81.1	18.9	100	37.9	14.0	51.9
ZrTP14	4 / 2 .	11.6	2.4	14.0	82.8	17.2	100	38.7	12.8	51.5
ZrTP14	4 / 3 .	11.4	2.5	13.9	82.2	17.8	100	38.4	13.2	51.6
ZrTP14	4 / 4 .	11.3	2.5	13.7	82.1	17.9	100	38.4	13.3	51.6
ZrTP14	4 / 5 .	11.3	2.4	13.8	82.3	17.7	100	38.5	13.1	51.6
ZrTP14	4 / 6 .	11.4	2.5	13.9	81.8	18.2	100	38.3	13.4	51.7
ZrTP14	4 / 7 .	11.6	2.4	14.1	82.7	17.3	100	38.7	12.8	51.5
ZrTP14	4 / 8 .	11.5	2.5	14.0	81.9	18.1	100	38.3	13.4	51.7
ZrTP14	4 / 9 .	12.5	2.9	15.4	81.3	18.7	100	38.0	13.8	51.8
ZrTP14	4 / 10 .	11.5	2.4	13.9	82.6	17.4	100	38.6	12.9	51.5
Average		11.8	2.6	14.4	82.1	17.9	100	38.4	13.3	51.6
ZrTP34	12 / 1 .	9.4	1.7	11.1	85.0	15.0	100	39.7	11.1	50.8
ZrTP34	12 / 2 .	9.6	1.7	11.3	84.6	15.4	100	39.5	11.4	51.0
ZrTP34	12 / 3 .	9.4	1.6	11.0	85.3	14.7	100	39.9	10.9	50.8
ZrTP34	12 / 4 .	10.2	1.8	12.0	85.0	15.0	100	39.7	11.1	50.8

ZrTP34	12 / 5 .	9.6	1.6	11.3	85.4	14.6	100	39.9	10.8	50.7
ZrTP34	12 / 6 .	9.5	1.7	11.2	85.2	14.8	100	39.8	11.0	50.8
ZrTP34	12 / 7 .	9.0	1.6	10.6	85.3	14.7	100	39.9	10.9	50.8
ZrTP34	12 / 8 .	9.3	1.7	11.0	84.8	15.2	100	39.6	11.3	50.9
ZrTP34	12 / 9 .	9.4	1.6	11.0	85.5	14.5	100	40.0	10.7	50.7
ZrTP34	12 / 10 .	9.3	1.6	10.9	85.2	14.8	100	39.8	10.9	50.8
Average		9.5	1.7	11.1	85.1	14.9	100	39.8	11.0	50.8
ZrTP35	13 / 1 .	10.9	5.3	16.2	67.2	32.8	100	31.4	24.3	55.7
ZrTP35	13 / 2 .	11.1	5.4	16.5	67.2	32.8	100	31.4	24.3	55.7
ZrTP35	13 / 3 .	11.1	5.3	16.4	67.6	32.4	100	31.6	24.0	55.6
ZrTP35	13 / 4 .	11.0	5.3	16.4	67.4	32.6	100	31.5	24.1	55.6
ZrTP35	13 / 5 .	11.1	5.5	16.6	66.9	33.1	100	31.3	24.5	55.8
ZrTP35	13 / 6 .	11.1	5.3	16.3	67.8	32.2	100	31.7	23.8	55.5
ZrTP35	13 / 7 .	11.1	5.2	16.3	67.9	32.1	100	31.7	23.8	55.5
ZrTP35	13 / 8 .	10.9	5.3	16.3	67.3	32.7	100	31.5	24.2	55.7
ZrTP35	13 / 9 .	11.0	5.3	16.3	67.5	32.5	100	31.5	24.1	55.6
ZrTP35	13 / 10 .	11.0	5.2	16.2	67.6	32.4	100	31.6	24.0	55.6
Average		11.0	5.3	16.3	67.4	32.6	100	31.5	24.1	55.6
ZrTP40	14 / 1 .	7.5	4.0	11.6	65.1	34.9	100	30.4	25.8	56.3
ZrTP40	14 / 2 .	7.7	4.1	11.8	65.4	34.6	100	30.6	25.6	56.2
ZrTP40	14 / 3 .	7.1	3.8	10.9	65.2	34.8	100	30.5	25.7	56.2
ZrTP40	14 / 4 .	7.3	3.8	11.1	65.7	34.3	100	30.7	25.4	56.1
ZrTP40	14 / 5 .	7.7	4.1	11.9	65.2	34.8	100	30.5	25.8	56.2
ZrTP40	14 / 6 .	7.7	4.0	11.7	65.9	34.1	100	30.8	25.3	56.1
ZrTP40	14 / 7 .	7.7	4.2	11.9	64.9	35.1	100	30.3	26.0	56.3
ZrTP40	14 / 8 .	7.8	4.2	12.0	65.0	35.0	100	30.4	25.9	56.3
ZrTP40	14 / 9 .	7.8	4.0	11.8	66.0	34.0	100	30.8	25.2	56.0
ZrTP40	14 / 10 .	7.8	4.2	12.0	65.1	34.9	100	30.4	25.8	56.3
Average		7.6	4.0	11.7	65.3	34.7	100	30.5	25.7	56.2
ZrTP47	7 / 1 .	23.4	0.7	24.1	97.2	2.8	100	45.4	2.1	47.5
ZrTP47	7 / 2 .	23.8	0.6	24.5	97.4	2.6	100	45.5	2.0	47.5
ZrTP47	7 / 3 .	23.7	0.6	24.4	97.5	2.5	100	45.6	1.9	47.4
ZrTP47	7 / 4 .	23.8	0.6	24.4	97.4	2.6	100	45.5	1.9	47.4
ZrTP47	7 / 5 .	23.8	0.6	24.4	97.7	2.3	100	45.7	1.7	47.4
ZrTP47	7 / 6 .	23.9	0.6	24.4	97.6	2.4	100	45.6	1.8	47.4
ZrTP47	7 / 7 .	23.8	0.6	24.4	97.4	2.6	100	45.5	1.9	47.5
ZrTP47	7 / 8 .	23.7	0.6	24.3	97.4	2.6	100	45.5	1.9	47.4
ZrTP47	7 / 9 .	23.9	0.7	24.6	97.2	2.8	100	45.5	2.0	47.5
ZrTP47	7 / 10 .	23.6	0.6	24.2	97.4	2.6	100	45.5	2.0	47.5
Average		23.7	0.6	24.4	97.4	2.6	100	45.5	1.9	47.4

ZrTP46	8 / 1 .	9.1	2.0	11.0	82.1	17.9	100	38.4	13.3	51.6
ZrTP46	8 / 2 .	9.1	2.1	11.2	81.4	18.6	100	38.1	13.8	51.8
ZrTP46	8 / 3 .	9.1	2.0	11.1	82.0	18.0	100	38.3	13.3	51.7
ZrTP46	8 / 4 .	8.9	2.0	11.0	81.5	18.5	100	38.1	13.7	51.8
ZrTP46	8 / 5 .	9.0	2.0	11.0	81.9	18.1	100	38.3	13.4	51.7
ZrTP46	8 / 6 .	9.4	2.1	11.5	81.9	18.1	100	38.3	13.4	51.7
ZrTP46	8 / 7 .	9.0	1.9	10.9	82.6	17.4	100	38.6	12.9	51.5
ZrTP46	8 / 8 .	9.0	2.0	11.0	82.1	17.9	100	38.4	13.2	51.6
ZrTP46	8 / 9 .	9.0	2.0	10.9	81.8	18.2	100	38.3	13.4	51.7
ZrTP46	8 / 10 .	8.5	1.9	10.4	81.5	18.5	100	38.1	13.7	51.8
ZrTP46	8 / 11 .	8.8	1.9	10.7	82.3	17.7	100	38.5	13.1	51.6
Average		9.0	2.0	11.0	81.9	18.1	100	38.3	13.4	51.7
ZrTP49	6 / 1 .	7.4	0.3	7.7	96.4	3.6	100	45.1	2.6	47.7
ZrTP49	6 / 2 .	6.9	0.2	7.2	96.6	3.4	100	45.2	2.5	47.7
ZrTP49	6 / 3 .	7.4	0.3	7.7	96.2	3.8	100	45.0	2.8	47.8
ZrTP49	6 / 4 .	7.1	0.2	7.4	96.7	3.3	100	45.2	2.4	47.6
ZrTP49	6 / 5 .	7.1	0.3	7.4	95.8	4.2	100	44.8	3.1	47.9
ZrTP49	6 / 6 .	7.2	0.2	7.4	97.0	3.0	100	45.4	2.2	47.6
ZrTP49	6 / 7 .	8.3	0.3	8.6	96.5	3.5	100	45.1	2.6	47.7
ZrTP49	6 / 8 .	7.0	0.3	7.3	96.5	3.5	100	45.1	2.6	47.7
ZrTP49	6 / 9 .	7.1	0.2	7.4	96.9	3.1	100	45.3	2.3	47.6
ZrTP49	6 / 10 .	7.1	0.3	7.4	96.5	3.5	100	45.1	2.6	47.7
Average		7.3	0.3	7.5	96.5	3.5	100	45.1	2.6	47.7
ZrTP51	5 / 1 .	3.8	1.2	5.0	76.1	23.9	100	35.6	17.7	53.3
ZrTP51	5 / 2 .	4.5	1.4	5.9	76.2	23.8	100	35.6	17.6	53.2
ZrTP51	5 / 3 .	3.5	1.2	4.7	73.6	26.4	100	34.4	19.5	53.9
ZrTP51	5 / 4 .	3.9	1.2	5.1	76.1	23.9	100	35.6	17.7	53.3
ZrTP51	5 / 5 .	3.9	1.2	5.1	76.5	23.5	100	35.8	17.4	53.1
ZrTP51	5 / 6 .	4.4	1.2	5.6	78.0	22.0	100	36.5	16.3	52.8
ZrTP51	5 / 7 .	3.7	1.2	4.9	75.8	24.2	100	35.4	17.9	53.3
ZrTP51	5 / 8 .	4.1	1.4	5.4	75.1	24.9	100	35.1	18.5	53.6
ZrTP51	5 / 9 .	4.1	1.4	5.6	74.2	25.8	100	34.7	19.1	53.8
ZrTP51	5 / 10 .	3.8	1.2	5.0	75.9	24.1	100	35.5	17.8	53.3
Average		4.0	1.3	5.2	75.8	24.2	100	35.4	17.9	53.4
ZrTP52	9 / 1 .	7.0	2.3	9.4	74.9	25.1	100	35.0	18.6	53.6
ZrTP52	9 / 2 .	8.3	2.7	11.0	75.5	24.5	100	35.3	18.2	53.4
ZrTP52	9 / 3 .	7.9	2.7	10.6	74.5	25.5	100	34.8	18.9	53.7
ZrTP52	9 / 4 .	7.0	2.4	9.4	74.3	25.7	100	34.7	19.0	53.8
ZrTP52	9 / 5 .	6.9	2.3	9.3	74.7	25.3	100	34.9	18.8	53.7

ZrTP52	9 / 6 .	6.8	2.3	9.1	74.6	25.4	100	34.9	18.8	53.7
ZrTP52	9 / 7 .	6.7	2.2	8.8	75.4	24.6	100	35.3	18.2	53.4
ZrTP52	9 / 8 .	6.9	2.3	9.2	75.1	24.9	100	35.1	18.4	53.5
ZrTP52	9 / 9 .	7.0	2.4	9.3	74.7	25.3	100	34.9	18.7	53.6
ZrTP52	9 / 10 .	7.0	2.4	9.3	74.8	25.2	100	35.0	18.7	53.6
Average		7.2	2.4	9.6	74.9	25.1	100	35.0	18.6	53.6
ZrTP53	10 / 1 .	8.7	5.2	13.9	62.7	37.3	100	29.3	27.6	56.9
ZrTP53	10 / 2 .	8.7	5.1	13.8	62.8	37.2	100	29.3	27.6	56.9
ZrTP53	10 / 3 .	8.7	5.0	13.7	63.4	36.6	100	29.6	27.1	56.7
ZrTP53	10 / 4 .	8.7	5.2	13.9	62.9	37.1	100	29.4	27.5	56.9
ZrTP53	10 / 5 .	8.7	5.2	13.9	62.7	37.3	100	29.3	27.6	56.9
ZrTP53	10 / 6 .	8.6	5.2	13.8	62.6	37.4	100	29.3	27.7	56.9
ZrTP53	10 / 7 .	8.8	5.1	13.9	63.3	36.7	100	29.6	27.2	56.8
ZrTP53	10 / 8 .	8.8	5.2	13.9	63.0	37.0	100	29.4	27.4	56.8
ZrTP53	10 / 9 .	8.7	5.2	14.0	62.5	37.5	100	29.2	27.8	57.0
ZrTP53	10 / 10 .	8.7	5.1	13.8	63.1	36.9	100	29.5	27.3	56.8
Average		8.7	5.1	13.9	62.9	37.1	100	29.4	27.5	56.9
ZrTP54	11 / 1 .	13.3	0.4	13.8	96.7	3.3	100	45.2	2.4	47.6
ZrTP54	11 / 2 .	13.3	0.5	13.8	96.4	3.6	100	45.1	2.7	47.7
ZrTP54	11 / 3 .	13.3	0.5	13.8	96.3	3.7	100	45.0	2.8	47.8
ZrTP54	11 / 4 .	14.4	0.5	14.9	96.7	3.3	100	45.2	2.4	47.6
ZrTP54	11 / 5 .	13.4	0.5	13.8	96.7	3.3	100	45.2	2.5	47.7
ZrTP54	11 / 6 .	14.7	0.5	15.2	96.7	3.3	100	45.2	2.5	47.7
ZrTP54	11 / 7 .	13.4	0.5	13.9	96.6	3.4	100	45.2	2.5	47.7
ZrTP54	11 / 8 .	13.4	0.5	13.9	96.3	3.7	100	45.0	2.7	47.7
ZrTP54	11 / 9 .	13.5	0.4	13.9	96.9	3.1	100	45.3	2.3	47.6
ZrTP54	11 / 10 .	13.4	0.4	13.9	96.8	3.2	100	45.2	2.4	47.6
Average		13.6	0.5	14.1	96.6	3.4	100	45.2	2.5	47.7